Past, present, and future climate impacts of aviation

by
Carla Grobler

B.Eng., University of Pretoria (2013)
B.Eng. (Hons), University of Pretoria (2014)
M.Eng., University of Pretoria (2016)
M.Sc., Massachusetts Institute of Technology (2023)

Submitted to the Department of Aeronautics and Astronautics
in partial fulfillment of the requirements for the degree of
Doctor of Philosophy in Aeronautics and Astronautics
at the

MASSACHUSETTS INSTITUTE OF TECHNOLOGY

February 2024

Authored by: Carla Grobler
Department of Aeronautics and Astronautics
December 13, 2023

Certified by: Steven R.H. Barrett
Professor of Aeronautics and Astronautics,
Thesis Supervisor

Certified by: Ronald G. Prinn
Professor of Earth, Atmospheric, and Planetary Sciences,
Committee Member

Certified by: Irene C. Dedoussi
Associate Professor, Faculty of Aerospace Engineering, TU Delft
Committee Member

Certified by: Florian Allroggen
Research Scientist, Aeronautics and Astronautics
Committee Member

Accepted by: Jonathan P. How
Professor of Aeronautics and Astronautics
Chair, Graduate Program Committee

Abstract

Past, present, and future climate impacts of aviation

By

Carla Grobler

Submitted to the Department of Aeronautics and Astronautics
in partial fulfillment of the requirements for the degree of
Doctor of Philosophy in Aeronautics and Astronautics
at the Massachusetts Institute of Technology

Thesis supervisor: Steven R.H. Barrett
Title: Professor of Aeronautics and Astronautics

Abstract

Commercial aviation is one of the hardest-to-decarbonize contributors to climate change and accounts for approximately 5% of anthropogenic radiative forcing due to its CO_2 and non-CO_2 emissions. As the industry grows faster than its efficiency improvements, aligning its growth with international climate goals becomes increasingly urgent and challenging. To enable data-driven decision-making, this thesis investigates aviation's historical emissions, present-day climate impacts, current damages due to marginal emission changes, and potential pathways to reach net-zero climate impacts by 2050.

First, the research develops a consistent bottom-up emissions inventory for commercial civil passenger aviation from 1980-2019, quantifying how emissions patterns such as spatial, temporal, and compositional characteristics have varied over time. Results show that, while fuel consumption increased by 330%, capacity, measured as available seat miles, grew by 560%. This growth has been regionally heterogeneous, with the emissions share over Asia growing from 7% to 23%, while emissions share over North America decreased from 55% to 25%. Over this time, the share of nighttime fuel consumption increased from 30% to 38%, due to an increase in aircraft utilization. Additionally, there has been a shift in the emissions composition, with the nitrogen oxides (NO_x) emissions index increasing by 20%, while the non-volatile particulate emissions index decreased by 70%.

Second, this thesis quantifies aviation's present-day climate effects using the bottom-up emissions inventory described above. Since contrails are responsible for an estimated 57% of aviation's effective radiative forcing, we place a particular focus on modeling contrails. Using a medium-fidelity aircraft plume model and ERA5 reanalysis weather data, our results indicate that contrail impacts increased by 460% from 1980 to 2019, outpacing growth in annual fuel consumption. Per flight distance, contrail impacts varied less than 10% over this time. However, underlying drivers did not remain constant. The fraction of flight segments that cause contrails increased by 32%, while the radiative forcing per distance of contrail decreased by 24%. We additionally quantify for the first time how different assumptions regarding the treatment of contrails mixing with ambient air could change their lifetime by a factor of three.

Third, this thesis calculates the impacts of marginal changes in aviation emissions on climate and air quality, supporting cost-benefit analyses of emissions interventions. Climate and air quality impacts are monetized on a per unit emissions basis, using a simplified climate model and sensitivities from the GEOS-Chem global chemistry-transport model. We find that cruise emissions account for 90% of impacts per fuel unit, with 49-81% arising from air quality effects depending on the discount rate. Collectively NO_x, CO_2, and contrails cause 97% of the total impact. By estimating the first-order contribution to variance we find that the equilibrium climate sensitivity, climate damage function, and value of statistical life contribute to the greatest uncertainty in outputs.

Finally, we evaluate pathways through which alternative energy carriers and avoidance of non-CO_2 impacts could lead aviation towards net-zero climate impacts by the year 2050. We consider the alternative energy carriers: synthetic fuels from biomass; synthetic fuels from green hydrogen and atmospheric CO_2; and the direct use of green liquid hydrogen. We also perform a meta-analysis to evaluate how these alternative fuels could affect the non-CO_2 impacts and how contrails can be avoided through small scale adjustments in flight altitude. We find that 50% of fleet-wide contrail length can be avoided for a 0.88% fleet-wide fuel burn penalty (5th to 95th percentile range 0 to 2.51). Thereafter avoiding subsequent contrails becomes more fuel costly, with an additional 20% avoidance requiring double the additional fuel. Together with continued efficiency gains, and assuming 50% avoidance of contrails, such an energy transition could reduce annual lifecycle aviation CO_2 emissions by 89-94% compared to year-2019 levels, despite a 2-3-fold growth in demand by 2050. If these costs were passed directly on to passengers, ticket prices would rise by no more than 15% compared to a no-intervention baseline. However, the pathways we identify reduce aviation CO_2-equivalent emissions by 46-69% only; more action is required to mitigate non-CO_2 impacts.

Collectively, this thesis provides perspective into aviation's past, present, and future climate impacts. These results indicate substantial growth and impacts over the past 40 years, and highlight CO_2 and contrails as the largest contributors. Though, through sustained investment in alternative fuels, and contrail avoidance measures, our results also indicate, future mitigation is possible. However, to meet the global climate goal of net zero emissions by 2050, the transition needs to start now.

Acknowledgments

Completing this doctoral journey has been akin to playing in an orchestra where past maestros have composed the symphony I now perform. While it is beyond my capacity to individually recognize everyone who has played a role in this journey, I am eager to gratefully highlight the following.

First and foremost, I owe a debt of gratitude to my supervisors, Seb, Florian, and Steven. Their relentless guidance, encouragement, and insightful critiques have shaped the contours of this thesis. I am also deeply thankful to the members of my committee, Irene and Professor Ronald Prinn, whose input and direction were crucial to my research. My heartfelt thanks to Ray and Jayant for all your guidance over the years.

I'm also deeply grateful for the developers behind the open-source software - specifically, the creators of the Pandas and GeoPandas libraries. Your commitment to the open-source community has not only facilitated my research but also the work of many others in countless ways.

Without financial support, this research would not have been possible. I am grateful to the FAA, Energy Foundation, the VoLo Foundation, and the MIT Martin Family Fellowship for Sustainability, and the CSIR in South Africa. Though the views presented in this thesis are my own, I am deeply appreciative of the opportunities your funding has afforded me.

To my friends at the Laboratory for Aviation and the Environment (LAE), I cannot thank you enough for the camaraderie and for creating an environment that is as inspiring as it is supportive. To the "LAE newbies" – Drew, Ines, Prashanth, Kingshuk, Thibaud, and honorary members; Akshat and Guillaume – your companionship and humor have been the highlights of many days. A special note of thanks to Prashanth, whose presence and support were unwavering, especially towards the final stages of this journey. I also wish to thank Esther, and the "COVID cohort" – China, Joonhee, Jad, Jamie, Louis, and Lukas – for their solidarity and friendship as we came out through unprecedented times. Juju for your friendship, your fun and thoughtful questions, and all the dining hall dinners. Thank you also for the whole LAE & ICAT lunch club. Taking a break with you all was the highlight of my day - many days. Also special thanks to Thibaud, Vincent, and Micheal for your willingness to teach me all about APCEMM and contrails. To the Back Bay CG, thank you for being a family so far from home for Paul, myself, and Adriaan. Joyce, I'm sad I only got to know you during the final parts of my journey here. I know you will always be able to teach me many things. Thanks for being so efficient, and especially thank you for your help in scheduling the defense - your organizational skills brought order to my chaos.

Mamma en Pappa, your example has been my guiding light – dankie vir alles. To my new enlarged family (Ma Louise, Pa Fanus, van der Zees, Strausse, & Groblers) thank you for your unwavering support for Paul and me. Anja, Johan, & Marli, thank you for being the coolest of brothers and sisters, and for all the COVID Zoom and Hanabi.

To my little boy, Adriaan, the cutest and most cooperative napper – your smiles have possibly been the highlight of the whole PhD, and the best breaks I've ever taken.

And finally, to Paul, my husband and stalwart supporter, your love, patience, and understanding made our Boston home a sanctuary of warmth and inspiration. Your support has been the wind beneath my wings. I cherish the thought of our upcoming adventures together. I love you deeply.

Each one of you has left a mark on my journey, and for this, I am forever grateful. Thank you.

Table of Contents

Chapter 1

Introduction

In today's interconnected world, aviation has evolved into an indispensable component of the global economy. Estimated to contribute 65.5 million jobs, and 3.6% of global gross domestic product in 2016 (ATAG, 2018; ICAO, 2019), aviation facilitates trade and enables swift mobility for millions of people, as well as rapid transportation of goods across the world.

While a precious commodity, aviation is responsible for emissions that cause adverse impacts on the environment, with the industry accounting for 2.4% of global annual anthropogenic CO_2 emissions and influencing the climate through a variety of non-CO_2 forcing pathways (Brasseur et al., 2016; Lee et al., 2020). Collectively, these non-CO_2 climate impacts are estimated to triple aviation's effective radiative forcing, where effective radiative forcing is a measure of the net energy balance change at the top of the atmosphere (Lee et al., 2020). These non-CO_2 pathways include a direct black carbon warming impact, a direct high-altitude water vapor warming impact, a semi-direct fuel sulfur cooling impact, and a set of multi-scale indirect impacts of mixed sign resulting from oxides of nitrogen (NO_x) emissions. The indirect NO_x impacts include the short-term formation of nitrate aerosol (cooling) and production of tropospheric ozone (warming), which, in turn, leads to an increase in OH radical concentrations, and a consequent reduction in atmospheric methane concentrations (cooling), and subsequent reduction in tropospheric ozone (cooling) and stratospheric water vapor (cooling) (Wild et al., 2001). Finally, aviation emissions also cause condensation trails (contrails), artificial line-shaped clouds that form in the wake of an aircraft under sufficiently cold and moist atmospheric conditions. If contrails persist for more than a few hours, they spread, absorbing water vapor from the atmosphere, thus becoming indistinguishable from natural cirrus clouds. Notably, of these non-CO_2 impacts, the most significant is associated with contrails, which are estimated to account for double the effective radiative forcing of aviation's cumulative CO_2 emissions (Lee et al., 2020). The impacts of these emissions differ from other industries, since ~90% of the fuel burn occurs in the cruise flight phase at high altitudes (Simone et al., 2013).

Collectively, these adverse climate effects raise significant concerns among environmental scientists, policymakers, and the aviation industry itself. The unique challenge stems from the inherently difficult nature of decarbonizing the aviation sector, characterized by weight constraints and the complex array of non-CO_2 forcing pathways. Moreover, due to the industry's substantial investments in long-lived assets and high-cost infrastructure, today's decisions regarding investments and technology will have far-reaching consequences for future emissions.

Decarbonization of the aviation sector demands not only a thorough understanding of **historical** emissions and their **current** consequences but also the identification of the range of potential **future** energy and technological pathways that align with these global climate objectives.

1.1. Current knowledge and research needs

Though previous studies have investigated facets of this challenge, key knowledge gaps remain in the understanding of **past** emissions, **present** impacts, and **future** pathways for aviation to decarbonize.

1.1.1. Research need: Trends in aviation emissions since the start of the jet age

Accurately capturing how aviation's emissions have evolved since the start of the jet age is essential for understanding this pressing problem. Its importance is threefold. Firstly, quantifying these emissions is crucial for quantifying the present-day climate impacts of aviation. Such a time horizon is critical given that aviation emissions continue to impact the climate for decades to centuries, through long-lived climate forcers, such as CO_2 and methane, in addition to producing long-lived changes in global surface temperature. Secondly, without accurate records of past emissions, interpreting observed or modeled changes and calibrating models becomes challenging. Third, understanding these emissions is instrumental in forecasting future emission trends, which would enable informed mitigation strategies and policy development to tackle these climate problems.

However, a consistent bottom-up emissions inventory commencing with the jet age is unavailable. As such, estimates of aviation's non-CO_2 impacts remain approximate. One significant obstacle in deriving an accurate historic emissions inventory for aviation is the fragmentation of historical data sources. Emissions inventories have been developed focusing on specific years and/or periods of aviation emissions, including: studies by NASA and Boeing focusing on years 1976-1999 (Baughcum et al., 1996b, 1996a; Sutkus et al., 2001) AERO2K for the year 2002; emissions inventories from the U.S. Federal Aviation Administration's (FAA) Aviation Environmental Design Tool (AEDT) covering 2005 to 2015 (Wilkerson et al., 2010) a recent emissions inventory by Quadros et al. (2022) for 2017 to 2020; as well as a high resolution emissions inventory derived using ADS-B data by Teoh et al. (2023). While these studies are valuable for studying certain timeframes, they face the challenge of varying assumptions and methodologies across different research efforts. This inconsistency inhibits the ability to create a cohesive historical emissions inventory with consistent trends. Additionally, for periods preceding 2005, these studies often focus on a limited set of emissions species, excluding critical factors such as non-volatile particulate matter (nvPM) emissions and their climate impacts. As such, this precludes estimates of contrail impacts, which are a major climate forcer.

To gain a comprehensive understanding of cumulative climate impacts, calibrate present-day observations and models, and provide a solid foundation for future projections, the derivation of a consistent, bottom-up emissions inventory spanning the jet age is a necessity.

1.1.2. Research need: Accumulated present-day climate impacts of aviation

Understanding how these emissions since the start of the jet age have contributed to aviation's climate impacts is essential for guiding future strategies. Firstly, evaluating the current and future climate effects due to the past emissions can aid in determining the remaining emissions allowance to meet different climate targets. Secondly, discerning which emissions trends have influenced climate impacts aids in forecasting future climate effects and directing appropriate strategies. Moreover, knowing the relative magnitudes of the different forcing pathways highlights which emission types or pathways warrant concentrated research and mitigation attention.

While some studies have sought to estimate aviation's cumulative climate impacts, their methods have limitations. One prevalent method is the global fuel burn or emissions scaling approach as applied in recent studies aiming to quantify aviation's cumulative climate impacts (Klöwer et al., 2021; Lee et al., 2020). However, this method does not account for or inform how the evolving spatial, temporal, and compositional nature of emissions have affected the subsequent climate impacts over time.

Contrail impacts are especially sensitive to such differences in emissions characteristics. Changes in the emissions region can affect contrail impacts by up to a factor of two (Lund et al., 2017a). The altitude of emissions is also important, with a 6000 ft change in cruise altitude leading to 10-50% change in subsequent radiative forcing (Fichter et al., 2005; Frömming et al., 2012; Grewe et al., 2017a). Additionally, the season of emissions can affect the subsequent impacts by up to a factor of two to five (Stuber et al., 2006; Yin et al., 2018) and emissions composition, such as a 50 to 90% change in particle number emissions, can affect the subsequent climate impacts by 20 to 90% (Burkhardt et al., 2018; Caiazzo et al., 2017; Teoh et al., 2020).

1.1.3. Research need: Evaluation of trade-offs of present-day emissions interventions

To rapidly identify avenues for reducing aviation's atmospheric impacts, and target the emissions species with the largest impacts, decision makers require a method to rapidly evaluate the benefits and trade-offs of present-day emissions changes. However, evaluating these emissions benefits and emissions trade-offs remains complex.

Firstly, comparison difficulties arise due to a mismatch in climate impact time scales between the different emissions species. While emitted CO_2 remains in the atmosphere for decades to centuries after it is emitted (Solomon et al., 2010), the non-CO_2 aviation-related forcers, manifest their climate effects over shorter periods—typically a few days to decades.

Adding to the complexity, aviation emissions also have an adverse impact on air quality. The industry is estimated to cause 16,000 to 24,000 premature mortalities annually through population exposure to fine particulate matter and ozone (Eastham and Barrett, 2016; Prashanth et al., 2022; Quadros et al., 2020). These climate and air quality trade-offs are complex to consider, since global temperature change, and change in mortalities are not on the same basis and cannot easily be compared. Moreover, design or policy decisions that might decrease emissions of a species that leads to high climate impacts, such as CO_2, might lead to changes in emissions of a species, such as NO_x, that lead to air quality impacts (Lefebvre, 1983; Lieuwen and Yang, 2013; Miller et al., 2022).

To evaluate these trade-offs, various metrics have been published. However, these metrics either: only accounted for the climate impacts and did not evaluate air quality (Fuglestvedt et al., 2010);

are designed for primarily non-aviation emissions (Berk et al., 2006; Driscoll et al., 2015; Shindell et al., 2016); or do not include cruise emissions, which make up ~90% of aviation's fuel burn (Dorbian et al., 2011).

Therefore, to facilitate rapid evaluation of emissions interventions, consistent metrics are necessary that quantify both climate and air quality impacts on a common basis for changes in each of the different emissions species.

1.1.4. Research need: Pathway for aviation to reach net zero climate impacts by 2050

Achieving the goal of the Paris climate agreement is a global priority. This agreement strives to cap global warming at 1.5 °C above preindustrial times (UNFCCC, 2017). Research indicates that without considering negative emissions, every sector must neutralize its climate impacts by 2050 (United Nations, 2023).

This goal is particularly challenging for aviation, a sector with high projected growth, long-lived assets, no commercially available, scalable carbon-neutral technology, and non-CO_2 climate impacts on the same order of magnitude as its CO_2 impacts.

Various studies have investigated energy and CO_2 pathways for aviation to reach net zero CO_2 emissions (Girod et al., 2012; Gössling et al., 2021; Grewe et al., 2021; IEA, 2021, 2019; Kar et al., 2009; Leipold et al., 2021; Schäfer et al., 2015; Sharmina et al., 2021; US Government, 2015; van der Sman et al., 2021). However, most of these studies explore limited (regional scopes

(Hassan et al., 2018; Schäfer et al., 2015; US Government, 2015; van der Sman et al., 2021); exclude non-drop-in fuels, such as hydrogen (Girod et al., 2012; Gössling et al., 2021; Grewe et al., 2021; IEA, 2021, 2019; Kar et al., 2009; Leipold et al., 2021; Schäfer et al., 2015; Sharmina et al., 2021; US Government, 2015; van der Sman et al., 2021); do not examine transition costs (Kar et al., 2009; Leipold et al., 2021); or do not quantify non-CO_2 impacts (Girod et al., 2012; Gössling et al., 2021; IEA, 2021; Kar et al., 2009; Schäfer et al., 2015; Sharmina et al., 2021; US Government, 2015; van der Sman et al., 2021). Additionally, none of these studies included measures to avoid the non-CO_2 impacts of aviation, such as contrails, thereby neglecting approximately half of aviation's warming impacts.

As such, for aviation to meet the goals set out by the Paris agreement, cost, energy, and emissions pathways need to be identified that account for both the alternative energy options, as well as avoidance of the non-CO_2 impacts.

1.2. Thesis contributions and organization

Bridging these gaps is critical to inform effective policies and investments that align aviation's growth with global climate objectives. This thesis aims to address these gaps by analyzing aviation's **past**, **present**, and **future** climate impacts to support informed mitigation efforts.

Chapter 2 presents the first bottom-up emissions inventory for commercial civil passenger aviation spanning the jet age from 1980 to 2019. The inventory is derived with consistent assumptions, allowing emissions trends to be investigated. These trends include regional changes in emissions, altitude of emissions, seasonality, hourly trends, and emissions composition. This work enables the first quantification of aviation's cumulative present day climate impacts, and investigation of how these climate impacts have varied over time.

Chapter 3 quantifies, for the first time, the present-day cumulative climate impacts due to aviation emissions, while accounting for changes in the aircraft fleet, global distribution of traffic, and meteorology over time. An in-depth quantification of contrail impacts is presented using a medium fidelity aircraft plume model, which simulates the contrail formation, persistence, and evaporation while keeping track of particle sizes. Using these results, we show how contrail formation and subsequent effects have varied over time, and which factors have contributed to these variations.

Chapter 4 presents a quantification of the climate and air quality impacts of a marginal unit of aviation emissions, for present-day emissions patterns. This work provides insights into which aviation emissions species lead to the highest climate and air quality damages. Presented on a consistent basis for climate and air quality, these results can be used as decision tool to rapidly evaluate both climate and air quality impacts of emissions trade-offs. Furthermore, since we present these impacts on a cost basis, these results facilitate rational decision making.

Chapter 5 focuses on how the aviation industry could mitigate these impacts by presenting the costs and emissions for various energy pathways as aviation aims to reach net zero climate impacts by 2050. We explicitly quantify non-CO_2 impacts, and potential costs and benefits of contrail avoidance. This work was done with collaborators, including Lynnette Dray who led the pathway analysis of the aviation system, Andreas W. Schäfer, Christoph Falter, Florian Allroggen who investigated the fuel costs and availability, and together with Marc E.J. Stettler, my role was to lead the quantification of contrail avoidance, and quantify the climate impacts of the various pathways.

Each chapter includes its own introductory statement, literature review, methods and results sections, and chapter conclusions. Each chapter also discusses how these results can be used by decisions makers to enable mitigation of future emissions and impacts.

As the aviation industry seeks to align with global climate goals, this thesis provides timely insights to inform these mitigation efforts. By quantifying historical emissions, current impacts, and future solutions, the research profiles aviation's climate footprint, and options to reduce it. Though uncertainties remain, the findings directly support policies and investments needed to cost-effectively decarbonize aviation by 2050.

Chapter 2

Emissions inventory for commercial civil aviation spanning the jet age from 1980 to 2019

2.1. Introduction

Aviation emissions since the start of the jet age continue to cause present-day climate impacts through CO_2 and non-CO_2 impacts (Grobler et al., 2019; Lee et al., 2020). These emissions are estimated to account for 3.5% of present-day global anthropogenic effective radiative forcing (Lee et al., 2020). In addition, aviation emissions cause adverse global air quality through the production of fine particulate matter and ozone, leading to an estimated 16,000 to 24,000 premature mortalities annually (Eastham and Barrett, 2016; Prashanth et al., 2022; Quadros et al., 2020).

These impacts are sensitive to the emissions characteristics, including the emissions region, altitude, season, and composition. For example, Lund et al. (2017a) found a factor two increase in the global surface temperature change depending on the region of aviation emissions. Gilmore et al. (2013) found global ozone production attributable to aviation emissions varies by up to a factor five depending on the location and season of the emissions. Contrails impacts, which are responsible for 57% of aviation's effective radiative forcing (Lee et al. 2020), could be affected by soot emissions per unit fuel burn, with sources indicating a 73-80% reduction in particle number emissions could lead to a 45-82% reduction in contrail impacts (Burkhardt et al., 2018; Teoh et al., 2020). Furthermore, impacts have been shown to be sensitive to altitude of emissions, with contrails RF decreasing by 45% for a 6000 ft reduction in cruise altitude (Fichter et al., 2005) and NO_x related warming by to change by 40% for a uniform 2000 ft increase or decrease in cruise altitude (Søvde et al., 2014).

Current studies suggest the spatial-temporal pattern of aviation emissions have changed over time, with present day aircraft being more efficient, cruising at different altitudes, and leading to a different emissions composition. In addition, global emissions patterns have changed with aviation traffic growth in East Asia outpacing growth in the rest of the world by 40 percentage points over the last 20 years (ICAO, 2020).

These emissions not only affect climate impacts in the past, but also affect the present-day and future climate and air quality impacts, since these impacts continue to propagate over years to decades through their impact on global surface temperature and changes in global surface ozone (Cameron et al., 2017; Klöwer et al., 2021; Yim et al., 2015).

Current estimates of present-day climate and air quality impacts rely on bottom-up emissions inventories from single years of aviation emissions (Brasseur et al., 2016; Cameron et al., 2017; Søvde et al., 2014). These emissions inventories include: the NASA-Boeing inventory for years 1979-1999 (Baughcum et al., 1996b, 1996a; Sutkus et al., 2001); AERO2K, which is based on the year 2002 (Eurocontrol, 2003); AEIC for 2006 (Simone et al., 2013); emissions inventories from the U.S. Federal Aviation Administration's (FAA) Aviation Environmental Design Tool (AEDT) covering 2005 to 2015 (Wilkerson et al., 2010); a recent emissions inventory by Quadros et al. (2022) for 2017 to 2020; as well as a high resolution emissions inventory derived using ADS-B data by Teoh et al. (2023). However, since these emissions inventories only focus on specific emissions years, and the studies do not have consistent assumptions, these studies do not inform how emissions location, time or compositions have changed over time. In addition, only more recent emissions inventories have included estimates of non-volatile Particulate Matter (nvPM), thereby limiting their usefulness for studying contrails over time. As such, present day quantifications of aviation's cumulative climate impacts have been limited to global fuel or emissions scaling approaches (Klöwer et al., 2021; Lee et al., 2020).

In this chapter, we derive the first bottom-up emissions inventory for global commercial civil passenger aviation spanning the jet age from 1980 to present day. This inventory will capture differences in region, altitude, time of day, season, and chemical composition of the emissions over this time span. As such, we will obtain insights into how changes in regional traffic, fleet composition as well as aircraft and engine design have changed the significance of pathways through which aviation impacts the climate and air quality.

2.2. Methods

2.2.1. Methods overview

We derive the bottom-up emissions inventory using aviation schedule data to identify aircraft traffic patterns (Section 2.2.2). This traffic data is combined with aircraft performance data, to derive fuel burn, and emissions locations, using great circle routes (Section 2.2.3). Finally, a description of how carbon dioxide (CO_2), water vapor (H_2O), oxides of nitrogen (NO_x), oxides of sulfur (SO_x), carbon monoxide (CO), hydrocarbon (HC), and non-volatile particulate matter (nvPM) emissions quantities are derived is presented (Section 2.2.3).

2.2.2. Aviation schedule data

To compile our bottom-up emissions inventory, aviation traffic data is obtained from the Official Airline Guide (OAG), in the form of global schedule data. For the timeframe 1980-2010, this data is obtained on a 5-year frequency. From 2013-2019, this data is on an annual frequency. Given the sparsity of coverage of OAG data for freight, we focus this study on passenger flights, and only include flights from the OAG data that carry passengers or a mix of passengers and freight.

In 1980, this data includes 110 unique aircraft types, and 4163 unique airports globally. By 2019, the number of unique aircraft types has expanded to 191, and 4163 airports are included. Fields used in this thesis include departure and arrival airports, local time of departure and arrival, flight time, flight distance, number of seats, aircraft type, and operating carrier.

The schedule data is cleaned to remove duplicate flights. This includes the removal of duplicates due to code-share agreements, and the removal of multileg flights since these flights are also included in the data as individual flights. After cleaning, the data includes 14.2 million departures in 1980, and 38.7 million in 2019, with totals differing less than 1% from passenger flight industry statistics provided by the International Civil Aviation Organization (ICAO) for the year 2019 (ICAO, 2020).

To ensure emissions times are accurately captured, departure and arrival times are converted from local times, as listed in the OAG schedule data, to Coordinated Universal Time (UTC) time using the python library *pytz* (Bishop, 2022). This library provides time zone offsets for all global locations, for any user specified date, thereby accounting for changes in time zones over time, such as any advent or termination in daylight savings time.

Using schedule data provides a consistent data source spanning the full period from 1980-2019. However, this approach does not capture real-time flight changes such as last-minute cancellations or delays. Furthermore, the OAG data likely omits some charter flights, which may have comprised a notable share of European operations during the mid-1990s. The OAG data availability and coverage also varies for certain regions and time periods. For example, flight records might be limited for the Soviet Union prior to its dissolution in 1991. While these factors introduce uncertainties, schedule data enables a long-term perspective unmatched by other data sources. The targeted inclusion of charter and other supplemental flight data could reduce coverage gaps in future work.

2.2.3. Fuel burn and emissions quantification

Fuel burn and emissions are quantified using the Aviation Emissions Inventory Code (AEIC) (Simone et al., 2013). This model integrates the OAG aircraft schedule data with aircraft performance data and airport locations to quantify fuel burn and subsequent emissions. A full model description is available in Simone et al. (2013) and a model overview, including model updates made during this thesis, is provided here.

For the cruise flight phase, here taken as the flight portion above 3000 ft, the Eurocontrol Base of Aircraft Data (BADA) version 3.16 is applied to quantify aircraft performance and fuel burn (Eurocontrol, 2022). This version comprises 264 unique aircraft, with an additional 1568 aircraft modeled using surrogates. Fuel burn for the landing and take-off (LTO) flight phase, here defined as the flight potion below 3000 ft, is determined using ground-level fuel burn data from the ICAO Aircraft Engine Emissions Databank (EDB) (ICAO, 2022), in conjunction with times-in-mode (TIM) as described in Stettler et al. (2011).

Emissions quantities of CO_2 and water vapor are directly correlated to fuel burn. They are quantified using emission indices of 3.159 kg_{CO2}/kg_{fuel} and 1.231 kg_{H2O}/kg_{fuel}, respectively as based on the chemical composition of Jet-A (Barrett et al., 2010b; Hileman et al., 2010). Sulfur emissions are contingent on the fuel sulfur content and are assumed at a concentration of 600 ppm, in alignment with the findings of Hileman, Stratton, and Donohoo, (2010).

Engine parameters and operating conditions affect emissions of NO_x, CO, HC, nvPM. As such, ground level measurements, for each different engine, at various thrust settings, is used as reported in the EDB (ICAO, 2022).

During the LTO flight phase, emissions indices at various engine thrust settings are directly available from the EDB for NO_x, CO, and HC. Direct measurements of nvPM mass and number emissions in the EDB are limited to more recent engines. For older engines, the EDB only reports SMOKE numbers, a metric indicating the change in reflectance of a filter paper after engine exhaust gas has passed through (ICAO, 2008). When available, direct measurements from the EDB are applied. In cases where only SMOKE numbers exist, nvPM mass and number emissions are derived using the Smoke Correlation for Particle Emissions - CAEP11 (SCOPE11) method (Agarwal et al., 2019).

For the cruise flight phase, the emissions measurements of NO_x, CO, HC, are adapted to cruise altitude by leveraging the Boeing Fuel Flow Method 2 (Baughcum et al., 1996b). For cruise emissions of nvPM, values from the EDB, either from SMOKE or direct measurements, are adjusted for cruise altitude, implementing the Doppelheuer-Lecht adjustment and the SCOPE11 correlation (Ahrens et al., 2022). We note that the Doppelheuer-Lecht altitude adjustment remains uncertain, and Peck et al. (2013) found these emissions can differ from measurements by up to 55.5%.

The OAG schedule data includes 110 unique aircraft types in 1980 and 191 unique aircraft in 2019. However, some of these aircraft types included in the OAG data represent several subtypes with diverse engine options, which can influence the emissions quantities of NO_x and nvPM by factors of 1.5 and 10, respectively (Quadros et al., 2022). To enhance the accuracy of emission representation for aircraft with multiple engine combinations, the schedule file is augmented to represent aircraft subtypes. Our main set of results are based on aircraft-engine matchings in line with fleet fuel burn fractions from NASA-Boeing studies (Baughcum et al., 1996a, 1996b; Sutkus et al., 2001). Here these aircraft-engine matchings are compiled for the aircraft that collectively account for at least 80% of the available seat-distance in each year for the years 1980, 1990, and the year 2000. These aircraft definitions are tabulated in Appendix J. These definitions are used to randomly assign each of the lines in the schedule file to the specific aircraft-engine combination listed in the table, such that the in the proportion of seat-distance on each aircraft subtype matches the fraction listed in the table. These aircraft-engine matchings are compiled for the years 1980, 1990, and 2000. To derive our emissions after the year 2000, we use the matching definitions from the year 2000, because the NASA-Boeing studies are only available until the year 2002. We additionally present a sensitivity study (Section 2.3.5), using the aircraft-engine matchings from Quadros et al. (2022), which presents an alternative set of aircraft-engine matchings. For the sensitivity study, the same set of matchings are applied for all years. These definitions are tabulated in Appendix K.

Emission location is determined by great circle routes. Annual averaged winds are accounted for by taking annually averaged winds from MERRA2 weather data. Lateral inefficiencies due to operational routing inefficiencies, and deviations for weather and congestion, are accounted for using the flight dataset analysis presented in Reynolds (2008). However, this thesis does not account for airport specific variations in inefficiencies, such as loiter times at high-traffic airports, including Atlanta and Heathrow. Additionally, shifts in operational and routing efficiencies over the years remain uncaptured.

Aircraft are assumed to fly a mean of 7000 ft below the aircraft cruise ceiling that is reported by BADA 3.16 for each aircraft. Given that flights at varying altitudes can be operated by the same aircraft, variability is introduced through a triangular uncertainty distribution applied to the flight altitude. The mid value is set 7,000 ft below the BADA-defined aircraft ceiling, with the ranging from -6750 to +6750 ft around the mid value in line with Lee (2005). However, it is worth noting that there may be uncaptured biases in the aircraft flight altitude over different time frames due to changes in aircraft operations.

For the years 1980 to 1995, we use global passenger load factors and local US based load factors as reported by Airlines for America (A4A) (Airlines For America, 2022a, 2022b). From 2000, regional load factors are reported by ICAO annual statistics (ICAO, 2020). These load factors are presented in Figure 1. These load factors are applied according to the take-off and landing airports of each flight. If a flight is from one region to another, the average load factor is used.

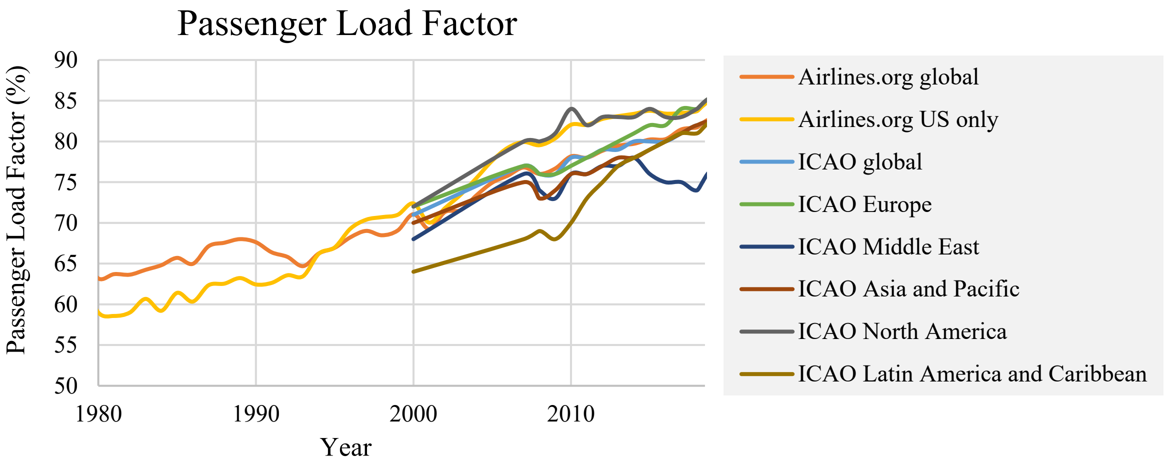

Figure 1: Global and regional passenger load factors over time

2.2.4. Inventory resolution

Emissions inventory is gridded to a global 1° by 1° grid with 200 ft altitude bands, at a monthly temporal resolution. These emissions can be used with an atmospheric model, such as a chemistry transport model or climate model to calculate atmospheric impacts. To gain a more nuanced understanding of emissions trends by the time of day, we have derived hourly emissions for the years 1980, 1990, 2000, 2010, and 2019 in 2D grids at a resolution of 4° by 5°. Additionally, emissions and aircraft data is compiled by flight chords that can be used to derive contrail impacts.

2.3. Results

Trends in fuel consumption and Available Seat Kilometers (ASK) are presented in Section 2.3.1, including how the fuel burn from this emissions inventory compares to other emissions inventories in the literature. Regional changes in fuel consumption, changes in altitude, time of day and season are subsequently presented in Sections 2.3.2, 2.3.3 and 2.3.4. Finally, trends in emissions composition are presented in Section 2.3.5.

2.3.1. Trends in fuel consumption and available seats

Fuel burn, flight distance, and ASK data from 1980 to 2019 are detailed in Table 1 and Figure 2. Over this period, there was a rise in aviation fuel consumption, with total fuel expanding from 61.2 Tg to 265 Tg, marking a 330% increase. Simultaneously, the available seat-kilometers (ASK), a measure of airline capacity, went up even more – by 560%, expanding from 1.5×10^{12} to 9.9×10^{12} seat-km. As such, our data shows an enhancement in fuel efficiency per available seat mile with fuel burn by ASK decreasing by 35% over the last 40 years.

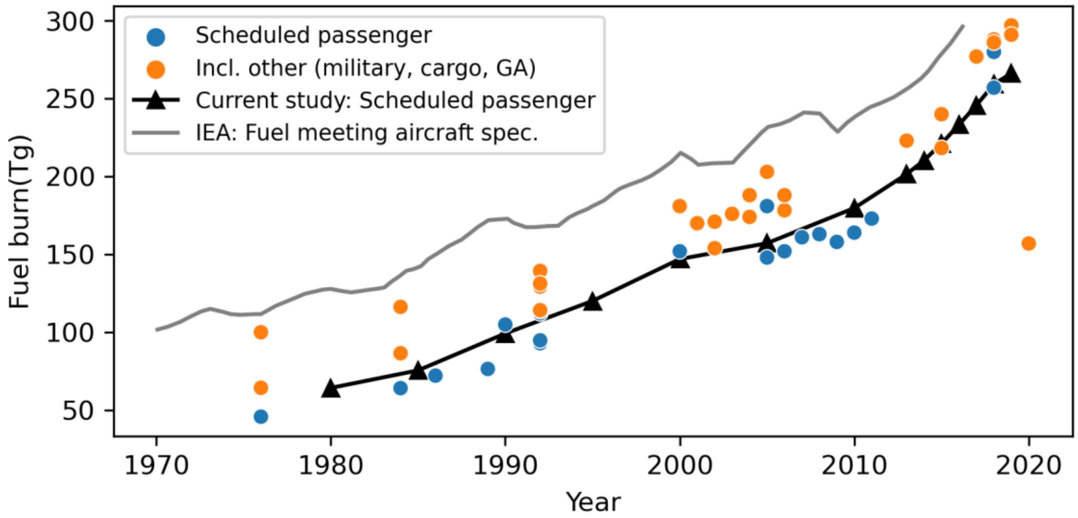

Figure 2: Comparison of our preliminary annual fuel burn totals with fuel burn totals in literature

Table 1: Annual fuel and distance totals

Year	Fuel burn (Tg)	Distance ($\times 10^9$ km)	ASK ($\times 10^{12}$ km)	Fuel per ASK (g/ASK)
1980	61.6	8.9	1.5	41.0
1985	72.8	11.0	1.9	39.1
1990	97.1	15.2	2.6	37.5
1995	118.3	19.8	3.4	35.1
2000	145.4	25.8	4.4	32.9
2005	156.0	30.1	5.1	30.6
2010	178.6	35.6	6.2	28.9
2015	219.9	43.3	7.9	27.7
2019	264.7	52.5	9.9	26.8

This increase in fuel burn by ASK over time is decomposed in Figure 3 and Figure 4. Figure 3 shows a near linear efficiency improvement rate of 0.37 g/ASK per year, with a regression fit value of R^2 of 0.996. Flights less than 1000 Nautical Mile (NM) follow a similar improvement rate, however, for longer haul flights (greater than 2000 NM) the decrease in fuel burn per ASK is slower, occurring at a rate of 0.21 g/ASK per year.

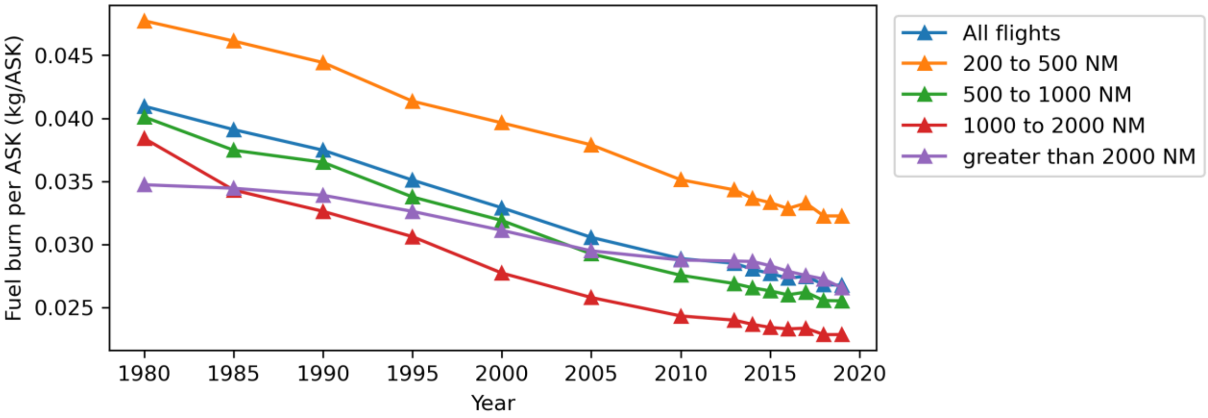

Figure 3: Fuel burn by seat distance

Figure 4 contrasts fuel burn by ASK for different flight distance bands for the year 1980 and 2019. In both years, the highest fuel burn by ASK occurs for short flights (less than 200 NM). In 2019, flights between 200 NM and 2000 NM lead to the lowest fuel burn per ASK after which fuel consumption increases.

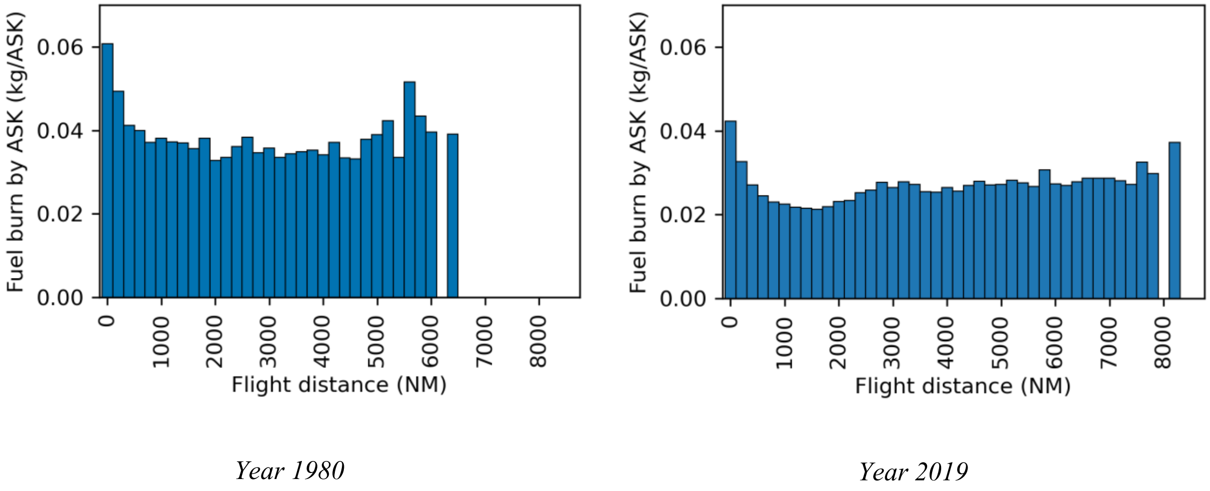

Year 1980 *Year 2019*

Figure 4: Fuel burn by Available Seat Kilometers (ASK) for various flight distance bands for the year 1980 and 2019.

Increase in efficiency over this period is likely driven by a variety of factors, including improvements in technology such as increasing engine efficiency and decreased airframe weight and drag for similar aircraft sizes. In addition, aircraft seat capacities have changed over this time. Figure 5 shows fuel burn by flight distances and number of seats. During this time, total flight distance increased from 9.5×10^9 km to 53×10^9 km, representing an increase of 460%, while ASK increased by 560%. This indicates more seats per flight on average.

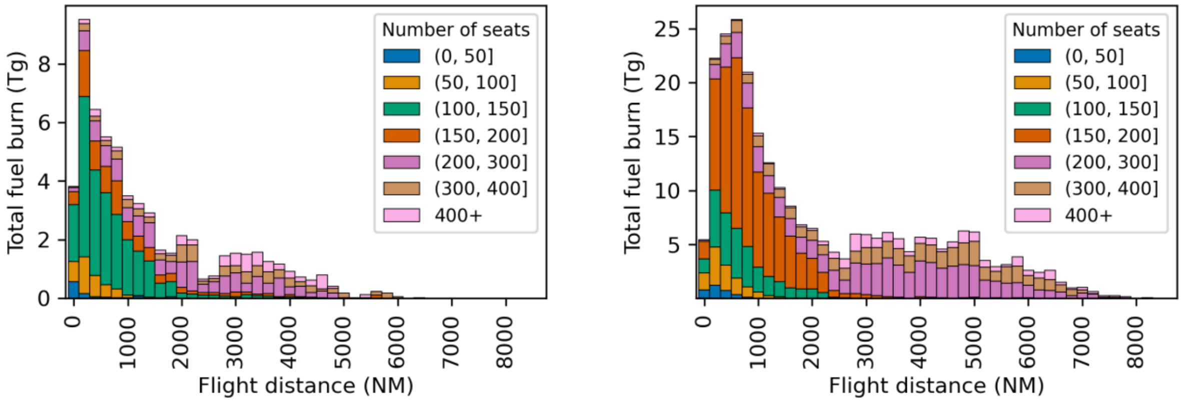

Year 1980 *Year 2019*

Figure 5: Fuel burn by number of seats and flight distance

When comparing these values with other studies our derived fuel burn totals align closely with research with the same scope as this thesis, quantifying the fuel consumption from scheduled passenger flights, as plotted in Figure 2. Also included in Figure 2, is the International Energy Agency (IEA) aviation fuel totals for each year. In 1980, the IEA's statistics were 66 Tg higher, a difference of 50% compared to our findings. By 2019, this gap narrowed, with the IEA's figures being 10% or 31 Tg higher than ours. The IEA's data encompasses total annual consumption of fuels that meet jet fuel specifications. This includes fuels not exclusively used for flights but also for ground-based applications like engine testing, ground vehicles, and other purposes. As such, these IEA totals can be considered to be an upper limit of aviation jet fuel usage (Olsen et al., 2013).

2.3.2. Region of emissions

The total fuel burn, representing the specific locations of emissions, is depicted in Figure 6. Over the span from 1980 to 2019, there has been a noticeable shift in these emission locations.

This shift is further illustrated in Figure 7, which shows how the spatial distribution of these emissions has changed by latitude and longitude over the years. These results indicate aviation emissions have remained predominantly concentrated in the northern hemisphere. Specifically, in 1980, 93% of emissions were occurring in the northern hemisphere, which remained similar in 2019 with 91% of fuel burn occurring in the northern hemisphere in 2019.

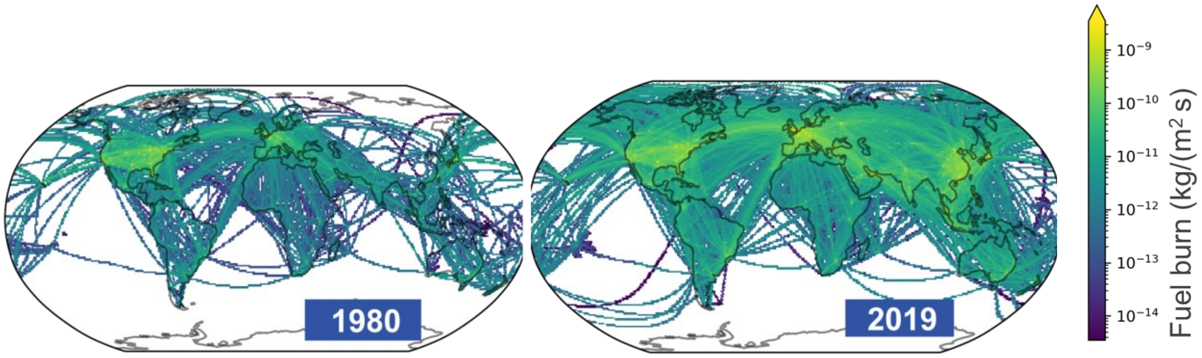

Figure 6: Location of emissions in 1980 (left) and 2019 (right)

However, there have been substantial longitudinal changes in emissions over time (Figure 7). In 1980, much of the emissions occurred between 125° W and 75° W, corresponding to emissions over the Americas. Figure 7 shows how these emissions have shifted from these longitudinal bands to Europe and Asia.

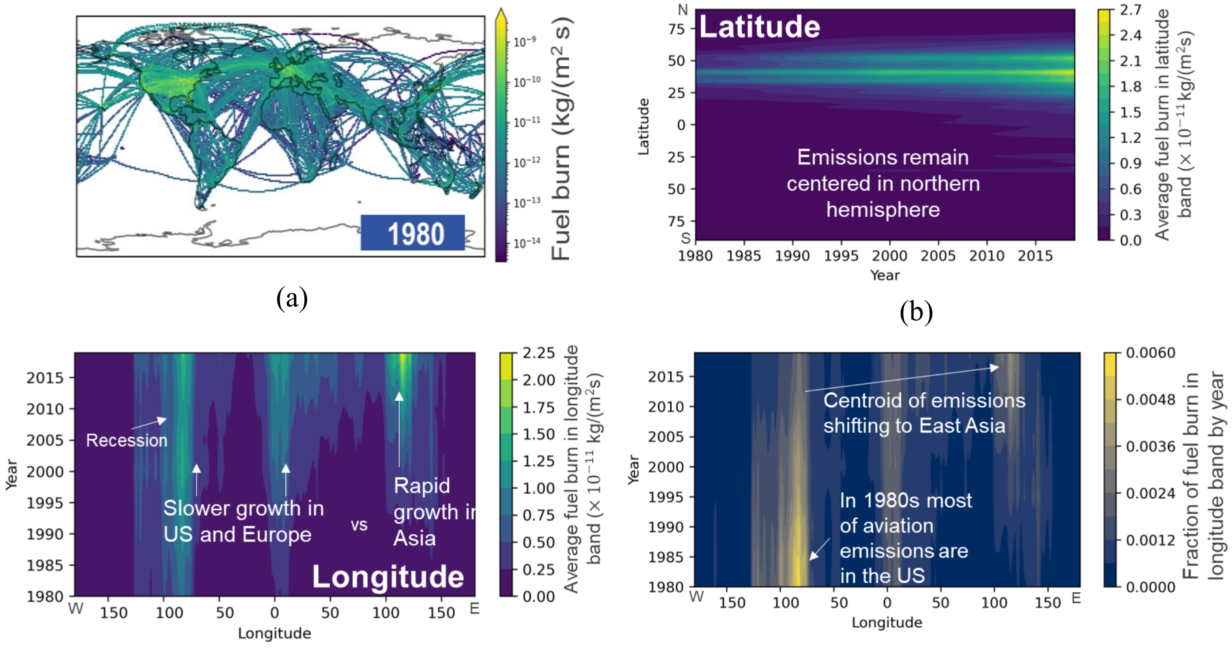

(a) (b)

(c) (d)

Figure 7: Changes in location of fuel burn over time. For location reference, (a) shows the location of emissions in 1980 on the global map. (b) and (c) show the emissions integrated over the latitude and longitude bands, respectively. (d) shows results from (c), but with emissions in each year normalized to the total in the year.

To quantify these shifts, we have calculated emissions totals in global emissions regions as presented by Lund et al. (2017a). These emissions and regions are plotted in Figure 8. In 1980, the largest contribution of fuel burn was from North America, and by 2019 North America, Europe, and East Asia have similar contributions to total global annual fuel burn. Over this period, the emissions share in North America decreased from 55% to 25%, while the share in East Asia increased from 7% to 23%. This change in regional distribution is likely to affect the magnitude of climate and air quality impacts over time, since emissions in different regions lead to different climate impacts, sometimes differing by more than a factor of two (Lund et al., 2017a).

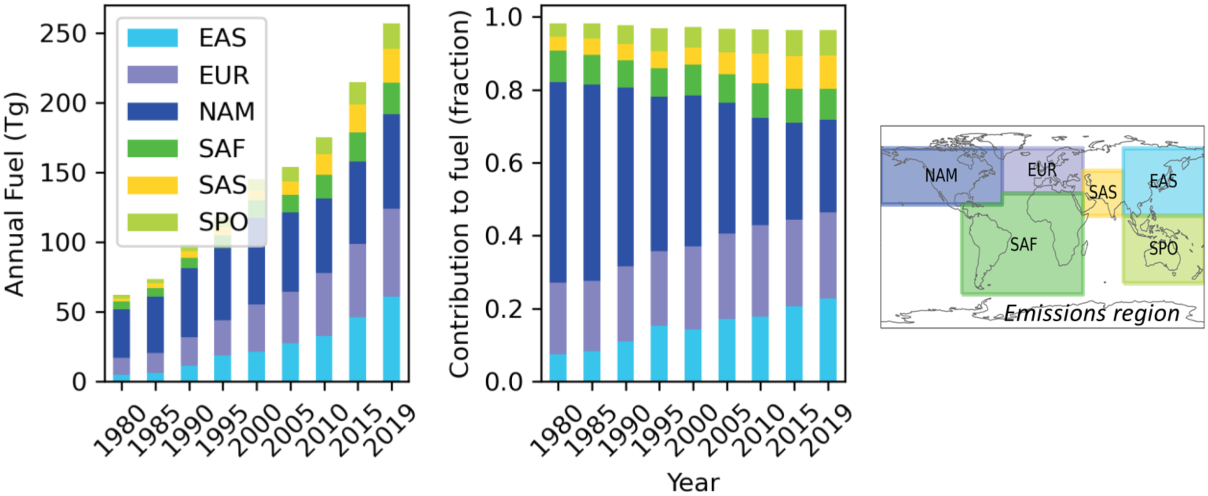

Figure 8: Evolutions of region of aviation emissions over time. Emissions outside of the 6 indicated areas are negligible; totals can be inferred as the difference between the totals in the center lower panel and 1.0.

2.3.3. Emission by altitude

We additionally present the emissions by altitude they occur (Figure 9). We find that the proportion of emissions occurring at cruise altitudes has increased over time. In 1980, 56% of fuel burn was above 9 km altitude. This percentage increased to 61% and 67% in 2000 and 2019, respectively. This is likely due to a larger proportion of longer flights (Figure 5). We note that trends in cruise altitude are not necessarily captured, since our methods, which are based on schedule data, do not explicitly account for differences in aircraft operational procedures over time.

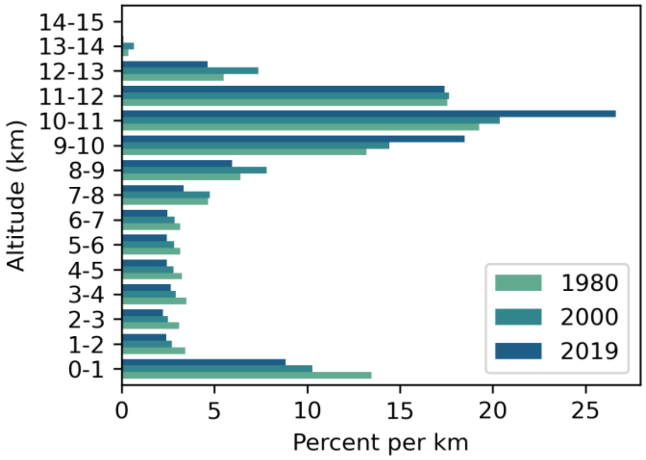

Figure 9: Altitude where emissions occur. For each year the normalized emissions occurring in at each kilometer in the atmosphere is plotted. For each year, the sum of the plotted bars adds up to 100%.

2.3.4. Temporal variation

2.3.4.1. Seasonality and weekly variation

Our results show that the northern hemisphere summer accounts for 24% of global annual fuel burn, where summer is taken as the months of June, July, and August. In contrast, the northern hemisphere winter accounts for only 18% of fuel burn, with winter is taken as December, January, and February. This result shows little variation from 1980 to 2019, with these percentages consistent for the year 1980, as well as 2019 (Figure 10).

Fuel burn shows a weekly trend as plotted in Figure 10. Highest fuel burn occurs on a Friday, and lowest global fuel burn occurs on a Tuesday. This fuel burn is 6% higher on a Tuesday than on a Friday in 1980, and this difference reduces to 4.5% in 2019. This differs from the weekly trend in the number of flights, where the number of flights per day is 27% lower on the weekend days of Saturday and Sunday than during the other days of the week. In 2019, this difference between weekend and weekday has reduced to 12%. This difference between weekday and weekend flights is driven by short haul flights. And the difference between 1980 and 2019, indicates an increase in aircraft, airport, and crew utilization.

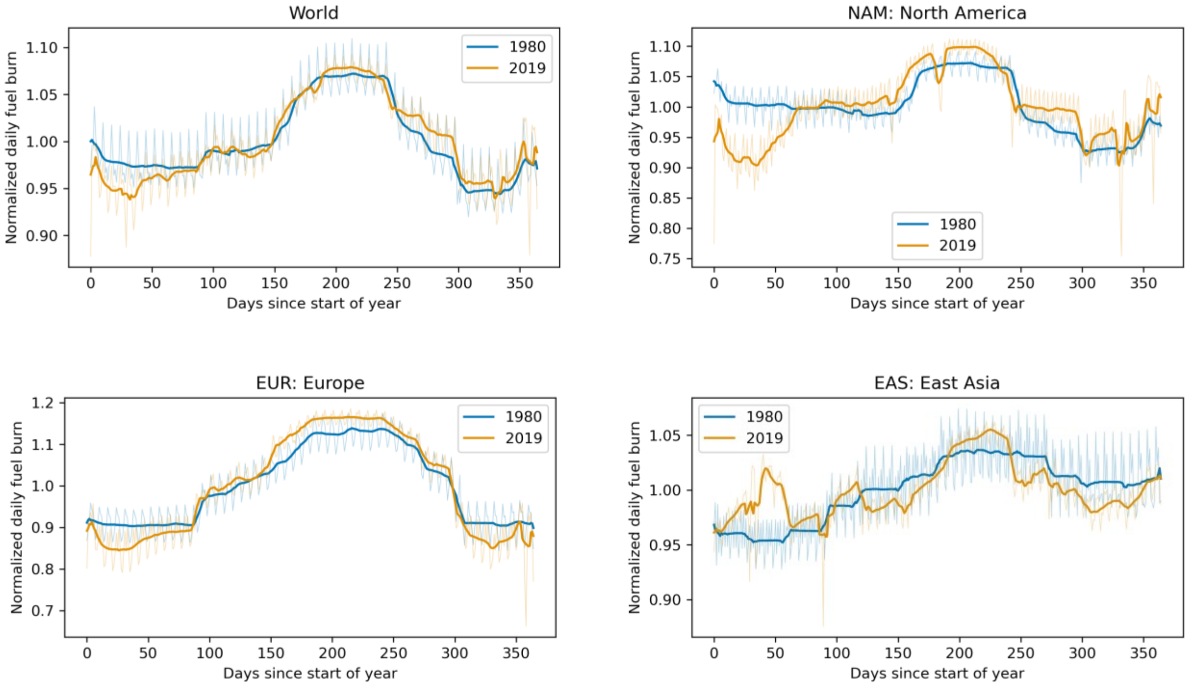

Figure 10: Seasonal and weekly variation in fuel burn

2.3.4.2. Distribution of emissions by time of day

We also investigated the difference in the time of day that emissions occur. This is important since contrail lifetimes are typically only a few hours, and their radiative impacts are sensitive to the time of day that contrails occur and persist (Stuber et al., 2006). We consider three regions (US East Coast, Europe and East Asia), and plot the fraction of fuel burn occurring in each region by hour of the day (Figure 11). Also plotted on the figure is the local solar daytime/nighttime at the center of the region.

In all four regions, our results show that the share of the fuel burn occurring during the night increased. In 1980, global fuel burn occurring at local nighttime was 30% of total annual fuel burn. This increased by 8 percentage points to 38% in 2019. This increase in nighttime fuel burn is likely due to an increase in aircraft utilization. This increase in nighttime fuel burn is caused by an increase in fuel burn from short haul flights (<1000 NM in length), where nighttime fuel burn increased from 23% to 28% from 1980 to 2019. In contrast, for long haul flights (>4000 NM) in 1980, a larger proportion of fuel burn occurred during the local nighttime (60%) than during the local daytime, likely since passengers prefer overnight long-haul flights. In 2019, this fraction decreased to 53%, also indicating an increase in aircraft and crew utilization.

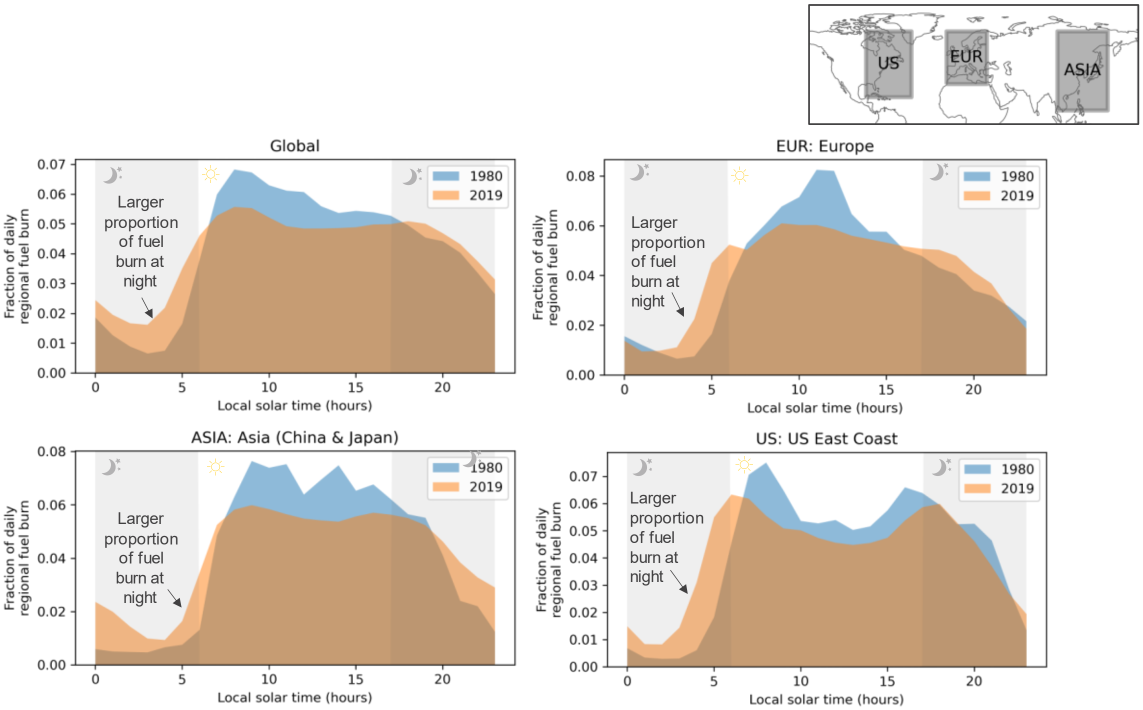

Figure 11: Difference in fuel burn by time of day between 1980 and 2019. In all regions considered the fraction of fuel burn occurring during the night increases.

2.3.5. Composition of emissions

While CO_2, water vapor, and sulfur emissions are directly proportional to the fuel quantity, NO_x, nvPM, and CO and HC emissions are sensitive to engine technology and operating conditions (Section 2.2.3). This section covers how the emissions composition of NO_x, nvPM, CO, and HC have changed over time. These emissions are tabulated in Table 2 with NO_x, and nvPM emissions indices and literature comparisons further illustrated in Figure 12.

Table 2: Aviation emissions over time

Year	NO_x (Gg NO_2)	nvPM (Gg)	CO (Gg)	HC (Gg)	EI NOx (g/kg)	EI nvPM (g/kg)	EI HC (g/kg)	EI CO (g/kg)
1980	878	8.19	1580	1860	14.3	0.133	30.200	25.60
1985	1080	8.40	1520	1340	14.9	0.115	18.400	20.90
1990	1440	8.88	1370	1130	14.8	0.091	11.600	14.20
1995	1800	8.97	1350	882	15.2	0.076	7.460	11.40
2000	2250	9.40	1460	656	15.5	0.065	4.510	10.10
2005	2450	8.70	1420	610	15.7	0.056	3.910	9.09
2010	2920	8.64	1350	240	16.4	0.048	1.340	7.58
2015	3740	9.31	1420	176	17.0	0.042	0.799	6.47
2019	4540	10.60	1580	184	17.2	0.040	0.694	5.98

We find the NO_x emissions index increased by 20% over the study period, rising from 14.3 to 17.2 g_{NO2}/kg_{fuel} between 1980 and 2019. The overall increasing trend aligns with other historical inventories, though derived indices vary by up to 19% between studies for a given year. This highlights the difficulty in comparing trends across different inventories using inconsistent assumptions. Within a given year, the NO_x emissions index varies significantly across engines, differing by over an order of magnitude based on engine technology (Figure 12). When combined with rising fuel burn, total global NO_x emissions increased 420% between 1980 and 2019.

Despite a 330% fuel burn increase over the period, nvPM emissions rose just 29% from 8.19 Gg to 10.6 Gg. The nvPM emissions factor decreased 70% from 0.13 to 0.04 g_{nvPM}/kg_{fuel} (Figure 12). This substantial reduction likely influenced contrail formation over time. Moreover, literature estimates of nvPM begin only in 2005, precluding historical comparison. Where the data overlaps, our results match reported values.

Emissions indices for CO and HC also fell 78% and 77%, respectively.

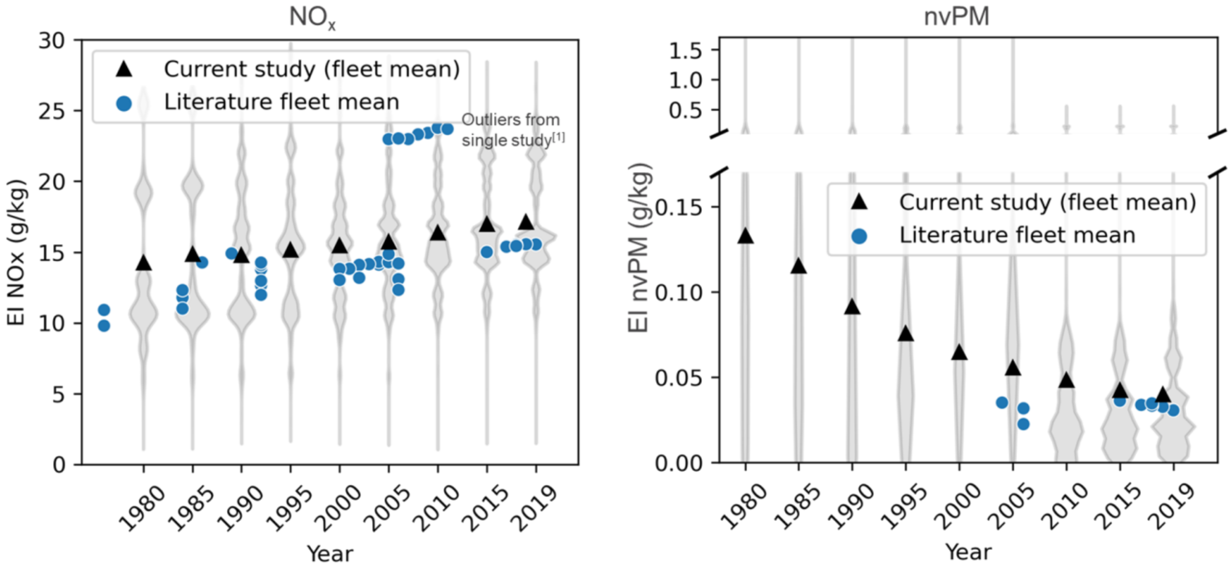

[1] Waisuik et al (2016) Commercial Aircraft Fuel Burn and Emissions Inventory for 2005–2011. Atmosphere 7, 78.

Figure 12: Trends in EI_{NOx} and EI_{nvPM} over time with comparison to literature.

Aircraft-engine matching assumptions influence results. Using an alternative matching method from Quadros et al. (2022) changes the derived EI_{NOx} by 14% in 1980 and 3% in 2019, and EI_{nvPM} by 18% in 1980 and 57% in 2019 (Figure 13). Compared to our NASA-Boeing-based matchings that capture evolving aircraft types, the Quadros et al. (2022) matchings yield a 36% $\mathrm{EI}_{\mathrm{NOx}}$ increase from 1980-2019 versus our 20%. Using the Quadros et al. (2022) matchings lead to 60% $\mathrm{EI}_{\mathrm{nvPM}}$ decrease versus the 70% in our baseline results. This highlights the need for consistent assumptions when comparing historical emissions.

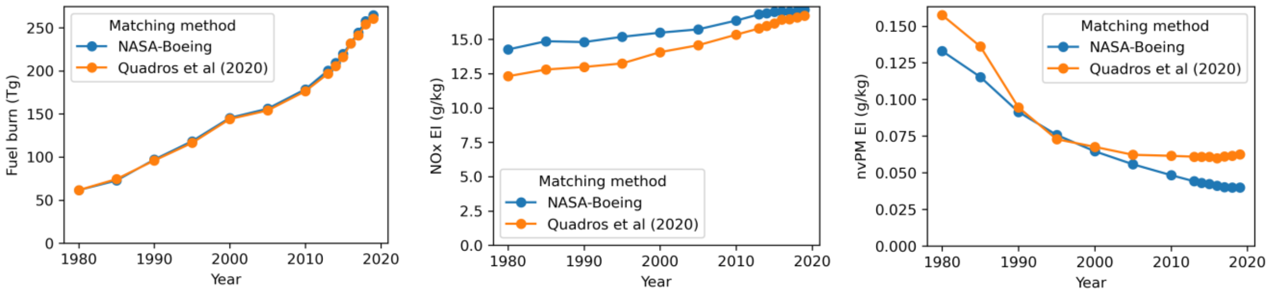

Figure 13: Comparison between fuel burn and emissions results for different aircraft-engine matching methods.

2.4. Discussion of uncertainty

These results are derived using OAG schedule data combined with assumptions of great circle routes and standardized aircraft performance, alongside ground-level emissions measurements adjusted to cruise altitude. While these methods enable the investigation of trends over time, they introduce uncertainties to our results.

One source of uncertainty is the reliance on aviation schedule data, which provides a basis for estimating flight locations, frequencies, distances, and aircraft used. However, this data does not capture real-time operational changes, including delays, diversions, and cancelations. Furthermore, it omits unscheduled flights, including charter flights, and could underrepresent flights in regions with less robust data reporting practices, such as the former Soviet Union. Our reliance on great circle routes for flight locations introduces additional uncertainty, as these theoretical paths could differ from actual flight routes. While we account for additional fuel burn and emissions due to average routing inefficiencies, we cannot fully account for variations in routing inefficiencies or the interaction between aviation traffic patterns and meteorology.

Emission estimation presents further challenges and uncertainties. Our results rely on measurements from the EDB, representing emissions from a single engine at ground level (ICAO, 2022). This approach does not account for differences in individual engines variability in maintenance. Furthermore, for the older engines, direct measurements of nvPM mass and number emissions are often unavailable, and only SMOKE number is available as a proxy. The adjustment of nvPM to cruise altitude, based on the Dopelheuer-Lecht method, introduces additional uncertainty, showing discrepancies of up to 55% compared to measurements at altitude.

Moreover, due to limitations in data availability, our model uses surrogate aircraft, including those in BADA, leading to uncertainties in emissions from various aircraft subtypes. Quadros et al. (2022) indicated that emissions from aircraft subtypes can vary by a factor of 1.5 and 10 for NO_x and nvPM respectively. Our sensitivity study, covering two different aircraft subtype representation methods (Section 2.3.5), shows up to a 57% variation between the two methods considered. However, applying a consistent method for defining subtypes over time results, as applied in this chapter, in less than 16 percentage point difference in EI_{NOx} and EI_{nvPM} changes over time between these two methods. This highlights the importance of using consistent assumptions when investigating emissions trends over time, as we applied in this chapter.

This chapter focuses on investigating how emissions have changed over time. Despite these uncertainties, the consistent methods applied in this chapter provide insights into how emissions have changed over time. This consistency underlines the value of our analysis, even as we acknowledge the uncertainties inherent in our approach.

2.5. Discussion and conclusion

This thesis presents the first bottom-up emissions inventory for global commercial civil passenger aviation spanning four decades from 1980 to 2019. By leveraging aviation flight data and aircraft performance modeling, we quantify aviation's historical emissions while capturing changing spatial, temporal, and compositional characteristics.

These changing emissions characteristics quantified in this thesis have implications for accurately quantifying and mitigating aviation’s climate impacts. Many current studies focusing on aviation’s climate and air quality impacts from a year of aviation emissions, rely on the emissions inventories, which is based on flight patterns from the year 2002 or 2006 (Brasseur et al., 2016; Burkhardt et al., 2018; Eastham and Barrett, 2016; Lund et al., 2017a). This includes the emissions for the Coupled Model Intercomparison Project (CMIP), which uses a scaled emissions inventory for aviation, where emissions from a base year are scaled to fuel burn from the IEA. The results derived in this chapter indicate that spatial, temporal, and compositional characteristics of emissions have varied over time, likely affecting the results obtained in such studies.

The emissions trends identified here could inform emissions projections for the future. We find aviation emissions growth has slowed over North America, while growth in East Asia outpaces other regions. This suggests future emissions may continue growing faster in East Asia than North

America. Furthermore, the increase in nighttime fuel burn indicates rising aircraft utilization across short and long-haul flights over time. The amount of fuel burn on different days of the week has also equalized, indicating an increase in aircraft utilization. Additionally, more long-haul flights have occurred in recent times as aircraft capabilities expanded.

These results also show rising NO_x emissions, despite sustained regulation aiming to reduce NO_x. This indicates current regulation may be ineffective at reducing NO_x, and alternative approaches could be necessary, further supporting conclusions from Miller et al. (2022).

This work has limitations that could be addressed in future efforts. Firstly, matching specific engine variants to aircraft models contributes uncertainty in NO_x and nvPM indices. Additionally, quantifying nvPM emissions at cruise altitudes has high uncertainty, since the Doppelheuer-Lecht correlation used here is based on limited experimental data. Changes in operational factors like airport congestion and routing inefficiencies over time are also not fully captured. Finally, covariation between traffic and meteorology could affect contrail formation trends. However, this multidimensional inventory significantly advances understanding of aviation's emissions.

Future work could expand this inventory to include charter flights for a comprehensive record of emissions. Incorporating flight data, such as ADS-B data could better represent operational factors. The results here are limited by the proprietary nature of the BADA dataset used. An open-source emissions inventory not reliant on proprietary data would enable broader applications.

In conclusion, this chapter presents a new multidimensional emissions inventory to enable comprehensive assessment of aviation's historical climate impacts. The results highlight changing emissions characteristics that are often overlooked but likely influence climate and air quality impact assessments. By quantifying these trends in aviation’s emissions, this work can directly inform impact assessments, and support efforts in projecting future emissions.

Chapter 3

Accumulated present-day climate impacts of commercial civil aviation

3.1. Introduction

Current estimates suggest aviation emissions are responsible for 4-6% of global anthropogenic radiative forcing (Lee et al., 2020). These effects accumulate and will persist for centuries to come (Klöwer et al., 2021; Lee et al., 2020; Terrenoire et al., 2019). Accurately quantifying these impacts is useful, since it will allow for evaluating the current and future climate effects due to past emissions, which is essential for determining the remaining emissions allowance. It also involves discerning which emissions trends have significantly influenced climate impacts, aiding in forecasting future climate effects and directing appropriate mitigation strategies. Moreover, understanding the relative magnitudes of the different forcing pathways highlights which emission types or pathways warrant concentrated research and mitigation efforts.

The bottom-up emissions inventory presented in Chapter 2 shows that aviation emissions characteristics, such as temporal patterns, geographical distribution, and emissions composition have continued to vary from 1980 to present day.

Contrails, which are estimated to account for 57% of aviation's effective radiative forcing in 2018 (Lee et al., 2020), are especially sensitive to such differences in emissions characteristics. Contrails form when water vapor in the exhaust plume condenses onto particles in the plume, under sufficiently cold and moist atmospheric conditions. How long they persist is affected by the local atmospheric conditions, as well as the number and size of the ice particles. Their subsequent radiative impacts, which are both due to the reflection of incoming short-wave radiation, and the trapping of outgoing long-wave radiation, are also affected by a variety characteristics. These include the ice particle size distribution, time of day and season, winds, which affect how spread-out a contrail becomes, and differences in surface albedo beneath the contrail (Burkhardt and Kärcher, 2011; Kärcher, 2018).

As a result, annual contrail impacts have been shown to vary by up to a factor 2 depending on region of emissions (Bock and Burkhardt, 2019; Lund et al., 2017a). Additionally, shifts in the time of day that the emissions occur likely also affects the subsequent impact. A study, focusing on a limited regional scope, found that night flights contribute to 60 to 80% of contrail forcing, despite only accounting for 25% of the traffic (Stuber et al., 2006). The emissions composition also likely affects the subsequent global impacts, with studies finding a 50 to 90% change in particle number emissions can change the subsequent climate impacts by 20 to 90% (Burkhardt et al., 2018; Teoh et al., 2020). However, uncertainty remains, and another study found a +5 to -13% change in global RF from contrail due to a modelled 66% decrease in aircraft particle number emissions (Caiazzo et al., 2017). The altitude of emissions likely also affects the global annual contrail RF, with studies indicating a change of 10 to 50% for an aggregate 2000 to 6000 ft change in cruise altitude (Fichter et al., 2005; Frömming et al., 2012; Grewe et al., 2017a). Additionally, the season of emissions could affect the subsequent global RF impact by up to a factor 2 to 5 (Stuber et al., 2006; Yin et al., 2018).

Collecting work from studies that quantified global RF from various aviation forcers, Lee et al. (2009, 2020), present an aggregate perspective of the impacts from aviation, estimating the accumulated RF from different aviation CO_2 and non-CO_2 forcing pathways. Using these estimates Lee et al. (2010) and Klöwer et al. (2021) present estimates of the accumulated temperature change. However, neither Lee et al. (2010) or Klöwer et al. (2021) presented temperature change broken out by the different non-CO_2 forcing pathways. A further limitation of these assessments is their reliance on fuel and emissions scaling, overlooking the nuances of the impacts of heterogeneities in the emissions composition, time, region and altitude over the years. As a result, the present-day atmospheric surface temperature change due to aviation emissions remains uncertain. Moreover, it remains unknown how contrail forcing has evolved over time, and what the underlying factors are that might have driven these changes.

In this chapter, we investigate the accumulated present-day and future climate impacts due to aviation emissions since the start of the jet age. Given contrail's comparatively high contribution to these impacts, we place special focus on aviation contrail impacts and the relationship to changes in the aviation emissions over time. This work is enabled for the first time by the bottom-up emissions inventory presented in Chapter 2. Contrail formation and behavior are modeled using the APCEMM intermediate-fidelity contrail model (Fritz et al., 2020) using ERA5 reanalysis data (Hersbach et al., 2020). We also incorporate a reduced-order climate model (APMT-IC) to quantify radiative forcing from CO_2 and other non-CO_2 forcers (Grobler et al., 2019). Additionally, we use this model to quantify how these emissions and their resulting forcings have and will continue to affect global atmospheric surface temperature.

3.2. Methods

We model contrail impacts from flight operations between 1980 and 2019 using an aircraft plume model combined with weather reanalysis data (Section 3.2.1). This approach captures formation, evolution, and dissipation from individual contrails, while using the weather patterns for the year of operations.

In Section 3.2.2, we explain the methods used to calculate radiative forcing and temperature change for both CO_2 and non-CO_2 emissions associated with aviation. This will enable us to compare relative impacts from the various aviation climate forcers and inform how much past aviation emissions contribute to the global temperature change budget at different times in the future.

3.2.1. Contrail properties and subsequent radiative forcing

Contrail properties and evolution are evaluated using the Aircraft Plume Chemistry, Emissions and Microphysics Model (APCEMM) developed by Fritz et al. (2020). This model is higher fidelity than 1D gaussian plume models, and captures inhomogeneity of the contrail in 2D, and resolves different ice particle sizes at each timestep. Therefore, this model captures effects that 1D gaussian plume models cannot, like differential crystal settling. However, as a result, APCEMM has a higher computational cost, and simulating contrails from all flights in a year is not computationally tractable. To address this problem, we use a sampling approach to simulate contrails from a representative set of flight segments each year in question, where a flight segment is defined as a kilometer of flight distance. This approach is based on previous work by Agarwal (2021) and Elmourad (2023):

Step 1: Chorded emissions inventories are derived for the years 1980 1990, 2000, 2010, and 2019 (Chapter 2).

Step 2: Using the chorded emissions inventories, 100,000 individual flight segments are sampled for each year, using a distance-based random sampling (Section 3.2.1.1).

Step 3: Since we are only interested in applying the aircraft plume model for cases that result in contrail formation, each of the selected flight segments are evaluated to test if a persistent contrail could form for the given the ambient conditions and engine properties (Section 3.2.1.2).

Step 4: For each of the segments that could result in the formation of a persistent contrail, we use APCEMM, a medium fidelity aircraft plume model, to derive contrail properties. This model is combined with ambient weather data from ERA5 (Section 3.2.1.3).

Step 5: Then the contrail properties are used to calculate the radiative impacts using RRTM code together with ERA5 reanalysis weather data (Section 3.2.1.4).

Step 6: Finally, the data from the individual chords is combined to determine aggregate radiative impacts and investigate trends in the impacts (Section 3.2.1.5).

Additionally, given APCEMM has a higher spatial resolution than the ERA5 weather data, our model can prevent far-field changes in water vapor content from affecting our modeled contrail (Section 3.2.1.6). As a result, our contrail lifetimes are longer than contrail lifetimes from some other studies (Teoh et al., 2022, 2020). For comparison purposes, we derive an extra set of results that truncates contrail lifetime, with contrail evaporation conditions based on only the ERA5 weather data (Section 3.2.1.6). This set of data serves as a lower bound for our contrail results.

3.2.1.1. Step 2: Selecting flight segments to evaluate

For each year, contrail properties are evaluated for a representative sample of flight segments, where a segment is a point location from the flight. The segment is extracted using a distance-weighted sampling method (Agarwal, 2021). This selection involves compiling a vector of every flight kilometer flown in the year and keeping track of which kilometer is attributable to which flight. These flight distances are taken from the emissions inventory in Chapter 2. For each sampled segment, a random number is drawn from a uniform distribution. The minimum is set to zero and the maximum is set to the total flight distance in the year under consideration. For instance, if the random number generator selects 450 km, the flight corresponding to the 450th km in the vector of flight distances would be selected for the sampled set. If this flight spans the 400th to 500th km of the total flight distance from the year, the flight data at 450 km would be extracted and included in the sample set. This provides a set of flight conditions with a distance weighted sampling.

For each year, a sample of 100,000 segments are selected. This has been shown to lead to less than 1% variation in the estimate of the global mean radiative impact (Agarwal, 2021).

For each sampled segment, the time, location (altitude, latitude, and longitude), aircraft weight, flight speed, fuel flow and nvPM emissions are extracted from the chorded emissions inventory derived in Chapter 2.

3.2.1.2. Step 3: Screening for persistent contrail conditions

Since not all the sampled segments will lead to the formation of a persistent contrail, all the selected chords are first screened to check if they could meet the persistent contrail conditions (PCC) for an assumed upper bound formation criteria. A segment meets the persistent contrail condition if (i) the ambient conditions have a relative humidity with respect to ice (RHi) greater than 100%, and (ii) the exhaust plume will become super saturated with respect to water vapor as it mixes with the ambient, as described by the Schmidt-Appleman criteria (Schumann, 1996). The latter condition depends on the engine thermal efficiency, with higher engine thermal efficiencies leading to increased contrail formation, given the reduced heat energy available in the exhaust plume. As an upper bound, this PCC screening is performed for an engine thermal efficiency of 50%, which represents the upper bound of engine thermal efficiencies for assumed combustor and turbine efficiencies of 0.9 (Cumpsty and Heyes 2015:49). The ambient temperature and specific humidity values are taken from the ERA5 weather data (Hersbach et al., 2020) for the nearest grid-cell at the time and location of the occurring flight segment. This weather data is further described in Section 3.2.1.3.

3.2.1.3. Step 4: Contrail modeling using APCEMM and ERA5 weather data

Modeling of contrail microphysics using APCEMM

The contrail properties for each of the selected and screened chords is simulated using the Aircraft Plume Chemistry, Emissions, and Microphysics Model (APCEMM) (Fritz et al., 2020), including updates as described in Agarwal (2021) and Elmourad (2023). This model is a Lagrangian model and was developed to model chemical interactions and microphysics of an aircraft plume, under a variety of conditions. In this work, we only use the ice microphysics part of the model.

The model is schematically outlined in Figure 14. It starts out by simulating the jet regime and vortex phase, which are characterized by rapid mixing, and lasts in the order of 100 seconds after emissions occur. The model uses a box model with uniform temperature and species concentrations (Kärcher, 1998, 1995) as the plume entrains air from the ambient. During this phase, the model calculates the number of initial ice particles based on the soot number emissions, and the water vapor available in the plume. It also accounts for subsequent ice crystal losses due to turbulent temperature fluctuations, and adiabatic heating of the plume driven by downwash from the aircraft wing-tip vortices (Fritz et al., 2020).

Thereafter the diffusion regime of the plume is modelled using a spatially resolved, 2D gridded spectral method (Gottlieb and Orszag, 1977). This part of the simulation includes modeling of diffusion, advection, and shear. Consistent with Agarwal (2021), the spatial resolution is set to 100 m in the horizontal direction and 10 m in the vertical direction, and the time step set to 600 s. The ice particles are modeled using 38 size bins from a minimum radius of 50 nm to a maximum of 80 µm, where the size range for each bin varies depending on the current simulation conditions (Fritz et al., 2020).

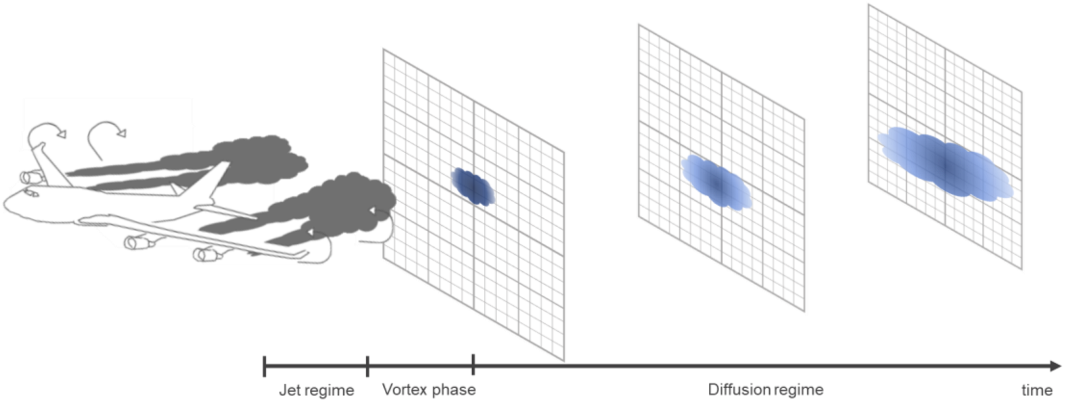

Figure 14: Schematic outline of Aircraft Plume Chemistry, Emissions, and Microphysics Model (APCEMM) (Fritz et al., 2020)

Contrails are assumed to have evaporated when both the ice mass falls below 10^{-2} kg/m and the number of crystals falls below 10^{6} crystals/m, thereby ending the APCEMM simulation. Any remaining APCEMM simulation is terminated at 24 hours, due to the low likelihood of contrails persisting longer than this, consistent with other contrail studies (Schumann et al., 2015; Teoh et al., 2020).

Engine thermal efficiency, which is required to specify APCEMM inputs, is calculated using Eurocontrol Base of Aircraft Data (BADA) version 3.16 (Eurocontrol, 2022) for the flight conditions of each segment. The thrust specific fuel consumption (TFSC) is obtained from BADA, and we use Cumpsty and Heyes (2015) to derive the thermal efficiency (Appendix C).

Weather data for contrail simulation in APCEMM

We use the ERA5 reanalysis product from the European Centre for Medium-Range Weather Forecasts (ECMWF) to estimate prevailing atmospheric conditions (Hersbach et al., 2020). This data is available on a regular latitude-longitude grid at a 0.25° by 0.25° resolution with 37 pressure levels from 1000 hPa to 1 hPa at hourly temporal resolution. The dataset is available from the year 1959 onwards, and we use the weather data corresponding to each year for which contrails are evaluated.

The ambient specific humidity field is initialized from the ERA5 data from the time and location where aircraft pass. For the remainder of the simulation, the mixing ratio of water vapor in each APCEMM grid cell is calculated by APCEMM and not updated from the weather data. We use APCEMM in this way, since the contrail influences the local water content, and the water content will be advected along with the contrail air mass.

In addition, APCEMM requires ambient temperature and wind shear for the contrail. Since these factors can be influenced by external factors such as radiation and pressure changes, the temperature and winds are updated from the ERA5 weather data for each timestep.

Advection of the contrail through the atmosphere is calculated using the Advection for Flight and Contrail Analysis (AFCA) package and ERA5 wind data. This package is a C++ library developed to enable optimized Lagrangian trajectory analysis related to aviation's climate impacts. It applies numerical integration using a fourth-order Runge-Kutta scheme along with interpolated horizontal and vertical wind data to provide simulated air parcel trajectories (Meijer, 2023). Using this advected trajectory, ERA5 temperature, pressure, and wind data is extracted along the advected path of the contrail.

3.2.1.4. Step 5: Calculation of radiative impacts using RRTM

The Rapid Radiative Transfer Model (RRTM) is employed to assess the impact of individual contrails on the radiative forcing budget of the atmosphere. This method for calculating radiative forcing for contrails impacts from APCEMM output was developed by Agarwal (2021) and later extended by Elmourad (2023) to incorporate ERA5 weather data. This approach uses the standalone version of RRTM.

RRTM applies spectral absorption coefficients from the line-by-line radiative transfer model (LBLRTM), using the correlated-k method (Mlawer et al., 1997). The correlated-k method groups absorption lines of gases into bands and averages their effects, allowing for faster calculations across a spectrum while maintaining reasonable accuracy. RRTM is applied to calculate shortwave and longwave calculations separately. For longwave forcing calculations, surface emissivity values for each of the 16 emissivity bands used by RRTM come from NASA's MODIS aboard the Terra and Aqua satellites, with an 8-day temporal resolution and a 2° by 2.5° horizontal resolution.

Surface properties such as surface albedo are taken from ERA5. Similarly, weather data, including temperature, pressure, humidity profiles, and natural cloud attributes such as cloud cover fraction, specific cloud ice water content, specific cloud liquid water content, specific rainwater content, and specific snow water content are also taken from ERA5. As described in Elmourad (2023), this natural cloud data is used to calculate the liquid water path and ice water path. Both the ERA5 weather data and the surface data from NASA's MODIS are taken for the advected contrail location as described in Section 3.2.1.3.

To quantify the radiative impact of contrails, two runs are performed – one with contrails and one without. The difference calculates the radiative forcing due to contrails.

3.2.1.5. Step 6: Collecting data

The annual global radiative forcing is calculated across all samples, as presented in Eq 1.

$$\mathrm{RF_{annual}} = \frac{1}{\mathrm{A_{earth}} \cdot \mathrm{t_{yr}}} \cdot \left(\frac{\mathrm{N_{PCC}}}{N}\right) \cdot \left(\frac{1}{N_{PCC}} \cdot \sum_{i=1}^{N} \frac{\mathrm{EF_i}}{\mathrm{D_{contrail}}}\right) \cdot \mathrm{D_{yr}} \qquad \text{Eq 1}$$

Here $\mathrm{N_{PCC}}$ represents the number of the flight segments in the selected sample that result in persistent contrail formation. N represents the total number of segments in the sample. $\mathrm{EF_i/D_{contrail}}$ represents the energy forcing per meter contrail in Joule/m. $\mathrm{D_{yr}}$ represents the total distance flown in the year in meter. Additionally, energy forcing is converted to radiative forcing, by normalizing the energy forcing by the area of the year ($\mathrm{A_{earth}}$) in meters, and the total number of seconds in a year ($\mathrm{t_{yr}}$).

$\mathrm{N_{PCC}/N}$, represent the fraction of flight segments in a year that results in persistent contrails. Additionally, $\frac{1}{N_{PCC}} \cdot \sum_{i=1}^{N} \frac{EF_i}{D_{contrail}}$ represents the average energy forcing per distance contrail in the year in Joule/m. Collectively, the product of these two expressions represents the average energy forcing per flight distance in Joule/m. In this thesis, we use EF/$m_{contrail}$ to refer to the energy forcing per distance contrail, and EF/m_{flight} to refer to the energy forcing per distance contrail.

Results section 3.3.1 presents various trends based on this fraction of flight segments with persistent contrails, and impact per distance contrail and per distance flight.

3.2.1.6. Additional set of results for alternative weather data formulation

The spatial resolution of the available weather data products at aircraft cruise altitudes presents challenges for accurate contrail modeling. The ERA5 grid cells are approximately ~0.8 km high by ~30 km in width. In contrast, contrails only span ~0.1 km at 10 minutes after formation. After 10 hours, contrails typically span 10~30 km in width (Karcher, 2018), which is still smaller than the ERA5 grid. As a result, there is a mismatch in length scales between the ERA5 grid resolution and contrail length scale.

In particular, this presents a challenge for ensuring of water vapor mass in the vicinity of the contrail remains conserved. Water vapor that starts out near the contrail is likely advected with the contrail. However, in the ERA5 weather data, water vapor mass is averaged out in each grid cell. As illustrated in Figure 15, given the differences in length scales, far-field changes in the water vapor mass could be averaged into the ERA5 grid cell that contains the contrail.

This difference in length scale could result in a premature evaporation of the contrail in the simulation. The literature has found that these large grid-cells are often weakly subsaturated (Teoh et al., 2022). Therefore, studies that apply the ERA5 weather data without adjusting to ensure continuity in sub-grid-scale variation, could result in shorter contrail lifetimes.

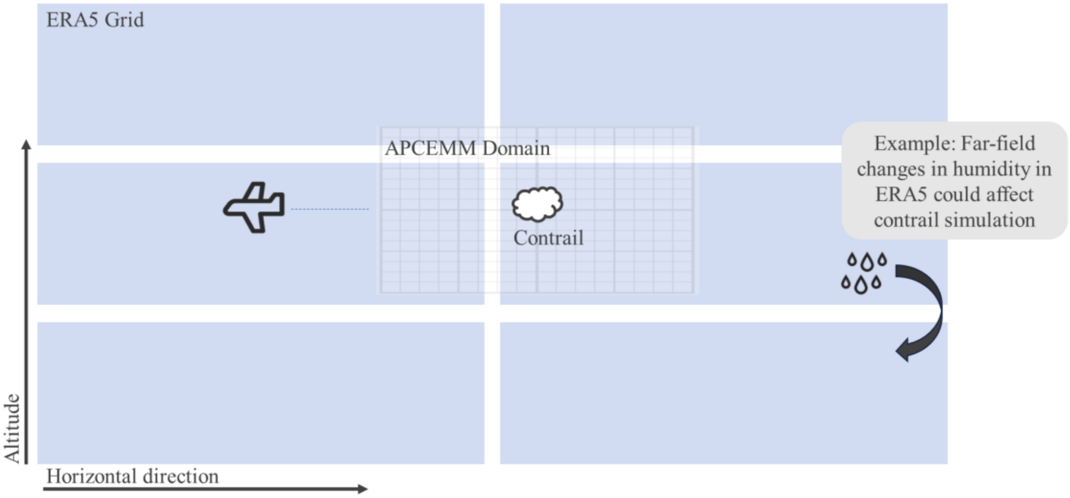

Figure 15: Illustration of how far field changes in humidity could affect the simulated contrail lifetime

In our APCEMM simulations, the humidity field is initialized from the ERA5 weather data. For the remainder of the simulation, this humidity field is calculated from the water vapor available from the previous APCEMM time step, while accounting for mixing between APCEMM grid cells. An example of the difference in the relative humidity field is presented in Figure 16. Given the finer APCEMM grid resolution (100 m width by 10 m high), this means that we have continuity in sub-grid-scale variations as the simulation continues, and water vapor that is initially near the contrail, will remain in proximity to the contrail, leading to smaller sensitivity to far-field changes in water vapor mixing ratios.

Since recent studies that applied the ERA5 weather data did not account for this continuity in sub-grid scale variations in water mass (Teoh et al., 2022, 2020), we also present a second set of results for comparison purposes. Here, contrail lifetime is truncated once the advected ERA5 data becomes subsaturated, and we label these results “Truncated lifetime (RHi <100%)”. This lifetime is shown in Figure 16 (a). Here we use this truncated lifetime as a lower bound estimate for our contrail lifetimes and subsequent impacts.

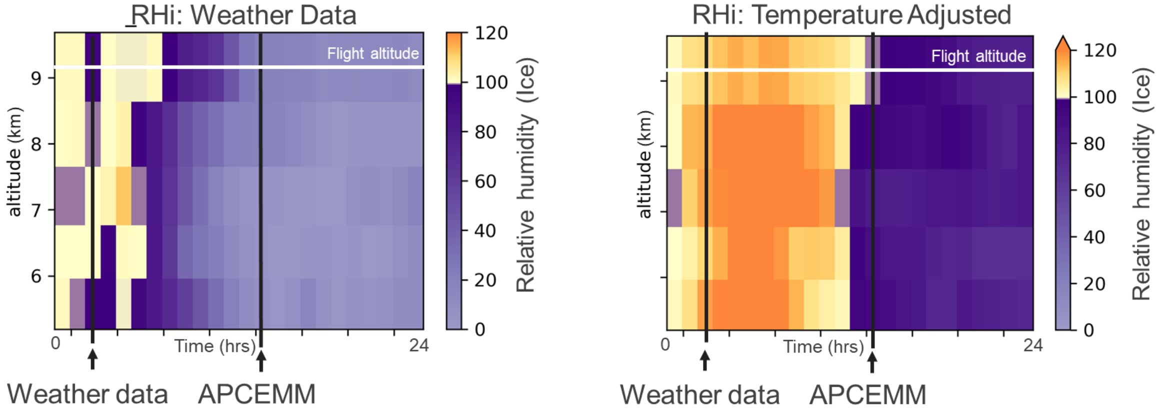

(a) (b)

Figure 16: Comparison between relative humidity over time between (a) using ERA5 humidity at each time step and (b) calculating relative humidity from the available water vapor and ERA5 temperature at each time step.

3.2.2. Quantifying temperature change effects using APMT-IC

3.2.2.1. Model overview

The contribution of each of the climate forcers to RF in a specific year, and global temperature change are quantified using the Aviation environmental Portfolio Management Tool - Impacts Climate (APMT-IC) (Mahashabde et al., 2011; Marais et al., 2008; Wolfe, 2015, 2012). The APMT-IC model is developed as a simplified climate model capable of estimating the impact of aircraft emissions on the climate and quantifying the uncertainties associated with these impacts. Uncertainty distributions are derived using a quasi-Monte Carlo method.

In this thesis, various updates were made to this model. This Chapter describes the modeling approach of the physical impacts captured in APMT-IC, as well as outlining model updates made to these parts of the model. These model updates, performed for this work of this thesis, are published in literature in Grobler et al. (2019), de Jong et al. (2018), and Dray et al. (2022).

As input, the model takes inputs in the form of annual emissions (Section 3.2.2.2). These emissions are used to derive CO_2 concentration (Section 3.2.2.3), and subsequent radiative forcing (3.2.2.4) from CO_2.

For the short-lived climate forcing pathways of semi-direct sulfate, direct stratospheric water vapor, direct soot forcing, and indirect NO_x forcing pathways, RF is quantified using an emissions scaling approach (Section 3.2.2.5). While this does not capture the impact of spatial temporal variations on RF over time, these forcing pathways are estimated to be collectively responsible for a relatively small proportion (~13%) of aviation's cumulative radiative forcing (Lee et al., 2020). Global annual RF from contrails can either be quantified in APMT-IC using a distance based scaling approach (Chapter 4 & 5), or as in this Chapter, annual RF can be specified directly (Section 3.2.2.5 & 3.3.1.1).

Radiative forcing is linked to global annual temperature change using a two-box ocean atmosphere model (Berntsen and Fuglestvedt, 2008) (Section 3.2.2.7).

This chapter focusses on the physical impacts, radiative forcing and temperature change, due to aviation emissions. However, in Chapters 4 and 5, APMT-IC is applied to use the calculated global temperature change to estimate the health, welfare, and ecological costs of anthropogenic climate change. This damage module, including updates made during this thesis are described in Chapter 4 and Chapter 5 (Sections 4.3.2.2 and 5.3.2.2).

3.2.2.2. Input emissions

As inputs, APMT-IC takes annual total fuel-burn, CO_2, and NO_x emissions. The model is additionally updated to take emissions inputs from quantities of nvPM, and H_2O and distance flown. In this chapter, APMT-IC is run for the emissions derived from Chapter 2, as listed in Table 1 and Table 2.

3.2.2.3. Modelling CO_2 concentration

CO_2 has a long atmospheric lifetime, and we expect at least 20% of present-day CO_2 emissions to remain in the environment for the next 1000 years (Joos et al., 2013). Resultingly, the model considers the long-lasting, integrated climate impact of CO_2, and models 800 years following an emissions scenario.

APMT-IC models the CO_2 concentration due to aviation emissions using an impulse response function (IRF) approach, which models the fraction of an emission pulse remaining in the atmosphere as a function of time (Berntsen et al., 2010; Joos et al., 2013). Emissions from different years are combined using a convolution approach.

The atmospheric CO_2 from an emissions pulse is non-linearly dependent on the changes in non-aviation (or background) CO_2 emissions, with changes such as temperatures increases, and saturated carbon sinks, affecting the removal rate of additional CO_2 from the atmosphere. To capture these effects, APMT-IC is updated to represent the CO_2 concentration response under different future emissions scenarios.

A set of IRFs are calculated using the Model for the Assessment of Greenhouse-gas Induced Climate Change (MAGICC6), which is capable of capturing these non-linear carbon cycle feedbacks (Meinshausen et al., 2011a).

To derive the IRFs, MAGICC6 is run for different scenarios of all-source atmospheric CO_2 emissions and concentrations obtained from the Representative Concentration Pathways (RCP) of the Intergovernmental Panel on Climate Change (IPCC) (Moss et al., 2010). The four pathways developed in the RCPs represent future emissions projections from a larger set of scenarios in the literature (van Vuuren et al., 2011), spanning the range of expected radiative forcing values for 2100. These scenarios were further extended to include emissions projections up to the year 2500 (Meinshausen et al., 2011b).

Figure 17 shows the different APMT-IC IRFs. For the time between 2010 and 2100, IRFs are calculated at a 10-year emissions resolution for each of the four RCP scenarios. Between 2100 and 2500, a 100-year emissions resolution is applied. RCP emissions are defined until the year 2500 only (Meinshausen et al., 2011b). As such, IRF behavior after 2500 has been extrapolated using an exponential function. Similarly for the years 1970 to 2009 extrapolation is applied. Emissions before 1970 are modeled using IRF from Joos et al. (2013).

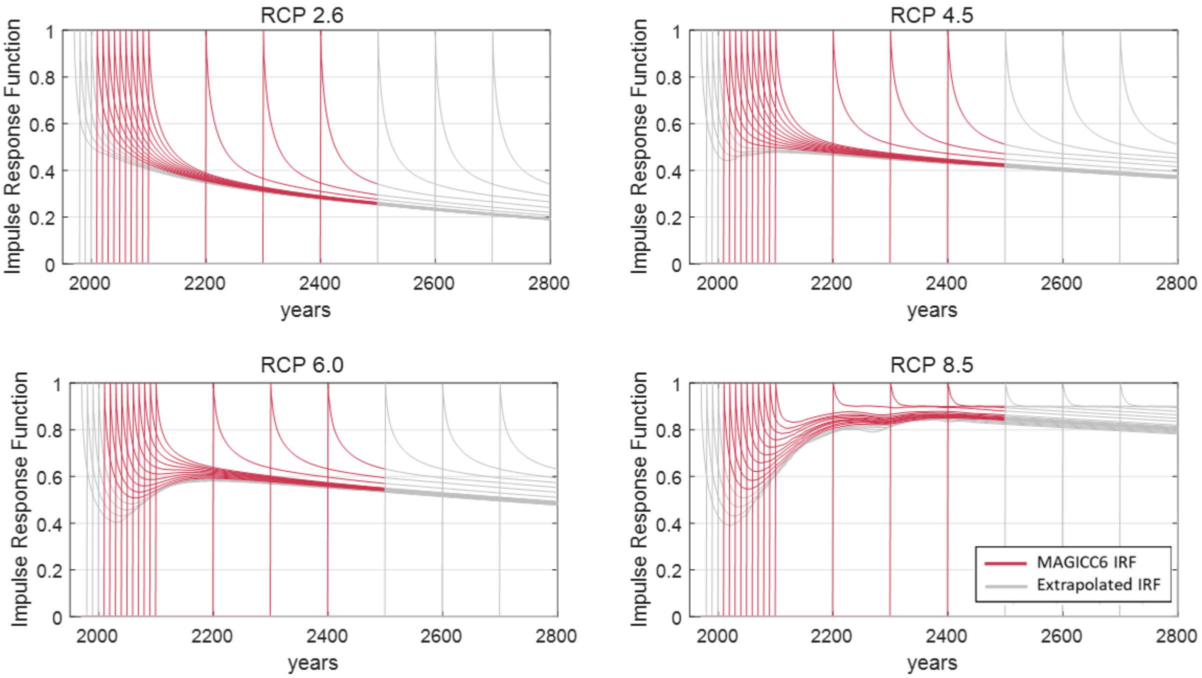

Figure 17: Impulse response functions for different RCP scenarios derived using Model for Greenhouse-gas Induced Climate Change (MAGICC6)

3.2.2.4. Modelling RF from CO_2

The resulting CO_2 radiative impacts are computed using the radiative transfer function included in Fifth Assessment Report of the IPCC (Myhre et al., 2013, 1998). Similar to the CO_2 concentration response, RF from aviation's emissions is non-linearly dependent on the background CO_2 concentration, due to saturation of the spectral absorption bands.

To capture this non-linearity, APMT-IC models CO_2 radiative forcing using a marginal impact approach, where aviation's CO_2 RF is estimated by first calculating the total anthropogenic CO_2 RF and then subtracting the total anthropogenic CO_2 RF without aviation emissions (Eq 2).

$$\begin{aligned}\mathrm{RF}(\text{Aviation CO}_2) \\ &= \mathrm{RF}(\text{Total Anthropogenic CO}_2) \\ &- \mathrm{RF}(\text{Total Anthropogenic CO}_2 - \text{Aviation CO}_2)\end{aligned} \qquad \text{Eq 2}$$

Background (all-source) anthropogenic CO_2 concentrations are taken from the Representative Concentration Pathways (RCP) as provided by the Intergovernmental Panel on Climate Change (IPCC) (Moss et al., 2010).

3.2.2.5. RF from non-CO_2 forcers

For the short-lived climate forcing pathways of semi-direct sulfate, direct stratospheric water vapor, direct black carbon forcing, and indirect NO_x forcing pathways, RF is quantified using an emissions scaling approach. These forcing pathways are estimated to be collectively responsible for a relatively small proportion (~13%) of aviation's cumulative radiative forcing (Lee et al., 2020).

To model the radiative impacts of aerosols (nitrate, sulfate, and black carbon), stratospheric water vapor, and indirect ozone from NO_x emissions, the average radiative forcing of these impact pathways is scaled to their respective annual emissions. These forcing pathways are assumed to last less than a year after emissions (Sausen et al., 2005; Sausen and Schumann, 2000) and mathematically this scaling can be written as

$$RF_{short,j}(t) = \frac{Q(t)}{Q\left(t = t_{ref}\right)} \mathrm{R}F_{short,j}\left(t = t_{ref}\right) \qquad \text{Eq 3}$$

where, $RF_{short,j}$ represents the radiative forcing of species j. $Q(t)$ represents the emissions quantity.

For the updated model implementation, these RFs are from a multi-model study, supplied by Aviation Climate Change and Research Initiative (ACCRI), which derived annual RF from the year 2006 AEDT emissions (Brasseur et al., 2016).

Table 3 shows the reference emissions as well as reference RF for each species. Monte Carlo uncertainty distributions, based on these values, are derived following a simplified rule. If three or more RF values are available in Brasseur et al. (2016), APMT-IC V24b uses a triangular distribution to model the RF distribution for that short-lived forcer, where the distribution's minimum value is the minimum value from Brasseur et al. (2016), and similarly the distribution maximum value is the maximum RF value from Brasseur et al. (2016). The mid value for the triangular distribution is found by taking the mean of the RF values presented in Brasseur et al. (2016) for a particular short-lived forcer. If only two RF values are presented in Brasseur et al. (2016), APMT-IC V24b uses a uniform uncertainty distribution, once again where the distribution upper and lower bounds correspond to the RF values in Brasseur et al. (2016).

Table 3: Values used for the short-lived, non-CO_2 impacts based on Brasseur et al. (2016).

Parameter	Values	Distribution	Units
RF black carbon (nvPM)	0.6, 1	Uniform	mW/m^2
RF sulfate aerosols	-9, -4.8, -3	Triangular	mW/m^2
RF stratospheric water vapor	1.3, 2	Uniform	mW/m^2
RF contrails	12.4, 37.9, 80	Triangular	mW/m^2
RF nitrate aerosols	-7.5, -3	Uniform	mW/m^2
Reference year fuel burn	188.1	Constant	Tg
Reference year distance	3.87×10^{10}	Constant	km
Reference year NO_x emissions	2.67	Constant	Tg NO_x as NO_2

We model longer-lived ozone and methane impacts from NO_x based on a review of literature estimates, as described in Mahashabde et al. (2011). For results in this chapter and Chapter 5, the NO_x related methane effect is increased by 14%, due to an updated estimate of the short-wave RF from a line-by-line radiative transfer study (Etminan et al., 2016; Lee et al., 2020).

Global annual RF from contrails can either be quantified using a distance-based scaling approach (Chapter 4 & 5), or annual total RF can be specified directly. In this chapter annual RF from contrails are taken from our assessment of contrail RF as presented in Sections 3.3.1.1. The lower bound for each year is defined by the truncated contrail lifetime results (RHi < 100%), and upper bound is defined by the full APCEMM lifetime results. A uniform uncertainty distribution is applied between these two bounds.

The climate impacts of other aviation emissions including non-methane volatile organic compounds (NMVOC), carbon monoxide (CO), and organic carbon (OC), are not quantified since they have been shown to be negligible (Brasseur et al., 2016). The indirect impact of BC deposition on ice, and the impacts of aviation emissions on cloud formation are not quantified, as these impacts remain highly uncertain (Lund et al., 2017a).

3.2.2.6. Effective radiative forcing and climate efficacies for non-CO_2 forcers

The effect of the radiative forcing of non-CO_2 climate forcers on temperature change can differ from the impact of CO_2 for the same quantity of RF, due to differences in horizontal and vertical radiative distributions in the atmosphere.

Effective radiative forcing (ERF) and climate efficacies are concepts introduced in literature to account for differences in the atmosphere's temperature response, from the same level of RF from non-CO_2 and CO_2 forcing (Bickel et al., 2020a; Lee et al., 2020; Ponater et al., 2021).

Specifically, climate efficacy quantifies the relative effectiveness of a radiative forcing agent to cause changes in the equilibrium surface temperature compared to CO_2, expressed as the ratio of temperature change per unit of radiative forcing for the agent versus CO_2. Quantifying this effect requires long term ensemble climate model runs, and often aviation forcers need to be scaled up, to extract a signal from the temperature change. (Hansen et al., 2005; Ponater et al., 2021) In contrast, the derivation of ERF allows rapid atmospheric adjustments from non-CO_2 RF to normalized before determining the ratio of ERF. These atmospheric adjustments include changes in cloud cover, water vapor, temperature profiles, and surface albedo (Bickel et al., 2020a).

Except for contrails, we do not apply ERF/RF or efficacy adjustment factors. For aviation, these adjustment values are still associated with large uncertainties as very few studies exist (Lund et al., 2017a). Wuebbles et al. (2010) argue that "too few climate models have assessed aviation efficacies to justify their use in policy". This is in-line with other studies that do not apply an adjustment (Fuglestvedt et al., 2010).

However, various estimates for efficacy and ERF/RF are available for contrails, all indicating a lower temperature response per unit RF as compared to CO_2 (Bickel et al., 2020a; Ponater et al., 2021; Rap et al., 2010). As a result, we include an adjustment factor to contrail RF based on these studies. Ponater et al. (2005) find an efficacy adjustment factor of 0.59, Rap et al. (2010) find an efficacy adjustment factor of 0.31, and Bickel et al. (2020) find an ERF/RF adjustment factor best estimate of 0.35. We combine these estimates from literature and apply a triangular uncertainty distribution with a mid-value of 0.417, minimum value of 0.31 and maximum value of 0.59.

We note some unquantified uncertainties that are not captured in this approach. Firstly, while this ERF/RF adjustment captures the difference in temperature change from short term RF, this ERF/RF may not necessarily provide an accurate measure of long-term temperature response (Bickel et al., 2020b; Ponater et al., 2021). Secondly, the adjustment factors from Ponater et al. (2006) and Rap et al. (2010) represent long-term climate feedback for linear contrails only, derived using contrail formation more than 50 times expected contrail coverage in 2050. This upscaling may cause saturation of feedback effects such as cloud formation (Fuglestvedt et al., 2010; Lund et al., 2017a; Wuebbles et al., 2010).

3.2.2.7. Temperature change model

Changes in global surface temperature associated with aviation emissions are calculated using a probabilistic two-box ocean model (Berntsen and Fuglestvedt, 2008). In this thesis, the equilibrium climate sensitivity (ECS) uncertainty distribution is updated to the Roe and Baker (2007) uncertainty distribution, with parameters calibrated to the US Government interagency working group on social cost of carbon. The resulting ECS has a mean of 3.5 °C for a doubling of CO_2 (US Government, 2016), which falls within the 2.1 to 4.7 °C range of the IPCC Coupled Model Intercomparison Project 5 (CMIP5) (Flato et al., 2013).

3.2.3. Emissions before 1980

The emissions inventory presented in Chapter 2 presents emissions for 1980 to 2019. However, smaller quantities of emissions also occurred before 1980. In line with other studies, we do not quantify emissions before 1940 (Klöwer et al., 2021; Lee et al., 2020; Sausen and Schumann, 2000). Between 1940 and 1980, we assume a linear annual growth starting at zero fuel burn in 1940 and ending at 61.6 Tg fuel burn in 1980. For this period, we use emissions indices from the year 1980 as quantified in Chapter 2. This collectively accounts for 21% of total aviation fuel burn from 1940 to 2019. This method could overestimate the emissions occurring between the year 1940 and 2019, since it assumes a constant annual fuel burn growth quantity. Future studies could improve upon this method by using an assumed annual growth rate and calculating emissions backwards from the year 1980.

As an upper bound, we also run APMT-IC for IEA fuel burn totals with our annual emissions indices and contrail impacts per distance flight.

3.3. Results

3.3.1. Contrail radiative forcing results

3.3.1.1. Global results over time

On net, we find that contrail impacts have increased from 33 to 185 mW/m^2 from 1980 to 2019 using the full APCEMM lifetimes as plotted in Figure 18. In comparison, IPCC estimated 50 mW/m^2 for flight operations in 2011, and Lee et al. (2020) estimated 111.4 mW/m^2 (range 33.4-

189.4) for flight operations in 2018 as plotted in Figure 18. Both these estimates include scaling factors that increase emissions to account for non-scheduled flights, such as military operations. In contrast, we only include emissions from commercial civil passenger flights in this thesis. As a result, these comparison datapoints would be smaller if scaled to only include impacts from commercial civil passenger flights, as presented in this thesis.

As described in Section 3.2.1.6, our "full APCEMM lifetime" results are based on APCEMM simulations that account for continuity in water mass around the contrail as the simulation proceeds. In contrast, studies that have updated the water content around the contrail in each timestep using the ERA5 weather data (Teoh et al., 2022, 2020), could prematurely expose contrails to far field changes in humidity (Section 3.2.1.6). This modeling difference is caused by the mismatch between ERA5 grid cell sizes (~30 km width) and the contrail length scale (0.1 to 10 km). For comparison purposes, we present a second set of results, which are more analogous to this method in literature, where we truncate the contrail lifetime when the ERA5 relative humidity with respect to ice (RHi) around the contrail falls below 100% (see Sec 3.2.1.6). In the figures in this section, we label these results as "Truncated lifetime (RHi<1)". For these truncated lifetime results, contrail RF increased from 9.9 to 62 mW/m^2 from 1980 to 2019, which is lower than the central values from IPCC and Lee et al. (2020).

The increase in global contrail RF, is predominantly driven by the increase in flight distance, which increased from 9.5 to 53×10^{12} km from 1980 to 2019 (Table 2).

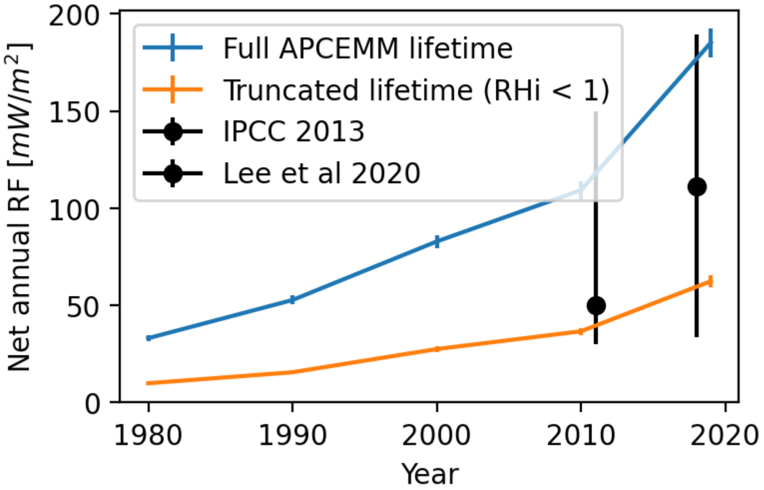

Figure 18: Global contrail RF over time from 1980 to 2019 for results from this thesis, and results from IPCC 5th Assessment Report (Myhre et al., 2013)*, as reported by Kärcher* (2018)*, and results from Lee et al.* (2020)*. Error bars for our results represent the standard error of the mean only.*

Figure 19 shows how the fraction of flight segments that form persistent contrails, and radiative impact per contrail and flight distances have varied. Over this time period, we find that the fraction of flight segments that cause contrails has increased by 32% from 3% to 4% globally. In contrast, the mean energy forcing per distance contrail ($EF/m_{contrail}$) decreased by 24% from 1.8 to 1.4 × 10^9 J/m. As a result, the mean energy forcing per flight distance (EF/m_{flight}) remains within 10% of its magnitude in 1980.

The magnitude of these energy forcing per distances are higher than those derived by Teoh et al. (2020) which found $EF/m_{contrail}$ of 0.75 × 10^9 J/m for the Japanese airspace. This difference is likely due to differences in treatment of atmospheric mixing around the contrail as described in Section 3.2.1.6.

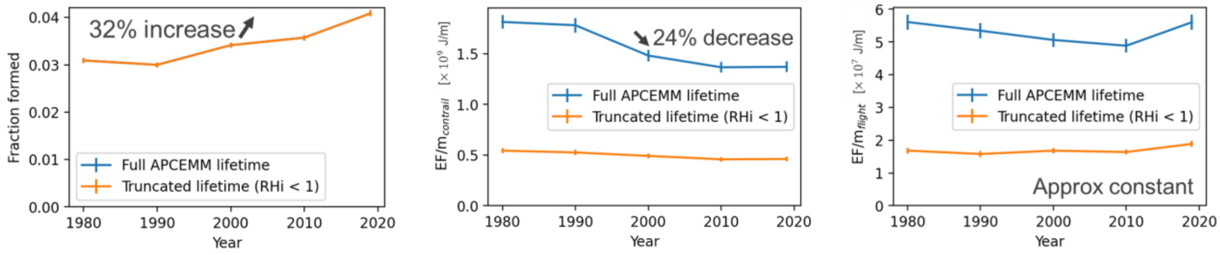

(a) (b) (c)

Figure 19:Changes in fraction flight segments causing contrails and contrail radiative impacts over time. Error bars represent the standard error of the mean.

While the data above focusses on the mean impacts over time, significant variation exists in individual contrail impacts. Focusing on the contrail simulations for 2019, Figure 20 shows the distribution of results for individual contrail radiative impacts for the full APCEMM lifetime, as well as the truncated contrail lifetimes. We find EF/$m_{contrail}$ of 1.4×10^9 J/m for the full APCEMM lifetime, with a standard deviation of 3.3×10^9 J/m. Using the trucated lifetime, the EF/$m_{contrail}$ is 0.46×10^9 J/m with a standard deviation of 1.3×10^9 J/m.

The figure also shows the lifetime of the contrails, and an average contrail lifetime of 10 and 4.8 hours and a standard deviations of 5.5 and 3.9 hours for the full APCEMM lifetime and the lifetime truncated for RHi<1, respectively. Literature estimates for contrail lifetime are shorter. Teoh et al. (2020) find mean contrail age of 3.2 hours in a contrail modeling study over the Japanese airspace. The differences in lifetime between our full APCEMM lifetime and theirs could be due to differences in how we capture continuity in sub-grid-scale variation in water mass. Gierens et al. (2018) find mean contrail lifetime of 3.7 hours using a satellite-based observation study. However, uncertainty remains given the difficulty of identifying both young contrails on satellite images, which do not yet show up on the satellite data, and mature contrails, which have become optically thin.

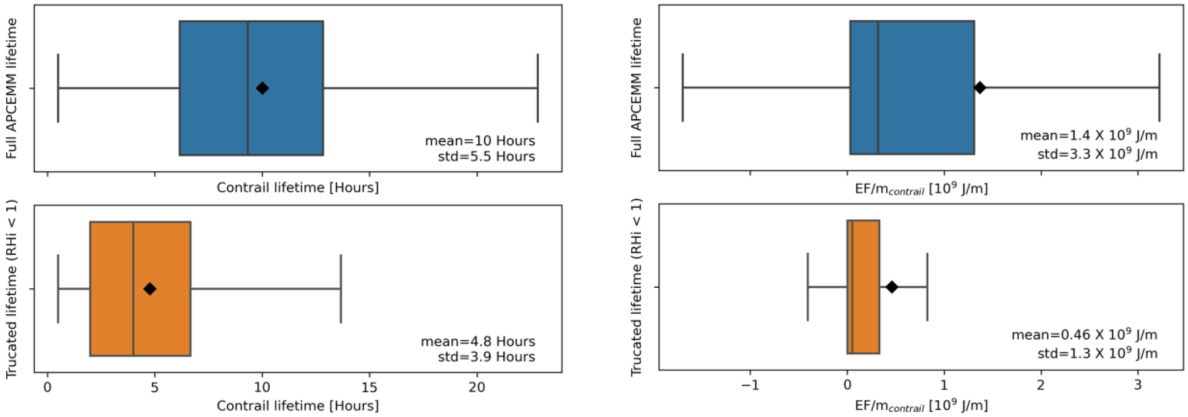

(a) (b)

Figure 20: Variation in (a) contrail lifetime and (b) contrail forcing for the results with the full APCEMM lifetime, and the truncated contrail lifetime (Section 3.2.1.6) for the year 2019.

3.3.1.2. Effect of underlying trends on total global contrail RF

Effect of thermal efficiency on contrail formation

Quantifying engine thermal efficiency, we find the mean engine thermal efficiency increased by from 0.36 to 0.43 over the period 1980 to 2019, representing an increase of 22% (Figure 21). This increase in engine thermal efficiency is responsible for an increase in the contrail formation fraction, since an increase in engine thermal efficiency increases the slope of the Schmidt-Appleman mixing line, in turn expanding the range of atmospheric conditions under which contrails can form.

This increase in engine efficiency is responsible for half of the increase in contrail formation reported in the previous section as shown in Figure 21 and Figure 22. Figure 21 (b) shows the fraction of flight segments that lead to contrail formation, assuming uniform engine thermal efficiencies between 0.2 and 0.5, as well as the engine efficiencies derived from the BADA data for the aircraft in the current year (Figure 21). This figure shows, that if the thermal efficiencies had remained constant, but the location and time of emissions had varied as in the flight operation data, contrail formation fraction would have increased by 16%-18%.

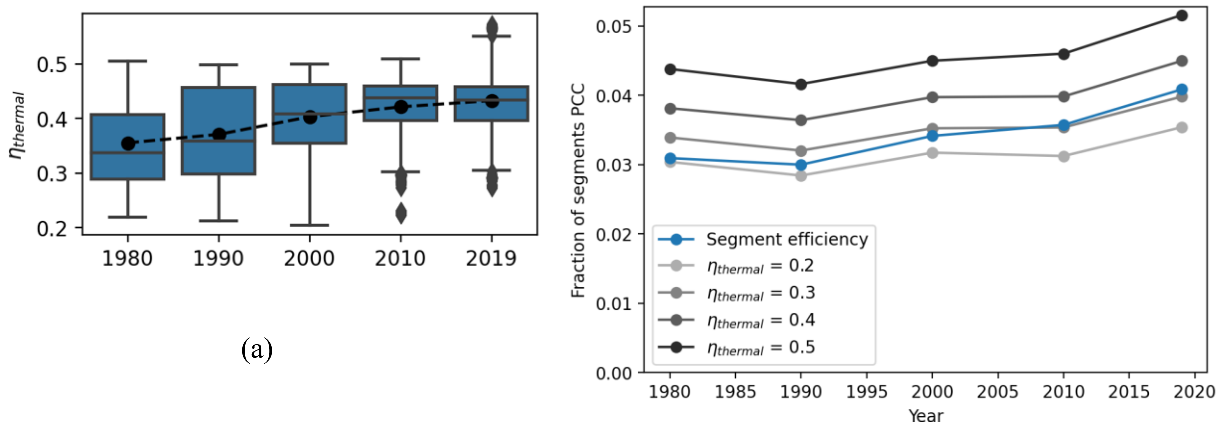

(a)

(b)

Figure 21: Distribution of (a) angine thermal efficiency and trends in (b) contrail formation fraction over time. In figure (b), the "Segment efficiency" represents the calculated efficiency of the flight segment, while the other lines show contrail formation fraction for a constant thermal efficiency.

This increase is not significantly affected by changes in the background weather data. Figure 22 shows the fraction of flight segments that lead to contrail formation if the 2019 operational patterns occurred against the weather data from 1980 to 2019. The variation in these data points for each uniform engine efficiency line is less than 4%, indicating that changes in the atmosphere is responsible for only a small effect.

As such, other differences in flight operations are responsible for the other half of the change in contrail formation fraction, such as location, altitude, and time of emissions.

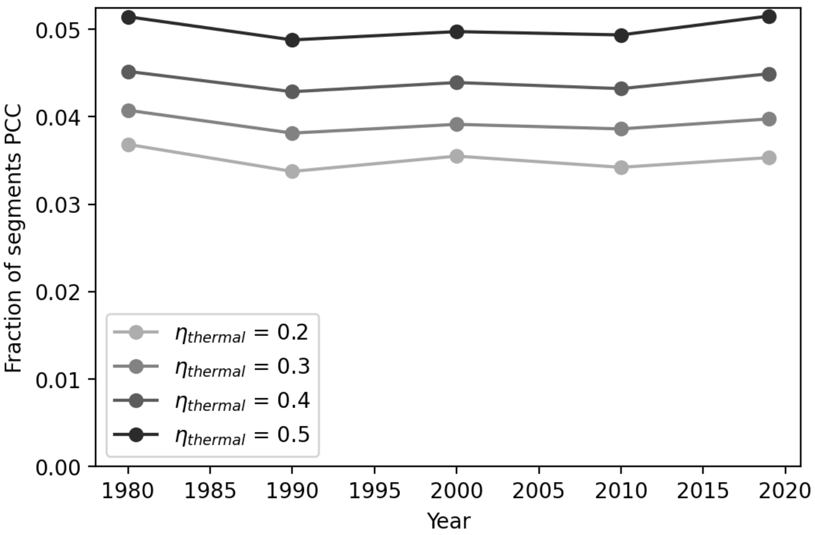

Figure 22: The fraction of flight segments that lead to persistent contrails if the 2019 emissions occurred with the weather data from 1980 to 2019. Each line shows contrail formation fraction for a constant thermal efficiency.

Effect of altitude, region, time, and aircraft size

Figure 23 to Figure 25 show how contrail formation fraction, $EF/m_{contrail}$, and EF/m_{flight} vary with various emissions characteristics. These plots include all the evaluated chords from 1980 to 2019. These factors include latitude, altitude, month, local time of day, as well as aircraft characteristics, such as aircraft mass, and the mission fuel consumption per mission distance. The mean over the samples, and the standard error of the mean is plotted in each graph. Only data points where the relative standard error of the mean is below 15% are included.

The figure shows results for both definitions of lifetime and is normalized by the mean value to show the trends of each metric for both definitions of lifetime. Collectively, these plots show that these trends are not sensitive to the selection of the two lifetime definitions.

In interpreting these plots, it is important to note that these plots represent correlation only, since another underlying factor could be driving both the plotted factor and the contrail impact metric.

For example, aircraft size and cruise altitude could co-vary, and increasing contrail impacts could be driven by aircraft size, or by an increase in cruise altitude.

Contrail formation fraction and subsequent EF impacts co-vary with the altitude and location of emissions, with the strongest co-variance resulting from differences in flight latitude. These plots show that both contrail formation fraction and EF/$m_{contrail}$ increase with latitude. As a result, EF/m_{flight} varies from half to 2.5 times the mean value, increasing with increasing latitude. Contrail impacts also vary by altitude. Contrail formation fraction peaks between altitudes of 10 km and 12 km, varying from a quarter of the mean to factor 1.5 of the mean. In contrast, the EF/$m_{contrail}$ remains relatively constant (~20% variation), and differences in EF/m_{flight} is predominantly driven by the lower formation fraction.

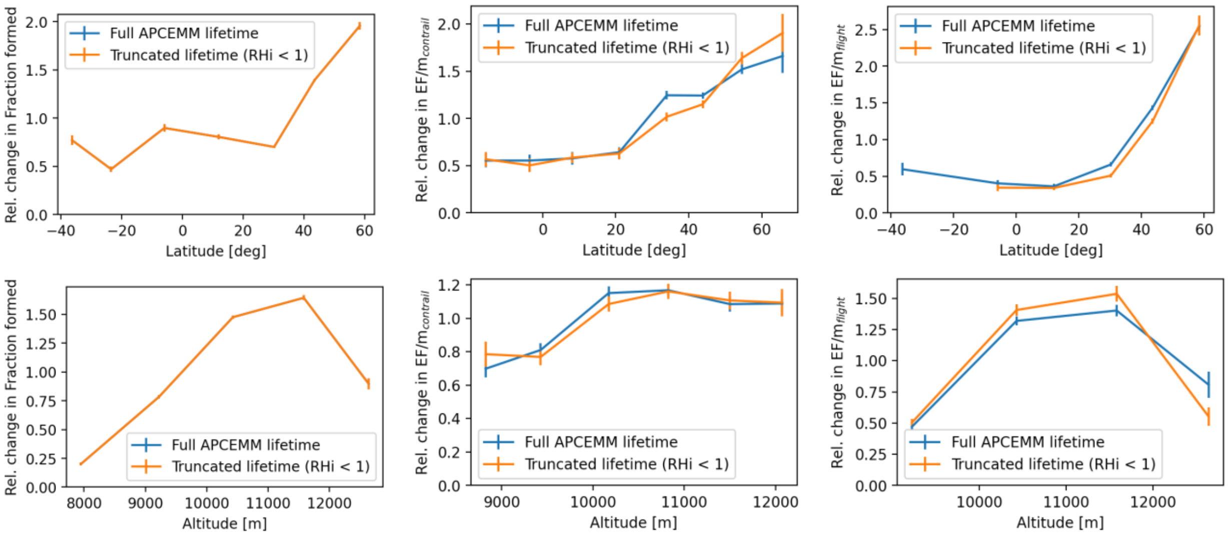

Figure 23: Relative change in fraction of flight segments that form contrails, and contrail impacts by altitude and latitude. Error bars represent the standard error of the mean only.

Contrail impacts also vary by time of year. For flights occurring in the northern hemisphere, both the formation fraction, and EF/m$_{contrail}$ peak during the northern hemisphere winter, leading to a strong correlation between EF/m$_{flight}$ and month, with impacts varying between half and 50% increase above the annual mean. Since daily emissions are ~10% lower during the winter, this seasonal sensitivity leads to lower contrail impacts than if flights were distributed uniformly throughout the year.

Contrail impacts co-vary with time of day, with lowest EF/m$_{contrail}$ occurring for early morning flight segments between 4 am and 10 am local time. This could be driven by daytime contrails that reflect more incoming radiation, leading to a smaller net effect. A lower formation fraction also occurs during the day, amplifying the co-variance. Some of these differences can also be caused by differences in flight characteristics between night and day. For example, a higher proportion of short haul flights occur during the day than during the night, and a higher proportion long haul flights occur during the night than during the day (Section 2.3.4.2).

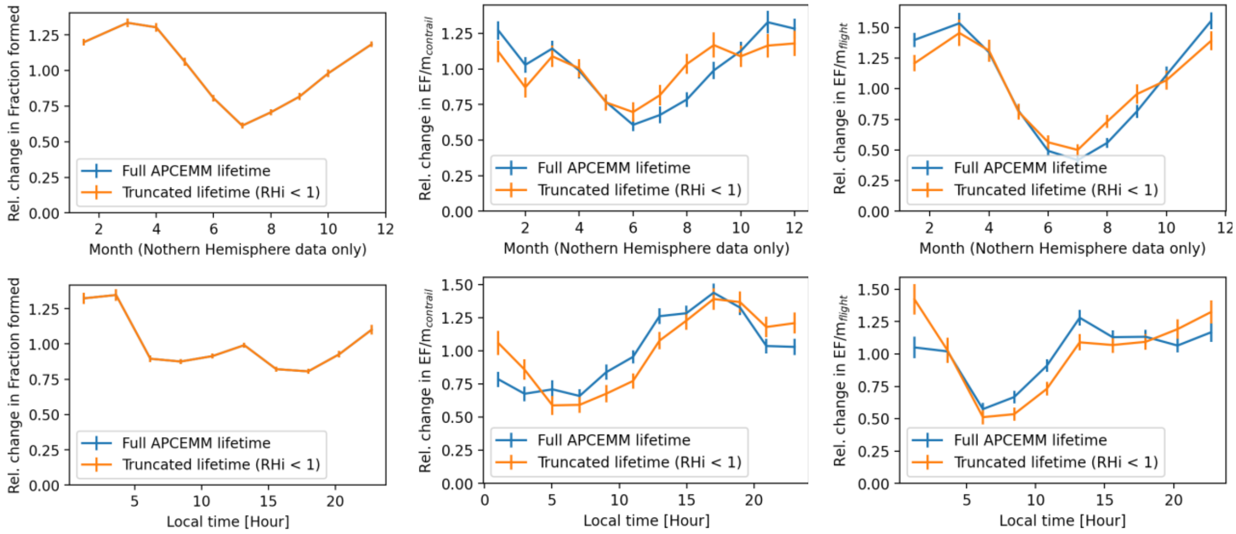

Figure 24: Relative change in fraction of flight segments that form contrails, and contrail impacts by month and time of day. Error bars represent the standard error of the mean only.

Aircraft size characteristics, as represented by aircraft mass, and fuel consumption per distance flown, also co-vary strongly with contrail EF/m_{flight}. Both the contrail formation fraction and the $EF/m_{contrail}$ contribute to this trend. This could be driven by a variety of underlying differences, such as differences in time of day or altitude that these aircraft are operated, differences in particle number emissions index, and differences in region. Further research would be necessary to extract the effect of aircraft size on contrail impacts.

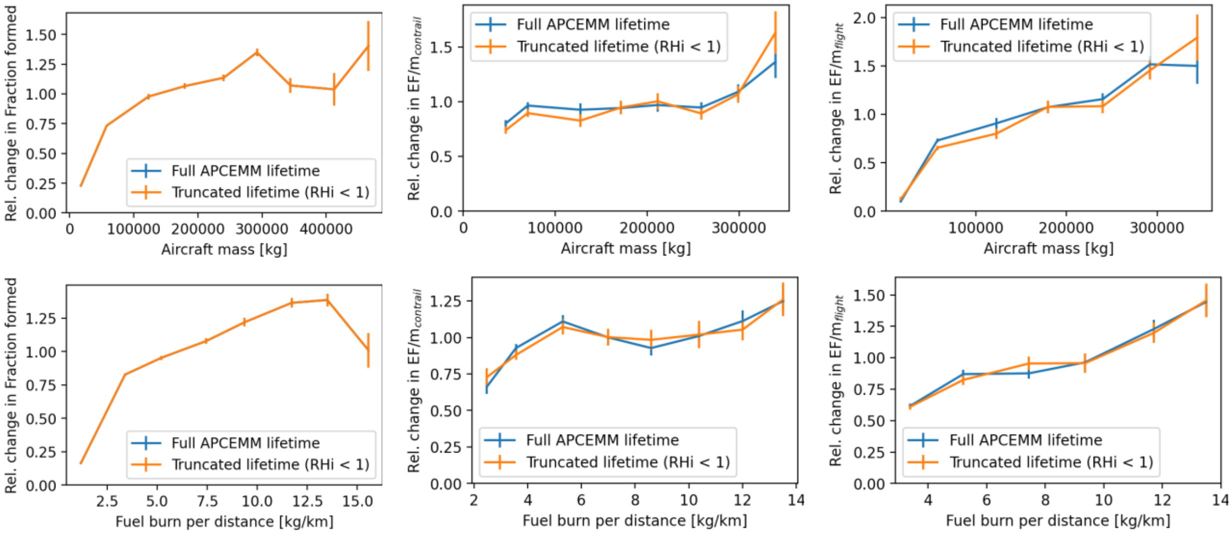

Figure 25: *Relative change in fraction of flight segments that form contrails, and contrail impacts by aircraft mass and mission fuel burn by mission distance. Error bars represent the standard error of the mean only.*

Contrail results by region

We present our contrail impacts broken out by the world regions defined in Lund et al. (2017a) (Figure 26). Flight segments are grouped into different regions, and contrail formation and energy forcing from 1980 and 2019 are extracted for each of the regions.

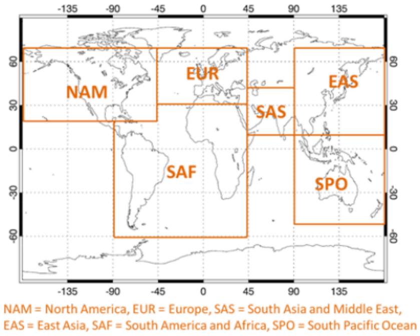

Figure 26: Emissions regions defined by Lund et al. (2017a)

In both these years, our results indicate higher formation fraction and $EF/m_{contrail}$ for flight segments over Europe (Figure 27). As a result, EF/m_{flight} is also higher over Europe than other regions. In 1980, the fraction of contrail formation in North America and East Asia were similar. However, in 2019, the fraction of contrail formation in North America was more than double that of East Asia, with the fraction of contrail formation increasing over North America and decreasing over East Asia. Over this time, a substantial proportion of global fuel burn shifted from North America to East Aisa, with the global share of emissions in North America halving, while the share in East Asia tripled (Section 2.3.2). Despite this shift in emissions, our global contrail formation fraction still increased by 32% (Figure 19 (a)). Collectively these trends indicate the global increase in the fraction of flight segments that cause contrails is not driven by the regional shift in emissions from 1980 to 2019.

The results also indicate that $EF/m_{contrail}$ in North America and East Asia remain similar to each other in both 1980 and in 2019. The $EF/m_{contrail}$ decreased from 1980 to 2019 for all regions, indicating that it is also not a regional shift that led to the 24% global mean decrease in $EF/m_{contrail}$ indicated in Figure 19.

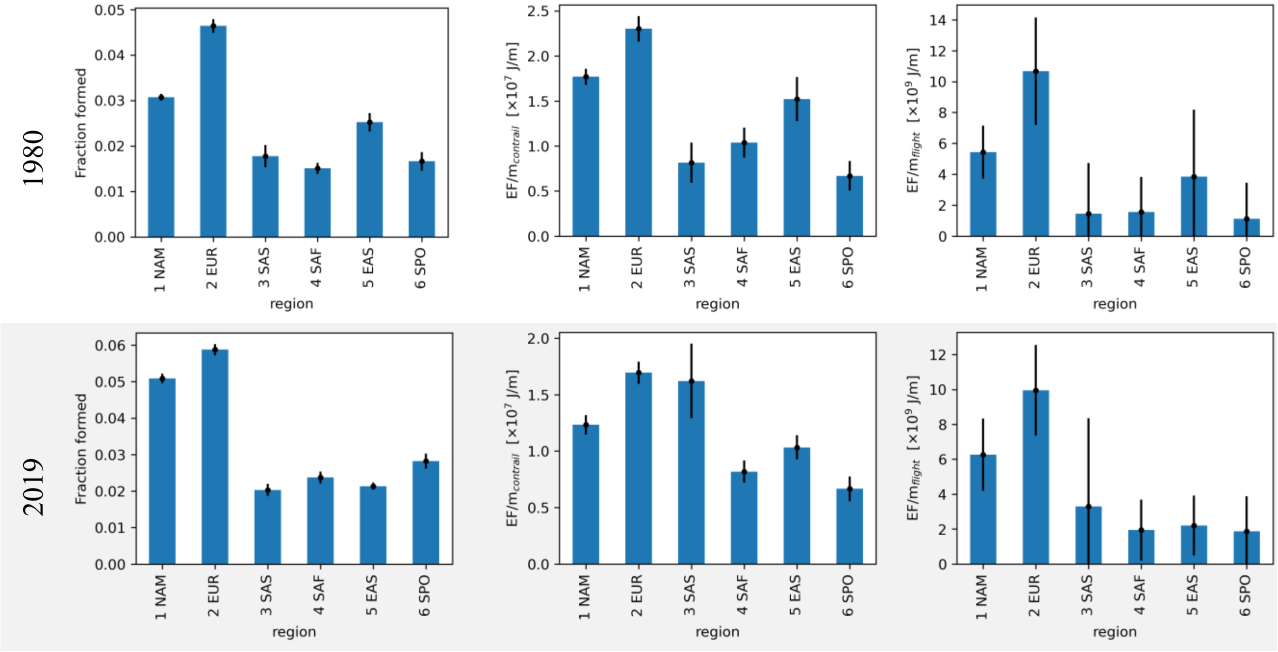

Figure 27: Contrail impacts by region in 1980 (top) and 2019 (bottom).

Given the same region definition is used, these results can be compared the regionalized contrail impacts presented in Lund et al. (2017a). Figure 28 and Figure 29 present a comparison to Lund et al. (2017a), with Figure 28 presenting Global Warming Potential (GWP). In this figure, our results from Figure 27 are adapted to normalize by quantity aviation CO_2 emissions in the region, consistent with the values in Lund et al. (2017a). Likely due to the differences in methods, our GWP results differ from that of Lund et al. (2017a). The largest difference occurs for emissions over Europe, where our contrail GWP is 6 times larger than that of Lund et al. (2017a). Additionally, for emissions over North America, our GWP is 3.3 times larger than that of Lund et al. (2017a). For one region only, the South America and Africa region, our results are smaller than that presented in Lund et al. (2017a). The larger magnitude of impacts in our study is potentially driven by our longer the contrail lifetimes. Additionally, the RF estimates from Lund et al. (2017a) are derived using the global climate model ECHAM5-CCMod. Therefore, their RF results already include the rapid feedback of contrails on cloud formation. As a result, their results are more similar to Effective Radiative Forcing (ERF) (Lee et al., 2020).

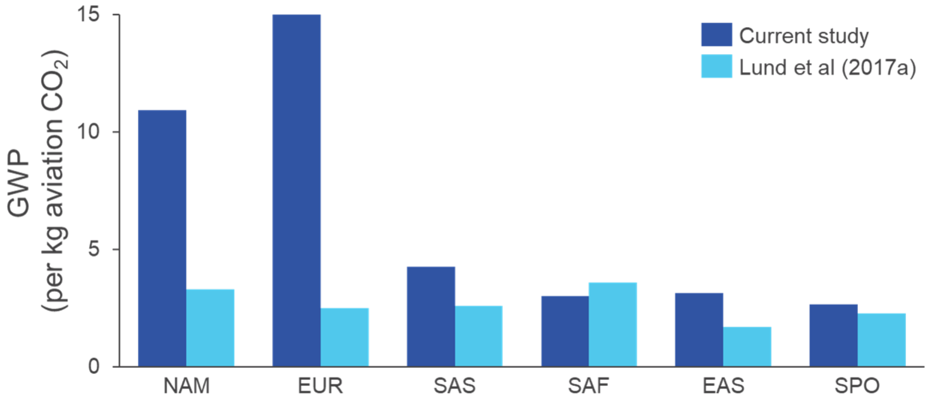

*Figure 28: Comparison of our contrail impacts by region to region*alized contrail results presented in Lund et al. (2017a).

Figure 29 presents a normalized comparison of our results to the regionalized GWP, and Absolute Global Temperature Potential (AGTP) presented in Lund et al. (2017a). Here the comparison shows we find a larger variance between regional impacts than the comparison study. Additionally, this figure shows that the distribution of our normalized regional impacts is more similar to the regionalized AGWP presented in Lund et al. (2017a), where Lund et al. (2017a) also indicates higher impacts in North America and Europe, than in other regions. However, given these differences, this comparison indicates that further work is needed to establish consensus in contrail impacts by region.

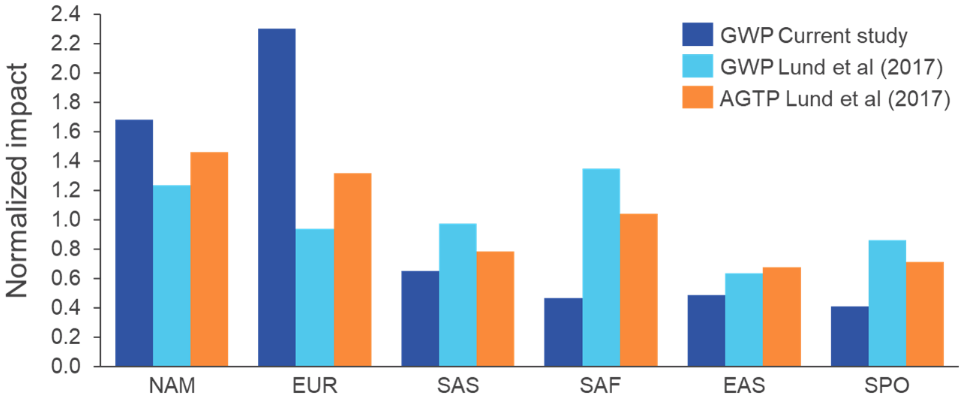

Figure 29: Comparison of contrail impacts by region to regionalized contrail results presented in Lund et al. (2017a)

Role of nvPM particle emissions in contrail impacts

Investigating the role of particle number emissions on contrail impacts, Figure 30 shows contrail formation fraction, EF/$m_{contrail}$, and EF/$m_{contrail}$ for various levels of particle number emissions index. Similar to Figure 25, these plots include all the evaluated chords from 1980 to 2019. The mean over all the samples, and the and standard error of the mean is plotted in each graph. Only data points where the relative standard error of the mean is below 15% are included.

These plots indicate that the contrail formation fraction co-varies with particle emissions index. Since particle emission index is expected to have little effect on the formation criteria, this trend is likely driven by a confounder. One possibility is a difference in aircraft characteristics, such as engine thermal efficiency, where older aircraft could both have lower engine efficiency, and higher soot emissions than newer aircraft.

In our dataset, the impacts vary with particle number emissions, with EF/$m_{contrail}$ increasing for increasing particle number emissions. This result is in line with other studies, which found decreasing particle number emissions results in a decrease in contrail impacts (Burkhardt et al., 2018; Teoh et al., 2020), but differs from another study that found little impact from changing particle number emissions (Caiazzo et al., 2017).

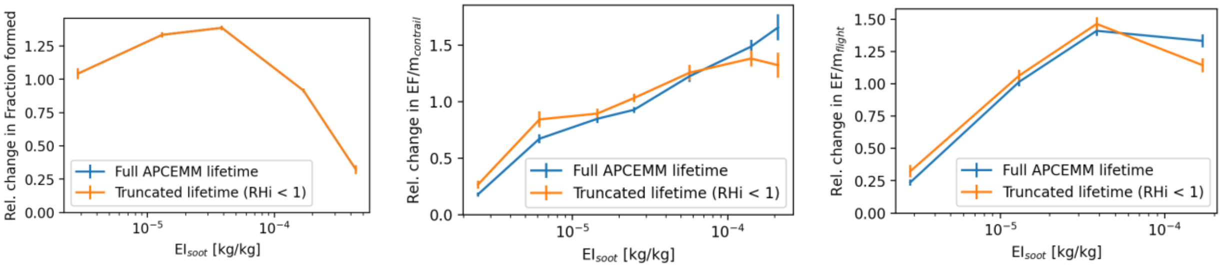

Figure 30: How contrail formation fraction and impacts co-vary with particle number emissions index. Error bars represent the standard error of the mean only.

To control for confounders, an additional set of simulations using a sub-sample containing 10% of the 100,000 chords in the 2019 dataset are performed. Of these 10,000 chords, 390 lead to persistent contrails.

These APCEMM simulations are repeated by changing only the particle number emissions index by a factor of 0.1, 0.5, 2, and 10, respectively, and keeping all other variables the same. Our results indicate that for a halving or a doubling of $EI_{nvPM,num}$, the $EF/m_{contrail}$ changes by -25% or +18%, respectively (Figure 31). For a 0.1 and a 10 times multiplier on $EI_{nvPM,num}$ the $EF/m_{contrail}$ changes by -65% and +68%, respectively. These results are similar to those presented in Burkhardt et al. (2018), that found a 50% and 90% decrease in initial ice particles leads to a ~20% and ~70% decrease contrail RF, respectively.

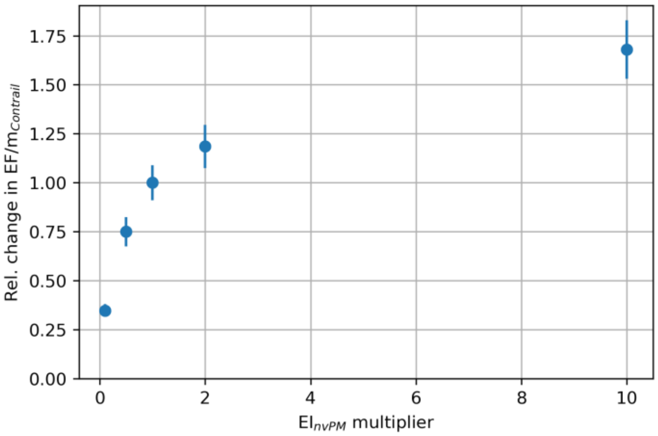

Figure 31: Changes in contrail impacts due to changes in engine particle number emissions. Error bars represent the standard error of the mean only.

3.3.2. Total climate impacts over time (APMT-IC)

Using APMT-IC we find that the RF in the year 2019, due to accumulated emissions from commercial civil passenger aviation industry is 77 mW/m^2 (5th to 95th percentile range 46 to 107) (Figure 32). CO_2 accounts for 24 mW/m^2, while contrails account for 54 mW/m^2 of the total. While individual NO_x components are large (-16 mW/m^2 for the NO_x related methane forcing and 32 mW/m^2 for the NO_x related short term ozone effects), these components cancel, and NO_x is responsible for only 2.2% of RF in 2019.

However, after 2019, when our simulated emissions have stopped, contrail, aerosols, and stratospheric water vapor forcing ends, with only the longer-lived forcing components, remaining. These components include CO_2 and the longer-lived NO_x effects from methane and ozone destruction. The year after emissions end, the NO_x related impacts, which are cooling, and the CO_2, which is warming, are approximately equivalent. As a result, in 2020, total forcing is only 4 mW/m^2. Since the NO_x related impacts decay faster than CO_2, in 2030, 11 years after emissions stopped in the simulation, 85% of the maximum CO_2 forcing remains, while only 41% of the NO_x related ozone and methane forcing remains.

The effect of the radiative forcing persists longer through its effects on global change in surface temperature. In 2019, total warming attributable to commercial civil passenger aviation is 30×10^{-3} °C (range 17.5×10^{-3} to 49×10^{-3}). In this year, a third of this temperature change is due to CO_2, and 70% is due to contrails. In 2030, 10 years after emissions and subsequent contrail forcing has stopped in our simulation, contrails are responsible for 3×10^{-3} °C, while CO_2 is responsible for 10×10^{-3} °C. By 2050, 30 years after simulated emissions have ended, almost all the remaining temperature change is due to CO_2 with CO_2 accounting for 8.7×10^{-3} °C, and contrails accounting for 0.6×10^{-3} °C.

We additionally present the radiative impact, and temperature change for fuel burn totals from the IEA, along with emissions indices from our bottom-up emissions inventory (Figure 33 and Figure 34). In 2019, the total RF and total temperature change are 32% and 30% higher, respectively, than the totals using our bottom-up emissions inventory presented in Chapter 2. This difference is smaller than the uncertainty range. The magnitude of the RF is similar to those from Lee et al. (2020) which found net radiative forcing from aviation of 100 mW/m^2, however, our net NO_x RF is lower than theirs, due to the inclusion of nitrate aerosol forcing in this thesis. Our study also results in higher contrail impacts than in Lee et al. (2020), however their study does not present radiative forcing that continues after emissions stopped in 2018.

These results indicate the importance of emphasizing the metric and time horizon or time preference used when comparing various aviation climate forcers. As discussed, using accumulated RF or temperature change in 2019 as impact metric, contrails seem relatively the most important forcer, responsible for 70% of the impacts. However, 20 years later, after aviation emissions have been turned off in our model runs, contrail forcing is zero, while 85% of the maximum CO_2 forcing remains. At this time, the temperature change due to CO_2 is more than 10 times larger than surface temperature change due to contrails.

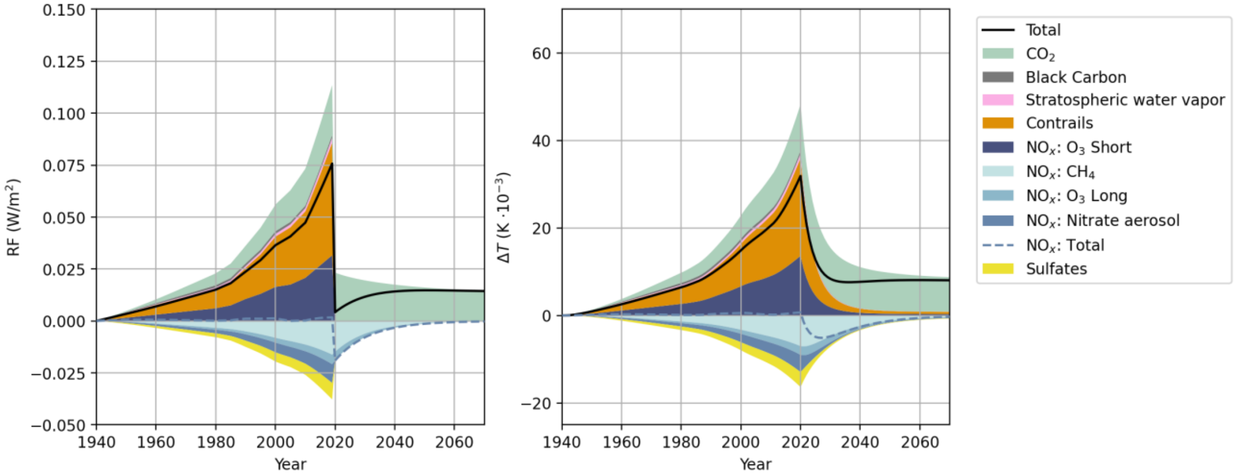

Figure 32: Climate impacts by emissions species for bottom-up emissions inventory from Chapter 2. For the derivation of these figures, emissions are stopped in the simulation in the year 2020. The plotted RF and temperature change after the year 2020 are as a result of historical emissions only.

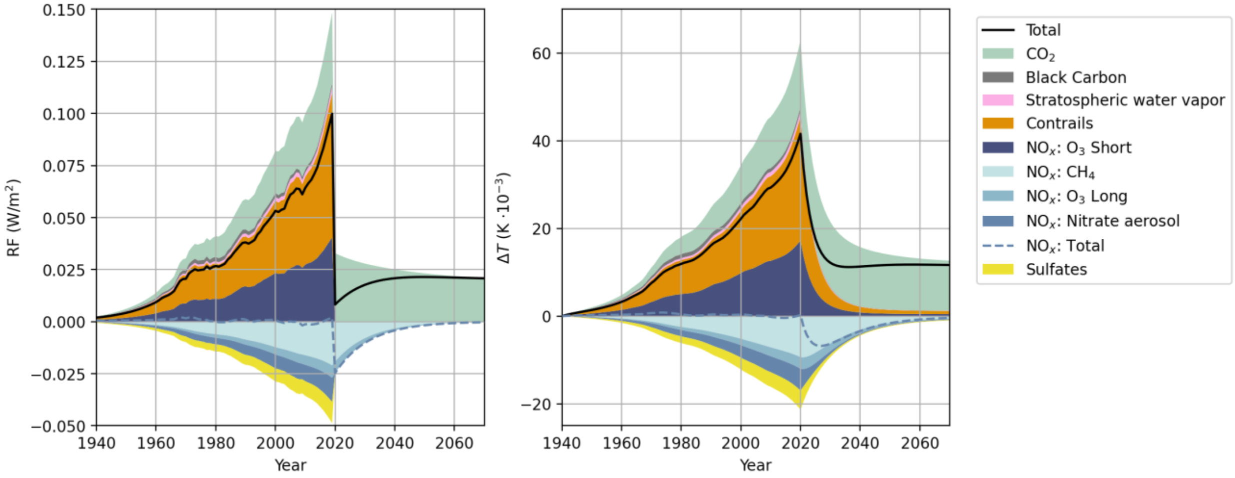

Figure 33: Climate impacts by emissions species for IEA fuel burn totals and equivalent emissions. For the derivation of these figures, emissions are stopped in the simulation in the year 2020. The plotted RF and temperature change after the year 2020 are as a result of historical emissions only.

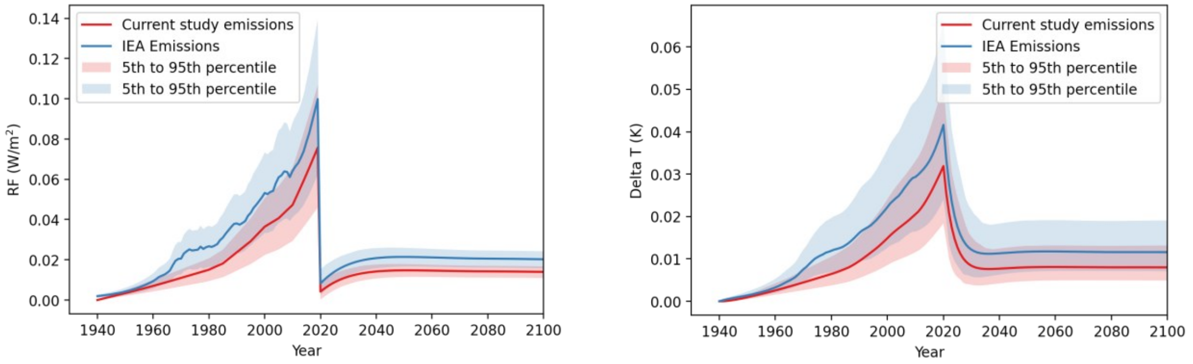

Figure 34: Comparison of total RF and temperature change for emissions based on bottom-up emissions inventory from chapter 2 and fuel totals from IEA (Lee et al. 2020). For the derivation of these figures, emissions are stopped in the simulation in the year 2020. The plotted RF and temperature change after the year 2020 are as a result of historical emissions only. Uncertainty range is also plotted in terms of the 5th to 95th percentile range.

3.4. Discussion of uncertainty

The results presented in this chapter are influenced by several uncertainties in contrail modeling. Firstly, our results rely on a single contrail model. Differences between model results in literature suggest that using alternative models could yield different trends than those presented here. For instance, in a multi-model study of global annual contrail impacts, global contrail RF varied from 12.4 to 51.3 mW/m^2 for the same set of input emissions of the year 2006 (Brasseur et al., 2016).

Another area of uncertainty for contrail modeling lies in the emissions data detailed in Chapter 2, particularly regarding non-volatile particulate matter (nvPM) number emissions. Accurately capturing these emissions is important since both our results (Section 3.3.1.2) and other literature indicate that contrail impacts could be sensitive to nvPM particle emissions (Burkhardt et al., 2018; Caiazzo et al., 2017; Teoh et al., 2020).

Furthermore, various studies have indicated the need for improved weather data at cruse altitude (Agarwal et al., 2022; Davis et al., 2017; Jiang et al., 2015; Teoh et al., 2022). Studies have raised concerns that reanalysis weather data might overestimate water content at cruise altitudes (Agarwal et al., 2022; Jiang et al., 2015). In contrast, other studies have found ERA5 weather data often appears weakly subsaturated compared to measurements (Gierens et al., 2020; Rädel and Shine, 2010; Reutter et al., 2020; Schumann et al., 2021; Teoh et al., 2022; Tompkins et al., 2007). In addition, this thesis identifies additional source of uncertainty due to the coarse weather data resolution, that introduces complexity in ensuring continuity of water vapor mass around the contrail in a simulation (Section 3.2.1.6). We show that different methods of applying the weather data can lead to a factor 3 change in the resulting global contrail RF from a year of aviation contrail simulations.

We account for these and other uncertainties in modeling global RF and temperature change due to aviation in our simple climate model, through a Monte Carlo simulation. This leads to the range of results presented in Section 3.3.2, which shows global accumulated RF from global passenger civil aviation ranging from 46 to 107 mW/m^2 and temperature change ranging from 17.5×10^{-3} to 49×10^{-3} °C. These sources of these uncertainties are explored further in Chapter 4, where we present a sensitivity study using first order contribution to variance. This sensitivity study shows that the largest contributions to output uncertainty arise from equilibrium climate sensitivity, with contrail RF also being a significant factor.

3.5. Discussion & Conclusion

The present-day cumulative climate impacts due to aviation emissions are quantified in this chapter, revealing that both the annual radiative forcing and the surface temperature change have increased from 1940 to present-day due to aviation emissions. We find that in 2019, the commercial civil passenger aviation industry is responsible for 3-4% of the aspirational 1.5 °C temperature limit set by the Paris Climate Agreement.

In this year the largest contribution to this temperature change is from contrails, which are investigated in more detail in this chapter. Our data illustrates notable variations based on location, time, and aircraft size. Such variations suggest that flights with specific characteristics might contribute more significantly to these climate impacts.

Our findings echo the results from some existing research (Burkhardt et al., 2018; Teoh et al., 2020), supporting the notion that a reduction in particle emissions can somewhat mitigate contrail impacts, and differ from Caiazzo et al. (2017) which found a decrease in initial ice crystal number could have little effect on contrail forcing. Similar to Burkhardt et al. (2018), we find a 90% reduction in particle number emissions corresponds to only a ~70% reduction in contrail Radiative Forcing (RF).

This reduction has implications for potential mitigation strategies which only focus on reducing particle number emissions. One such strategy involves the switch to Sustainable Aviation Fuels (SAF), which are drop-in alternative fuels derived from non-fossil fuel sources. SAF is often touted as an avenue to mitigate the contrail impacts, since emissions measurements suggest these fuels could result in lower particle number emissions on the order of 50 to 90% (Beyersdorf et al., 2014; Moore et al., 2017; Speth et al., 2015; Timko et al., 2010; Voigt et al., 2021). With aviation traffic growing rapidly, as indicated by the doubling of flight distance from 2000 to 2019 (Table 1), the reduction of contrail benefits from a 90% reduction in particle number emissions would be equivalent to 15 years' worth of growth, assuming a 4% year on year growth rate.

The results presented here suggest that differences in flight characteristics, such location, time, and aircraft characteristics all play a role in subsequent contrail impacts. This highlights the need for a reduced-order contrail model to capture the role of these factors in future contrail projections. In addition, understanding how contrail impacts scale, perhaps in relation to fuel burn, soot, or flight distance, is an avenue warranting further exploration.

It is also important to acknowledge the high degree of uncertainty associated with contrail impacts. This work indicates expanded uncertainty from contrail impacts due to how weather data is applied in contrail modeling. By accounting for continuity in sub-grid-scale variation over time in our model, we find contrail impacts are three times higher than if weather data is applied similarly to other studies.

Furthermore, these results highlight that the impacts from aviation occur on different timescales underscoring the necessity to explicitly consider timescale when comparing different aviation climate forcers. To illustrate, comparing the temperature change in the year 2019 due to contrails and CO_2 from cumulative aviation emissions, contrails have a larger effect, accounting for 70% of temperature change due to aviation. However, 30 years later, almost all the remaining temperature-change from these emissions are due to CO_2 emissions, with CO_2 emissions accounting for 10 times the temperature change of contrails.

In summary, this chapter has laid a foundation for understanding the cumulative climate impacts of aviation emissions, highlighting areas that require further research and attention. Addressing aviation's contribution to global temperature change demands both mitigation of contrail impacts and CO_2 emissions, as well as further tools to evaluate benefits of changes in these emissions.

Chapter 4

Climate and air quality costs of present-day marginal aviation emissions

4.1. Publication statement and co-authors

The work in this chapter was published in Environmental Research Letters and can be referenced using the following citation:

Grobler, C., Wolfe, P. J., Dasadhikari, K., Dedoussi, I. C., Allroggen, F., Speth, R. L., Eastham, S. D., Agarwal, A., Staples, M. D., Sabnis, J., & Barrett, S. R. H. (2019). Marginal climate and air quality costs of aviation emissions. *Environmental Research Letters*, *14*(11), 114031. https://doi.org/10.1088/1748-9326/ab4942

The work presented in this chapter was performed in collaboration with various co-authors as listed in the publication citation above. Notably, Kingshuk Dasadhikari performed the air quality impact analysis, using GEOS-Chem sensitivities. It was my role to perform the updates to APMT-IC, evaluate the climate impacts, quantify the uncertainty for both climate and air quality, perform the sensitivity study, and draft the manuscript. All authors guided the work, commented on the results, and contributed to the manuscript.

This work represents the first work for this thesis, and the published paper (Grobler et al., 2019) pre-dates the rest of the work from this thesis. After the work for this chapter was completed, various updates were made to APMT-IC as updated literature became available. This includes updates to (1) the contrail-cirrus forcing and subsequent expected atmospheric temperature response to this forcing (Bickel et al., 2020a; Lee et al., 2020), to explicitly separate out the contrail RF and ERF; (2) a 15% reduction in the magnitude of the NO_x related methane effect to account for short-wave forcing (Etminan et al., 2016) and (3), to the damage function used to calculate the cost of global warming. The biggest of these differences is from updating the damage function. This update is based on more recent work by Howard and Sterner (2017). This damage function is based on a meta-analysis of a larger number of damage estimates from literature and explicitly treats dependencies between different underlying studies to avoid overrepresentation of results from specific studies. This update increased the mean climate damage metrics by a factor ~2.8. The sensitivity study presented in this chapter (and included in the published paper (Grobler et al., 2019)), indicates that the damage function is one of the parameters that leads to the largest uncertainty in our analysis.

To remain consistent with the published work, this chapter presents the results that are included in the published paper (Grobler et al., 2019). However, for thoroughness**,** an additional set of metrics are also derived using the updated APMT-IC. This set of results is presented in Appendix F.

4.2. Introduction

In addition to aviation's climate impacts, aviation emissions adversely affect human health (Masiol and Harrison, 2014) and have been associated with ~16,000 premature mortalities annually (Eastham and Barrett, 2016; Yim et al., 2015).

Efforts to mitigate the climate and air quality impacts of aviation emissions have historically focused on technological and operational approaches to improve fuel efficiency (Hileman et al., 2008; ICAO, 2017; Marais et al., 2013), emissions standards (ICAO, 2016a, 2008), market-based measures to reduce CO_2 emissions (ICAO, 2018; World Bank Group, 2018), or the use of alternative aviation fuels (Staples et al., 2018). However, reductions of one emissions species can come at the cost of increasing emissions of another species, either in absolute terms or by limiting the potential reductions offered by new technologies. For instance, NO_x emissions could be decreased by designing engines with lower combustor temperatures, but this would result in lower thermodynamic efficiencies, leading to higher CO_2 emissions (Lefebvre, 1983; Lieuwen and Yang, 2013). To evaluate the costs and benefits of different policy and technology scenarios, these trade-offs must be quantified (Mahashabde et al., 2011). The unique characteristics of each emission species as well as temporal and spatial variation in their impact patterns further complicate evaluating such efforts.

Previous impact trade-off studies have focused on various emissions reductions scenarios for non-aviation sources, primarily at ground-level (Berk et al., 2006; Dedoussi et al., 2019; Driscoll et al., 2015; Shindell et al., 2016). However, since 91% of all aviation fuel burn occurs during cruise, applying these results to aviation emissions would lead to incorrect population exposure patterns due to differences in transport, chemical interactions, and deposition (Barrett et al., 2010a; Cameron et al., 2017; Yim et al., 2015). In addition, high altitude emissions have different climate impacts due to the potential for contrail formation, changes in aerosol radiative impacts (Ban-Weiss et al., 2012), and extended aerosol lifetimes for emissions above the cloud deck (Lund et al., 2017b).

This gap is partially filled by existing studies which focused on either the climate or the air quality impacts of aviation. Air quality impacts were calculated for both near ground emissions (Brunelle-Yeung et al., 2014; Levy et al., 2012b; Masiol and Harrison, 2014; Unal et al., 2005; Yim et al., 2013) and for cruise or full flight emissions (Barrett et al., 2010a; Cameron et al., 2017; Eastham and Barrett, 2016; Yim et al., 2015). Climate impact studies typically estimated the total speciated radiative forcing from one year of aviation emissions (Brasseur et al., 2016; Lee et al., 2009; Penner et al., 1999; Sausen et al., 2005), or focused on studying one climate forcer, including specifically contrails (Bock and Burkhardt, 2019; Burkhardt and Kärcher, 2011; Chen and Gettelman, 2016, 2013; Schumann and Graf, 2013) and aviation NO_x emissions (Holmes et al., 2011; Hoor et al., 2009; Köhler et al., 2008; Skowron et al., 2015; Søvde et al., 2014; Stevenson et al., 2004; Wild et al., 2001). In addition, Lund et al. (2017a) presented regionalized aviation impact climate metrics. Freeman et al. (2018) aimed to identify optimal aviation climate policy considering the trade-offs between NO_x emissions and CO_2 emissions, disregarding the air quality impacts from NO_x emissions.

While the aforementioned studies are valuable for understanding the emissions-to-impact mechanisms, they do not enable consistent comparative assessments of aviation emissions trade-offs considering both climate and air quality impacts. A limited number of studies are available which focus on evaluating these trade-offs. Mahashabde et al. (2011) evaluated climate, air quality, and noise trade-offs for a set of specific aviation NO_x emissions control scenarios. Dorbian et al. (2011) presented metrics to evaluate both the climate and air quality impacts of aviation. These climate metrics are computed per unit of full flight fuel burn, and the air quality costs are quantified for emissions in the landing and take-off flight phase where only ~10% of fuel burn occurs. As such, Dorbian et al. (2011) provided a foundation for the climate and air quality assessments of fuel burn reduction, but disregarded air quality impacts from cruise emissions and did not provide insights into the emissions trade-offs of different species.

This chapter presents the first set of speciated emissions cost metrics for both climate and air quality (ground level population exposure to fine particulate matter ($PM_{2.5}$) and tropospheric ozone) per unit of aviation emissions. To evaluate impacts for different flight phases, we present metrics for cruise, and landing and take-off (LTO) emissions, defined as emissions above and below 3000 feet, respectively. In addition, air quality metrics are calculated by world region, so that the variation of societal costs with local and regional operations, atmospheric conditions, and population distribution are captured.

As examples of the utility of these cost metrics, we apply them to evaluate the effects of a global expansion in aviation, consistent in magnitude with current annual growth in aviation. We use this as a benchmark for three scenarios. First, we consider a growth scenario with fuel efficiency increases and reductions in NO_x emissions factors consistent with 10-year technology improvements goals (ICAO, 2007; Lee et al., 2009). Second, we build on the work of Freeman et al. (2018) and quantify the trade-offs between the climate and air quality impacts of NO_x emission reductions, which are also associated with climate impacts due to increasing CO_2 emissions. Finally, we re-assess the climate and air quality trade-offs of jet fuel desulfurization (Barrett et al., 2012).

These scenarios demonstrate how decision makers can use the results from this chapter to estimate climate or air quality impacts of aviation policies, operational procedures, and technologies. As such, our results aim to enable decision making for the aviation sector. We therefore treat all aviation emissions as the marginal perturbation beyond emission from all other sectors so that aviation emissions are assumed to be the only controllable source of emissions. We subsequently refer to our results as marginal impacts.

4.3. Methods

4.3.1. Aviation Emissions

For this chapter, aviation emissions are calculated using emissions inventories obtained from the U.S. Federal Aviation Administration's (FAA) Aviation Environmental Design Tool (AEDT) for the year 2015 (Wilkerson et al., 2010). AEDT provides fuel burn and emission rates for NO_x, hydrocarbons (HC), and primary particulate matter, for individual flight segments in space and time, for all annual commercial civil flights globally. The AEDT inventory contains flights with total fuel burn at 240 Tg for the year 2015. AEDT has been validated against other aircraft emissions inventories and its results are found to be consistent with other inventories including AERO2K and REACT4C (Olsen et al., 2013; Simone et al., 2013). The AEDT emissions constitute inputs to the air quality and climate modeling approaches presented below.

4.3.2. Climate Impact

Aviation's contribution to climate change is quantified using the Aviation environmental Portfolio Management Tool - Impacts Climate (APMT-IC) (Mahashabde et al., 2011; Marais et al., 2008; Wolfe, 2015, 2012). How this model is applied to calculate the radiative forcing and temperature change from aviation emissions is described in more detail in Section 3.2.2. For comprehensiveness, an overview is presented here. Additionally, this section describes how APMT-IC calculates health, welfare, and ecological costs.

APMT-IC computes probabilistic estimates of aviation's climate impacts under multiple economic and policy scenarios, using a quasi-Monte Carlo method with 100,000 members.

As described in Section 3.2.2.3, APMT-IC calculates the radiative forcing (RF) associated with CO_2 emissions using an impulse response function approach, which models the fraction of a CO_2 emissions pulse remaining in the atmosphere as a function of time (Joos et al., 2013). To capture the sensitivity of these functions to baseline (all-source) CO_2 concentrations (Moss et al., 2010), the impulse response functions for this thesis are derived using the Model for the Assessment of

Greenhouse-gas Induced Climate Change (MAGICC6) (Meinshausen et al., 2011a) (Section 3.2.2.3). The resulting aviation CO_2 RF is computed using the radiative transfer function included in the Fifth Assessment Report of the IPCC (Myhre et al., 2013, 1998). This approach captures the climate-carbon feedbacks for aviation CO_2 emissions, but does not capture the climate-carbon feedbacks of non-CO_2 climate forcers, which likely results in an underestimate of the relative importance of short-lived climate forcers (Gasser et al., 2017).

RF due to non-CO_2 emissions (sulfates, black carbon (BC), water vapor and NO_x) are calculated by tracking their respective direct and indirect effects. These include: a direct black carbon warming impact; a direct high-altitude water vapor warming impact; a semi-direct fuel sulfur cooling impact; a multi-scale indirect NO_x impact of mixed sign; and contrail and contrail-cirrus pathways. The short-term indirect NO_x impacts cover the short-term formation of nitrate aerosol (cooling) and production of tropospheric ozone (warming), both of which last less than one year after emission. Furthermore, NO_x increases OH radical concentrations, and thus reduces methane concentrations, which subsequently reduces tropospheric ozone and stratospheric water vapor impacts. These methane-related impacts are cooling and develop over the perturbation lifetime of methane (~11 years) (Wild et al., 2001). Contrails, an indirect impact of emitted black carbon and water vapor, form when water vapor condenses on particles under sufficiently cold and humid conditions. Longer-lasting contrails diffuse and take on water vapor from the ambient environment, leading to large, diffuse contrail-cirrus clouds. Although the exact magnitude of the contrail-cirrus impact remains uncertain, it has been quantified as a warming impact comparable to the magnitude of aviation-attributable CO_2 RF (Dorbian et al., 2011; Kärcher, 2018; Lee et al., 2009).

We base our non-CO_2 RF estimates for these pathways on the results from FAA's Aviation Climate Change Research Initiative (ACCRI) Phase II report (Brasseur et al., 2016) which compiled RF estimates from multiple research groups using different climate or chemistry transport models and satellite observations for contrail estimates.

We scale the BC, H_2O, contrails, nitrate, and sulfate aerosol RFs calculated in ACCRI to each of their respective precursor emissions[1]. We estimate the RF associated with short-term and longer-lived ozone and methane perturbations due to NO_x emissions using the absolute global warming potentials (AGWPs) and atmospheric lifetimes for each of these three forcing pathways individually (Hoor et al., 2009; Stevenson et al., 2004; Wild et al., 2001). These indirect NO_x forcing pathways, along with the nitrate aerosol response, cause a net-NO_x RF response resulting from a cancelation of multiple signals at a given time. On net, initially this NO_x RF response is warming, and later switches to cooling.

Other RFs attributable to aviation are not included. RF due to other non-CO_2 aviation emissions, including non-methane volatile organic compounds (NMVOC), carbon monoxide (CO), and organic carbon (OC) have been shown in prior studies to be negligible (Brasseur et al., 2016). The indirect radiative impacts of aviation emissions on cloud formation are too uncertain to justify inclusion (Lee et al., 2020; Lund et al., 2017a). Similarly, the impact of aviation-attributable BC

---

[1] Contrail impacts are scaled by fuel burn as described in Section 4.3.4.

on snow albedo is not included here, as it remains highly uncertain for this emissions regime (Fuglestvedt et al., 2010).

Once RFs have been calculated, APMT-IC converts these to global temperature change using a probabilistic two-box ocean model (Berntsen and Fuglestvedt, 2008) in combination with the Roe and Baker (Roe and Baker, 2007) equilibrium climate sensitivity (ECS) distribution. The ECS has a mean of 3.5 °C for a doubling of CO_2 (US Government, 2016), which differs less than 4% from the IPCC Coupled Model Intercomparison Project 5 (CMIP5) ECS mean of 3.37 °C and falls within the 1.5 to 4.5 °C range of the IPCC AR5 (Flato et al., 2013).

4.3.2.1. Breaking out RF by flight phase

The climate impacts of full flight emissions are broken out by LTO and cruise flight phases by considering different literature estimates for each climate forcer. For contrails and stratospheric water vapor, radiative forcing only results from cruise emissions, therefore we attribute the full flight radiative forcing from Brasseur et al. (2016) to the cruise flight phase. For black carbon, sulfate, and nitrate aerosols, ground level estimates from the Intergovernmental Panel on Climate Change (IPCC) Fifth Assessment Report (AR5) are used for the LTO flight phase. For the cruise flight phase the fleet-wide LTO RF is subtracted from the fleet-wide full flight RF from Brasseur et al. (2016) (Table 3). LTO and cruise emissions fractions are obtained from AEDT for the year 2006 to align with the base emissions for the full flight RF from Brasseur et al. (2016). For the indirect NO_x forcing pathways, of short-term ozone, methane, and long-term ozone, radiative forcing by flight phase is derived from Wild et al. (2001), which presents radiative impacts for both full flight and ground emissions. Once again, LTO impacts are found from the ground level emissions impacts, and the cruise flight phase emissions are found by subtracting the LTO impacts from the full flight impacts. Finally, we do not include an adjustment for CO_2 emissions, since it becomes well-mixed in the atmosphere, and its long-term radiative impacts are not sensitive to emissions location. Mathematical details are presented in the Supplement of Grobler et al. (2019).

4.3.2.2. Updates to modelling of background temperature change

Background anthropogenic temperature change, which is temperature change resulting from all anthropogenic emissions, is necessary to calculate damages from aviation emissions. Previous versions of APMT-IC computed the background temperature change from background CO_2 concentrations. However, this does not account for the contribution of other background climate forcers, such as N_2O, CH_4, and aerosols, on background temperature change. Therefore, this is updated for the work of this thesis to use temperatures derived using MAGICC6 (Meinshausen et al., 2011a) for each of the RCP scenarios (Moss et al., 2010).

To ensure consistency within a Monte Carlo draw, the background temperature and aviation temperature change uncertainty are paired, since uncertainty factors driving a large temperature response from aviation forcing would likely also result in a relatively high temperature change from aviation effective radiative forcing. Pairing the background and aviation temperature change in this way affects the subsequent damages, due to non-linearities in the damage function.

Therefore, the temperature change data is generated using MAGICC6 for the different equilibrium climate sensitivity values (1.5K, 2K, 3K, 3.5K, 4K, 5K, 6K) for each RCP scenario. For each

Monte Carlo draw, APMT-IC linearly interpolates the background temperature change from the MAGICC6 results. Figure 35 shows the APMT-IC V24b background temperature change for different RCP scenarios, along with the 5th IPCC Coupled Model Intercomparison Project (CMIP5) temperature estimates.

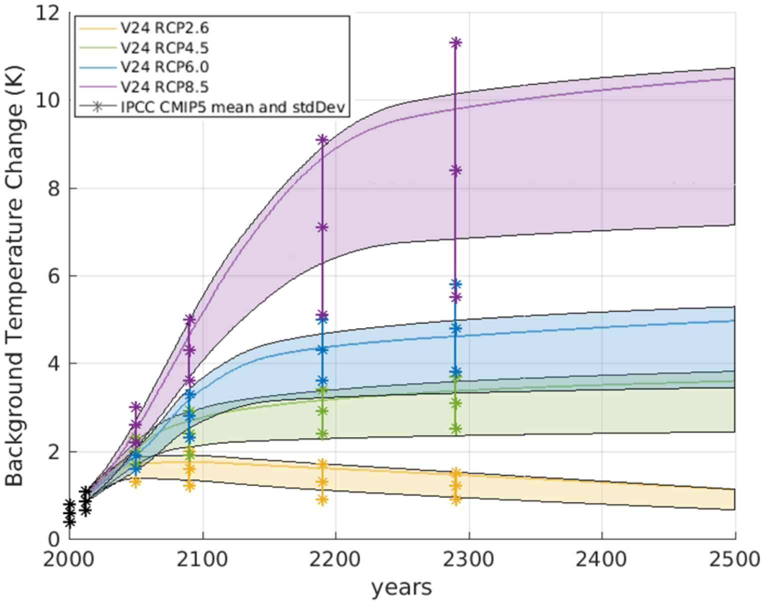

Figure 35: Background Temperature Change, with APMT-IC uncertainty based on Roe and Baker (2007). The shaded regions indicate the [33,67] percentile range and the solid line indicates the mean temperature change. The skewed distribution is driven by the distribution of the ECS.

4.3.2.3. Climate damages

Finally, APMT-IC uses the calculated global temperature change to estimate the health, welfare, and ecological costs of anthropogenic climate change using (i) the damage function of the Dynamic Integrated Climate Economy (DICE) model (Nordhaus, 2017); and (ii) projections of future economic output from the OECD Shared Socio-Economic Pathways (SSP) (Dellink et al., 2017). To determine the marginal impact of aviation emissions, damages are computed as the difference between damages in a baseline emission scenario, and a scenario where these aviation emissions are included.

In this chapter, marginal speciated aviation climate impacts are derived from a one kilo-tonne pulse of aviation fuel burn occurring in 2015. Future damages from this emissions pulse are discounted using a set of discount rates between 2% and 7%, consistent with widely used policy guidance (e.g., (OMB, 2003)). To ensure damages are captured for all discount rates, a time horizon of 800 years is used.

4.3.3. Air Quality Impact

We quantify air quality impacts attributable to a marginal increase in existing emissions in terms of the costs of premature mortalities resulting from population exposure to fine particulate matter ($PM_{2.5}$) and tropospheric ozone (O_3). We use the adjoint of the GEOS-Chem chemistry-transport model (Henze et al., 2007) to calculate the sensitivity of global costs due to emissions at any location. The GEOS-Chem adjoint has been widely adopted to compute the impacts from (i) combustion emissions in general (Barrett et al., 2015; Dedoussi and Barrett, 2014; Lee et al., 2015; Turner et al., 2015); and (ii) aviation emissions on a global and regional level (Ashok et al., 2014; Gilmore et al., 2013; Koo et al., 2013). Impacts are calculated using the sensitivities and AEDT emissions of NO_x, SO_x, HC, CO, BC, and OC for flight operations in 2015. Results are divided by emissions to produce the cost per unit of mass emitted. Direct air quality impacts of CO_2, contrail-cirrus, and water vapor emissions are considered negligible and not quantified here.

Adjoint simulations are performed on a GEOS-Chem global 4° × 5° model resolution (latitude × longitude) and 47 vertical hybrid sigma-eta pressure levels extending from the surface to 0.01 hPa, resulting in a ~550 m grid height at cruise altitude. The model uses meteorological data from NASA Global Modeling and Assimilation Office, produced using the Goddard Earth Observation System (GEOS-5.2.0) for the year 2009. The EDGAR 4.3.1 and NEI 2011 emissions inventories are used for all anthropogenic sources of non-aviation emissions (Crippa et al., 2016; US EPA, 2015). NO_x emissions from lightning are calculated based on Murray et al. (2012).

We compute population exposure using the LandScan population density product, defined at approximately 1 km (30” × 30”) spatial resolution globally (Oak Ridge National Laboratory, 2015). Premature mortality impacts are estimated for $PM_{2.5}$ and ozone by applying concentration response functions (CRFs) from epidemiological literature. For $PM_{2.5}$, we estimate changes in cardiovascular disease mortality using the concentration response data from Hoek et al. (2013). For ozone, we calculate changes in respiratory disease mortality using concentration response data from Jerrett et al. (2009), consistent with the World Health Organization Global Burden of Disease calculations (GBD 2016 Risk Factors Collaborators, 2017). These CRFs are applied for population exceeding 30 years of age and considering the 2015 baseline incidence data from the World Health Organization (WHO, 2018).

Finally, following Barrett et al. (2012), the societal impacts associated with premature mortalities are monetized using a country-specific Value of Statistical Life (VSL) approach. We conduct income-based country adjustment to the 1990 US VSL (US EPA, 2014) by applying an income elasticity of 0.7 (US EPA, 2016) on the basis of the Worldbank GDP in PPP per capita for 2015.

Using this adjustment, the US VSL in 2015 is USD 10.2 million. An additional set of results are calculated using a global population-weighted average VSL of USD 3.81 million.

As per EPA recommendations (US EPA, 2004), we include a cessation lag between time of exposure and mortality. 30% of mortalities are assumed to occur in the first year after emission, 50% are uniformly distributed between 2 and 5 years after emission, and the remaining 20% are uniformly distributed 6 to 20 years after emission. Future damages are discounted using a set of discount rates between 2% and 7%.

We quantify four sources of uncertainty in monetized air quality impacts using quasi-Monte Carlo simulations with 100,000 members. These uncertainties include uncertainties attributable to (i) atmospheric modeling in GEOS-Chem, (ii) the concentration response functions, (iii) VSL estimates in 1990, and (iv) income elasticity of VSL.

Firstly, uncertainty in GEOS-Chem ground-level concentration changes is bounded by comparisons to other models for this regime and to in-situ measurements. The uncertainty in the response of ground level ozone concentration to aviation emissions is derived from an inter-model comparison of aviation's impacts on air quality (Cameron et al, 2017). Due to the large stochastic variability included in the outputs of coupled Climate Response Models (CRMs), we only include the output from the Chemical Transport Models (CTM) and uncoupled runs of the Climate Response Models (CRM) reported in Cameron et al. (2017). The GEOS-Chem ozone response (0.43 ppbv) differed by less than 5% from the multi-model mean of 0.41 ppbv, while the standard deviation between the model outputs was 20% of the mean value. Using this result as guidance, we add a multiplicative uncertainty to ozone concentration using a triangular distribution with a central value of one and a standard deviation of 0.2. The upper bound of uncertainty (2.0) associated with the changes in $PM_{2.5}$ concentration at ground level ($\Delta\chi_{x,j,i,\mathrm{PM}_{2.5}}$) is also derived from Cameron et al. (2017), where the GEOS-Chem average ground-level $PM_{2.5}$ concentration due to aviation emissions is half of that reported by the other two CTM models. The lower bound of uncertainty (0.36) is set by comparisons between in situ concentration measurements and GEOS-Chem output for all-source emissions, where studies have found GEOS-Chem overestimates the annual average nitrate $PM_{2.5}$ by up to 2.8 times over most of the US (Heald et al., 2012; Walker et al., 2012). Using these two results, we add a multiplicative uncertainty to the $PM_{2.5}$ concentration with a triangular distribution with a minimum value of 0.36, an upper bound of 2.0, and a mean value of 1.0.

Secondly, uncertainty in the concentration response is modeled by applying a triangular distribution to the slope of the CRF, based on the central value and 95% confidence intervals reported in the epidemiological literature (Hoek et al., 2013; Jerrett et al., 2009). We do not consider alternative CRFs in our uncertainty bounds. In particular, the CRF from Turner et al. (2016) could lead to larger ozone-related air quality impacts, because it considers annual average concentrations, and not only summertime concentrations (Jerrett et al., 2009). Since aviation's impacts on ozone peaks during winter (Cameron et al., 2017; Eastham and Barrett, 2016), this could increase the estimated air quality impacts of aviation.

Thirdly, uncertainty in the 1990 US VSL is modeled using a Weibull distribution, based on the 1990 US EPA estimate (US EPA, 2014). Finally, we model uncertainty in income elasticity by applying bounds of 0 and 1.4 on a triangular distribution (Robinson and Hammitt, 2015; US EPA, 2016).

We do not quantify the error due to model resolution or uncertainty in relative toxicity of the $PM_{2.5}$ components. Although the 4°×5° model resolution does not allow us to capture localized emissions peaks in highly populated regions near airports (Arunachalam et al., 2011; Fenech et al., 2018; Li et al., 2016; Thompson et al., 2014), this is likely to affect only LTO emissions and is difficult to correct for without higher-resolution simulations. Regarding species toxicity we follow EPA practice and assume equal toxicity between the $PM_{2.5}$ species, although there is evidence for BC toxicity to be up to ~10 times higher than for other $PM_{2.5}$ species (Hoek et al., 2013; Levy et al., 2012a).

4.3.4. Normalization of impacts

Our results are presented on a per mass of emissions basis, to facilitate their use in quantifying emissions trade-offs.

Since contrail formation is driven by multiple characteristics of aircraft emissions, no clear normalization approach is evident. Previous literature normalized these impacts by unit of fuel burn or CO_2 emitted (Dorbian et al., 2011; Fuglestvedt et al., 2010; Lund et al., 2017a), or by total flight distance (Fuglestvedt et al., 2010; Lund et al., 2017a). However, neither method captures the (i) role of soot; (ii) dependence on the water vapor emissions factor through changes in fuel type; (iii) strong spatial and temporal dependence resulting from relative humidity patterns, cloud cover, and time of day; (iv) increase in contrail formation likelihood with increased engine efficiency; or (v) dependence on size of the aircraft (Lund et al., 2017a; Paoli and Shariff, 2016). Since no other method has been proposed, we present the results in this chapter using the established normalization methods. This is with the explicit caveat that these results, as well as the other short-lived emission results, are unlikely to apply for emissions patterns dissimilar to the present day, and for contrails in case of significant changes in engine efficiency or technology.

4.3.5. Determining model sensitivity

For both climate and air quality, additional analysis is performed to quantify the contribution of uncertainty in each variable to overall uncertainty in the output. To calculate the contribution to variance of each uncertain input variable, we estimate total effect indices (S_{T_i}) using Saltelli's method (Saltelli et al., 2008). These indices indicate the fractional contribution of each uncertain input variable to the output variability, both through its direct (first order) contribution, as well as through its interaction with other variables (see Appendix E.8).

Using this method, the S_{T_i} values are only approximate, because these values are based on Monte Carlo simulation. To ensure adequate convergence, we use a sobol' set with N=100,000 to draw the initial (N, 2k) matrix for the climate results, and for air quality we use 1,000,000 members to derive this sensitivity study.

4.4. Results and Discussion

4.4.1. Global Results

Table 4 presents the globally averaged marginal air quality and climate costs of emissions based on global full flight emissions. These values can be used for analyzing the climate and air quality impacts associated with a spatially and temporally homogenous change in global emissions. Costs are in 2015 USD and mass is reported in metric tonnes. The climate and air quality results are presented for a discount rate of 3% and results for discount rates of 2%, 2.5%, 5%, and 7% are provided in Appendix E. The air quality results are found to change by 3% to -11% for discount rates of 2% and 7%, respectively.

Table 5 presents cost metrics broken down by flight phase. Climate and air quality results are presented for a 3% discount rate. Air quality results are presented for country specific VSL with metrics for globally averaged VSL presented in Appendix E. The results indicate that the largest climate impacts per unit of emission occur in cruise, most likely due to increased atmospheric residence time of emissions at altitude. In contrast, the largest air quality impacts per unit of emission are identified during the LTO phase, due to the co-location of airports and population centers. However, because ~90% of fuel burn occurs in cruise, cruise emissions still dominate the air quality impact.

The (near-ground) social cost of emission results from Shindell (2015) fall within the 5th-95th percentile uncertainty bounds of the LTO results presented here, with the exception LTO NO_x climate results. Shindell's (2015) climate NO_x results are between ten to twenty times smaller than our estimate. This difference has a small impact on the overall results since the climate NO_x impact is at least two orders of magnitude less than the air quality NO_x impact. The difference is likely due to the cancelling of warming and cooling NO_x radiative pathways (see Sec 4.3.2), leading to a small net NO_x climate costs, and subsequent large percentage differences of net radiative impacts between different sources (Fuglestvedt et al., 2010; Myhre et al., 2013).

Table 4: Global aggregate climate and air quality metrics considering a 3% discount rate.
[$ per metric tonne emission (2015 USD)]. 5th and 95th percentile results are presented in brackets.

		Climate	Air Quality		Total**
			Country Specific VSL	Globally Averaged VSL	
CO_2	[$/tonne CO_2]	45 (6.7 to 120)	N/A	N/A	45 (6.7 to 120)
NO_x†	[$/tonne NO_x as NO_2]	-910 (-2,500 to -120)	23,000 (3,500 to 72,000)	22,000 (3,400 to 71,000)	22,000 (2,500 to 71,000)
Contrail-Cirrus*	[$/tonne Fuel Burn]	82 (10 to 230)	N/A	N/A	82 (10 to 230)
Contrail-Cirrus*	[$/Flight km]	0.23 (0.028 to 0.64)	N/A	N/A	0.23 (0.028 to 0.64)
Fuel Sulfur	[$/tonne S]	-18,000 (-47,000 to -2,400)	30,000 (4,700 to 100,000)	31,000 (4,800 to 110,000)	13,000 (-25,000 to 88,000)
BC	[$/tonne BC]	47,000 (6,800 to 130,000)	14,000 (1,800 to 44,000)	12,000 (1,600 to 41,000)	61,000 (17,000 to 150,000)
H_2O	[$/tonne H_2O]	2.5 (0.36 to 6.7)	N/A	N/A	2.5 (0.36 to 6.7)
NMVOC	[$/tonne NMVOC]	N/A	7,700 (1,100 to 21,000)	5,200 (830 to 17,000)	7,700 (1,100 to 21,000)
CO	[$/tonne CO]	N/A	290 (43 to 860)	230 (36 to 770)	290 (43 to 860)
OC	[$/tonne OC]	N/A	11,000 (1,500 to 37,000)	9,800 (1,400 to 34,000)	11000 (1,500 to 37,000)
Total Cost	[$/tonne Fuel Burn]	200 (30 to 530)	360 (56 to 1,200)	350 (55 to 1,100)	560 (180 to 1,400)

Climate impacts of NMVOC, CO, and OC were not quantified. Similarly, air quality impacts of CO_2, contrail-cirrus, and H_2O were not quantified. These are indicated as not available (N/A) in the table.

† Net-NO_x climate results are calculated as the sum of the impact of four indirect NO_x pathways. These individual pathways are tabulated in Appendix E.

* Note that either normalization (per tonne of fuel burn or per flight km) must be used exclusively. For engine technology and fuel properties sufficiently different from current patterns, contrail-cirrus impact scaling remains highly uncertain (See Section 4.3.4).

** Total calculated for Country Specific VSL

We further compare our full-flight climate results to Dorbian et al. (2011), and find that for all forcers, uncertainty bounds between the two studies overlap, with their central estimate for cirrus and total fuel burn metrics falling within our uncertainty bounds. However, the absolute value of their NO_x, sulfur, BC, and stratospheric water vapor results exceed our uncertainty bounds. This can be attributed to updated radiative forcing assumptions for the short-lived climate forcers and the inclusion of a nitrate cooling pathway as a NO_x-related impact (Brasseur et al., 2016).

Table 5: Cost metrics broken down by flight phase. $/tonne of LTO and cruise emission (2015 USD). 5th and 95th percentile results are presented in brackets.

		Landing and Take-off		Cruise	
		Climate	Air Quality	Climate	Air Quality
CO_2	[$/tonne CO_2]	45 (6.7 to 120)	N/A	45 (6.7 to 120)	N/A
NO_x	[$/tonne NO_x as NO_2]	-590 (-1,600 to -81)	37,000 (5,900 to 98,000)	-940 (-2,600 to -120)	21,000 (3,600 to 66,000)
Contrail-Cirrus*	[$/tonne Fuel Burn]	N/A	N/A	92 (11 to 260)	N/A
Fuel Sulfur	[$/tonne S]	-2,600 (-7,000 to -360)	32,000 (5,200 to 88,000)	-20,000 (-53,000 to -2700)	30,000 (5,300 to 97,000)
BC	[$/tonne BC]	18,000 (2,000 to 52,000)	66,000 (10,000 to 170,000)	52,000 (7,500 to 140,000)	7,000 (1,200 to 22,000)
H_2O	[$/tonne H_2O]	N/A	N/A	2.8 (0.41 to 7.5)	N/A
NMVOC	[$/tonne NMVOC]	N/A	19,000 (3,000 to 49,000)	N/A	2,300 (390 to 7,000)
CO	[$/tonne CO]	N/A	520 (80 to 1,400)	N/A	200 (32 to 620)
OC	[$/tonne OC]	N/A	110,000 (16,000 to 270,000)	N/A	7,000 (1,200 to 22,000)
Total Cost	[$/tonne Fuel Burn]	130 (20 to 340)	590 (96 to 1,600)	210 (31 to 560)	340 (57 to 1,100)

Results are for a 3% discount rate. For air quality, only results derived using a country specific VSL are presented here. Climate impacts of NMVOC, CO, and OC were not quantified. Similarly, air quality impacts of CO2, contrail-cirrus, and H2O were not quantified. These are indicated as not available (N/A) in the table.

* For engine technology and fuel properties sufficiently different from current patterns, contrail-cirrus impact scaling remains highly uncertain. See Section 4.3.4 for details.

The reduced-order climate metrics presented here are calculated for 2015 background atmospheric composition and surface temperature. Under the RCP 4.5 and SSP 1 scenarios, future background temperature change and global GDP are both projected to increase, leading to increased marginal damages in the non-linear DICE climate damage function. Therefore, when used for future emission years, the climate cost estimates increase by 2% per year for CO_2 which has a long lifetime, and by 4.7% per year for short-lived forcers (assuming a 3% discount rate). A full overview of these "adjustment rates" for future emission years is presented in Appendix E. Similarly, we expect the VSL to increase by 2.5% per year, assuming an income elasticity of 0.7 and average year on year growth in GDP as in the SSP 1 scenario (Dellink et al., 2017).

The air quality costs presented in Table 4 are presented for both country-specific and globally averaged VSL while results in Table 5 are derived based on country-specific VSL values only. When uniformly applying the global average VSL value, we find less than 10% difference for the cruise impacts, whereas the estimates for the LTO phase decrease by 30% to 50%. This difference between LTO and cruise is likely due to the more localized nature of LTO emissions and their impacts (Yim et al., 2015).

For quickly analyzing scenarios in which fuel burn totals change but emissions composition and distribution remain approximately constant (e.g., operational improvements, sector growth, market-based measures reducing aviation operations), we present the climate and air quality cost per unit of fuel burn. Following Dedoussi et al. (2019) we refer to these costs as the Climate and Air Quality Social Cost (CAQSC) per unit of fuel burn. These are calculated from the speciated cost metrics presented above.

Table 6 presents CAQSC for each flight phase, Figure 36 presents the results for the full flight emissions, while Figure 37 presents the breakdown of full flight CAQSC by flight phase. The results indicate that ~90% of the CAQSC results from cruise emissions. NO_x, CO_2, and contrails are collectively responsible for 58, 25, and 14% of the overall cost, respectively, totaling 97%. Air quality impacts account for 64% of total impacts, which is highly sensitive to the discount rate given the long-term nature of climate impacts as compared to the short time scale for air quality impacts (driven by 20-year cessation lag). As such, a 2% discount rate reduces the contribution of air quality impacts to 50%, and a discount rate of 7% increases the contribution of air quality impacts to 80%. Furthermore, 63% of the air quality portion of the full flight CAQSC is caused by the $PM_{2.5}$ impact pathway with the remainder caused by the ozone pathways. This result is consistent with Eastham and Barrett (2016) who found that 58% of the premature mortalities attributable to aviation are due to $PM_{2.5}$ exposure, with the remainder from ozone.

Both the speciated costs and the CAQSC are derived using a marginal impacts assessment (see Section 4.3.2.3). Due to non-linearities in climate and air quality responses, the marginal costs differ from the average cost of a unit of emission. The latter would be derived by apportioning the global all-sector damages to the emissions in question and would be used for determining aviation's fractional contribution to global anthropogenic damages. As discussed in Section F.6., the marginal costs of the aviation-attributable impacts are approximately double the average costs.

Table 6: CAQSC of aviation fuel burn. $/tonne of fuel burn in flight phase (2015 USD). 5th and 95th percentile results are presented in brackets.

	Landing and Take-off	Cruise	Full Flight		
			Climate	Air Quality	Total
CO_2	140 (21, 370)	140 (21, 360)	140 (21, 360)	N/A	140 (21, 360)
NO_x	550 (70, 1600)	300 (35, 1000)	-14 (-37, -1.8)	340 (52, 1100)	330 (38, 1100)
Contrail-Cirrus*	0	92 (11, 260)	82 (10, 230)	N/A	82 (10, 230)
Fuel Sulfur	18 (0.92, 58)	6.3 (-18, 52)	-11 (-28, -1.4)	18 (2.8, 62)	7.6 (-15, 53)
BC	4.1 (0.98, 11)	2.1 (0.48, 5.2)	1.7 (0.25, 4.5)	0.5 (0.067, 1.6)	2.2 (0.6, 5.3)
H_2O	0	3.5 (0.51, 9.3)	3.1 (0.45, 8.2)	N/A	3.1 (0.45, 8.2)
NMVOC	11 (1.6, 31)	0.27 (0.042, 0.85)	N/A	1.2 (0.17, 3.4)	1.2 (0.17, 3.4)
CO	4.3 (0.62, 12)	0.39 (0.06, 1.2)	N/A	0.72 (0.11, 2.1)	0.72 (0.11, 2.1)
OC	0.77 (0.098, 2.2)	0.11 (0.015, 0.37)	N/A	0.16 (0.022, 0.53)	0.16 (0.022, 0.53)
Total Cost	730 (180, 1900)	550 (170, 1400)	200 (30, 530)	360 (56, 1200)	560 (180, 1400)

Results are for a 3% discount rate. Results for alternative discount rates can be found in Appendix E. The air quality results are based on a country specific VSL.

Climate impacts of NMVOC, CO, and OC were not quantified. Similarly, air quality impacts of CO_2, contrail-cirrus, and H_2O were not quantified. These are indicated as not available (N/A) in the table.

* For engine technology and fuel properties sufficiently different from current patterns, contrail-cirrus impact scaling remains highly uncertain. See Section 4.3.4 for details.

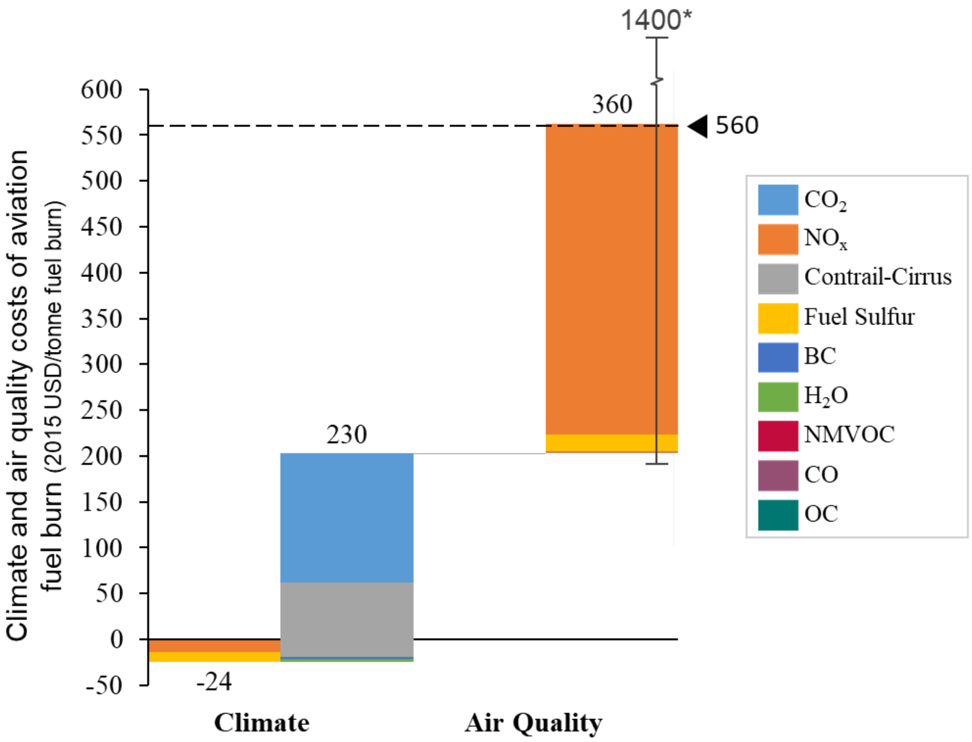

Figure 36: Climate and air quality costs per unit fuel burn for 3% discount rate

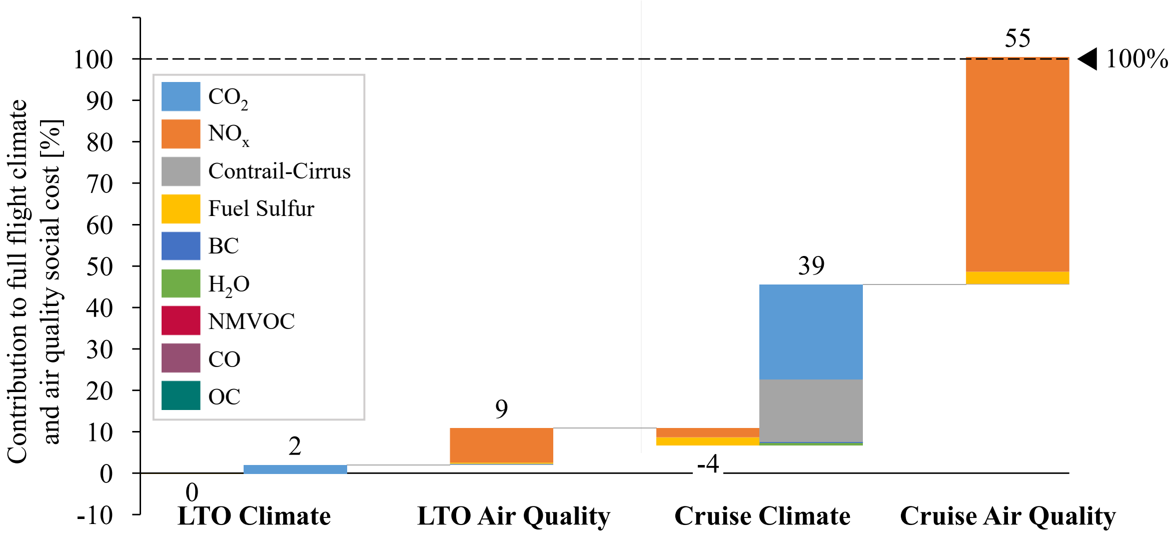

Figure 37: Breakdown of full flight CAQSC by flight phase and species

4.4.2. Results for Regional Emissions

The global metrics presented in Section 4.4.1 do not capture regional differences in the climate and air quality sensitivities to a unit of aviation emissions. In turn, the results can only be used to analyze homogenous global trends or policies. Regionalized air quality metrics, which quantify global damages due to homogenous changes in emissions in a region, can be used to analyze future aviation scenarios with shifting geographical traffic distributions, policy interventions in selected regions, or heterogeneous adoption of new technologies across the globe [†]. Regionalized climate metrics are not presented. Even though regionalized physical impact metrics exist (Lund et al., 2017a), very high uncertainty remains regarding the quantification of regionalized damages (Nordhaus, 2017).

Figure 38 presents air quality results for regionalized full flight emissions, and Table 7 shows results for regionalized emissions metrics by flight phase. The results show that the highest cost per unit of emissions is for emissions over Europe. For the cruise flight phase, this remains true regardless of whether global or country-specific VSL is used (Appendix E) which likely points to the transport of cruise emissions and their chemical products by prevailing westerly winds from Europe to the populous Asia-Pacific region. For LTO emissions, the magnitude of the impacts varies significantly with the VSL assumption (Appendix E), with costs decreasing by a factor of two in Europe, North America, and the US under a globally averaged VSL assumption. This is

---

[†] Since the impacts are presented averaged over the region, the metrics must still be used with caution when evaluating highly localized (in space or time) trends (e.g. an individual route).

because the costs of LTO emissions are more localized and therefore driven by local characteristics such as local VSL and population density.

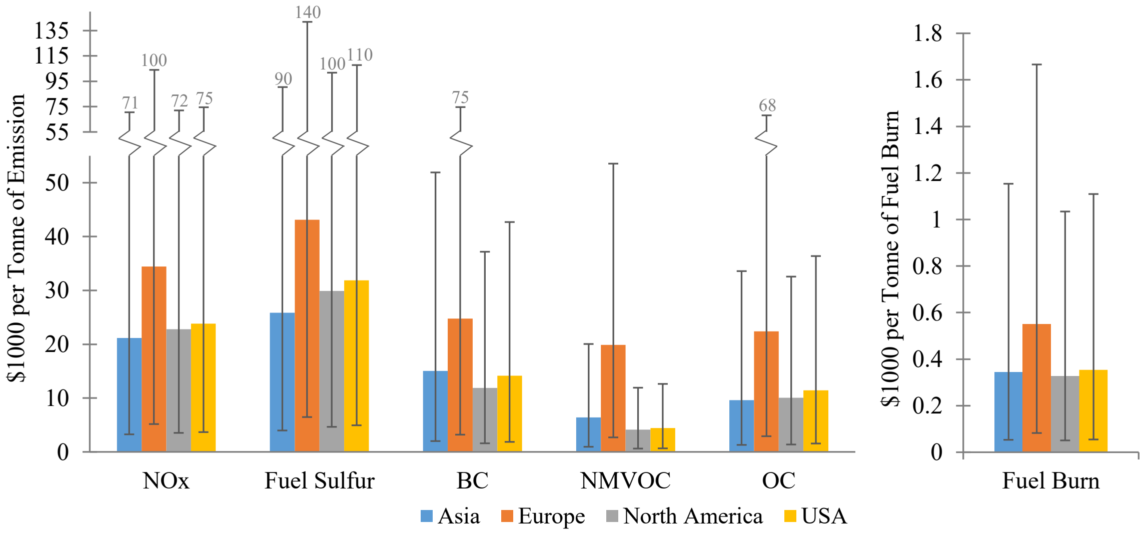

Figure 38: Regionalized Air Quality Metrics: \$/tonne of full flight emission

Table 7: Regionalized LTO and Cruise Air Quality Cost Metrics

		LTO				Cruise			
		Asia-Pacific	Europe	North America	USA	Asia-Pacific	Europe	North America	USA
NO_x	[\$/tonne NO_x as NO_2]	44,000	67,000	18,000	20,000	19,000	31,000	23,000	24,000
Sulfates	[\$/tonne S]	37,000	52,000	20,000	24,000	25,000	42,000	31,000	33,000
BC	[\$/tonne BC]	83,000	120,000	41,000	50,000	5,700	11,000	7,200	7,400
NMVOC	[\$/tonne NMVOC]	18,000	56,000	7,400	8,000	2,000	3,200	2,400	2,400
CO	[\$/tonne CO]	480	1,100	380	400	180	270	220	220
OC	[\$/tonne OC]	110,000	190,000	60,000	76,000	5,700	11,000	7,200	7,400
Total	[\$/tonne Fuel Burn]	720	1,100	280	320	310	480	330	360

Uncertainty and results for globally averaged VSL can be found in Appendix E.
The region represents where emissions occur and does not necessarily correspond to where the impact occurs.

4.5. Model Sensitivity and Uncertainty

The sensitivity of the climate and air quality metrics to each uncertain parameter considered in this thesis is estimated by deriving total-effect indices. These indices represent the fraction of the total output uncertainty attributable to an uncertain input variable though both its direct (i.e., first-order) contribution to output variance, as well as the higher-order effects due to its interactions with other variables (Saltelli et al., 2008).

For the climate impacts, we find the uncertainty associated with the equilibrium climate sensitivity and the climate damage function to be the largest contributors to overall outcome uncertainty, with total effect indices of 0.64 and 0.45, respectively. For the air quality impacts, we find the uncertainty associated with the VSL_{1990} to be the largest contributor to uncertainty, with a total-effect index of 0.85. Uncertainty in the GEOS-Chem $PM_{2.5}$ concentration and income elasticity have total-effect indices of 0.12 and 0.13, respectively, while other uncertainties each have indices of 0.07 or less. Total-effect indices are tabulated in Appendix E.8.

Because higher-order effects are included in the total effect indices for each variable, the sum of all the total effect indices may exceed one. For the climate model, the sum over all the total-effect indices was 1.16, while for air quality the sum was 1.15, indicating significant effect interaction. An additional discussion on uncertainty, Monte Carlo convergence, as well as sensitivity to RCP and SSP scenarios is Appendix E.

4.6. Example use: Analysis of Aviation Growth and Mitigation Scenarios

The results presented in previous sections can be applied to support decision making about policies, operational procedures, and technologies in the aviation sector. Here we present analyses of the climate and air quality impacts of global air traffic growth as well as three approaches which could reduce these impacts. These approaches include (i) fleet improvements; (ii) NO_x stringencies with a CO_2 trade-off; and (iii) fuel desulfurization.

4.6.1. Uniform emissions growth of 4.7%

Aviation passenger traffic is projected to grow at 4.7% per year (ICAO, 2016b). If emissions grew at the same rate throughout all markets and if there were no improvements in fuel efficiency throughout the global fleet, annual fuel burn would have increased by 11×10^6 tonnes from 2015 to 2016. Further assuming no changes in emission composition, this fuel burn increase would have been attributable to total climate and air quality costs at 6,400 million USD (90% confidence interval 2,000 to 16,000).

4.6.2. Growth of 4.7% with improved aircraft entering fleet

Over the history of aviation, new aircraft with system level design improvements have continuously entered the fleet. Assuming (i) new aircraft are delivered to match growth; (ii) these aircraft have NO_x emissions indices 45% below the current fleet average, to meet ICAO targets[‡]; and (iii) these aircraft also have a 10% reduction in CO_2 intensity per seat mile below fleet average[§], we could have reduced the additional costs of growth from 2015 to 2016 by 1,800 million USD (90% confidence interval 360 to 5,760) to 4,600 million USD. In turn, the climate and air quality costs of a year's aviation traffic growth could be offset by replacing ~12% of the fleet average with new aircraft. This percentage could be lower if the oldest, most polluting aircraft are replaced first and if additional climate and air quality impacts of reductions in other emissions species were considered.

4.6.3. NO_x stringencies

Engine level NO_x stringencies have been considered to achieve NO_x reduction targets (ICAO, 2016a). However, the benefit of such stringencies is limited in part by a fundamental NO_x-CO_2 trade-off. Higher combustor temperatures result in increased thermodynamic efficiency, thereby reducing fuel burn. However, higher combustor temperatures also lead to increased NO_x formation, as described by the Zeldovich mechanism (Kundu et al., 1998).

[‡] Consistent with the ICAO target set for NOx reductions for 2016 in production aircraft when compared to 2006 (ICAO 2007).

[§] Consistent with a ~1% per year improvement in CO2 intensity per seat mile over 10 years (Lee et al. 2009).

Freeman et al. (2018) studied the optimal climate policy of this trade-off and assumed a baseline case where a 20% reduction of aviation NO_x leads to a 2% increase in CO_2 emissions. We build on this work and calculate the climate and air quality impacts of introducing new aircraft into the fleet that achieve these goals relative to the fleet average, neglecting any other changes in emissions which might be associated. Again, we assume new aircraft to be delivered to match growth homogenously throughout all markets. We find the costs associated with the CO_2 increase to be 32 million USD (90% confidence range 4.8 to 82), and the benefit of the NO_x decrease to be 730 million USD (90% confidence range 80 to 2,500). This yields a net benefit of 700 million USD (90% confidence range 58 to 2,500) during the first year of operation of the new aircraft. While this result suggests that stricter NO_x regulation is likely net-beneficial from a climate and air quality perspective, a full cost benefit analysis needs to account for additional issues such as feasibility constraints, development costs and the increase in fuel requirements.

4.6.4. Ultra-low fuel sulfur

Another approach for reducing emissions from the aviation sector is sulfur removal from jet fuel (Barrett et al., 2012). Sulfur, an element naturally occurring in fossil fuels, is currently estimated to be present in jet fuel at a concentration of 550 to 750 ppm, which exceeds the 15 ppm of standard US highway diesel.

Reducing the fuel sulfur content from the assumed average 600 ppm to 15 ppm would reduce fuel sulfur emissions of one tonne fuel by 0.585 kg. At the same time, Barrett et al. (2012) estimated fuel sulfur removal to result in a 2% increase in the life cycle CO_2-equivalent (CO_2e) emissions, predominantly due to decreased refinery efficiencies. We find CO_2e emissions increase by 75kg CO_2e/tonne fuel by assuming a specific energy of 43 MJ/kg. In sum, we find fuel desulfurization to result in a combined climate and air quality benefit of 10.8 USD/tonne fuel burn (90% confidence interval -11 to 55). Assuming this low fuel sulfur is used in all flights, the total annual benefit would be 1,000 million USD (90% confidence interval -4,300 to 12,000). However, the uncertainty bounds show that desulfurization could also lead to a disbenefit, due to the loss of climate benefits of cruise level sulfur emissions.

Given the localized air quality impacts of sulfur emissions during LTO, one can expect the benefits of jet fuel desulfurization to be particularly high for the LTO cycle in Europe (Section 4.4.2). If it were possible to remove sulfur only from fuel used during LTO in Europe, the combined climate and air quality benefits would be 26 USD/tonne fuel burn (90% confidence interval -1.2 to 82). This benefit is more than double the sulfur removal benefit per unit of global full flight fuel burn, suggesting it could be beneficial to use low sulfur fuel on short flights in the European region. However, a full cost benefit analysis would be required to analyze the net societal benefit of this approach (e.g., Barrett et al. 2012).

4.7. Summary and conclusions

This chapter presents a method for comparing the climate and air quality impacts of aviation emissions, by estimating the social costs per unit of emitted mass by species. The cost metrics are broken down by flight phase and by the region of emission, both per tonne of emission and per tonne of fuel burn (the CAQSC metric).

4.7.1. Limitations of current approach and future research needs

Our results are applicable for the assessment of marginal changes in aviation emissions inventories, such as short- or medium-term changes in air traffic, or advancements in aircraft technology or operations. However, the results presented here are not applicable to evaluate all emissions scenarios and exclude the impact of some uncertain factors.

Firstly, the results presented would not be applicable for evaluating certain emission scenarios. These scenarios include highly localized emissions changes, e.g., resulting from in-flight altitude or changes in flight tracks. Additionally, our results are not applicable to evaluate changes in contrail impacts due to changes in engine or fuel technologies. To capture contrail impacts over a wider range of emissions scenarios, development of a more representative scaling method for contrail impacts would be necessary. Given the large impact of contrails (14% of impacts, see Table 6), this remains a major research need.

Secondly, our results do not consider the impacts associated with some uncertain physical modeling aspects. Our climate results exclude the impact of climate-carbon feedbacks, the impact of differing temperature responses due to different climate forcers, and the impact of aerosol-cloud interactions. In particular, aerosol-cloud interactions could have a large impact on results, but the scientific literature has yet to agree on the sign of this impact (Lund et al., 2017a). Moreover, the impacts due to BC are likely underestimated in this work, resulting from (i) the exclusion of BC radiative impact on albedo changes (Sec 4.3.2), (ii) not accounting for differential toxicity in air quality impacts, and (iii) the use of a large modeling grid (Sec 4.3.3). Further advances in epidemiological, atmospheric modeling research, and computational efficiency are necessary to include these effects.

Third, derived uncertainty bounds for the cost metrics remain large, ranging from 10% to 200% of the mean cost values. Only two physical modeling factors, equilibrium climate sensitivity and contrail RF, contribute significantly to this uncertainty, while monetization of impacts induces significant uncertainty for both the climate and the air quality results. For air quality, this uncertainty is largely associated with the value of statistical life, while for the climate model, the uncertainty results from the damage function. For this chapter, we apply the DICE damage function and its uncertainty, which is derived from 26 underlying studies (Nordhaus, 2017). However, we note an even larger range of values has been reported in literature, with central social cost of carbon estimates ranging from 36 [2007] USD to 417 USD/tonne (Pindyck, 2019; Ricke et al., 2018; US Government, 2016). This suggests further research into these valuation methods is necessary to further reduce uncertainties.

Finally, different economic valuation approaches can have significant impacts on our results. For instance, some regulators use the Value of Life Years (VOLY) lost instead of VSL to quantify the costs associated with air pollution. Since air quality damage disproportionally affects an older segment of population, a VOLY approach will likely lead to lower air quality impacts. For example, Tollefsen et al. (2009) find the air quality damages of a VOLY approach to be 64 to 68% of the VSL impacts.

4.7.2. Research application

Using the stated assumptions, results from this chapter indicate that three components are responsible for 97% of climate and air quality damages per unit fuel burn, with individual contributions of NO_x at 58%, CO_2 at 25%, and contrails at 14%. These species can subsequently be seen as primary targets for future strategies to reduce the atmospheric impacts of aviation emissions.

To reduce the climate impact of aviation, measures aimed at reducing CO_2 emissions and contrails are expected to lead to the greatest net climate benefit. In contrast, we find 94% of air quality impacts (which are 64% of total impacts) to be driven by NO_x. This suggests that measures aimed at reducing NO_x emissions could lead to the greatest net benefits, even if such measures lead to a small but uncertain climate NO_x disbenefit and small increase in CO_2 emissions.

Collectively the results presented in this chapter can enable policymakers and aviation stakeholders to rapidly evaluate benefits of emissions interventions, thereby enabling rational, data-driven decisions as the industry aims to mitigate the increasing emissions identified in Chapters 2 and 3.

Chapter 5

Cost and emissions pathways towards net-zero climate impacts in aviation by 2050

5.1. Publication and contributors

The work in this chapter was published in Nature Climate Change and can be referenced using the following citation:

Dray, L., Schäfer, A. W., Grobler, C., Falter, C., Allroggen, F., Stettler, M. E. J., & Barrett, S. R. H. (2022). Cost and emissions pathways towards net-zero climate impacts in aviation.

Nature Climate Change 2022 12:10, *12*(10), 956–962. https://doi.org/10.1038/s41558-022-01485-4

The work presented in this chapter was performed in collaboration with Lynnette Dray, Andreas Schaefer, Florian Allroggen, Steven Barrett, Marc Stettler, and Christoph Falter. The pathway scenario analysis and integration of technologies into the model AIM2015 was completed by Lynnette Dray. Christoph Falter, Andreas Schaefer and Florian Allroggen conducted the fuel pathway cost and availability analyses. It was my role to lead the quantification of contrail avoidance, and to perform climate impact assessment of the various pathways. All authors commented on the results and contributed to the manuscript.

5.2. Introduction

As highlighted in Chapters 2 and 3, aviation emissions are not on a trajectory consistent with Paris Climate Agreement goals (Grewe et al., 2021; Sharmina et al., 2021). Reducing climate impacts is particularly challenging for aviation, a sector with high growth rates, long-lived assets, non-CO_2 impacts of similar magnitude to those from CO_2 (Grobler et al., 2019; Lee et al., 2020), and no commercially-available, scalable carbon-neutral technology.

Previous studies investigating aviation pathways towards zero CO_2 and/or climate impacts have highlighted the difficulty of meeting emissions goals (Grewe et al., 2021; Hassan et al., 2018; Ivanovich et al., 2019), particularly when considering non-CO_2 climate impacts (Grewe et al., 2021). Most mitigation scenarios project net positive aviation CO_2 in 2050 (IEA, 2021; Leipold et al., 2021; US Government, 2015). For studies looking at net zero within the aviation sector, significant scale-up in alternative fuel use (either drop-in fuels (Gössling et al., 2021; Kar et al., 2009; Schäfer et al., 2015) or hydrogen (Girod et al., 2012), and potentially demand-reducing measures (Åkerman et al., 2021; Sharmina et al., 2021), are widely identified as necessary conditions. Most studies investigating pathways towards zero climate impacts explore limited regional scopes (Hassan et al., 2018; Schäfer et al., 2015; US Government, 2015; van der Sman et al., 2021); exclude non-drop-in fuels, such as hydrogen (Gössling et al., 2021; Grewe et al., 2021; IEA, 2021; Kar et al., 2009; Schäfer et al., 2015; Sharmina et al., 2021; US Government, 2015; van der Sman et al., 2021); do not examine transition costs (Kar et al., 2009; Leipold et al., 2021); or do not quantify non-CO_2 impacts (Girod et al., 2012; Gössling et al., 2021; IEA, 2021; Kar et al., 2009; Schäfer et al., 2015; Sharmina et al., 2021; US Government, 2015; van der Sman et al., 2021). Moreover, none of these studies considers additional measures to avoid non-CO_2 impacts, such as contrail avoidance.

In this chapter, we evaluate the extent to which fuel pathways could lead aviation towards net-zero climate impacts: synthetic fuels from biomass, synthetic fuels from green hydrogen and atmospheric CO_2, and the direct use of green liquid hydrogen. We additionally include air transport efficiency improvements and explore non-CO_2 impact mitigation through operational changes. We consider Tank-to-Wake (TTW) fuel combustion CO_2 and a range of non-CO_2 TTW impacts (direct warming from black carbon; semi-direct sulfate aerosol cooling; direct warming from stratospheric water vapor; indirect warming from contrails; and indirect NO_x impacts including short lived nitrate aerosol cooling, short-lived ozone warming, and cooling from destruction of atmospheric methane (CH_4) and reduction of tropospheric ozone). For Well to Tank (WTT) emissions from the fuel supply chain (including feedstock production or extraction, land use change, feedstock conversion and transportation) we consider direct warming impacts from CO_2, CH_4 and nitrous oxide (N_2O), and indirect impacts from CH_4 (warming from tropospheric ozone, stratospheric water vapor, and additional CO_2). In addition, we provide estimates of the costs and demand impacts associated with this transition.

5.3. Methods

We assess technology adoption scenarios towards a net-zero aviation sector through a system level approach. The model builds on combining (1) the global aviation systems model (AIM) to model future market development, demand feedbacks and technology adoption in a consistent framework; (2) the reduced-order climate model APMT Impacts Climate to capture CO_2 and non-CO_2 impacts of aviation emissions under current and future scenarios; (3) detailed assessments of techno-economic characteristics and lifecycle GHG emissions of alternative fuel pathways; (4) a meta-study for assessing the opportunities and costs of contrail avoidance through flight route adjustments; and (5) a detailed scenario approach.

5.3.1. Aviation Integrated Model (AIM)

The Aviation Integrated Model (AIM) is an open-source global aviation systems model simulating future passenger and freight demand for trips between 878 city regions worldwide (1,169 airports; 40,264 distinct flight segments); airline fleets and operations; operating costs and impact on itinerary-level ticket prices, freight rates and technology choices; airport schedules and delay;

emissions outcomes including CO_2, NO_x and PM; and how outcomes change in the presence of different policies or new technologies. AIM2015 and its component modules have been widely used for policy assessment, including for the EC (ICF Consulting, 2020) and UK DfT (Dray and Doyme, 2019) Details of model structure, methodology, and validation are given in literature (Dray and Schäfer, 2021; Dray et al., 2019).

AIM2015 allows us to capture second-order impacts of energy transition-related policies. For example, AIM2015's cost model includes a detailed flight segment-level model of fuel and non-fuel operating costs by aircraft and route type (Dray et al., 2019). If a technology with higher operating costs is used on that segment, the model projects impacts on itinerary ticket prices and freight rates, and subsequent impacts on demand and required amounts of fuel. For this thesis, global fuel blending mandates, beginning in 2025 and rising to 100% in 2050, are simulated and, in the case of hydrogen aircraft, a mandatory hydrogen requirement for new purchases is simulated (phased in over 5 years from hydrogen aircraft first entry into service). A Net Present Value (NPV) model is used to assess uptake of other new aircraft technologies and technology-fuel combinations within those consistent with mandate requirements. For drop-in fuels, adoption is based on the lowest cost to airlines once any mandate requirements, carbon, NO_x or contrail-related costs are factored in, with other fuels additionally used where supply or blending limits prevent satisfaction of demand. These models are further described in Dray et al. (2018), including assumptions about airline costs and performance modelling.

The characteristics of future generations of conventional aircraft and operational emissions mitigation measures or retrofits to existing aircraft are taken from literature (ATA and Ellondee, 2018; Dray et al., 2018; Schäfer et al., 2015). For electric aircraft, performance characteristics, including range limitations, are taken from literature (Gnadt et al., 2019) for single-aisle aircraft, and Hepperle (2012) for regional jets. Operating cost characteristics are derived from Schäfer et al. (2018). For this thesis, LH2 aircraft were added to the model. Literature LH2 aircraft performance characteristics range from more to less energy-efficient than conventional designs (Brewer, 1991; Clean Sky, 2020), depending mainly on assumptions about tank design. In addition, considerable uncertainty exists about hydrogen aircraft capital and maintenance costs. For simplicity, we assume energy intensity and nonfuel operating costs of LH2 aircraft equal to those of conventional aircraft of a comparable generation and size, i.e., that the operating cost difference between conventional and hydrogen aircraft is dominated by fuel costs. We assume hydrogen combustion rather than fuel cell-powered propulsion, as the extra weight of fuel cells reduces their feasibility for mid- and long-haul flights (Clean Sky, 2020). A detailed fuels module was also developed for this study to simulate alternative fuel costs and characteristics over time. The assumptions used in this module are documented separately below (Section 5.3.3). Model scenario-related inputs are discussed in Section 5.3.5.

5.3.2. Climate impact modeling

We model the climate impacts of aviation emissions using the Aviation environmental Portfolio Management Tool - Impacts Climate (APMT-IC) as described in Chapter 2 & 4 and in Grobler et al. (2019). As described in previous Chapters, APMT-IC probabilistically evaluates the physical climate impacts from global aviation emissions and estimates the associated monetary damages.

In this chapter, our use of this model is two-fold. First, we use it to derive Global Warming Potentials (GWP) for each of the precursor emissions. These GWP values are used to convert non-CO_2 emissions to CO_2 equivalent emissions (CO_2eq). Second, we use it to calculate radiative forcing and atmospheric surface temperature change response for each of the future emissions pathways generated by AIM.

The implementation of APMT-IC used here is described in Chapter 3 & 4 and in literature (de Jong et al., 2018; Grobler et al., 2019). The model has been updated to capture recent research results (1) on the contrail-cirrus forcing and subsequent expected atmospheric temperature response to this forcing (Bickel et al., 2020a; Lee et al., 2020); (2) on the cost of global warming; (3) updates to account for non-CO_2 impacts of drop-in alternative fuels, LNG, and LH2; and (4) to capture the effects of ground emissions of methane and nitrous oxide (N_2O).

5.3.2.1. Contrail radiative forcing

Following Lee et al. (2020), which surveyed a range of results from literature, we update the contrail-cirrus radiative forcing (RF) in APMT-IC to explicitly separate the estimation of RF and effective RF (ERF, the change in energy forcing after certain short-term climate feedbacks have occurred). For RF, we apply a triangular uncertainty distribution with a minimum value of 20.9 mW/m^2, mid value of 69.78 mW/m^2, and upper bound of 118.62 mW/m^2 for distance flown in 2006 (Bock and Burkhardt, 2016; Burkhardt and Kärcher, 2011; Chen and Gettelman, 2013; Schumann et al., 2015). This contrail radiative forcing is similar to the radiative forcing calculated in Chapter 3 for the year 2006 which ranges from 33 to 99 mW/m^2. As in Chapter 3, we also align with the ERF/RF adjustment from Lee et al. (2020) and apply a triangular uncertainty distribution with a mid-value of 0.417, minimum value of 0.31 and maximum value of 0.59 (Bickel et al., 2020a; Ponater et al., 2006; Rap et al., 2010). This results in an effective radiative forcing distribution ranging from 7.5 to 65 mW/m^2 with a mean of 31 mW/m^2. This distribution overlaps with the distribution from Chapter 4, and the mean of this distribution falls within the distribution of effective radiative forcing from Chapter 4, where a triangular uncertainty distribution is applied with minimum 12.4, mid value of 37.9, and maximum of 80 mW/m^2.

We note some unquantified uncertainties are not captured in using an ERF/RF adjustment in this way. Firstly, while this adjustment captures the difference in temperature change from short term RF, this ERF/RF may not necessarily provide an accurate measure of long-term temperature response (Bickel et al., 2020a; Ponater et al., 2021). Secondly, the adjustment factors from literature (Ponater et al., 2006; Rap et al., 2010) represent long-term climate feedbacks for linear contrails only, derived using contrail formation more than 50 times expected contrail coverage in 2050. This upscaling may cause saturation of feedback effects such as cloud formation (Fuglestvedt et al., 2010; Lund et al., 2017a; Wuebbles et al., 2010).

5.3.2.2. Damage function

The second update aligns estimated costs of global warming with more recent literature values. Previously, and in Chapter 4, APMT-IC used the damage function from the Dynamic Integrated Climate-Economy (DICE) model (Nordhaus, 2017), which is consistent with the social cost of carbon as proposed by the US Interagency Working Group on Social Cost of Carbon (US

Government, 2016). This damage function was based on a meta-analysis of 17 studies quantifying market and non-market damages (Nordhaus, 2017). Recent reports indicate that traditional integrated assessment models, including DICE, lag recent research on climate damages (Greenstone, 2016; US Government, 2021). In this chapter, we apply the damage function from Howard and Sterner (2017). This damage function is based on a meta-analysis of a larger number of damage estimates from literature and explicitly treats dependencies between different underlying studies to avoid overrepresentation of results from specific studies and is also applied in literature (Hänsel et al., 2020). This change leads to social cost of carbon of 246 USD_{2020}/tonne CO_2 (90% confidence interval 61.4 to 624) for RCP2.6 and SSP2 background scenarios and a 2% discount rate. For a 3% discount rate, RCP4.5 and SSP1 the social cost of carbon in 2020 is 158 USD_{2020}/tonne CO_2 (90% confidence interval 46.4 to 352) in 2020 USD. These values are in-line with recent literature global social cost of carbon estimates of 80 - 805 USD (Hänsel et al., 2020; Pindyck, 2019; Ricke et al., 2018).

5.3.2.3. Non-CO_2 impacts of non-petroleum fuels

Modeling approach

Finally, due to changes in the non-CO_2 emissions footprint of LH2, LNG and SAF, the subsequent climate impacts are also expected to differ (Grewe et al., 2017a; Withers et al., 2014). For each fuel considered, we derive adjustment factors by emission species based on a literature survey. These factors capture changes in RF per unit fuel energy for each fuel relative to conventional Jet-

A. A summary of these adjustment factors is provided in Table 8 and a discussion of underlying literature is provided in the following sections.

Table 8: Factor adjustments to forcing from drop-in alternative fuels, LH2, and LNG for aviation climate forcers.

	Relative contribution of forcer GWP_{100} (%)	RF factor adjustment		
		Drop-in alternative fuels	LH2	LNG
CO_2	70.4	Account for non-biogenic CO_2 emissions	Zero in-flight emissions	Account for non-biogenic CO_2 emissions
NO_x	-5.74	Unchanged	Unchanged	Unchanged
Contrail-cirrus**	39.7	0.58 (0.19, 1.18)	0.85 (0.1, 1.6)	1.0 (0.3, 1.7)
Stratospheric water vapor	2.25	1.09	2.6	1.55
Black carbon	1.09	(0.049, 0.47)	0	0.15 (0, 0.5)
Fuel sulfur	-7.65	0	0	0

Triangular uncertainty distributions are applied to LH_2 and LNG contrail cirrus and LNG black carbon. Uniform uncertainty distributions are applied to drop-in alternative fuels contrail cirrus, and drop-in alternative fuels black carbon impacts.
** Contrail-cirrus includes both linear contrails and the subsequent contrail-cirrus radiative impact.

Adjustments to non-CO_2 radiative forcing from LH2 combustion

LH2: Contrails

Differences in water vapor and soot emissions from the combustion of LH2 are expected to lead to differences in contrail properties and subsequent impacts.

The first emissions difference expected to change contrail impact of LH2, is the energy specific water vapor emissions index (EI_{H2O}), which is the amount of water vapor emitted per unit of fuel energy. For conventional fuel, EI_{H2O} is 0.029 kg/MJ. This emissions index is a factor 2.6 higher for LH2 (Gierens et al., 2008). This difference affects the expected frequency of contrail formation. More specifically, the additional water vapor available in the LH2 exhaust plumes extends the range of temperature and humidity over which contrails can form, typically increasing this temperature threshold by 10 K for LH2 aircraft (Schumann, 1996). This increase leads to higher radiative impacts. However, the increase in water vapor emissions is not expected to lead to significant increases in contrail ice-mass per unit length, since the bulk of contrail ice mass is taken up from ambient water vapor (Grewe et al., 2017a; Ström and Gierens, 2002).

The second emissions difference is the number of particles emitted. Combustion of conventional Jet-A leads to particle number emissions on the order of 10^{14} to 10^{15} particles per kg fuel (Kärcher and Yu, 2009; Moore et al., 2017; Stettler et al., 2013). In contrast, aircraft fueled by LH2 will have zero particle number emissions and only ambient particles will be available (equivalent to 10^{12} to 10^{13} per kg fuel) (Kärcher, 2018). In the process of contrail formation, these particles serve as ice nucleation sites. A decrease in particle number emissions is expected to lead to fewer ice crystals that are larger in size. This effect would lead to contrails with lower optical depth, since the larger crystals have lower cross-sectional area per unit ice mass. Additionally, a contrail with fewer, but larger particles is expected to have a shorter lifetime, since the heavier ice crystals will have a higher terminal velocity (assuming Stokes Law settling) and settle out faster into the warmer parts of the atmosphere where they can evaporate. Both these two particle related effects are estimated to reduce the contrail radiative impacts (Gierens et al., 2008; Kärcher, 2018; Noppel and Singh, 2007; Schumann, 1996).

A limited number of studies have focused on quantifying the contrail impacts of LH2 as an aviation fuel. Table 9 presents a summary of the relevant literature.

Table 9: Summary of LH2 and LNG fuel contrail literature

Citation	**Fuel**	**Factor adjustment to RF from contrails from Jet-A**	
		Without particle emissions effect	**With particle emissions effect**
Ström and Gierens (2002)	LH2	Microphysical properties only	
Marquart et al. (2001)	LH2	1.56	-
Marquart et al. (2005)	LH2	-	0.8 (range 0.7 to 1.3)
Ponater et al. (2006)	LH2	-	0.89
Grewe et al. (2017a)	67% LH2 and 33% biofuel	1.9	1.14* (range 0.76 to 1.9)

* Grewe et al. adjusted their results for the reduction in particle emission using an assumed 40% (range 0 to 60%) RF reduction due to an assumed 80% particle number emissions reduction based on Bock (2014). However, more recent sources have also found a larger upper bound adjustment (-68%) may be appropriate for a similar reduction (-73 to -90%) in particle number emissions (Burkhardt et al., 2018; Teoh et al., 2020).

Ström and Gierens (2002) studied the microphysical properties of individual contrails. They found LH2 contrails have similar ice mass but are optically thinner than contrails from Jet-A. Significant changes in sedimentation and subsequent contrail lifetime were not observed. Marquart et al. (2001), investigated the fleetwide contrail impact of LH2 aircraft. They found RF increases by a factor of 1.56 when LH2 aircraft are used. However, their study neglected the changes in aerosol particle emissions. Marquart et al. (2005) investigated both changes in the microphysical properties due to particles, as well as the RF impact on a global fleet-wide scale from LH2 fuel. Their central results indicate the global mean radiative forcing of contrails from LH2 fuel to be

20% lower than contrails from conventional fuel. The results were found to be highly sensitive to input assumptions such as particle size distributions and crystal shape. As such, their best guess is reported to fall within 30% of RF of contrails from Jet-A. Finally, Ponater et al. (2006) investigated global fleetwide contrail RF from LH2 contrails and found a central adjustment factor of 0.89 for LH2 contrails when compared to contrails formed from conventional fuel.

Grewe et al. (2017a) investigated contrail RF impacts of a blended wing body that uses a fuel blend of 67% LH2 and 33% biofuel on an energy basis. They found the increased water vapor leads to a 90% increase in contrail RF, assuming a flight altitude consistent with conventional aircraft. However, this result did not account for the competing impact of soot emissions. To compensate, they reduced their derived RF impact by an assumed 40% (range 0% to 60%) to account for an assumed 80% reduction in particle number emissions (Bock, 2014). More recent literature has found a larger range of RF reductions for similar changes in ice nuclei. While Caiazzo et al. (2017) found uncertain RF reduction (-13% to +5%) for a 66% reduction in initial ice nuclei, Burkhardt et al. (2018), and Teoh et al. (2020) found 69% and 68.9% (range 45% to 82%) RF reductions from a 90% and 73% fleetwide reductions in initial ice nuclei. This indicates an even higher adjustment uncertainty than applied by Grewe et al. (2017a). Additionally, while Grewe et al. (2017a) does not focus on pure LH2 combustion, its result of a +90% increase contrail impacts from LH2 and biofuel blend is higher than the factor 1.56 found by Marquart et al. (2001), suggesting a higher range of uncertainty is appropriate than when only the pure LH2 contrail literature is considered.

Using these literature results, we account for changes in RF from using LH2 fuel by applying a factor adjustment to the RF of contrails from conventional fuel. We capture the uncertainties by applying a triangular uncertainty distribution to the adjustment factor. We base our central value on the central results of Marquart et al. (2005) and Ponater et al. (2006) and set it to 0.85. Since only a limited number of studies are available, we select a symmetrical uncertainty range (+/- 0.75) around this central value leading to lower and upper lower bounds of 0.1 and 1.6. This captures the uncertainty range from Marquart et al. (2005) (factor 0.7 to 1.3), while also accounting for a +30% additional uncertainty suggested by Grewe et al. (2017a).

LH2: Stratospheric water vapor, soot, sulfur, NOx

Although the impact of water vapor, soot, sulfur, and NO_x for Jet-A is less than 10% that of in-flight CO_2 emissions from aviation (see Table 8), we account for differences in these climate forcers if aircraft combust LH2.

Firstly, LH2 is not expected to contain fuel sulfur. As a result, we set the sulfur related cooling to zero. In contrast, water vapor emissions per unit energy are expected to increase, as discussed above. Therefore, we increase the stratospheric water vapor warming in the model by a factor of 2.6. Since LH2 does not contain carbon atoms, no soot emissions are expected (Kärcher, 2018). Consequently, we set the soot warming to zero. Finally, changes in the combustor design may lead to differences in NO_x emissions from LH2 fueled aircraft. However, such combustors are not yet in operation, and it remains unclear how these NO_x emissions from LH2 fuel would compare to conventional fuel. In the absence of this data, we do not assume positive or negative changes to NO_x emissions. Resultingly, no changes in NO_x related RF are assumed.

Adjustments to non-CO_2 radiative forcing from LNG combustion

LNG: Contrails

Similar to LH2, the combustion of LNG fuel leads to increased water vapor emissions per unit fuel energy (factor 1.55 above conventional fuel) (Gierens et al., 2008), as well as almost no particle emissions (Kärcher, 2018). Consistent with the use of LH2, increased contrail occurrence is expected, but with decreased optical depth and decreased contrail lifetime.

While studies focusing on LNG contrails are sparse, Grewe et al. (2017a) investigated both LNG and LH2 contrails. The study presents the contrail RF impacts of a blended wing body that uses a fuel blend of 67% LNG and 33% biofuel on an energy basis. They found the increased water vapor leads to a 70% increase in contrail RF for the LNG blend, assuming a flight altitude consistent with conventional aircraft. However, this result did not account for the competing impact of soot emissions. To compensate, they reduced this RF value by 40% (uncertainty 0-60%) to account for an assumed 80% reduction in particle number emissions (Bock, 2014). While this study does not focus on pure LNG combustion, to the best knowledge of the authors, it is the only study that analyzed contrails from LNG fuel.

Using Grewe et al. (2017a), we account for changes in RF from LNG by applying a factor adjustment to the RF of conventional contrails. We capture the uncertainties by applying a triangular uncertainty distribution to the adjustment factor. The upper bound of the triangular distribution is set by Grewe et al. (2017a) as 1.7. Since further information of LNG contrails is not available, a symmetric triangular distribution centered around one is selected, resulting in a lower bound factor of 0.3.

LNG: Stratospheric water vapor, soot, sulfur, NO_x

LNG is expected to lead to emissions changes which affect the non-CO_2 climate impacts.

Similar to LH2 combustion, sulfur emissions are not expected from LNG combustion. Resultingly, the sulfur related cooling is set to zero. Additionally, we increase the stratospheric water vapor impact by a factor 1.55 compared to conventional fuels, consistent with the increase in water vapor emissions per unit energy (Gierens et al., 2008).

In contrast to LH2, soot emissions from LNG remain more uncertain. Like LH2, soot emissions from aviation LNG combustion are expected to be substantially lower than for petroleum-derived Jet-A, however the fraction reduction remains unknown (Grewe et al., 2017a). At the lower bound, Kärcher (2018) suggested aviation use of LNG would not result in particle emissions. Although data is sparse, another datapoint is provided by the US EPA (2009), which found soot emissions from stationary ground gas turbines to be half that of distillate oil. However, these measurements are not directly applicable here since they compare to distillate oil and were made using a water injection emissions control which are typically not used for aircraft engines. Finally, for aviation engines using a mixture of 50-50% of LNG and biofuels fuel, Grewe et al. (2017a) applied an assumed 85% soot reduction compared to conventional fuel. To capture this range, we apply a triangular uncertainty distribution bounded at factors zero and 0.5, consistent with Kärcher (2018) and US EPA (2009), respectively. We set the mid value factor adjustment to 0.15, consistent with Grewe et al. (2017a). Finally, like LH2, we do not assume changes to NO_x emissions from LNG, since these emissions are driven by yet unknown combustion designs.

Adjustments to non-CO_2 radiative forcing from drop-in alternative fuels combustion

Drop-in alternative fuel: Contrails

Like LH2 and LNG, the contrail impacts of drop-in alternative fuels are expected to differ from fossil Jet-A due to competing impacts of fewer particle emissions and more water vapor emissions.

These emissions changes are due to differences in fuel composition, notably the proportion of straight chain (paraffins) and cyclically bound (aromatics) C-H molecules in the fuel. Typically, conventional fuel consists of 18% aromatics by volume (Edwards et al., 2010). In contrast, drop-in alternative fuels considered here are paraffinic, meaning they contain almost no aromatics (Gierens et al., 2016). In practice, drop-in alternative fuels are blended with conventional fuels to meet the present-day requirement of 8% vol. aromatics (a requirement to ensure seal swell) or synthetic aromatics could be added as a fuel additive (CAAFI, n.d.; Edwards et al., 2010).

Firstly, this lower abundance of aromatics in drop-in alternative fuels blends leads to a ~10% increase in water vapor emissions per unit mass of fuel because aromatics have a lower H:C atom ratio than paraffins. In turn, an increase in water vapor emissions will likely increase the frequency of occurrence of contrails (see above).

Secondly, since aromatic compounds are precursors for particulate emissions, drop-in alternative fuels are expected to have lower particulate emissions per unit mass of fuel, and in turn lower contrail impacts. Various studies have focused on quantifying the reduction in particle number emissions for biofuel blends. For a 50-50 blend by volume of Jet-A and a paraffinic biofuel, Moore et al. (2017) found a 26%–48% reduction in the particle number emissions index at cruise conditions. Similarly, Speth et al. (2015) found a neat paraffinic biofuel leads to a 75% reduction in particle emissions. Beyersdorf et al. (2014) found reductions of 95% and 85% for neat and blended fuels, respectively. Voigt et al. (2021) found a 50% to 70% reduction in soot and ice crystal numbers in a recent measurement study at cruise altitude from a low aromatic drop-in alternative fuels. Timko et al. (2010) found similar reductions at idle power, but at 85% power they did not find any reductions in particle number emissions. This indicates uncertainty in these measurements, and that particle number emissions reductions may be sensitive to combustor design and engine operation.

The impact of an assumed low soot scenario (80% reduction in initial ice crystal numbers) on global contrail RF was investigated by Burkhardt et al. (2018). They found such reductions in particle emissions led to a 50% reduction in contrail RF. Similarly, another study (2020) found a 73% initial ice nuclei reduction leads to a 69% (range 45% to 82%) decrease in contrail RF. However, Caiazzo et al. (2017) found little benefits from a 66% reduction in initial ice nuclei by finding contrail RF ranging between -13% and +5% for such a low soot scenario, with the uncertainty caused by different crystal shapes assumptions. Uncertainty due to different contrail crystal habits has been studied by Sanz-Morère et al. (2020) who found longer lived contrails, which are responsible for most of the contrail RF, to predominantly consist of asymmetrical shapes (columns and plates). However, neglecting the results in Caiazzo et al. (2017) for the relatively symmetrical shapes (spheres and droxtals) does not reduce the uncertainty range of Caiazzo et al. (2017) results.

Of these studies, only Caiazzo et al. (2017) also investigated the impact of increased water vapor emissions from drop-in alternative fuels on contrail RF. They considered the impact of lower ice nuclei number emissions (-75%) and accounted for the increased water vapor emissions (+11%)

per unit mass of fuel. They found net global contrail occurrence increased by 8%, while RF changed by -4 to 18% depending on the assumed crystal habit.

To account for these impacts while also capturing the uncertainty, we apply a triangular uncertainty factor adjustment to model the contrail impacts of drop-in alternative fuels. We base our upper bound on the upper bound from Caiazzo et al. (2017) and set it to +18%. Our mid value is based on the combined results from these three studies. Firstly, we use an 8% increase to account for the additional contrail occurrence due to additional water vapor (Caiazzo et al., 2017). Then we account for reduced ice nuclei by adjusting this RF by -8%, -50%, and -68% for results from Caiazzo et al. (2017), Burkhardt et al. (2018), and Teoh et al. (2020), respectively. Taking the mean of these three results leads to a mid-value for the triangular distribution of -42%. Finally, for our lower bound, we combine the +8% increase from Caiazzo et al. (2017) with the largest impact reduction due to changes in ice nuclei, which is 82% from Teoh et al. (2020). Resultingly the lower bound is set to a factor 0.19.

This results in a mean factor adjustment of 0.65 from the triangular distribution for a neat biofuel and factor 0.825 adjustment for a 50-50 biofuel blend with Jet-A. This result is similar to factor 0.8 SAF contrail adjustment adopted in Grewe et al. (2021) for a 50-50 biofuel blend with Jet-A based on Moore et al. (2017) and Burkhardt et al. (2018).

Drop-in alternative fuel: Stratospheric water vapor, soot, sulfur, NO_x

Similar to LH2 and LNG, the emissions composition of drop-in alternative fuels is expected to differ from conventional fuels, leading to differences in the stratospheric water vapor, soot, sulfur and NO_x. Although these impacts are relatively small (individually not exceeding 10% of CO_2

warming impacts - see Table 8) we account for these changes by adjust these impacts from drop-in alternative fuels in the model based on expected changes in their emissions. Additionally, we apply an additional factor adjustment of 0.98 to each of the expected emissions changes, to account for the varying energy density of drop-in alternative fuels compared to Jet-A (Hileman et al., 2010).

Like LH2 and LNG, drop-in alternative fuels are not expected to contain fuel sulfur. As a result, we set the sulfur related cooling to zero. Although NO_x emissions will cause some additional sulfate formation because of its effect on ozone, this mechanism is neglected. Secondly, we increase the stratospheric water vapor impact for drop-in alternative fuels by 9% RF increase per unit energy, consistent with the 11% increase of water vapor emissions per fuel weight but adjusted by a factor 0.98 for varying energy densities of the fuels (Hileman et al., 2010). Third, soot emissions from drop-in alternative fuels are expected to decrease significantly due to the absence of aromatics in the fuel. Measurements of this reduction range between a 95% and 52% reduction (see section above covering contrails from drop-in alternative fuels). Therefore, we apply a uniform uncertainty distribution where soot RF from fossil Jet-A is adjusted by between -95% and -52% per mass unit of drop-in alternative fuels fuel consumption. Once again, these factors are adjusted by a factor 0.98 to account for varying energy densities of drop-in alternative fuels and conventional fuels (Hileman et al., 2010). Finally, no changes in NO_x emissions are expected from drop-in alternative fuels since combustor design and operation are expected to remain consistent with Jet-A. Resultingly, we assume no changes in NO_x emissions for drop-in alternative fuels.

Adjustments to non-CO_2 radiative forcing from electric aircraft

Since electric aircraft do not lead to any combustion products, their direct in-flight emissions and subsequent direct CO_2 and non-CO_2 climate impacts are set to zero.

5.3.2.4. Climate impacts of lifecycle CO_2, CH_4 and N_2O emissions

APMT-IC explicitly models the concentration of CH_4, N_2O, and CO_2 by using an impulse response function approach. CO_2 concentration is modeled using the methods presented in Section 3.2.2.3, while removal of CH_4 and N_2O are modeled using their perturbation lifetimes as described in IPCC AR5 (Myhre et al., 2013), and in the case of N_2O, a three year delay is modeled for N_2O to reach its main sink in the stratosphere (Meinshausen et al., 2011a).

While CO_2 and N_2O predominantly impact climate through direct radiative forcing, CH_4 not only impacts climate through direct radiative forcing, but also through a number of indirect effects including tropospheric ozone, stratospheric water vapor, and eventual formation of CO_2 (Meinshausen et al., 2011a).

Direct radiative impacts are calculated using the radiative forcing transfer functions from Etminan et al. (2016) given by Eq 4 to Eq 6.

$$RF_{CO_2} = [a_1(C - C_0) + b_1|C - C_0| + c_1\bar{N} + 5.36] \times \ln(C/C_0) \qquad \text{Eq 4}$$

$$RF_{N_2O} = [a_2\,\bar{C} + b_2\bar{N} + c_2\bar{M} + 0.117] \times \left(\sqrt{N} - \sqrt{N_0}\right) \qquad \text{Eq 5}$$

$$RF_{CH_4} = [a_3\,\bar{M} + b_3\bar{N} + 0.043] \times \left(\sqrt{M} - \sqrt{M_0}\right) \qquad \text{Eq 6}$$

where coefficients are given by

$$\begin{array}{lll} a_1 = -2.4 \times 10^{-7}\ \mathrm{Wm^{-2}ppm^{-1}} & a_2 = -8.0 \times 10^{-6}\ \mathrm{Wm^{-2}ppm^{-1}} & a_3 = -1.3 \times 10^{-6}\ \mathrm{Wm^{-2}ppm^{-1}} \\ b_1 = 7.2 \times 10^{-4}\ \mathrm{Wm^{-2}ppm^{-1}} & b_2 = 4.2 \times 10^{-6}\ \mathrm{Wm^{-2}ppm^{-1}} & b_3 = -8.2 \times 10^{-6}\ \mathrm{Wm^{-2}ppm^{-1}} \\ c_1 = -2.1 \times 10^{-4}\ \mathrm{Wm^{-2}ppm^{-1}} & c_2 = -4.9 \times 10^{-6}\ \mathrm{Wm^{-2}ppm^{-1}} & \end{array}$$

C, M, and N indicate concentrations of CO_2, CH_4, and N_2O, respectively. The zero subscript in C_0, M_0, and N_0 indicate preindustrial concentrations of the corresponding species. The bar indicates a mean value between modeled and preindustrial concentrations calculated as $\bar{X} = 0.5(X + X_0)$, where X represents the species concentrations. These radiative transfer functions capture the impact of overlapping radiative bands between the different species, enhancing the precision of the model.

Through atmospheric chemical interactions, methane leads to the formation of tropospheric ozone (Seinfeld and Pandis, 2016). The radiative impact due to this tropospheric ozone is captured by

$$RF_{CH_4}^{Strat\ H_2O} = \alpha_{tropO_3} \times S_{CH_4}^{O_3}(\ln M - \ln M_0) \qquad \text{Eq 7}$$

where α_{tropO_3} denotes the radiative efficiency factor. We note, that although Meinshausen et al. (2011a) gives a value of 0.042, the MAGICC6 code indicates 0.0335 as an updated value. APMT-IC is programmed to be consistent with the updated value. $S_{CH_4}^{O_3}$ is a sensitivity coefficient of tropospheric ozone to methane concentration and is given by the MAGICC6 code as 5.

Indirect effects due to CH4 were captured in line with Meinshausen et al. (2011a). Stratospheric water vapor radiative forcing is captured by

$$RF_{CH_4}^{Strat\ H_2O} = \beta\alpha_{\mathrm{CH_4}} \times \left(\sqrt{M} - \sqrt{M_0}\right) \qquad \text{Eq 8}$$

Where β and $\alpha_{\mathrm{CH_4}}$ are constants corresponding to 15% and 0.036, respectively, and M and M_0 indicate concentrations of methane as in Eq 6.

Eventual CO_2 formation due to CH_4, is captured by calculating the yearly reduction of CH_4, and by conservation of mass, assuming all carbon atoms form CO_2. The CO_2 concentration is calculated using the impulse response functions from Section 3.2.2, and subsequent RF is calculated using Eq 4.

Because simple climate model temperature models are calibrated towards CO_2, climate efficacies have been introduced to calibrate the impact of non-CO_2 radiative forcing for use in reduced order temperature change models. Although climate efficacies for in flight emissions remain highly uncertain, climate efficacies are included for these life cycle ground emissions. Consistent with Meinshausen et al. (2011) values of unity are used in all cases, except tropospheric ozone, where an efficacy value of 0.85 is used.

5.3.3. Alternative fuel pathways

The following fuel and fuel production pathways are considered in this chapter:

- Liquid hydrogen (LH2): We consider liquid hydrogen produced via water electrolysis and subsequent liquefaction, both powered by renewable electricity. The electrolysis of water is modeled based on the proton-exchange membrane (PEM) technology and follows the varying load of renewable electricity. The produced hydrogen gas is stored in a compressed gas tank to enable continuous operation downstream. Liquefaction of hydrogen is performed at continuous load and the liquid product is stored for further use.

- Power-to-liquid fuels (PTL): We consider power-to-liquids based on hydrogen from water electrolysis and CO_2 from direct air capture. Hydrogen is produced at varying loads from PEM water electrolysis and stored in a compressed-gas tank. CO_2 is continuously extracted from the atmosphere via physical adsorption in a direct air capture process (DAC). CO_2 and H_2 are continuously converted to syngas (H_2+CO) via the reverse water gas shift process (RWGS). The syngas is converted into hydrocarbons via the Fischer-Tropsch process (FT), where the gaseous fraction is cycled back to the RWGS reaction to be turned into syngas. The resulting synthetic crude is converted into jet fuel and by-products using refining process steps.
- Biofuels: We consider biofuels produced from dedicated biomass and waste streams including the following pathways: HEFA (hydrogenated esters and fatty acids) process using dedicated vegetable oil crops (e.g., soybean, rapeseed, jatropha, palm oil) and FOGs (fats, oils, and greases; specifically used cooking oil and tallow), advanced fermentation of sugar crops, and Fischer-Tropsch synthesis of municipal solid waste, lignocellulosic material (forestry residues, agricultural residues, and dedicated feedstock such as switchgrass and miscanthus).
- Synthetic natural gas: Hydrogen is produced via water electrolysis using renewable electricity; CO_2 is captured from the atmosphere via low-temperature pressure-swing adsorption. Natural gas is then synthesized from H_2 and CO_2 via the Sabatier process, and the methane is subsequently liquefied for aviation use. Another pathway to synthetic

natural gas is via anaerobic digestion of biomass to produce biogas, which is then cleaned and liquefied.

The availability of fuels produced from electricity, water, and CO_2 (PTL, SLNG) is in principle unlimited as the feedstock potentials can be leveraged at practically any scale. However, the specific availability at a point in time depends on the rate at which production capacity can be ramped up and the policy priority given to aviation for using scarce input factors such as electricity or biomass. We assume the main constraint on LH2 ramp-up is fleet penetration of LH2 aircraft; for PTL and biofuels, maximum ramp-up rates are set using a combination of near-term literature estimates of supply and longer-term estimates of aviation fuel demand. For single-fuel pathways, biomass availability is modeled after Staples et al. (2018)'s F1-A1-S2 scenario, assuming full availability of the fuels for aviation such that biofuel potential is essentially unlimited (over twice the expected demand of less than 30 EJ/y in 2050). These assumptions are used as the fundamental availability for these pathways, while the specific use of fuels is then determined with the AIM model taking into account demand effects, mandate levels, scale-up behavior and prices. For the combined-pathway model runs a more constrained biomass supply is assumed, rising to a maximum of 21.7 EJ in 2050, based on literature (WEF, 2020).

Production costs: We determine alternative fuel pathway costs (except for biofuel pathways) with the levelized cost of energy approach. To this end, we determine the investment costs of the facilities based on energy and mass balances, and component cost estimates from the literature. We assume improvements of component efficiencies and energy demands in line with recent publications. The levelized costs of intermittent renewable electricity is assumed to be \$0.04/kWh today at a capacity factor of 30% and \$0.02/kWh at 50% in 2050, where these estimates are based on a mix of solar PV and onshore wind technologies. Additionally, we include energy storage for parts of the facilities that must run continuously and thus use an LCOE of \$0.10/kWh (year 2020) and \$0.05/kWh (year 2050) for renewable electricity that is available around the clock. The costs are annualized assuming a lifetime of 20 years and a discount rate of 10%. The minimum selling price of the different biofuel pathways is based on a discounted cash flow rate of return analysis as shown in literature (Bann et al., 2017)

GHG emissions: The life cycle emissions of electricity from solar PV and wind are assumed to be zero. While currently there are still embedded emissions in the production of PV modules and wind turbines, these are expected to approach zero with the decarbonization of the economy. For GHG emissions of biofuels, we use literature values from Staples et al. (2018) for the different pathways in our study. The authors indicate values for today and for 2050, and we use linear interpolation to get values in between. We neglect embedded emissions of all infrastructure for the fuel pathways due to the expected small impacts. We use literature information on different biofuel pathways to break out different species (CO_2, CH_4, N_2O) in direct emissions of greenhouse gases.(Seber et al., 2014; Staples et al., 2014; Stratton et al., 2010; Suresh, 2016) The climate impacts of hydrogen leakage (either from PTL or LH2 production) are not included here and remain highly uncertain due to uncertainties in leakage rates and climate impacts (Cooper et al., 2022; Ocko and Hamburg, 2022).

5.3.4. Contrail avoidance modeling

Reaching net zero climate impacts from aviation will require avoiding contrail formation. One strategy of contrail avoidance relies on small scale altitude adjustments to avoid flying through atmospheric locations with where contrails can form (Avila et al., 2019; Schumann et al., 2011; Sridhar et al., 2011). These diversions lead to a small fuel burn penalty (typically less than 5% of fleetwide fuel consumption) compared to a counterfactual case with fuel-optimal operations. In addition, only 2% of flights have been found to be responsible for 80% of contrail forcing in some regions; in turn, less than 2% of flights would have to be diverted to avoid contrail warming impacts (Teoh et al., 2020).

Contrail avoidance is modelled using results from our contrail avoidance meta-analysis based on a literature review of five different studies (Klima, 2005; Noppel et al., 2006; Sridhar et al., 2012, 2011; Yin et al., 2018). A summary of these studies is presented in *Figure 39*. This literature is discussed in more detail in Appendix G. Using these studies, we estimate the relationship between contrail avoidance and fleet-wide fuel burn penalty as shown in Eq 9, where f(x) represents the fraction increase in fuel burn for the x fraction contrail length avoided and C_0, C_1 and C_2 represent the shape parameters to be estimated.

$$f(x) = C_0 \left(-1 + \frac{C_1}{C_1 - x}\right)^{C_2} \qquad \text{Eq 9}$$

Performing this curve fit yields coefficients of $C_0 = 0.011$, $C_1 = 1.161$, and $C_2 = 0.906$. The resulting route mean square error (RMSE) is 0.0891, leading to a normalized RMSE of 11%, where this normalization is taken to the maximum fuel burn fraction increase. The central estimate of the curve fit indicates 50% of fleet-wide contrail length can be avoided for a 0.88% fleet-wide fuel burn penalty (5th to 95th percentile range 0 to 2.51). Thereafter avoiding subsequent contrails becomes more fuel costly, with an additional 20% avoidance requiring double the additional fuel.

Using this meta-analysis, a single mid-range contrail avoidance scenario is selected for our combined technology pathways in which 50% fleet-wide contrail avoidance can be achieved at a 1% fleet-wide fuel burn penalty. This represents a higher fuel burn penalty than the central estimate of the meta-analysis, to account for the range in estimates in literature. The 50% length avoidance is lower compared to other studies, which calculate maximum contrail impact avoidance of 70-80%. However, this mid-range value of 50% is selected since high rates of avoidance will cause increased strain on airspace and air traffic control (Teoh et al., 2020) and maximum rates of contrail avoidance may be difficult to achieve with current weather prediction data. This contrail avoidance trade-off likely differs for alternative energy carriers such as hydrogen, but data on these differences remains unavailable. Therefore, we apply the same results from Eq 9 for alternative fuels.

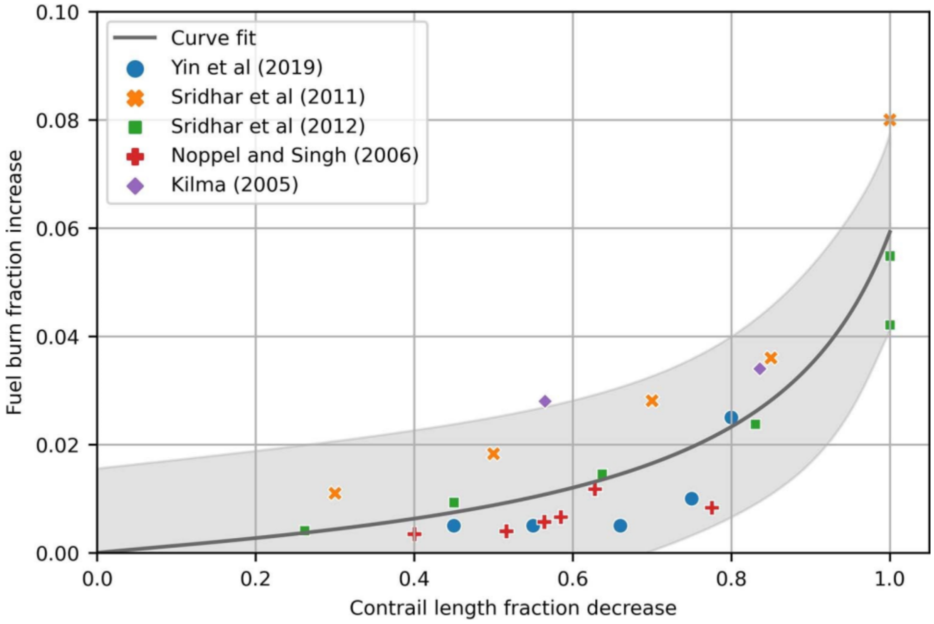

Figure 39: Fuel burn and contrail length trade-off - results from meta-analysis

5.3.5. Scenario approach

The global potential of technologies and fuels to reduce aviation emissions is limited by supply, ramp-up rate and fleet turnover. These factors interact with demand growth. As such, we examine outcomes across three demand scenarios, described below. For each demand scenario, we run: baseline model runs (with operational and efficiency improvements, but no energy transition or additional aviation policy); single-fuel pathways (model runs with operational and efficiency improvements and energy transition to a single alternative fuel (biofuels, PTL and hydrogen) only); and, based on the outcomes of the single-technology scenarios, combined pathways (model runs with operational and efficiency improvements, contrail avoidance, and biofuels as a bridging fuel to PTL or hydrogen).

Uncertain AIM scenario inputs include future population, GDP/capita, oil prices, and whether the relationship between demand growth and income growth will change as aviation systems mature. The development of scenarios for input assumptions which take account of the COVID19 pandemic is described in literature (Dray and Schäfer, 2021). Baseline population and GDP/capita growth rates are derived from the IPCC SSP scenarios (O'Neill et al., 2014), adjusted for COVID19 pandemic GDP/capita impacts (IMF, 2021), and impacts of movement restrictions on demand and load factors (IATA, 2021; ICAO, 2021). The scenarios used in this chapter are: a high growth scenario based on IPCC SSP1 socioeconomic factors, leading to aviation demand growth comparable to recent historical trends; a central scenario based on IPCC SSP2 socioeconomic factors, leading to demand growth similar to industry projections; and a low scenario based on IPCC SSP3 socioeconomic factors, which leads to post-pandemic demand growth which is lower than historical trends. The low demand scenario includes demand growth decoupling from economic growth, at the level used in literature (DfT, 2017); this assumes a gradual trend towards income elasticities of no more than 0.6 over a 70-year period. For reference cases, we use IEA SDS oil price projections (IEA, 2020a), which are consistent with a level of policy ambition which falls short of net zero CO_2 in 2050. Because seeking to achieve net zero CO_2 emissions in aviation implies a high level of climate ambition in other sectors, we use lower oil prices post-2040 in scenarios where there is significant use of alternative technology in aviation (transitioning from the SDS trajectory to the IEA NZE projections (IEA, 2021). Future technology costs and capabilities are also uncertain. For this chapter, the key sensitivity is to fuel costs and we address this through the use of alternative fuel cost projections.

5.4. Results

5.4.1. Overview of potential mitigation measures

A net-zero emissions pathway requires anthropogenic sources of climate forcing emissions, including both direct emissions and the emissions of the supporting energy system, to ultimately become equal to or less than their sinks. (Fuglestvedt et al., 2018) We disaggregate factors that affect aviation's climate forcing emissions using Eq 10. These emissions are driven by: aviation's level of activity (in revenue tonne-km, RTK); energy intensity (Energy/RTK); and CO_2eq emissions intensity per unit energy, where CO_2eq includes CO_2 and non-CO_2 impacts on both WTT and TTW scopes. Offsets can be used as an instrument to balance impacts from emissions which cannot be avoided.

$$\mathrm{CO_{2eq}} = \mathrm{RTK}\,\frac{\mathrm{Energy}}{\mathrm{RTK}}\,\frac{\mathrm{CO_{2\,eq}}}{\mathrm{Energy}} - \mathrm{offsets} \qquad \text{Eq 10}$$

Technology and policy solutions for each of these variables can contribute towards reducing aviation's emissions towards the net-zero goal.

RTK (Eq 10): Air Transportation Demand

The demand for air transportation depends mainly upon urban populations, associated per person income, and airfares. We expect the world to become wealthier and larger shares of the global population to gain access to air transportation (Dray et al., 2022). As such, in the absence of a transition towards low-carbon energy carriers and/or additional policy measures, we project demand for air transportation (measured in RTK) to grow by 2.4-4.1% p.a., corresponding to a doubling or tripling of 2019 demand by 2050. This is in line with established market forecasts (Air Transport Action Group, 2021; Dray and Schäfer, 2021; Shell, 2021). We do not consider policies which directly reduce air transportation demand (e.g., French government policy aiming at displacing short-haul flights with high-speed rail (Åkerman et al., 2021)). However, our model considers that cost increasing technologies, such as synthetic fuels, will lead to demand feedbacks. We capture these effects using the integrated aviation systems model AIM2015 (Dray and Schäfer, 2021; Dray et al., 2019).

Energy/RTK (Eq 10): Energy intensity of the air transport system

The energy intensity of the air transportation system is driven by the fuel efficiency of individual aircraft, operational efficiency (e.g., the air traffic management [ATM] system), and capacity utilization of flights (ATA and Ellondee, 2018). When combining our projected energy intensity reductions for new aircraft (ATA and Ellondee, 2018) with age distributions and retirement schedules of the current fleet, average passenger load factor growth, ATM improvements and market growth projections, system-level energy intensity per RTK declines by 1.3% per year (around 33% total) between 2019 and 2050; in combination with a doubling or tripling of RTK demand, aviation CO_2 emissions would increase by a factor of 1.3 to 2. Consequently, energy efficiency improvements alone are unlikely to reach even the carbon-neutral growth goal of the International Civil Aviation Organization (ICAO) (2019).

CO_2eq/Energy (Eq 10): Climate intensity of fuels

Currently, the aviation sector relies on fossil hydrocarbon Jet-A, which generates 73 g of combustion CO_2 per MJ, with an additional 14 g CO_2eq per MJ (using Global Warming Potential with a 100-year time horizon (GWP_{100})) from CO_2, CH_4 and N_2O emissions arising from WTT processes (oil extraction, refining, and crude oil and fuel logistics; Table 10) (Stratton et al., 2010). Alternative energy carriers, which partly or entirely mitigate fuel GHG emissions, include “drop-in” fuels usable in existing aircraft, and “non-drop-in” fuels, e.g., cryogenic fuels such as liquid hydrogen (LH2) and electricity, which require novel fuel infrastructure and aircraft designs (Table 10). Drop-in fuels are synthetic hydrocarbons produced from sequestered carbon atoms, e.g., from biomass (biofuels) or from the atmosphere (Power-to-Liquid fuels), so that direct CO_2 emissions are offset over the fuel lifecycle. Several other non-drop-in solutions are omitted due to low energy density and high toxicity (ammonia), low availability for aviation (low-cost SLNG), dominance by drop-in pathways (high-cost SLNG), or severely limited range and payload performance (all-electric aircraft). The capital requirements, inputs, costs, resource potential, and lifecycle GHG emissions vary between the fuel pathways (Table 10). Several underlying key technologies (e.g., CO_2 capture from the atmosphere) are still under development. In such cases, Table 10 represents ambitious future states of the technology.

Table 10: Characteristics of energy carriers suitable for commercial aviation

	Jet A	**Drop-in Fuels**			**Cryogenic Fuels**			**Electricity**
		Low-cost Biofuels (1)	**High-Cost Biofuels (1)**	**Power-to-Liquids**	**Low-Cost SLNG (2)**	**High-Cost SLNG**	**Liquid Hydrogen**	
Feedstock	**Crude oil**	**Waste & plant oils; FTL from MSW***	**Cellulosic biomass**	**Hydrogen & atmosph. CO_2 (3)**	**Animal manure, municipal wastewater**	**Hydrogen & atmosph. CO_2**	**Water & renewable electricity**	**Solar, wind**
Fuel Supply Characteristics								
Electricity intensity in 2020 (2050), kWh(el)/kWh(fuel) (4)	~ 0	0.02	<0.01	2.1 (1.9)	0.05	2.0 (1.8)	1.8 (1.5)	1.0
Capital intensity, mln $/boe/d in 2020 (2050) (5)	0.01-0.03	0.03-0.13	0.13-0.20	1.0 (0.3)	0.3	1.0 (0.3)	1.3 (0.4)	0.14 (0.07)
Production costs in 2020 (2050), $/bbl(JFE)	6 – 22 (6 – 110)	150 – 230 (130 – 210)	180 – 290 (160 – 260)	380 (100)	110 – 230 (110 – 230)	390 (110)	440 (130)	60 – 150 (30 – 70)
Fuel resource potential, EJ	24,000-98,000	0.3 – 20.5 (6)	60 – 110 (6)	unlimited	30 (6)	unlimited	unlimited	unlimited
Climate impact intensity, $gCO_2(eq)$/MJ								
Upstream (WTT)	14.3	-61.7 – -36.1	-62.7 – -51.0	-70.4	-104.7 – -45.8	-56.4	0.0	0.0
of which CO_2	11.9	-65.9 – -48.0	-63.0 – -58.8	-70.4	-75.1 – -57.0	-56.4	0.0	0.0
of which non-CO_2 (8)	2.4	1.3 – 23.1	0.4 – 11.4	0.0	-29.6 – 11.2	0 – 13.9	0.0	0.0
Combustion (TTW)	104.0	94.1	94.1	94.1	95.5	95.5	35.1	0.0
of which CO_2	73.2	70.4	70.4	70.4	56.4	56.4	0.0	0.0
of which non-CO_2, central value (uncertainty) (8)	30.8 (9.4 – 54)	23.7 (6 – 47)	23.7 (6 – 47)	23.7 (6 – 47)	39.1 (13 – 73)	39.1 (13 – 73)	35.1 (11 – 68)	0.0
Lifecycle (WTT + TTW)	118.3	32.4 – 58.0	31.4 – 43.1	23.7	-9.2 – 40.5	39.1	35.1	0.0
of which CO_2	85.1	4.5 – 22.4	7.4 – 11.6	0.0 (5)	-18.7 – -10.6	0.0	0.0	0.0
of which non-CO_2(8)	33.2	25.0 – 46.8	24.1 – 35.1	0.0	9.5 – 50.3	39.1 – 53.0	35.1	0.0
% of lifecycle Jet A	100	27 – 49	27 – 36	20	-8 – 34	33	30	0

(1) The biofuels production cost range is determined by feedstock and conversion pathways; lower end: HEFA fuels and waste; higher end: energy crops. (2) The cost range of low-cost SLNG is determined by feedstock; lower end: agricultural residues; higher end: energy crops. (3) See Supplementary Section 1.3 (Dray et al., 2022) (4) The electricity intensity captures external electricity input. Therefore, the electricity intensity of refineries is around zero, as nearly all electric power is produced onsite. (5) Capital intensity is measured in million dollars of investments per barrel of oil equivalent (boe) per day. (6) Higher number: sensitivity case. In the case of PTL, consistent with DAC costs of US$280 per tonne CO2 at hydrogen production costs of US$1 per kg. (7) Resource potential of low-cost biofuels from literature (Staples et al., 2018)(GEA, 2012)(IEA, 2020b). High-cost biofuels resource potential corresponds to the lower end and higher end ((Staples et al., 2018)(GEA, 2012)(IEA, 2020b)), assuming a 50% biomass to fuel conversion efficiency. The low-cost SLNG potential is based on literature (IEA, 2020b) (8) The CO2eq values in this table were derived using GWP100. The relative impact of CO2 to non-CO2 is sensitive to time horizon (Supplementary Sections 3.2 and 3.3 from (Dray et al., 2022)). CO2eq emissions of renewable electricity are assumed to be zero. FTL from MSW, Fischer–Tropsch liquids from municipal solid waste; bbl(JFE), barrel of jet fuel equivalent.

CO_2eq/Energy (Eq 10): Climate intensity of TTW non-CO_2 emissions

Aviation's CO_2 emissions footprint is exacerbated by WTT and TTW non-CO_2 impacts from onboard fuel combustion. While WTT non-CO_2 emissions are accounted for in the previous section, jointly, soot, stratospheric water vapor, contrails and contrail-cirrus, oxides of nitrogen, and sulfur TTW emissions contribute 30-67% to aviation's total radiative forcing impacts (Grobler et al., 2019; Lee et al., 2020). The largest contribution, 41-57% of in-flight climate impacts, has been attributed to contrail-cirrus (Grobler et al., 2019; Lee et al., 2020).

The different chemical composition of alternative fuels leads to differences in their non-CO_2 climate impact. Using GWP_{100}, shows the non-CO_2 impact from in-flight emissions for different fuels. We estimate TTW non-CO_2 impacts of drop-in alternative fuels to be 23% lower (range: 67% lower to 38% higher) than that of Jet-A (Table 10 & Figure 40). This decline is due to a 35% decrease in the contrail impact (Burkhardt et al., 2018; Caiazzo et al., 2017; Teoh et al., 2020), partially counteracted by an assumed reduction in sulfur-related cooling. For LNG we find the non-CO_2 impacts increase by 27%, mainly due to the elimination of the sulfur related cooling. Finally, we find the non-CO_2 impacts from LH2 are 14% higher per unit energy (range 52% lower to 120% higher) than from Jet-A, as a result of: (1) a factor 2.6 increase in warming from stratospheric water vapor emissions; (2) elimination of sulfur related cooling; and (3) a 15% reduction in contrail warming.

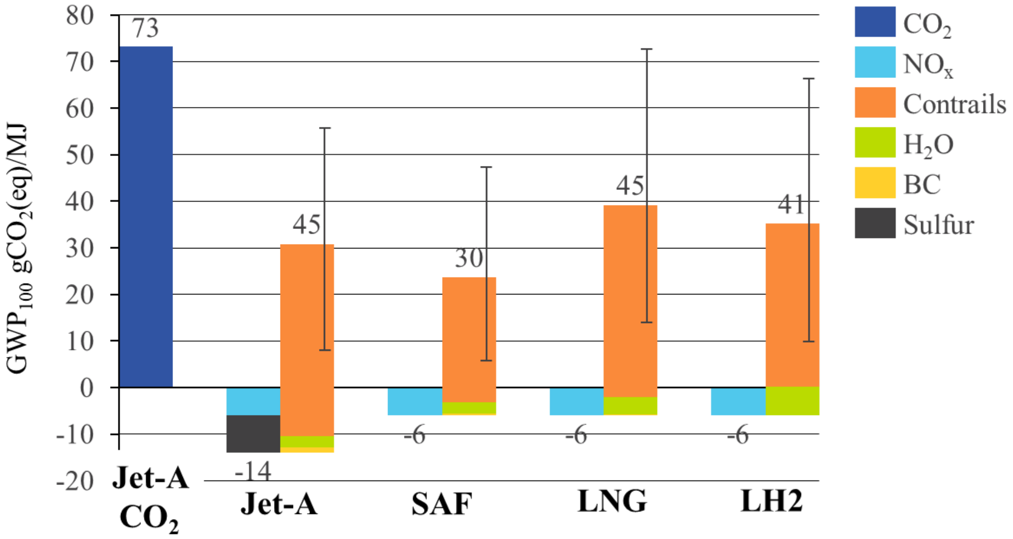

Figure 40: Resulting non-CO_2 GWP100 climate impacts for an emissions pulse of each fuel. Here the label SAF includes all drop-in alternative fuels.

These results are sensitive to the selected time horizon when compared to CO_2 emissions. Figure 41 shows in-flight non-CO_2 CO_2eq for each fuel considering a 20-year and a 500-year time horizon. Despite large relative differences compared to CO_2, the relative outcomes for different fuels remain consistent. For example, LNG is estimated to lead to the largest alternative fuel climate impact, while drop in alternative fuels are estimated to lead to the smallest impact, regardless of the GWP time horizon selected. This occurs since the atmospheric lifetimes of non-CO_2 forcers from in-flight combustion are shorter than all the GWP time horizons considered here.

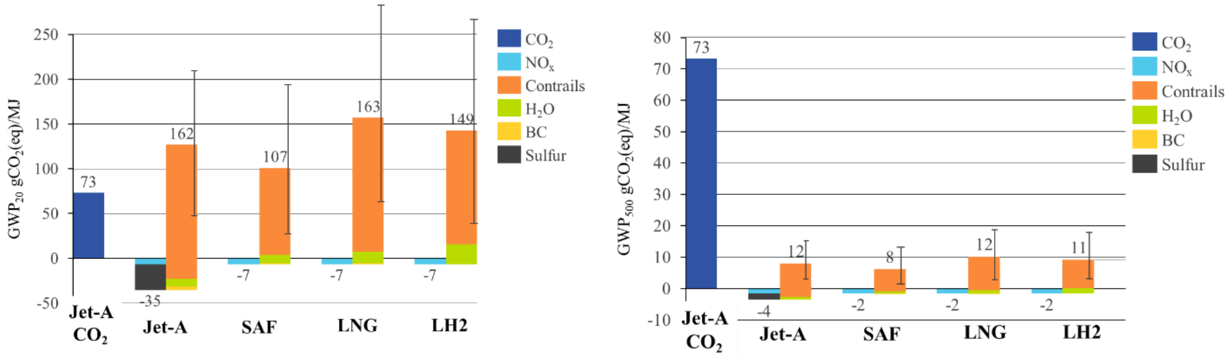

(a) (b)

Figure 41: CO2eq emissions results for in flight emissions using GWP with time horizons of (a) 20 and (b) 500 years for an emissions pulse of each fuel. Here the label SAF includes all drop-in alternative fuels.

Contrails form in regions with ice supersaturated atmospheric conditions, which have large horizontal (up to 400 km) extent and a small vertical height (typically less than 600 m) (Mannstein et al., 2005; Spichtinger et al., 2003), and can thus be avoided through cruise altitude adjustments. Studies suggest this strategy to result in a small fuel burn penalty at the benefit of a large, avoided contrail impact (Avila et al., 2019; Schumann et al., 2011; Teoh et al., 2020; Yin et al., 2018). Using results from our meta-analysis of contrail avoidance (see Methods), the rest of our assessment is based on an assumed 50% reduction of contrail length for a 1% increase in fuel burn.

Offsets (Eq 10)

Instead of directly reducing their own emissions, airlines can purchase certificates for CO2 emissions reductions in other sectors or carbon sequestration measures. Such an approach is implemented as part of ICAO’s Carbon Offsetting and Reduction Scheme for International Aviation (CORSIA). However, offset schemes may not fully ensure that emissions reductions would not have occurred otherwise, are permanent, are not double-counted, and are verified

(Cames et al., 2016; ICF Consulting, 2020). For these reasons, we do not consider offsetting in this chapter.

5.4.2. Potentials and costs of single-fuel pathways

The path towards a net-zero aviation system requires a potentially costly transition to low-carbon fuels. The most suitable fuels identified are biofuels, PTL, and LH2. Their climate impact mitigation potential is limited by available supply, how fast production can be ramped up, how ramp-up interacts with demand growth, and—for LH2 as a non-drop-in fuel—the rate of fleet turnover. To explore the boundaries of mitigation from each candidate fuel, we first analyze emissions reductions, fuel production infrastructure investment costs, and market response over time if each fuel is individually regulated into the market at maximum rates through mandates without supply limitations.

The integrated aviation systems model AIM2015 (Dray and Schäfer, 2021; Dray et al., 2019) allows modelling these fuel pathways and a no-intervention baseline under different demand scenarios, defined by socio-economic development, oil prices, technological change, and other factors (derived from IPCC's SSP scenarios adjusted for the impact of the COVID-19 pandemic (Dray and Schäfer, 2021)). Due to their cost-effectiveness, future conventional aircraft generations are adopted without additional policy intervention. For the hydrogen pathway, LH2 aircraft are mandated into the fleet from 2035 onwards following AIM2015's fleet turnover model. For drop-in fuels, mandates reaching 100% in 2050 are assumed. These runs build upon the World Economic Forum ambition of 10% biofuel share (around 1.5 EJ) in 2030 and imply drop-in fuel supply of nearly 26 EJ in 2050. (WEF, 2020) However, it is unclear to what extent the associated biomass of ~52 EJ/yr would be available for aviation use (Johansson et al., 2012; Staples et al., 2018; WEF, 2020).

In the baseline scenarios, aviation direct energy use is projected to increase from 13 EJ in 2019 to 18-29 EJ in 2050, depending on the demand scenario (Table 11). Associated lifecycle ("well-to-wake", WTW) CO_2 emissions increase from 1.1 to 1.5-2.5 Gt. Mitigating these CO_2 emissions requires discounted investments from \$0.5 tln to \$2.1 tln, depending on the pathway. Airfares increase by no more than 17% from year-2019 values and demand growth slows by no more than 0.6 percentage points p.a.

Table 11: Scenario variables and outcomes in the reference scenarios and single-pathway abatement scenarios

	Low Demand		Middle Demand		High Demand	
	Baseline (fossil Jet-A)	Single alternative fuel scenarios	Baseline (fossil Jet-A)	Single alternative fuel scenarios	Baseline (fossil Jet-A)	Single alternative fuel scenarios
RTK growth, %/yr (2019-2050)	2.4	1.8-2.4 (3)	3.7	3.1-3.7 (3)	4.1	3.5-4.0 (3)
Aviation direct energy use in 2050, EJ (c.t. 13 EJ in 2019)	17.7	15.0-17.6 (1)	26.4	22.3-25.8(1)	29.4	24.9-28.6(1)
of which EJ provided by alternative fuel	N/A	7.9-17.2(2)	N/A	12.9-25.6(2)	N/A	14.9-28.5(2)
Well-to-wake CO_2 emissions in 2050, Mt (c.t. 1,070 mln tonnes in 2019)	1,510	0-822 (3)	2,240	0-1,100(3)	2,490	0-1,170 (3)
Cumulative (2019-2050) well-to-wake CO_2 emissions, Gt	40.1	24.9-35.3 (4)	50.0	28.0-42.3(4)	53.4	29.5-44.7(4)
Cumulative discounted climate costs, tln US\$(2020) (10)	13.1	9.9-12.1(5)	15.9	11.7-14.3(6)	16.9	12.3-15.1(7)
Cumulative discounted (2019-2050) alternative fuel supply investments, tln US\$(2020)	N/A	0.54-1.36 (8)	N/A	0.83-1.93 (8)	N/A	0.94-2.12(8)

Change over 2019 constant-price airfare in 2050, % (per RPK)	-4.0	-2.1-14 (9)	-2.3	-0.8-16 (9)	-1.3	0.4-17 (9)

Table Notes:
(1) Lower end biofuels, higher end LH2. (2) Lower end LH2, higher end PTL.(3) Lower end PTL, higher end LH2. (4) Lower end biofuels, higher end LH2. (5) Central values and 95% CI: 13.1 (3.2-32.9; baseline); 10.1 (2.5-25.4; PTL); 9.9 (2.5-24.9; biofuel); 12.1 (3.0-30.4; hydrogen). For comparison purposes, climate costs are calculated using RCP2.4 and SSP2. (6) Central values and 95% CI: 15.9 (4.0 - 40.1; baseline); 12.2 (3.0-30.6; PTL); 11.7 (3.0-30.6; biofuel); 14.3 (3.6-36.1; hydrogen). (7) Central values and 95% CI: 16.9 (4.2 - 42.6; baseline); 13.0 (3.3-32.7; PTL); 12.3 (3.1-30.8; biofuel); 15.1 (3.8-38.0; hydrogen). (8) Lower end biofuels, higher end PTL. Discount rate = 2%. (9) Lower end LH2, higher end biofuels.

Following the single-fuel pathways, only PTL could reduce aviation lifecycle CO_2 emissions to zero as shown for the middle demand scenario in Figure 42. Despite the unconstrained 2050 energy supply, the single-LH2 pathway cannot achieve full market share due to fleet turnover constraints (Panels c and d). Biofuels could be adopted at a significant scale earlier than PTL and LH2 since production capacity is already being ramped up today. By 2050, under the assumptions of this thesis, the biofuel pathway would release around 220 million tonnes of CO_2 due to remaining fuel production WTT CO_2 emissions (Panel h). In addition, significant non-CO_2 impacts remain for all single-fuel pathways because alternative fuels still cause non-CO_2 impacts (Table 10), and no action to avoid contrails is included.

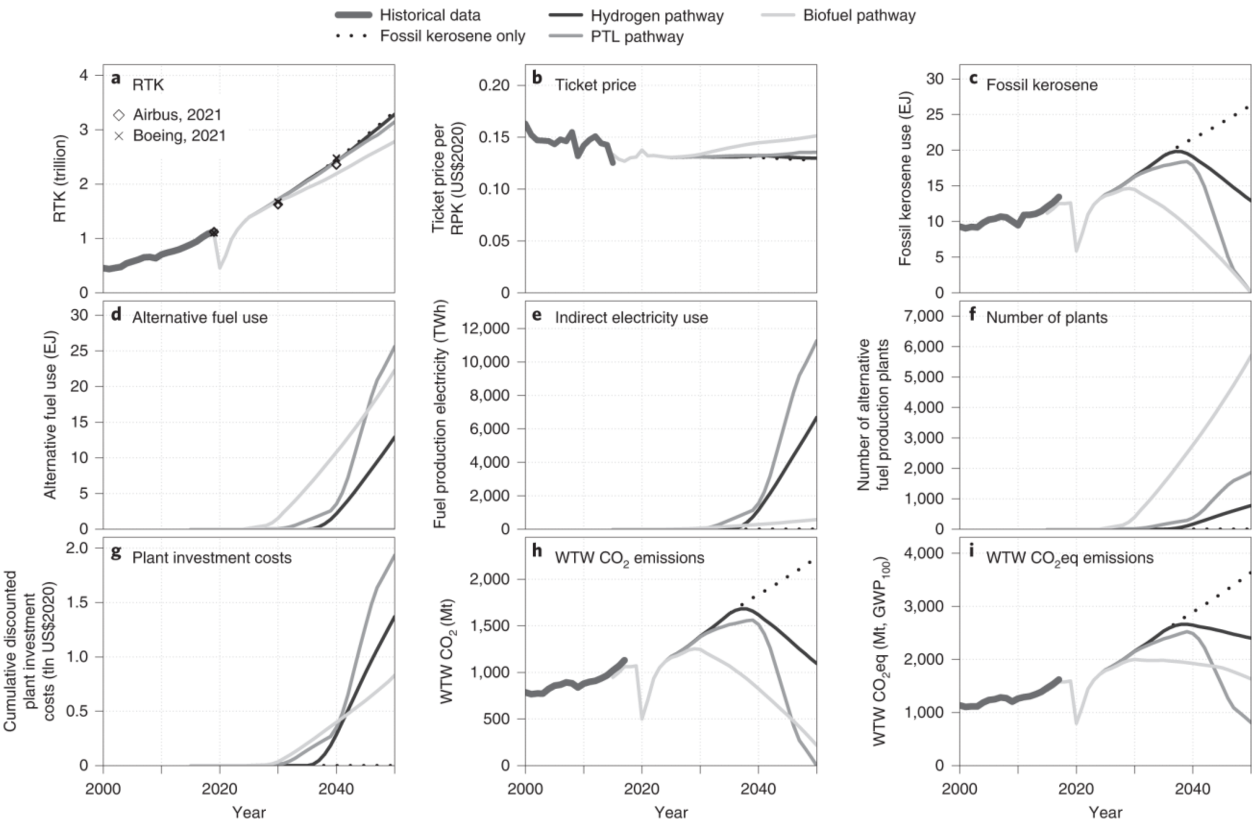

Figure 42: Model outputs for single-fuel pathways in the middle demand scenario.

Figure notes: (a) RTK, (b) average ticket price, (c) fossil jet fuel use, (d) alternative fuel use, (e) low-carbon electricity required for fuel production, (f) number of synfuel plants in operation, (g) cumulative discounted synfuel plant investment costs, (h) combined well-to-wake CO_2 emissions, (i) combined well-to-wake CO_2 equivalent GHG emissions including non-CO_2 effects on a GWP_{100} basis. Additional panels showing non-CO_2 effects by GWP_{20}, GWP_{500}, radiative forcing, and global mean surface temperature change are included in Dray et al. (2022). Historical RTK and ticket revenue data is from ICAO (2020)

Owing to the comparatively high electricity intensity of PTL and LH2 (Table 10), power generation accounts for 59% and 64%, respectively of the investment required in each pathway. By 2050, around 11,000 TWh and 6,700 TWh of electric power would be needed for PTL and LH2, respectively (panel e), equivalent to 41% and 25% of year-2020 world electricity generation. For the biofuel pathway, almost 6,000 fuel production plants would have to be built globally over the study period.

For each single-fuel pathway, air transportation continues to grow but at a lower rate compared to the reference development (panel a), due to higher operating costs raising airfares (panel b). The ramp-up of PTL production coincides with the cost of PTL declining sharply under aggressive assumptions for cost reductions in direct air capture, renewable electricity, and electrolysis. To assess the sensitivity of outcomes, we also simulated the middle demand scenario with 50% higher projected LH2 costs and twice the projected PTL costs in 2050 (Shell, 2021). Compared to the projected 2-6% increase in the average 2050 airfare over year-2019 values, the higher fuel costs result in an 8 and 16% ticket price rise for the LH2 and PTL case and an 7-18% reduction in year-2050 RTK over baseline values.

Figure 43 to Figure 45 show time series of radiative forcing and temperature change for these scenarios, as broken out by the different forcing pathways. These figures indicate that the largest contribution in 2050 due to emissions in the years 2015 to 2050 is from contrails. However, the radiative forcing impact from contrails only continues in the years that flight operations occur. In contrast, CO_2 radiative forcing persists for centuries. As a result, the temperature response due to contrails, while larger in magnitude in 2050, decays away within a few decades, while temperature change due to CO_2 persists for hundreds to thousands of years. While the individual components of the indirect NO_x forcing pathways are similar in magnitude to CO_2 for these emissions scenarios, these indirect NO_x related forcing pathways are opposite in sign, leading to smaller net negative or positive forcings due to NO_x emissions.

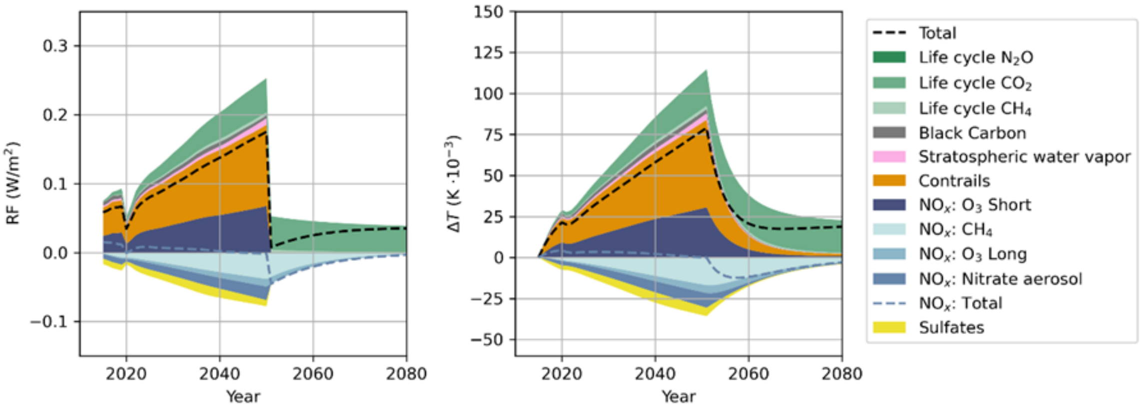

Figure 43: Radiative forcing and temperature change for Hydrogen fuel scenarios

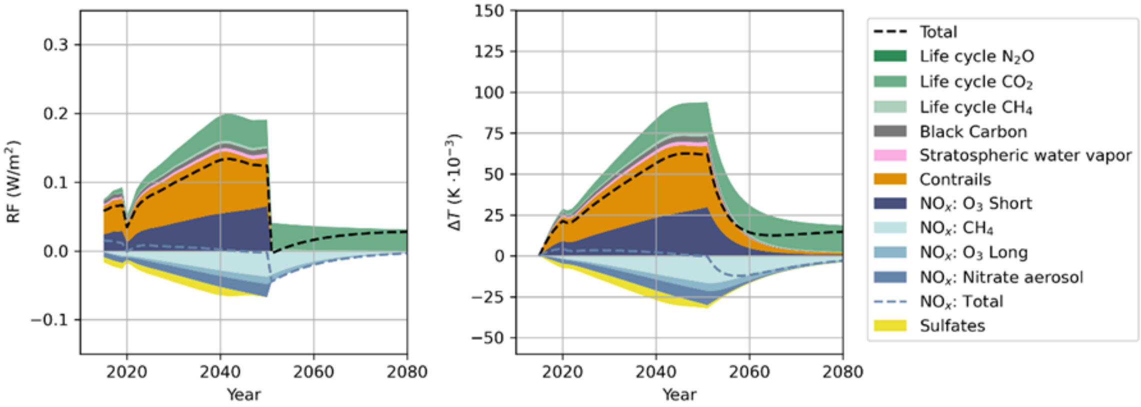

Figure 44: Radiative forcing and temperature change for PTL fuel scenarios

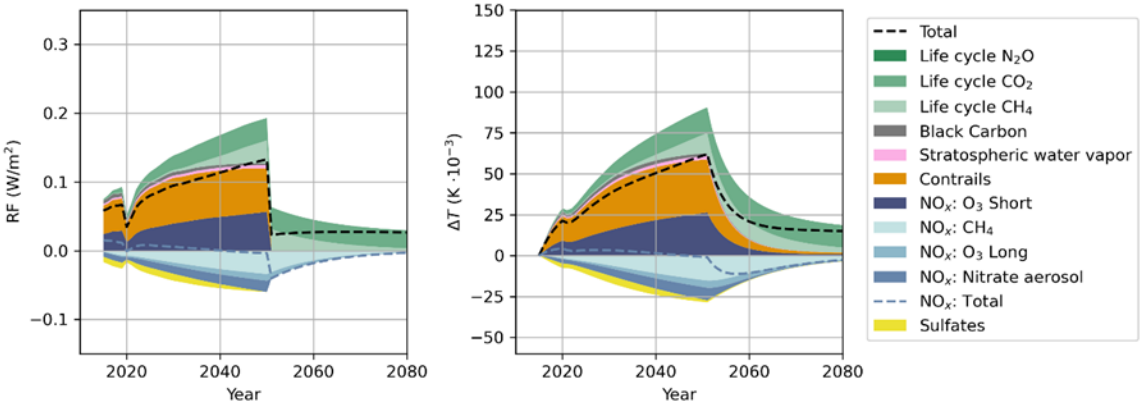

Figure 45: Radiative forcing and temperature change for biofuel scenarios

5.4.3. Potentials and costs of combined pathways

PTL and LH2 pathways have limited scale-up potential before the 2030s, whereas biofuels are likely to experience long-term supply constraints. Therefore, we define combined pathways, which include supply-constrained biofuels in combination with either LH2 or PTL. Furthermore, to address non-CO_2 impacts, the combined pathways consider contrail avoidance (see Section 5.3.4).

Cost-effective reductions in air transport system energy intensity reduce middle demand scenario year-2050 WTW CO_2eq emissions from 4,900 to 3,600 Mt, addressing around 26% of the potential CO_2eq emissions in 2050 (Figure 48 a, b). Over 40% of CO_2eq emission reductions result from low-carbon fuels, whereas demand effects—from higher airfares—lead to an additional decline of up to 10%. Altogether, the combined pathways can reduce year-2050 WTW CO_2 emissions by around 95% relative to baseline runs that include aircraft energy intensity improvements only, and by over 89% relative to 2019 levels. These reductions are enabled by year-2050 biofuel use of 6.6 EJ (biofuel + PTL pathway) and 11.2 EJ (biofuel + LH2 pathway); year-2050 PTL and LH2 use is 17.9 and 11.5 EJ, respectively.

However, year-2050 non-CO_2 impacts are around 10% higher than those in 2019 because only 60% of the cumulative non-CO_2 impacts compared to baseline runs can be addressed. This reflects that contrail avoidance is assumed to reduce contrail radiative forcing by 50% only, with additional benefits available from fuel composition changes. Figure 46 and Figure 47 show radiative forcing and temperature change from each of the climate forcers considered for central-growth combined-technology pathways. Other non-CO_2 impacts, e.g., from water vapor emissions, remain unaddressed.

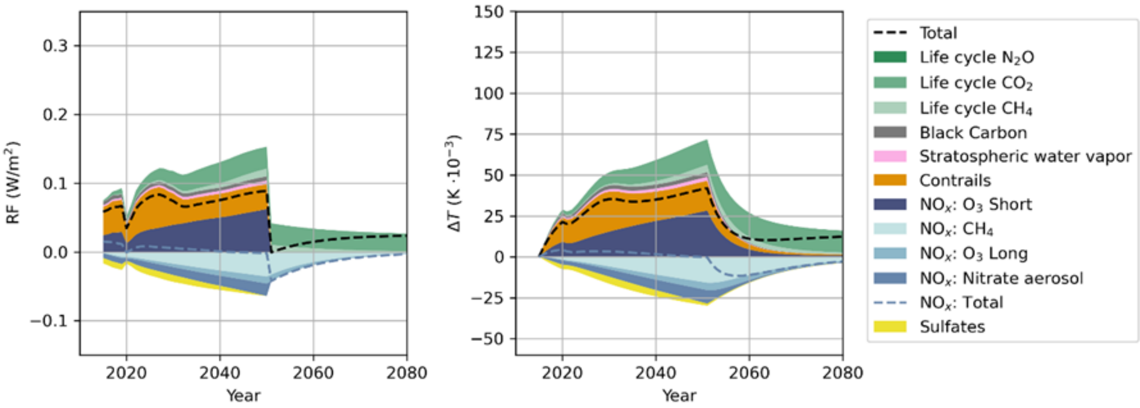

Figure 46: Radiative forcing and temperature change for combined PTL and biofuel scenarios

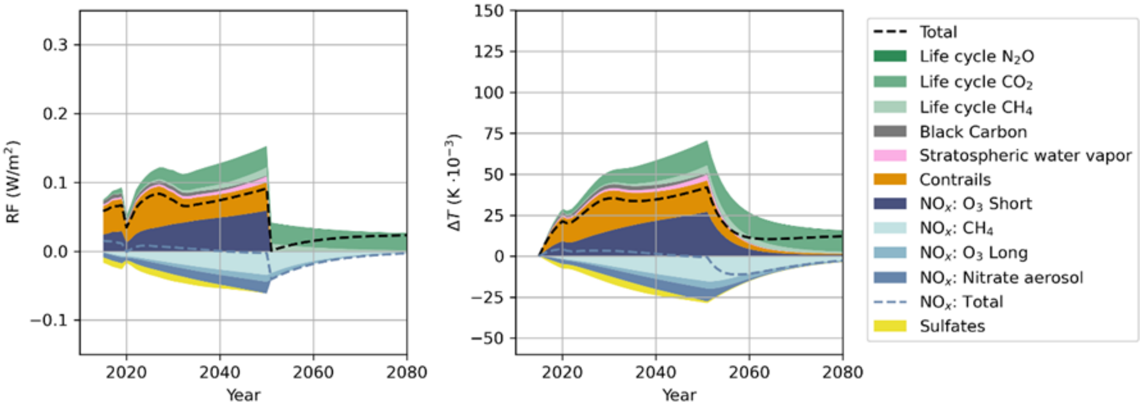

Figure 47: Radiative forcing and temperature change for combined LH2 and biofuel scenarios

The required discounted investments associated with the aviation energy transition are around $1.7 tln over the 30-year study period (12% lower than in the corresponding single-fuel PTL pathway), of which around 45% are associated with renewable power generation. In the context of a broader transition of a net-zero global energy system, middle demand scenario non-discounted investments are around 2.2% of those required in the global energy and industrial system. (IRENA, 2021)

Aircraft operating costs increase at most by 10-16% relative to the baseline Jet-A scenario over the study period. These increases are relatively small because alternative fuel costs decrease and aircraft energy efficiency increases over time, mitigating the cost increase associated with higher levels of alternative fuel mandate in later years. Almost the entire cost increase is passed through to ticket prices, leading to 0.3-0.4% p.a. lower average RTK growth rates for the middle demand scenario).

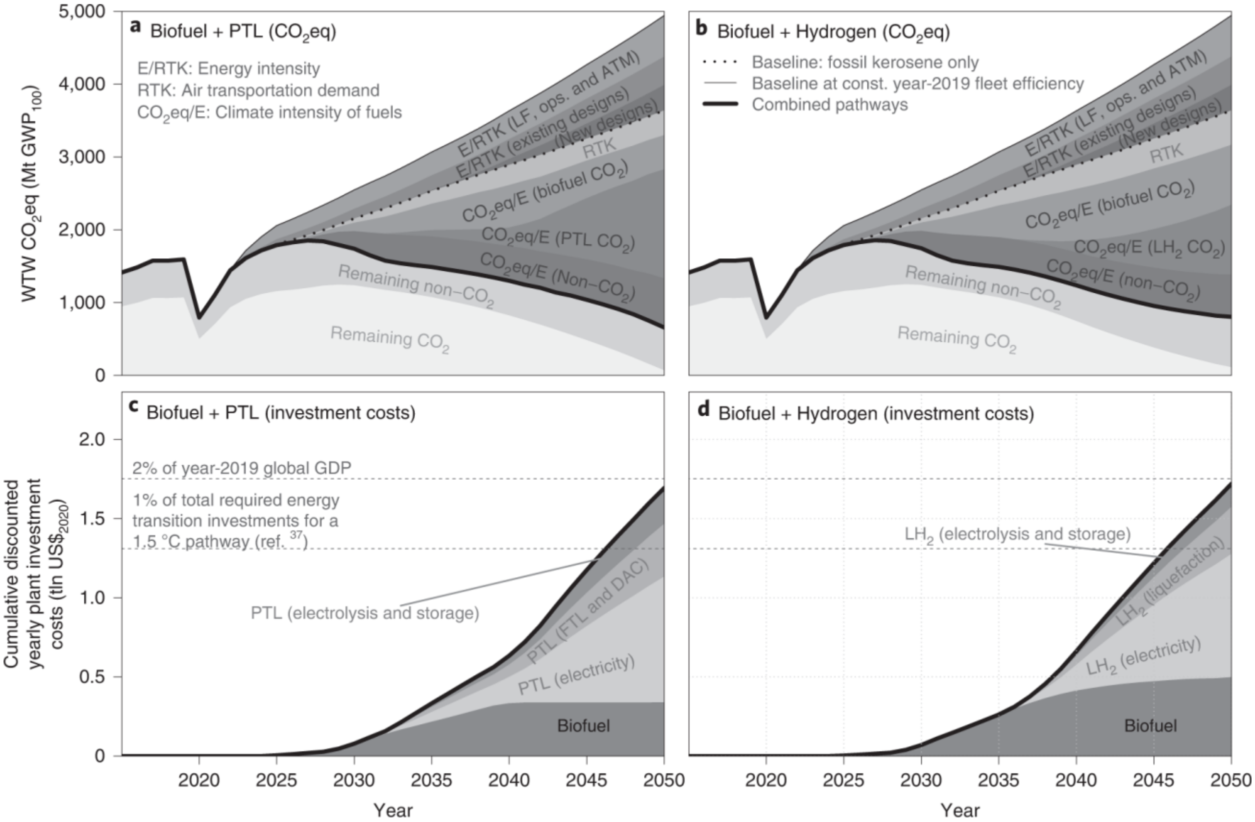

Figure 48: Middle demand scenario related model outputs for two combined pathways aimed at minimizing year-2050 aviation climate impact, biofuels + PTL and biofuels + hydrogen.

Figure notes: (a) Reduction in CO_2eq (GWP$_{100}$) emissions by type of mitigation strategy, biofuels + PTL pathway; (b) reduction in CO_2eq emissions by type of mitigation strategy, biofuels + hydrogen pathway; (c) cumulative discounted plant investment costs, biofuels + PTL pathway; (d) cumulative discounted plant investment costs, biofuels + hydrogen pathway. The contribution of each source to emissions reductions is approximate, as there is interdependency between mitigation measures. E/RTK (existing designs) includes changes in CO_2eq from aircraft designs with pre-2025 entry into service. E/RTK (LF, ops. & ATM) includes the impact of changes in load factor, operational mitigation measures (e.g., reduced taxi time), and changes in CO_2eq from network change over time (e.g., longer average flight length). RTK reduction results from higher airfares induced by the energy transition. Non-CO_2 includes contrail avoidance and non-CO_2 impacts of alternative fuel use.

5.5. Discussion and conclusion

An energy transition towards synthetic low-carbon fuels is a necessary condition for the aviation sector to achieve the net-zero goal. Improvements in air transport fuel efficiency, driven largely by market forces, can address about a quarter of the projected 2050 lifecycle WTW CO_2eq emissions. These cost-effective reductions will also be an important enabler for the needed energy transition since they reduce investment requirements for fuel production, limit the need for higher-cost fuels, and thus mitigate increases in airline operating costs and airfares.

Low-carbon alternative fuels can reduce 2050 lifecycle CO_2eq emissions by an additional 40% and—in combination with reduced air transport demand due to the higher costs of these fuels—bring aviation 2050 CO_2 emissions close to zero. This requires LH2 and PTL fuels with zero lifecycle CO_2eq emissions, i.e., the embedded emissions of power generation to be zero. Drop-in biofuels could play a critical role in the fuel transition over the coming decade, given their near-term availability. However, as biofuel production is scaled up over time, constrained biomass availability could limit production volumes and increase costs. Thus, biofuels could be supplemented by a second wave of fuels which use renewable electricity as a major feedstock – i.e., LH2 and drop-in PTL. PTL could fully displace other fuel sources by 2050; due to fleet turnover limitations, 100% use of LH2 is unlikely before 2080. The choice of either PTL or LH2 will depend on the cost of atmospheric CO_2 capture and syngas-to-fuel conversion, the upfront cost and practicability of hydrogen aircraft and fuel infrastructure, and potentially these fuels' non-CO_2 impacts. The extent and timing of the introduction of PTL and LH2 over biofuels depends on their relative cost to biofuels and technology readiness. Our analysis relies on optimistic assumptions from the literature; later technology readiness or higher costs could delay or reduce the scale of PTL or LH2 adoption.

The non-CO_2 effects are harder to abate and still have significant impact in 2050. Contrail avoidance partly addresses the non-CO_2 impact of aviation by reducing contrail impacts – perhaps conservatively estimated – by 50% for a 1% fuel burn penalty or 0.2% increase in aircraft direct operating cost. However, the reduction in non-CO_2 emissions is incomplete. Further research is needed to address the remaining gap, along with other impacts currently not considered in this analysis (e.g., climate impacts of hydrogen leakage (Cooper et al., 2022)).

The scale of the energy transition, requiring 1,000 GW-scale LH2 plants or 5,000-6,000 MW-scale-biofuel plants in 2050, as well as build-up of power generation infrastructure, requires investments of order $1-2 trillion (discounted to 2019). Without policy intervention, there does not seem to be a business case, as the alternative fuels are not projected to reach cost parity with fossil Jet-A. Large-scale, long-term and globally coordinated political incentives are needed to drive this transition.

At the same time, our models of market feedbacks suggest that the aviation sector could be able to fully cover the cost of the transition. The projected airfare increases associated with the transitions in the combined pathways are limited to 10-15% compared to a baseline without energy transition, with increasing fuel costs partly offset by energy efficiency improvements. As such, the air transport sector could continue to grow through this transition, thereby enabling larger shares of the global population to use and benefit from air transportation. However, in light of low airline profitability, less profitable carriers could be forced to exit markets. Our model cannot capture such changes to sector structure.

The analysis presented in this chapter shows that that the aviation sector could move towards a zero-impact CO_2 system if predictable, long-term incentives are created. Such measures do not require shifting the cost of the transition away from the aviation sector but can be absorbed by airlines and customers. However, the required technologies (i.e., biofuels, PTL, LH2 aircraft, and contrail avoidance) to achieve these goals still require development and scale-up. Additional measures, such as encouraging mode shifts, as well as measures to reduce non-CO_2 impacts, may further improve the viability of the transition. For the aviation sector to contribute substantially towards the goals of the Paris Agreement by mid-century, the transition needs to start now.

Chapter 6

Conclusions

6.1. Summary of findings and contributions

This thesis provides an investigation into commercial aviation's **historical** emissions trends, **current** climate impacts, and potential **future** pathways to reach net zero climate impacts by 2050. The key findings and contributions from each chapter are summarized below:

Chapter 2 presents the first bottom-up historical emissions inventory for global commercial civil passenger aviation spanning four decades from 1980 to 2019. Leveraging aviation schedules and aircraft and airport data, emissions and locations are quantified over time. Results show that growth in fuel consumption outpaced efficiency gains, with fuel consumption increasing by 330% over this time, while available seat kilometers increased by 560%. This growth is heterogeneous, and we find changes in emissions composition, region, altitude, season, and time of day. These changing emissions characteristics likely influence present and future climate and air quality impacts, underscoring the importance of developing solutions that account for aviation's evolving impacts.

Chapter 3 quantifies, for the first time, the present-day cumulative climate impacts from aviation emissions since the start of the jet age, incorporating these spatial, temporal, and compositional emissions changes over time. Using an intermediate-fidelity aircraft plume model with ERA5 reanalysis weather data, contrail radiative impacts are modeled over time. Findings show contrail forcing has more than quintupled since 1980. However, per flight distance, contrail impacts remained within 10% of its value in 1980. This is a net effect of a 32% rise in fraction of flight segments that produce contrails, being mitigated by a 24% decrease in the radiative forcing per distance of contrail. The increase in contrail formation is in part due to higher engine efficiencies which result in higher contrail formation likelihood. We additionally identify a potential increase in the quantified contrail impacts driven by the mismatch between contrail and the ERA5 weather data length scales. This expansion in the uncertainty range of RF from contrails linked to the inadequacy of weather data resolution in capturing continuity in water vapor around contrails. By integrating this continuity, this thesis reveals that contrail impacts could be tripled compared to existing estimates that overlook this factor. Using these results, including additional uncertainty, we find that contrails are responsible for 70% of temperature change due to aviation in the year 2019. Given this large and growing impact, this research reinforces the need for contrail mitigation efforts.

Chapter 4 presents climate and air quality costs for marginal changes in present-day aviation emissions. Valued on a common basis, these results allow decision-makers to rapidly evaluate emissions trade-offs and benefits of emissions reductions. We find that cruise emissions account for 90% of impacts per fuel unit, with 49-81% from air quality effects depending on discount rate. Collectively NO_x, CO_2, and contrails cause 97% of the total impact. Overall, these metrics facilitate data-driven decision making in aviation technology, operational, and policy options.

Chapter 5 explores how alternative fuels, including drop-in alternatives, and liquid hydrogen, can be coupled with contrail avoidance, and efficiency gains to enable cost-effective pathways for aviation's emissions to reach near net zero climate impacts by 2050. Modeling indicates combining these measures could reduce aviation lifecycle CO_2 emissions up to 94% below 2019 levels, with costs absorbed through higher airfares. However, challenges remain in fully mitigating non-CO_2 impacts. Mitigating this would require higher contrail avoidance than assumed in this thesis. Collectively, the large investment costs underscore the urgent need to advance technologies and incentives to align aviation's growth with climate goals.

6.2. Policy implications

This thesis indicates important policy implications for reducing aviation's climate impacts. Firstly, throughout this thesis, these results indicate the need for mitigation strategies that target both CO_2 and non-CO_2 impacts, with contrails the most important non-CO_2 climate forcer to focus on. Collectively, Chapter 2 and Chapter 3 indicate that both contrail impacts, and CO_2 emissions have grown since 1980, with the impacts from past emissions persisting into the future. Using a forward-looking metric, Chapter 4 indicates that these two forcing pathways are collectively responsible for more than 100% of the climate damages from a unit of present-day aviation emissions.

Chapter 5 indicates achieving net zero climate impacts by mid-century requires long-term, global incentives and investments in sustainable aviation fuels, efficiency gains, and operational changes, with an explicit need for contrail avoidance.

In addition, these results also indicate the importance of targeting NO_x emissions for emissions reductions. Chapter 4 indicates that, while NO_x emissions have a small, but uncertain positive or negative climate impacts, their air quality impacts are similar in magnitude to the combined CO_2 and contrail impacts, with relative contributions depending on discount rates. Despite sustained regulation that aimed to reduce NO_x emissions per unit fuel burn by 45% from 2006 to 2016 (ICAO, 2007), our results indicate that NO_x emissions growth has outpaced fuel burn growth over the last 40 years. This indicates that additional or alternative measures may be necessary to limit NO_x emissions.

6.3. Recommendations for future work

During this thesis, various future research needs are identified. Although uncertainty remains, we estimate contrail impacts to be on the same order of magnitude than of aviation CO_2. As a result, this work echoes other studies that indicate avoiding contrail impacts could produce substantial benefits, despite the current uncertainty. However, reducing the contrail related uncertainty could further inform future trade-offs between avoiding their impacts and increased monetary and environmental costs.

Several research avenues are identified for advancing the quantification of contrail impacts. Firstly, higher resolution weather data, with accurate specific water vapor fields remains a major research need. This would not only be valuable due to reasons already identified in literature, such as biases in humidity at cruise altitude (Agarwal, 2021; Teoh et al., 2022), but would also inform the additional uncertainty identified in this thesis. Here we identify additional uncertainty on contrail impact quantification, caused by the mismatch in length scales between the weather data grid size and contrail sizes. As a result of this mismatch, far-field changes in water mass content can affect the contrail in a modeling study that uses these large weather data grid cells to directly inform water mass in the air around the contrail as the simulation progresses. This thesis indicates that this uncertainty could increase the subsequent contrail impacts by a factor 3. Therefore, we reiterate the need for higher resolution weather data, and additionally identify the need for explicitly accounting for continuity in water mass in the vicinity of the contrail in modeling studies.

Secondly, to calibrate these modeling studies, additional observational studies are needed, in particular, to quantify the contrail lifetime.

Third, the development of accessible, open-source tools for estimating aviation emissions is another area in need of further research. Sharing of results between researchers is currently limited by user agreements of proprietary datasets. Such tools, independent of proprietary datasets, would facilitate collaboration and could help standardize the inputs, leading to enhanced comparability of contrail impact assessments.

Our data from Chapter 3 indicates variability in contrail impacts by region, altitude, time of day, season, and aircraft characteristics. Since a simplified model for global fleet-wide contrail impacts remains unavailable, our results in Chapter 4 and Chapter 5 rely on a distance scaling approach to quantify future climate costs. This highlights the need for a simplified contrail model for evaluating fleet-wide effects. Such a model would be instrumental for quick assessments of contrail forcing relative to other aviation-induced climate forcers.

Furthermore, in the context of hydrogen as an alternative aviation fuel, substantial further research is required. Uncertainties remain in the (i) quantity of hydrogen leakage, both at ground level and at altitude, and (ii) the climate impacts of hydrogen leakage at cruise altitude. The impact of hydrogen leakage at altitude is likely different to ground emissions, due to the differences in the chemical composition of the tropopause and stratosphere, where these emissions would occur. Furthermore, understanding how hydrogen combustion may alter contrail formation, and contrail avoidance potential remains a research need. Given hydrogen's potential in mitigating CO_2 emissions from aviation, it is crucial to resolve these uncertainties through both modeling and empirical studies.

Overall, the thesis revealed multiple high-priority research needs to support policies for sustainable aviation. Targeting these areas through modeling, experiments, and measurement campaigns can provide insights to further inform effective solutions.

6.4. Closing remarks

This thesis provides timely insights into aviation's evolving climate impacts and options for mitigation. The findings provide information for data-driven decisions to directly support policies and investments needed to cost-effectively decarbonize aviation by mid-century. Although uncertainties remain regarding contrails, hydrogen aircraft, and alternative fuel supplies, this research informs near-term decisions that can shape aviation's long-term climate footprint. With rapidly growing emissions, aligning aviation's development and climate goals is an urgent, solvable challenge, requiring immediate collaborative action.

Appendix

Appendix A APMT-IC: Modeling of NO_x effects

The climate impacts due to NO_x, not only include the nitrate cooling pathway included in Table 3, but also includes indirect ozone and methane warming and cooling pathways. These ozone-methane impacts occur on time scales of less than one year and on the atmospheric lifetime of methane. As such, these lifetimes are also considered when modeling these indirect impacts in APMT-IC.

To capture the timescales of these impacts, an Absolute Global Warming Potential (AGWP) approach is applied, where AGWP for species x is defined as

$$\mathrm{AGWP}_{TH,x} = \int_0^{TH} RF_x \,\mathrm{dt} \qquad \text{Eq 11}$$

Firstly, an emission of NO_x leads to an increase in the tropospheric ozone concentrations. Ozone is a strong warming climate forcer (Myhre et al., 2013), with a short atmospheric lifetime and its impacts are assumed to last for a single year. Therefore, the AGWP_{100} for this forcer is the same as the RF in the first year following 1 kg of emission. In this description, this pathway is referred to as the NO_x-O_3 short impact, and it is modeled using the AGWP and the specified NO_x emissions. Mathematically the radiative forcing is derived as

$$RF_{NO_x-O_{3,Short}}(t=1) = Q_{NO_x}(t) \cdot \mathrm{AGWP}_{NO_x-O_{3,Short}} \qquad \text{Eq 12}$$

Secondly, NO_x emissions lead to decrease of atmospheric methane due to a NO_x related increase in the hydroxyl radical, which reacts with CH_4 to reduce the CH_4 background concentrations. Methane is a strong climate forcer, and this decrease leads to a cooling impact. This process, referred to as the NO_x-CH_4 long impact, occurs over the atmospheric lifetime of methane of 10-12 years. To model this impact, APMT-IC uses the AGWP to compute the RF in the first year after emissions using

$$RF_{NO_x-CH_{4,Long}}(t=0) = \frac{AGWP_{100,NO_x-CH_{4,Long}}}{\int_0^{100} e^{-\frac{t}{\tau}}\,\mathrm{dt}} \qquad \text{Eq 13}$$

where τ is appropriate e-folding timescale. After the $RF_{NO_x-CH_{4,Long}}(t=0)$ has been computed, the impact in each year is quantified using an appropriate e-folding timescale τ as presented in Eq 14.

$$RF_{NO_x-CH_{4,Long}}(t) = Q_{NO_x}(t) \cdot \mathrm{R}F_{NO_x-CH_{4,Long}}(t=0) \cdot e^{-\frac{t}{\tau}} \qquad \text{Eq 14}$$

Thirdly, NO_x emissions result in a long-term reduction in O_3 concentrations, referred to as the NO_x-O_3 long impact. The OH radical discussed for NO_x-CH_4 long impacts also leads to the production of the hydroperoxyl radical, HO_2, which reacts with O_3 to reduce the ozone concentration over a timescale of 10-12 years. This effect is modeled using Eq 15 and Eq 16.

$$RF_{NO_x-O_{3,Long}}(t=0) = \frac{AGWP_{100,NO_x-O_{3,Long}}}{\int_0^{100} e^{-\frac{t}{\tau}}\,\mathrm{dt}} \qquad \text{Eq 15}$$

$$RF_{NO_x-O_{3,Long}}(t) = Q_{NO_x}(t) \cdot \mathrm{RF}_{NO_x-O_{3,Long}}(t=0) \cdot e^{-\frac{t}{\tau}} \qquad \text{Eq 16}$$

The AGWP and timescale values are shown in Table 12. These values are taken from Stevenson et al. (2004); Wild et al. (2001) and Hoor et al. (2009), and capture the uncertainty bounds of more comprehensive reviews of aviation NO_x impacts (Holmes et al. 2011). For a single Monte Carlo run, APMT-IC takes AGWP values ($AGWP_{NO_x-O_{3,Short}}$, $AGWP_{NO_x-CH_{4,Long}}$, $AGWP_{NO_x-O_{3,Long}}$) and an associated exponential decay timescale, τ, from one of the three sources. For example, if it selects the $AGWP_{NO_x-O_{3,Short}}$ value from Stevenson et al. (2004), the remaining RF values and the timescale are also be selected from Stevenson et al. (2004). This is because each of the three NO_x impacts are dependent upon one other and the models used to estimate them.

Table 12: AGWP and timescale values used to model the NO_x related ozone and methane impacts. AGWP is measured in units of $\frac{W\,yr}{m^2\,g\,NO_x}$ x 10^{-15}.

	Decay Timescale [yr]	$AGWP_{100}$ CH_4 (long)	$AGWP_{100}$ O_3 (long)	$AGWP_{100}$ O_3 (short)
Stevenson et al. (2004)	11.5	-4.2	-0.95	5.06
Wild et al. (2001)	11.8	-4.6	-1.5	7.9
Hoor et al. (2009)	10.7	-4.3	-1.8	7.4

Finally, we note that a NO_x related cooling climate impact also results from a methane related reduction in stratospheric water vapor. APMT-IC does not explicitly model this impact as part of the NO_x contributions, although it is partially included in the stratospheric water vapor listed in Table 3.

Appendix B APMC-IC: Modeling temperature response

While RF provides useful information on the climate impacts of aviation emissions, policy makers may require more information to be able to compare short-lived impacts relative to longer term impacts. A climate metric based on temperature change facilitates such a comparison. A large integrated earth-atmospheric-ocean model could be used to estimate temperature change. However, these models are too computationally expensive to evaluate many policy scenarios. To facilitate the comparison of many policy options, 1-box or 2-box models that simulate the mixed ocean layer and the deep ocean have been used within APMT-IC. These models incorporate the relevant physics to model the impact of RF changes on the temperatures of the atmosphere and ocean and are fast enough to rapidly analyze many policy scenarios. Wolfe (2012) tested three models including (i) a model developed in (Shine *et al.* 2005), which was originally implemented in APMT-IC, (ii) the Raper-Wigley model (Wigley and Schlesinger 1985; Raper *et al.* 2001) and (iii) the CICERO model (Schneider and Thompson, 1981; Berntsen and Fuglestvedt, 2008). The CICERO model was found to approximate the 100-year temperature response more closely for a variety of scenarios as presented by the IPCC (Wolfe, 2012) and was subsequently implemented in APMT-IC. In this section, an overview of the CICERO model is provided.

The original versions of the climate model incorporated the temperature response model developed in Shine et al. (2005). This model used climate sensitivity to estimate the change in the atmosphere/mixed layer temperature. The CICERO model advances this framework by modeling the temperature response of the deep oceans, T_2, in addition to that of the atmosphere/mixed layer ocean, T_1. The deep ocean temperature is an important addition as this helps simulate the long-term response of the ocean as a heat sink. The equations used are shown in Eq 17 and Eq 18.

$$\frac{\partial T_1}{\partial t} = \frac{RF(t)}{C_1} - \frac{T_1}{\tau} - \alpha_1(T_1 - T_2) \qquad \text{Eq 17}$$

$$\frac{\partial T_2}{\partial t} = \alpha_2(T_1 - T_2) \qquad \text{Eq 18}$$

To understand the physics modeled within these equations, we describe each term on the Right-Hand Side (RHS) separately. The first term in Eq 17, $\frac{RF(t)}{C_1}$, represents the rate of temperature change due to the estimated radiative forcing, where C_1 is the effective heat capacity of the atmosphere/mixed-ocean layer. The heat capacity indicates how much energy is required to result in a temperature change of the atmosphere. The second part of the RHS in Eq 17, $\frac{T_1}{\tau}$, captures the equilibrium temperature due to the radiative forcing given the feedbacks in the climate system. The final term, which is reciprocated in Eq 18, represents the exchange of heat between the deep oceans and the atmosphere/mixed-layer ocean. The coefficients α_1, and α_2, are computed by

$$\alpha_1 = \frac{c_w}{C_1}\left(F + \frac{K_z \rho}{\Delta z}\right) \qquad \text{Eq 19}$$

$$\alpha_2 = \frac{c_w}{C_2}\left(F + \frac{K_z \rho}{\Delta z}\right) \qquad \text{Eq 20}$$

where c_w is the specific heat of liquid water, F is the advective mass flux of water from the boundary layer to deep ocean (assumed constant), K_z is the turbulent diffusion coefficient for mixing between the mixed ocean layer and the deep ocean, ρ is the density of water, Δz is the mixing depth for turbulent mixing of heat and C_2 is the heat capacity of the deep ocean.

The τ parameter in Eq 17 is computed through

$$\tau = C_1 \lambda = C_1 \frac{\Delta T_{\times 2CO_2}}{RF_{\times 2CO_2}} \qquad \text{Eq 21}$$

where $RF_{\times 2CO_2}$ and $\Delta T_{\times 2CO_2}$ are the radiative forcing and temperature change due to a doubling of CO_2, respectively.

$\Delta T_{\times 2CO_2}$ is known as the equilibrium climate sensitivity (ECS), and determines the temperature reached at equilibrium. The IPCC estimated two thirds of the ECS probability distribution to fall between 2K and 4.5K but mentioned that larger values could not be excluded (Roe and Baker, 2007). Following recent peer reviewed social cost of carbon estimates (US Government, 2016) which used the Roe and Baker (2007) uncertainty distribution, APMT-IC V24b also uses the Roe and Baker (2007) ESC uncertainty distribution. The Roe and Baker (2007) ECS is derived through

$$\Delta T_{\times 2CO_2} = \frac{\Delta T_{\times 2CO_2,0}}{1 - f} \qquad \text{Eq 22}$$

where $\Delta T_{\times 2CO_2,0}$ is the climate sensitivity in the absence of climate feedback effects (estimated be 1.2K, (Roe and Baker, 2007)), and f is the normally distributed feedback factor, which represents the uncertainty of the climate feedbacks effects. Calibrating the Roe and Baker ECS distribution to the IAWG SCC parameters, resulted in a mean feedback factor of 0.618 and a standard deviation of 0.185. In line with the IAWG SCC, the ECS distribution was truncated at 10K.

By comparing the values used within Berntsen and Fuglestvedt (2008) to literature estimates, expected values as well as uncertainty ranges for each of the other temperature model parameters were derived. These values are tabulated in Table 13. We note here that these uncertainty ranges do not necessarily reflect physical ambiguity, but the modeling uncertainty associated with the underlying models. For example, the range of Δz values represents the various approaches to representing diffusive heat transfer with more complex models.

Table 13: Values used for the temperature response model. Triangular uncertainty distributions were used, unless otherwise stated.

	Values and Distribution
$\Delta T_{\times 2CO_2}$ [K]	Roe and Baker (2007)*
R$F_{2\times CO_2}$ [W/m^2]	3.5, 3.7, 4.2
c_w [J/K/kg $\times 10^3$]	4.2 (constant)
C_1 [J/K/m^2 $\times 10^8$]	1.791, 3.13, 4.48
C_2 [J/K/m^2 $\times 10^{10}$]	0.63, 1.26, 2.52
F [kg/m^2/s $\times 10^{-4}$]	0.62, 1.23, 2.46
K_z [m^2/s $\times 10^{-5}$]	4.4, 10 (uniform)
ρ [kg/m^3]	1000 (constant)
Δz [m]	500, 1000, 2000

*Calibrated to the Interagency Working Group on Social Cost of Carbon (US Government, 2016)

Appendix C Climate assessment: Engine calculations engine thermal efficiency

Thermal efficiency, η_{th}, is calculated from the definition of overall efficiency, $\eta_{overall}$ as given by

$$\eta_{th} = \frac{\eta_{overall}}{\eta_{prop}} \qquad \text{Eq 23}$$

We calculate $\eta_{overall}$ using its definitions of thrust specific fuel consumption.

$$\eta_{overall} = \frac{v}{TSFC \cdot LHV} \qquad \text{Eq 24}$$

Where v represents the flight velocity, TSFC represents the thrust specific fuel consumption (TSFC), as defined in the BADA manual as shown in the equation below.

$$TFSC = a_1 \left(1 + 1.944 \frac{v}{a_2}\right) \qquad \text{Eq 25}$$

Where a_1 and a_2 are coefficients defined in the BADA dataset for each of the different aircraft.

The propulsive efficiency is calculated using thermodynamic definitions for gas turbine engines.

$$\eta_{prop} = \frac{2v}{v + v_j} \qquad \text{Eq 26}$$

Where v_j is the jet velocity, which is derived using eq 6.9 from Cumpsty and Heyes (2015).

$$v_j = \sqrt{2\, c_p\, T_{t19} \left(1 - \frac{P_{amb}}{P_{t19}}\right)^{\gamma - \frac{1}{\gamma}}} \qquad \text{Eq 27}$$

Where T_{t19} and P_{t19} represent the total temperature and pressure at the fan exit, and γ represents the ratio of specific heats of air, taken as 1.4. P_{t19} is defined by

$$P_{t19} = P_{t2}\, \Pi_f \qquad \text{Eq 28}$$

where Π_f represents the overall pressure ratio of the fan, which is linearly interpolated between an assume 1.8 in 1980, and 1.5 in 2019. We perform a sensitivity study and find that the engine thermal efficiency is not sensitive to Π_f and changing from a value of 1.5 to 1.8, causes only a 2-3 percentage points difference on thermal efficiency.

P_{t2} is defined by the relationship

$$P_{t2} = P_{amb}\left(1 + \frac{\gamma - 1}{2} M^2\right)^{\frac{\gamma}{\gamma-1}} \qquad \text{Eq 29}$$

Similarly, T_{t19} is defined by

$$T_{t19} = T_{t2}\, \Pi_f^{\frac{\gamma-1}{\gamma}\eta_{fan}} \qquad \text{Eq 30}$$

Where η_{fan} is taken as unity in line with Cumpsty and Heyes (2015).

Finally, T_{t2} is definded by the relationship.

$$T_{t2} = T_{amb}\left(1 + \frac{\gamma - 1}{2} M^2\right) \qquad \text{Eq 31}$$

Where the Mach number, M, is derived from the flight speed, and ambient air conditions as given by

$$M = \frac{v}{\sqrt{\frac{\gamma\, R\, T}{M_{air}}}} \qquad \text{Eq 32}$$

Where M_{air} represents the molar mass of air, taken here as 28.97 g/mol.

Appendix D APMT-IC: Physical and Monetary Damage

Monetization of the physical damages due to temperature change forms the final component of the APMT-IC model. There are three major steps for quantifying the monetary damages in terms of the Net Present Value (NPV). Firstly, damage functions are used to estimate the climate impacts due to a temperature change as a percentage of GDP. The dollar values of these damages are quantified using GDP forecasts. Finally, the NPV of damages is calculated by discounting future damages to social costs today.

The framework for damage functions was developed in the Dynamic Integrated model of Climate and the Economy (DICE) (Nordhaus and Boyer, 2000), where climate damages were estimated as a percentage of GDP due to predicted changes in temperature. Nordhaus and Boyer based their assessment of damages on valuations of climate impact estimates in six major categories: agriculture, sea level rise, health, human settlements and ecosystems, other market sections affected by climate change, and non-market impact. They also account for the possibility of catastrophic climate change impacts and add 25% for any sectors not quantified by their damages estimations.

Estimates of the damages as a percentage of GDP are calculated using Eq 33, which incorporates both a linear sum and a quadratic sum of the temperature change to allow for the non-linearities in quantifying the climate damages.

$$D_k(t) = \frac{a_{1,k}\Delta\mathrm{T}(t) + a_{2,k}\Delta\mathrm{T}(t)^2}{1 + a_{1,k}\Delta\mathrm{T}(t) + a_{2,k}\Delta\mathrm{T}(t)^2} \qquad \text{Eq 33}$$

In Eq 33, ΔT is the temperature increase relative to preindustrial levels. The damage function requires two coefficients to be estimated, $a_{1,k}$ and $a_{2,k}$. For Chapter 4, damage function coefficients are taken from Nordhaus (2017). For Chapter 5, and updated climate costs of marginal emissions presented in Appendix F, damage function values are taken from Howard and Sterner (2017). Table 14 tabulates the parameter values. The coefficients are assumed to be normally distributed with standard deviation, σ.

Table 14: Values used within the damage functions

Coefficient	Values based on Nordhaus (2017)	Values based on Howard and Sterner (2017)
$a_{1,k}\left[\text{fraction}\frac{GDP}{K}\right] \times 10^{-3}$	0	-
$a_{2,k}\left[\text{fraction}\frac{GDP}{K^2}\right] \times 10^{-3}$	2.36	-
σ [fraction GDP] $\times 10^{-3}$	1.18	-

To convert the climate damages from a percentage of GDP to monetized estimates, the result from Eq 33 is multiplied by forecasts of GDP. GDP projections are provided by the OECD global reference Shared Socio-economic Pathways (SSPs) (Dellink et al., 2017). The SSPs allow for the development of a range of forecasts or "storylines" based on a society's ability to mitigate or adapt to the impacts of climate change (Dellink et al., 2017). The SSP scenarios are defined in 2005 USD-values. APMT-IC uses the World Bank GDP deflator to adjust the price levels.

Appendix E Supplementary results for Chapter 4

Table 15: Full Flight Results

		Climate					Air Quality	
		2% Disc. Rate	2.5% Disc. Rate	3% Disc. Rate	5% Disc. Rate	7% Disc. Rate	3% Disc. Rate Country Specific VSL	3% Disc. Rate Global Average VSL
CO_2	[$/tonne CO_2]	95 (14, 250)	62 (9.3, 160)	45 (6.7, 120)	17 (2.7, 44)	9.4 (1.5, 23)	N/A	N/A
NO_x: CH_4	[$/tonne NO_x as NO_2]	-2600 (-7000, -370)	-2200 (-5900, -330)	-2000 (-5100, -290)	-1300 (-3300, -210)	-960 (-2400, -150)	N/A	N/A
NO_x: O_3 Short	[$/tonne NO_x as NO_2]	2900 (380, 8200)	2600 (350, 7100)	2400 (330, 6500)	1900 (280, 5000)	1700 (260, 4300)	N/A	N/A
NO_x: O_3 Long	[$/tonne NO_x as NO_2]	-850 (-2300, -110)	-730 (-2000, -96)	-640 (-1700, -85)	-430 (-1100, -60)	-310 (-800, -45)	N/A	N/A
NO_x: Nitrate Aerosols	[$/tonne NO_x as NO_2]	-850 (-2400, -110)	-760 (-2100, -99)	-690 (-1900, -93)	-560 (-1500, -80)	-490 (-1300, -72)	N/A	N/A
NO_x: Total	[$/tonne NO_x as NO_2]	-1400 (-3700, -190)	-1100 (-3000, -150)	-910 (-2500, -120)	-360 (-1200, 22)	-66 (-620, 340)	23000 (3500, 72000)	22000 (3400, 71000)
Contrail-Cirrus	[$/tonne Fuel Burn]	100 (12, 290)	89 (11, 250)	82 (10, 230)	66 (8.7, 180)	58 (7.8, 150)	N/A	N/A
Contrail-Cirrus	[$/Flight km]	0.28 (0.032, 0.81)	0.25 (0.03, 0.7)	0.23 (0.028, 0.64)	0.19 (0.024, 0.5)	0.16 (0.022, 0.43)	N/A	N/A
Fuel Sulfur	[$/tonne S]	-21000 (-60000, -2800)	-19000 (-52000, -2500)	-18000 (-47000, -2400)	-14000 (-37000, -2100)	-12000 (-31000, -1900)	30000 (4700, 100000)	31000 (4800, 110000)
BC	[$/tonne BC]	58000 (7800, 160000)	52000 (7200, 140000)	47000 (6800, 130000)	39000 (5900, 98000)	34000 (5300, 83000)	14000 (1800, 44000)	12000 (1600, 41000)
H_2O	[$/tonne H_2O]	95 (14, 250)	62 (9.3, 160)	45 (6.7, 120)	17 (2.7, 44)	1.8 (0.28, 4.4)	0 (0, 0)	0 (0, 0)
NMVOC	[$/tonne HC]	N/A	N/A	N/A	N/A	N/A	7700 (1100, 21000)	5200 (830, 17000)
CO	[$/tonne CO]	N/A	N/A	N/A	N/A	N/A	290 (43, 860)	230 (36, 770)
OC	[$/tonne OC]	N/A	N/A	N/A	N/A	N/A	11000 (1500, 37000)	9800 (1400, 34000)
Total	[$/tonne Fuel Burn]	370 (53, 990)	260 (38, 700)	200 (30, 530)	110 (16, 290)	82 (12, 210)	360 (56, 1200)	350 (55, 1100)

Table 16: Cruise Results with Uncertainty

		Climate					Air Quality	
		2% Disc. Rate	2.5% Disc. Rate	3% Disc. Rate	5% Disc. Rate	7% Disc. Rate	3% Disc. Rate Country Specific VSL	3% Disc. Rate Global Average VSL
CO_2	[\$/tonne CO_2]	95 (14, 250)	62 (9.3, 160)	45 (6.7, 120)	17 (2.7, 44)	9.4 (1.5, 23)	N/A	N/A
NO_x: CH_4	[\$/tonne NO_x as NO_2]	-2900 (-7800, -420)	-2500 (-6600, -370)	-2200 (-5700, -330)	-1500 (-3700, -230)	-1100 (-2600, -170)	N/A	N/A
NO_x: O_3 Short	[\$/tonne NO_x as NO_2]	3300 (430, 9200)	2900 (390, 8000)	2700 (370, 7200)	2200 (320, 5600)	1900 (290, 4800)	N/A	N/A
NO_x: O_3 Long	[\$/tonne NO_x as NO_2]	-950 (-2600, -120)	-810 (-2200, -110)	-720 (-1900, -96)	-480 (-1300, -67)	-350 (-900, -50)	N/A	N/A
NO_x: Nitrate Aerosols	[\$/tonne NO_x as NO_2]	-860 (-2400, -110)	-760 (-2100, -100)	-700 (-1900, -94)	-570 (-1500, -81)	-500 (-1300, -73)	N/A	N/A
NO_x: Total	[\$/tonne NO_x as NO_2]	-1400 (-3900, -200)	-1200 (-3100, -160)	-940 (-2600, -120)	-340 (-1200, 54)	-20 (-590, 460)	21000 (3300, 69000)	21000 (3400, 70000)
Contrail-Cirrus	[\$/tonne Fuel Burn]	110 (13, 320)	100 (12, 280)	92 (11, 260)	75 (9.8, 200)	66 (8.9, 170)	N/A	N/A
Fuel Sulfur	[\$/tonne S]	-24000 (-67000, -3100)	-21000 (-58000, -2800)	-20000 (-53000, -2700)	-16000 (-41000, -2300)	-14000 (-35000, -2100)	30000 (4700, 100000)	32000 (4900, 110000)
BC	[\$/tonne BC]	64000 (8600, 180000)	57000 (8000, 150000)	52000 (7500, 140000)	43000 (6500, 110000)	37000 (5800, 92000)	7000 (980, 25000)	7200 (1000, 25000)
H_2O	[\$/tonne H_2O]	3.5 (0.48, 9.6)	3.1 (0.44, 8.4)	2.8 (0.41, 7.5)	2.3 (0.36, 5.9)	2 (0.32, 5)	N/A	N/A
NMVOC	[\$/tonne HC]	N/A	N/A	N/A	N/A	N/A	2300 (360, 7300)	2100 (340, 7000)
CO	[\$/tonne CO]	N/A	N/A	N/A	N/A	N/A	200 (31, 630)	180 (28, 610)
OC	[\$/tonne OC]	N/A	N/A	N/A	N/A	N/A	7000 (980, 25000)	7200 (1000, 25000)
Total	[\$/tonne Fuel Burn]	380 (54, 1000)	270 (39, 720)	210 (31, 560)	120 (18, 310)	90 (13, 230)	340 (53, 1100)	340 (54, 1100)

Table 17: Landing and Take-off Results with Uncertainty

		Climate					Air Quality	
		2% Disc. Rate	2.5% Disc. Rate	3% Disc. Rate	5% Disc. Rate	7% Disc. Rate	3% Disc. Rate Country Specific VSL	3% Disc. Rate Global Average VSL
CO_2	[\$/tonne CO_2]	95 (14, 250)	63 (9.2, 160)	45 (6.7, 120)	17 (2.7, 44)	9.5 (1.5, 23)	N/A	N/A
NO_x: CH_4	[\$/tonne NO_x as NO_2]	-550 (-1500, -78)	-470 (-1200, -68)	-410 (-1100, -61)	-270 (-690, -42)	-200 (-490, -32)	N/A	N/A
NO_x: O_3 Short	[\$/tonne NO_x as NO_2]	390 (54, 1100)	350 (49, 940)	320 (46, 850)	260 (40, 660)	230 (36, 560)	N/A	N/A
NO_x: O_3 Long	[\$/tonne NO_x as NO_2]	-180 (-490, -26)	-160 (-410, -23)	-140 (-360, -20)	-91 (-230, -14)	-66 (-160, -11)	N/A	N/A
NO_x: Nitrate Aerosols	[\$/tonne NO_x as NO_2]	-440 (-1300, -47)	-400 (-1100, -43)	-360 (-1000, -41)	-300 (-810, -35)	-260 (-690, -32)	N/A	N/A
NO_x: Total	[\$/tonne NO_x as NO_2]	-780 (-2200, -100)	-670 (-1800, -91)	-590 (-1600, -81)	-400 (-1100, -55)	-290 (-780, -40)	37000 (5200, 110000)	26000 (4000, 89000)
Contrail-Cirrus	[\$/tonne Fuel Burn]	0	0	0	0	0	N/A	N/A
Fuel Sulfur	[\$/tonne S]	-3200 (-8900, -410)	-2800 (-7700, -380)	-2600 (-7000, -360)	-2100 (-5500, -310)	-1800 (-4600, -280)	32000 (4300, 99000)	24000 (3400, 85000)
BC	[\$/tonne BC]	22000 (2300, 65000)	20000 (2100, 57000)	18000 (2000, 52000)	15000 (1700, 41000)	13000 (1500, 35000)	66000 (8400, 200000)	45000 (6300, 160000)
H_2O	[\$/tonne H_2O]	0	0	0	0	0	N/A	N/A
NMVOC	[\$/tonne HC]	N/A	N/A	N/A	N/A	N/A	19000 (2700, 52000)	12000 (1900, 40000)
CO	[\$/tonne CO]	N/A	N/A	N/A	N/A	N/A	520 (76, 1500)	360 (56, 1200)
OC	[\$/tonne OC]	N/A	N/A	N/A	N/A	N/A	110000 (13000, 310000)	66000 (9200, 230000)
Total	[\$/tonne Fuel Burn]	290 (42, 770)	190 (28, 490)	130 (20, 340)	49 (7.7, 120)	26 (4.1, 63)	590 (84, 1700)	430 (65, 1400)

Table 18: Regional Full Flight Results (3% Discount Rate)

		Country Specific VSL				Global Average VSL			
		Asia-Pacific	European	North American	USA	Asia-Pacific	European	North American	USA
NO_x	[\$/tonne NO_x as NO_2]	21000 (3300, 71000)	34000 (5200, 100000)	23000 (3500, 72000)	24000 (3700, 75000)	22000 (3500, 73000)	29000 (4500, 95000)	21000 (3300, 70000)	22000 (3400, 71000)
Fuel Sulfur	[\$/tonne S]	26000 (4000, 90000)	43000 (6500, 140000)	30000 (4700, 100000)	32000 (4900, 110000)	28000 (4300, 95000)	41000 (6300, 140000)	30000 (4700, 100000)	32000 (4900, 110000)
BC	[\$/tonne BC]	15000 (2000, 52000)	25000 (3200, 75000)	12000 (1600, 37000)	14000 (1900, 43000)	15000 (2200, 54000)	18000 (2500, 62000)	8500 (1200, 30000)	9200 (1300, 32000)
NMVOC	[\$/tonne HC]	6400 (950, 20000)	20000 (2700, 54000)	4100 (620, 12000)	4400 (660, 13000)	6100 (970, 20000)	11000 (1700, 37000)	3000 (480, 9900)	3200 (500, 10000)
CO	[\$/tonne CO]	260 (38, 860)	500 (73, 1400)	260 (39, 790)	270 (41, 830)	250 (37, 850)	340 (53, 1100)	210 (32, 700)	220 (33, 720)
OC	[\$/tonne OC]	9600 (1300, 34000)	22000 (2900, 68000)	10000 (1400, 33000)	11000 (1600, 36000)	10000 (1400, 35000)	16000 (2300, 57000)	8100 (1100, 28000)	8700 (1200, 30000)
Total	[\$/tonne Fuel Burn]	350 (53, 1200)	550 (83, 1700)	330 (51, 1000)	350 (55, 1100)	360 (57, 1200)	460 (73, 1500)	300 (48, 1000)	320 (51, 1100)

Table 19: Regional Cruise Results (3% Discount Rate)

		Country Specific VSL				Global Average VSL			
		Asia-Pacific	European	North American	USA	Asia-Pacific	European	North American	USA
NO_x	[\$/tonne NO_x as NO_2]	19000 (2900, 62000)	31000 (4700, 96000)	23000 (3600, 75000)	24000 (3800, 78000)	20000 (3100, 65000)	28000 (4400, 93000)	23000 (3600, 74000)	23000 (3700, 77000)
Fuel Sulfur	[\$/tonne S]	25000 (3900, 87000)	42000 (6400, 140000)	31000 (4800, 110000)	33000 (5100, 110000)	27000 (4100, 91000)	42000 (6400, 140000)	33000 (5000, 110000)	35000 (5300, 120000)
BC	[\$/tonne BC]	5700 (790, 20000)	11000 (1500, 38000)	7200 (1000, 25000)	7400 (1000, 26000)	6100 (860, 22000)	11000 (1500, 38000)	7300 (1000, 25000)	7400 (1000, 26000)
NMVOC	[\$/tonne HC]	2000 (300, 6300)	3200 (490, 9800)	2400 (370, 7400)	2400 (370, 7500)	1900 (300, 6300)	2800 (440, 9100)	2200 (340, 7100)	2200 (340, 7200)
CO	[\$/tonne CO]	180 (27, 580)	270 (40, 820)	220 (33, 680)	220 (34, 690)	170 (26, 570)	230 (35, 760)	190 (30, 640)	200 (30, 650)
OC	[\$/tonne OC]	5700 (790, 20000)	11000 (1500, 38000)	7200 (1000, 25000)	7400 (1000, 26000)	6100 (860, 22000)	11000 (1500, 38000)	7300 (1000, 25000)	7400 (1000, 26000)
Total	[\$/tonne Fuel Burn]	310 (48, 1000)	480 (74, 1500)	330 (52, 1100)	360 (56, 1200)	320 (51, 1100)	450 (70, 1500)	320 (51, 1100)	350 (55, 1100)

Table 20: Regional Landing and Take-off Results (3% Discount Rate)

		Country Specific VSL				Global Average VSL			
		Asia-Pacific	European	North American	USA	Asia-Pacific	European	North American	USA
NO$_x$	[$/tonne NO$_x$ as NO$_2$]	44000 (6400, 150000)	67000 (8600, 180000)	18000 (2500, 48000)	20000 (2800, 53000)	46000 (7100, 160000)	35000 (5100, 120000)	8300 (1300, 27000)	8900 (1400, 29000)
Fuel Sulfur	[$/tonne S]	37000 (5000, 130000)	52000 (6600, 150000)	20000 (2600, 57000)	24000 (3000, 66000)	38000 (5400, 130000)	32000 (4400, 110000)	8700 (1300, 30000)	10000 (1400, 35000)
BC	[$/tonne BC]	83000 (11000, 280000)	120000 (14000, 320000)	41000 (5000, 110000)	50000 (6000, 140000)	82000 (12000, 290000)	64000 (9000, 220000)	16000 (2300, 56000)	19000 (2700, 67000)
NMVOC	[$/tonne HC]	18000 (2600, 55000)	56000 (7400, 150000)	7400 (1000, 20000)	8000 (1100, 21000)	17000 (2700, 55000)	29000 (4400, 97000)	4500 (700, 15000)	4700 (740, 15000)
CO	[$/tonne CO]	480 (63, 1600)	1100 (150, 2800)	380 (54, 1100)	400 (56, 1100)	450 (62, 1600)	600 (95, 2000)	250 (38, 830)	260 (39, 860)
OC	[$/tonne OC]	110000 (15000, 380000)	190000 (23000, 530000)	60000 (7200, 170000)	76000 (9100, 210000)	110000 (16000, 390000)	100000 (14000, 360000)	23000 (3300, 82000)	29000 (4100, 100000)
Total	[$/tonne Fuel Burn]	720 (100, 2400)	1100 (150, 3100)	280 (39, 730)	320 (44, 830)	760 (120, 2600)	600 (88, 2100)	130 (20, 420)	140 (22, 470)

E.1.1. Air Quality Discount Rate Adjustments

As indicated, the air quality presented in Table 15 to Table 17 are derived using a 3% discount rate. Air quality results can be adjusted for a 2% and 7% discount rates by multiplying these above air quality results by 1.0311 and 0.9007, respectively. These differences are caused by the cessation lag between exposure and mortalities.

E.1.2. CAQSC cost of fuel burn

Table 21: CAQSC cost of fuel burn in different flight phases (USD/Tonne Fuel Burn in 2015) (3% discount rate)

	Landing and Take-off			Cruise			Full Flight		
	Climate	Air Quality	Total	Climate	Air Quality	Total	Climate	Air Quality	Total
CO_2	140 (21, 370)	N/A	140 (21, 370)	140 (21, 360)	N/A	140 (21, 360)	140 (21, 360)	N/A	140 (21, 360)
NO_x	-9 (-24, -1.2)	560 (79, 1600)	550 (70, 1600)	-14 (-38, -1.9)	320 (50, 1000)	300 (35, 1000)	-14 (-37, -1.8)	340 (52, 1100)	330 (38, 1100)
Contrail-Cirrus*	0	0	0	92 (11, 260)	N/A	92 (11, 260)	82 (10, 230)	N/A	82 (10, 230)
Fuel Sulfur	-1.6 (-4.2, -0.22)	19 (2.6, 59)	18 (0.92, 58)	-12 (-32, -1.6)	18 (2.8, 62)	6.3 (-18, 52)	-11 (-28, -1.4)	18 (2.8, 62)	7.6 (-15, 53)
BC	0.89 (0.096, 2.6)	3.2 (0.42, 9.6)	4.1 (0.98, 11)	1.8 (0.26, 4.9)	0.25 (0.034, 0.87)	2.1 (0.48, 5.2)	1.7 (0.25, 4.5)	0.5 (0.067, 1.6)	2.2 (0.6, 5.3)
H_2O	0	0	0	3.5 (0.51, 9.3)	N/A	3.5 (0.51, 9.3)	3.1 (0.45, 8.2)	N/A	3.1 (0.45, 8.2)
NMVOC	N/A	11 (1.6, 31)	11 (1.6, 31)	N/A	0.27 (0.042, 0.85)	0.27 (0.042, 0.85)	N/A	1.2 (0.17, 3.4)	1.2 (0.17, 3.4)
CO	N/A	4.3 (0.62, 12)	4.3 (0.62, 12)	N/A	0.39 (0.06, 1.2)	0.39 (0.06, 1.2)	N/A	0.72 (0.11, 2.1)	0.72 (0.11, 2.1)
OC	N/A	0.77 (0.098, 2.2)	0.77 (0.098, 2.2)	N/A	0.11 (0.015, 0.37)	0.11 (0.015, 0.37)	N/A	0.16 (0.022, 0.53)	0.16 (0.022, 0.53)
Total Cost	130 (20, 340)	590 (84, 1700)	730 (180, 1900)	210 (31, 560)	340 (53, 1100)	550 (170, 1400)	200 (30, 530)	360 (56, 1200)	560 (180, 1400)

Table 22: CAQSC cost of full flight fuel burn (USD/Tonne Fuel Burn in 2015) for 2% and 7% discount rates

	2% Discount Rate			7% Discount Rate		
	Climate	Air Quality	Total	Climate	Air Quality	Total
CO_2	300 (44, 790)	N/A	300 (44, 790)	30 (4.8, 73)	N/A	30 (4.8, 73)
NO_x	-21 (-55, -2.9)	350 (54, 1100)	330 (32, 1100)	-1 (-9.3, 5.1)	310 (47, 980)	300 (46, 970)
Contrail-Cirrus*	100 (12, 290)	N/A	100 (12, 290)	58 (7.8, 150)	N/A	58 (7.8, 150)
Fuel Sulfur	-13 (-36, -1.7)	19 (2.9, 64)	5.9 (-21, 53)	-7.5 (-19, -1.1)	16 (2.5, 56)	8.9 (-8.4, 49)
BC	2.1 (0.28, 5.8)	0.51 (0.069, 1.7)	2.6 (0.66, 6.5)	1.2 (0.19, 3)	0.45 (0.06, 1.4)	1.7 (0.5, 3.7)
H_2O	3.8 (0.52, 10)	N/A	3.8 (0.52, 10)	2.2 (0.35, 5.4)	N/A	2.2 (0.35, 5.4)
NMVOC	N/A	1.2 (0.18, 3.5)	1.2 (0.18, 3.5)	N/A	1.1 (0.16, 3)	1.1 (0.16, 3)
CO	N/A	0.74 (0.11, 2.2)	0.74 (0.11, 2.2)	N/A	0.65 (0.097, 1.9)	0.65 (0.097, 1.9)
OC	N/A	0.17 (0.023, 0.54)	0.17 (0.023, 0.54)	N/A	0.15 (0.02, 0.48)	0.15 (0.02, 0.48)
Total Cost	370 (53, 990)	370 (57, 1200)	740 (240, 1800)	82 (12, 210)	320 (50, 1000)	410 (110, 1100)

E.2. Climate Yearly Growth of Metrics

The magnitude of climate damages per unit of emission increases with time, given the middle of the road RCP 4.5 and SSP 1 scenarios used in Chapter 4. These growth rates are calculated by using APMT-IC to calculate the marginal costs per unit of emissions for emissions pulses in 2025, 2035, 2045, and 2055 for each discount rate. Subsequently a growth rate r is calculated for each forcer by using the derived cost data to perform a least-squares fit to the functional form of Eq 34.

$$NPV_{t=2015+\Delta t} = NPV_{2015}(1+r)^{\Delta t} \qquad \text{Eq 34}$$

In this equation, NPV_{2015} represents the marginal climate cost in 2015 and $NPV_{t=2015+\Delta t}$ represents the marginal climate costs due to an emissions pulse Δt years after 2015.

Table 23 shows the derived annual growth rate for each species under three different discount rates. These growth rates can be used along with Eq 34 to adjust the climate cost metrics presented in Section Appendix E for emissions in future years. To calculate the impact of future emissions of NO_x, the impact of the individual NO_x components must be computed individually and summed for the overall NO_x impact.

Table 23: Climate impact annual growth by species.

	2% Discount Rate	3% Discount Rate	7% Discount Rate
CO_2	1.6%	2.1%	3.2%
NO_x: CH_4	3.5%	3.8%	4.3%
NO_x: O_3 Short	4.3%	4.7%	5.0%
NO_x: O_3 Long	3.5%	3.8%	4.3%
NO_x: Nitrate Aerosols	4.3%	4.7%	5.0%

Contrail Cirrus	4.3%	4.7%	5.0%
Sulfates	4.3%	4.7%	5.0%
Black Carbon	4.3%	4.7%	5.0%
H_2O	4.3%	4.7%	5.0%

The growth rates in Table 23 show increasing marginal costs of emissions pulses in future years. This observed increase in the magnitude of marginal costs is driven by three factors. The first is a combination of increasing background temperature change under the RCP 4.5 scenario and the non-linear DICE damage function. As background temperature change increases, total damages increase approximately quadratically. As a result, the same amount of marginal temperature change will result in higher marginal damages as time passes, because of background temperature change increases. Secondly global GDP increases with time under SSP 1 scenario. Because damages are computed as a fraction of global GDP, as the GDP increases, so do the calculated damages, even if the temperature change remains constant. Third, for CO_2, the accumulation of CO_2 in the atmosphere with time under the RCP 4.5 scenario leads to slower removal of a marginal pulse of CO_2. This leads to more warming and more subsequent damage per unit of marginal CO_2 as time increases.

E.3. Sensitivity to RCP and SSP Scenario

Climate results presented in Table 15 to Table 22 are derived using RCP 4.5 and SSP 1 scenarios, which both represent middle of the road scenarios. Sensitivity to alternative scenarios is evaluated by computing climate results for alternative emissions and socio-economic scenarios, such as low and high RCP and SSP scenarios.

Table 24 presents changes to results under RCP 2.6 and RCP 8.5, representing low and high background emissions scenarios, respectively. Higher background CO_2 emissions lead to longer lasting aviation CO_2, in turn which leads to a decrease in the radiative forcing due to an extra unit of CO_2, however, increased background emissions also increase the background temperature change, which increases the marginal climate damages. On net, an increase in background emissions leads to an increase in damages for a warming forcer, and an increase in benefit for cooling forcers as illustrated by Table 24.

Table 25 presents changes to results under SSP 3 and SSP 5 scenarios representing low and high socio-economic scenarios, respectively.

Table 24: Climate model Sensitivity to RCP Scenario

	RCP 2.6 (Low Emission Scenario)			RCP 8.5 (High Emission Scenario)		
	2% DR	3% DR	7% DR	2% DR	3% DR	7% DR
CO_2	-25%	-18%	-7%	11%	14%	9%
NO_x: CH_4	-10%	-7%	-3%	17%	12%	7%
NO_x: O_3 Short	-7%	-3%	0%	13%	8%	3%
NO_x: O_3 Long	-10%	-7%	-3%	17%	12%	7%
NO_x: Nitrate Aerosols	-7%	-3%	0%	13%	8%	3%
NO_x: Total	-15%	-15%	-58%	22%	21%	75%
Contrail-Cirrus	-7%	-3%	0%	13%	8%	3%
Sulfur Impact	-7%	-3%	0%	13%	8%	3%
BC	-7%	-3%	0%	13%	8%	3%
H_2O	-7%	-3%	0%	13%	8%	3%
Total	-21%	-13%	-2%	11%	11%	4%

Table 25: Climate model Sensitivity to SSP Scenario

	SSP 3 (Low Socio-Economic Scenario)			SSP 5 (High Socio-Economic Scenario)		
	2% DR	3% DR	7% DR	2% DR	3% DR	7% DR
CO_2	-42%	-39%	-23%	79%	53%	19%
NO_x: CH4	-24%	-20%	-13%	27%	18%	9%
NO_x: O3 Short	-14%	-9%	-4%	23%	11%	3%
NO_x: O3 Long	-24%	-20%	-13%	27%	18%	9%
NO_x: Nitrate Aerosols	-14%	-9%	-4%	23%	11%	3%
NO_x: Total	-38%	-41%	-169%	33%	31%	119%
Contrail-Cirrus	-14%	-9%	-4%	23%	11%	3%
Sulfur Impact	-14%	-9%	-4%	23%	11%	3%
BC	-14%	-9%	-4%	23%	11%	3%
H_2O	-14%	-9%	-4%	23%	11%	3%
Total	-36%	-28%	-9%	68%	39%	8%

E.4. CO_2 Equivalent Climate Results per Unit of Fuel Burn

In this section, cost metrics are presented on a CO_2 equivalent per unit of fuel burn basis, in the form of a Net Present Value (NPV) ratio. The NPV ratios are calculated using the mathematical expression

$$\text{NPV Ratio} = \frac{\text{NPV}_{\text{X,per unit fuel burn}}}{\text{NPV}_{\text{CO}_2\text{,per unit fuel burn}}} \qquad \text{Eq 35}$$

where $\text{NPV}_{\text{X,per unit fuel burn}}$ represents the climate cost or benefit of emissions species X per unit of fuel burn, and $\text{NPV}_{\text{CO}_2\text{,per unit fuel burn}}$ represents the climate cost/benefit of CO_2 for a unit of fuel burn. Therefore, these ratios represent the relative importance of each of the short-lived climate forcers to the importance of CO_2 for each unit of fuel burn.

For this chapter, these results are derived by applying Eq 35 to each Monte Carlo simulation, and then the mean, and 5th and 9th percentile values are found from the set of 100,000 Monte Carlo simulations. Table 26 presents the results for the mean, 5th and 95th percentile of the NPV ratios.

Table 26: Climate Cost Metrics on a CO_2 equivalent per unit of fuel burn basis (Present Study)

	2% Discount Rate	3% Discount Rate	7% Discount Rate
CO_2	1.00 (1.00, 1.00)	1.00 (1.00, 1.00)	1.00 (1.00, 1.00)
NO_x	-0.07 (-0.10, -0.04)	-0.09 (-0.15, -0.05)	-0.03 (-0.24, 0.14)
Contrails*	0.33 (0.16, 0.53)	0.58 (0.28, 0.92)	1.95 (0.96, 3.08)
Fuel Sulfur	-0.04 (-0.06, -0.03)	-0.07 (-0.11, -0.05)	-0.25 (-0.36, -0.16)
BC	0.01 (0.00, 0.01)	0.01 (0.01, 0.01)	0.04 (0.03, 0.05)
H_2O	0.01 (0.01, 0.02)	0.02 (0.02, 0.03)	0.07 (0.06, .09)
Total Fuel Burn	1.24 (1.07, 1.43)	1.44 (1.15, 1.78)	2.77 (1.77, 3.92)

* Contrails include contrail-cirrus

These metrics correspond to the metrics presented in Table 2 in Dorbian et al. (2011). However, low and high results in Dorbian et al. (2011) are presented for low and high lens assumptions, and not by Monte Carlo Simulation.

For ease of comparison, the results presented in Dorbian et al. (2011) are presented in Table 17. The Dorbian et al. (2011) contrail and the total fuel burn results fall within our contrail uncertainty range, however NO_x, fuel sulfur, BC, H_2O fall outside our uncertainty range. Both Dorbian et al.

(2011)'s results and results from this thesis were derived using the same climate model (APMT-IC).

Table 27: Cost Metrics presented in Dorbian et al. (2011) on a CO_2 equivalent per unit of fuel burn basis. The values between the brackets represent model assumptions for low and high climate damages for both the numerator (the short-lived climate forcer) and the denominator (CO_2)

	2% Discount Rate	3% Discount Rate	7% Discount Rate
CO_2	1.00 (1.00, 1.00)	1.00 (1.00, 1.00)	1.00 (1.00, 1.00)
NO_x	-0.03 (-0.05, -0.03)	-0.03 (-0.06, -0.03)	0.18 (0.07, 0.15)
Contrails*	0.42 (0.1, 0.56)	0.74 (0.19, 1.06)	2.28 (0.62, 3.56)
Fuel Sulfur	-0.11 (-0.27, -0.01)	-0.2 (-0.51, -0.01)	-0.61 (-1.65, -0.03)
BC	0.08 (0.01, 0.14)	0.14 (0.01, 0.25)	0.43 (0.03, 0.85)
H_2O	0.07 (0.00, 0.13)	0.13 (0.01, 0.25)	0.41 (0.02, 0.83)
Total Fuel Burn	1.4 (0.8, 1.8)	1.8 (0.6, 0.25)	3.7 (0.1, 6.4)

* Contrails includes contrail-cirrus

The differences in results can be explained by changes in short-lived climate forcer uncertainty distributions. Table 18 shows the radiative forcing estimates for aviation used in Chapter 4, as well as in Dorbian et al. (2011). Changes in these estimates are due updated radiative estimates derived by the ACCRI phase two research initiative (Brasseur et al. 2016). Results for the overall total fuel burn remain similar because it is driven by the largest cost contributors, CO_2 and contrails, for which the uncertainty distributions have remained stable.

Table 28: Comparison of RF Uncertainty Distributions

Forcer	Chapter 4 Based on Brasseur et al. (2016)	Dorbian et al. (2011)
Contrails (and Contrail Cirrus)	37.9 (12.4 to 80)	33, (12.5 to 86.7)
Fuel Sulfur	-4.8 (-3 to -9)	-4.8, (-0.79 to -29.3)
BC	0.6 to 1 (Uniform Distribution)	3.4 (0.56 to 20.7)
H_2O	1.3 to 2 (Uniform Distribution)	2.8 (0.39 to 20.3)
Nitrates (One of four indirect NO_x impacts included in the climate model)	-7.5 to -3 (Uniform Distribution)	Not included

E.5. Results – Percentage $PM_{2.5}$ vs Ozone Impact

Table 29 presents the percentage of the total air quality impact arising from the $PM_{2.5}$ emission to impact pathway. The remainder of the impact arises from the population exposure to ozone.

In all flight phases, and for all species except CO, we find the $PM_{2.5}$ impact pathway the largest contributor to costs. Per unit fuel burn we find the $PM_{2.5}$ impact pathway to be responsible for 63% of the overall costs in full flight, similar to Eastham and Barrett (2016) who find an overall percentage of 58% mortalities from $PM_{2.5}$, and the remainder from ozone related impacts. In the LTO flight phase we find the $PM_{2.5}$ impact pathway to be responsible for 80% of the impact, and 60% in cruise.

Table 29: $PM_{2.5}$ Impact as a percentage of overall impact.

	Full Flight	LTO	Cruise
NO_x	62%	80%	59%
Sulfur Impact	80%	98%	79%
BC	100%	100%	100%
NMVOC	67%	71%	53%
CO	39%	39%	38%
OC	100%	100%	100%
Total Cost Per unit fuel burn	63%	80%	60%

E.6. Marginal and Average Costs

Due to non-linearities involved in both climate and air quality impacts, the marginal cost, which is the cost due to an additional unit of emission, differs from the average cost of a unit of anthropogenic emission. In line with the purpose of this chapter, we present marginal cost metrics, which are applicable to evaluate the impact of marginal emissions interventions. However, this approach is not appropriate when quantifying aviation's contribution to the total anthropogenic damages. To illustrate, we present an example based on the climate damage function.

The climate results are derived using a nonlinear damage function defined by Nordhaus (2017). Using this damage function, total damages due to anthropogenic emissions is calculated using Eq 36.

$$\mathrm{D}(\Delta \mathrm{T}_{\mathrm{all}}) = \frac{a\Delta T_{all}^2}{a\Delta T_{all}^2 + 1} \qquad \text{Eq 36}$$

Where ΔT_{all} is the temperature increase from preindustrial conditions and a represents the damage function coefficient defined as discussed in Section Appendix D.

The damages due to an average unit of background emission can be calculated by attributing a portion of the total damages to the unit of background emissions, for instance on a CO_2 equivalent emissions basis, or on a temperature change basis.

In contrast, the damages due to an additional unit of emissions, i.e., marginal damages, are estimated using

$$\mathrm{D_{Marginal}}(\Delta\mathrm{T_{all}}, \Delta\mathrm{T}) = \mathrm{D}(\Delta\mathrm{T_{all}}) - \mathrm{D}(\Delta\mathrm{T_{all}} - \Delta\mathrm{T}) \qquad \text{Eq 37}$$

While the marginal approach remains valid to evaluate the impact of emissions interventions, it would not accurately capture the total damages due to anthropogenic emissions if each sector is treated individually. Or put differently, if this same marginal approach (Eq 37) is used to calculate the impacts from all sectors individually, the damages from the sum of all the sectors will not be equal to the total damages as calculated with Eq 36.

For climate, we expect the marginal damages per unit temperature change to be larger than the total damages per unit temperature change, due to the quadratic nature of the non-linear damage function for the range of ΔT_{all} considered under the RCP scenarios ($\Delta\mathrm{T_{all}} < 10\ ^{\circ}\mathrm{C}$).

To quantify this, we can find the ratio of marginal damages per unit of temperature increase ($\Delta\mathrm{T}$) to the average damages per unit of temperature increase from preindustrial conditions ($\Delta\mathrm{T_{all}}$). Mathematically this can be written as

$$\text{Ratio} = \frac{\frac{\mathrm{D_{Marginal}}(\Delta\mathrm{T_{all}}, \Delta\mathrm{T})}{\Delta\mathrm{T}}}{\frac{D(\Delta\mathrm{T_{all}})}{\Delta\mathrm{T_{all}}}} \qquad \text{Eq 38}$$

By substituting the damage function and recognizing that for infinitesimal temperature increases, the numerator can be written as the derivative of the damage function, the ratio becomes

$$\text{Ratio} = \frac{2}{a\Delta T_{all}^{\ 2} + 1} \qquad \text{Eq 39}$$

For small all-source temperature increases, the marginal climate damages per unit of temperature change is subsequently approximately double the damages for an average unit of background temperature change. Under RCP 4.5 emissions scenario, total temperature increases are predicted to be between 1 and 5 °C and a = 0.00236 fraction $\frac{GDP}{°C^2}$. Therefore, the ratio of marginal to total is expected to be between 1.9 and 2.

This analysis is greatly simplified by the analytical climate damage function. However, for the air quality impacts, numerically derived using GEOS-Chem, an analytical damage function is not available and it is not clear how the marginal damages differ from the average damages without performing multiple additional numerical simulations.

E.7. Monte Carlo Convergence and Sensitivity Study

E.7.1. Convergence

The climate and air quality impact distributions are computed using quasi-random Monte Carlo simulations. Uncertain parameter draws are selected using a Sobol sequence. The relative standard error of the sample mean is used to quantify convergence. It is defined as

$$\hat{\sigma}_{St_{Error}} = \frac{\sigma}{\sqrt{N} \cdot \mu} \qquad \text{Eq 40}$$

where σ indicates the output standard deviation, N indicates the number of Monte Carlo simulations, and μ indicates the output mean. For the purpose of this work, we consider a relative standard error of the sample mean less than 1% to be converged.

Eq 40, a result of the central limit is theorem, can only be applied under the condition of a finite population variance. Finite population variance can be verified by indicating the variance of variance reduces as the number of samples increase. Figure 49 shows the variance of variance for the climate and air quality total fuel burn metrics as the number of Monte Carlo simulations increase. The figure is generated by running the climate and air quality models 1000 times for the number of samples indicated on the x-axis. These plots show that the variance converges as the number of samples increases. Therefore, the central limit theorem, and Eq 40 are expected to remain valid.

In this Chapter, we used 100,000 draws. At this number of draws, the relative standard error of the sample mean is less than 0.5% for both the climate and air quality results, indicating a satisfactory level of convergence.

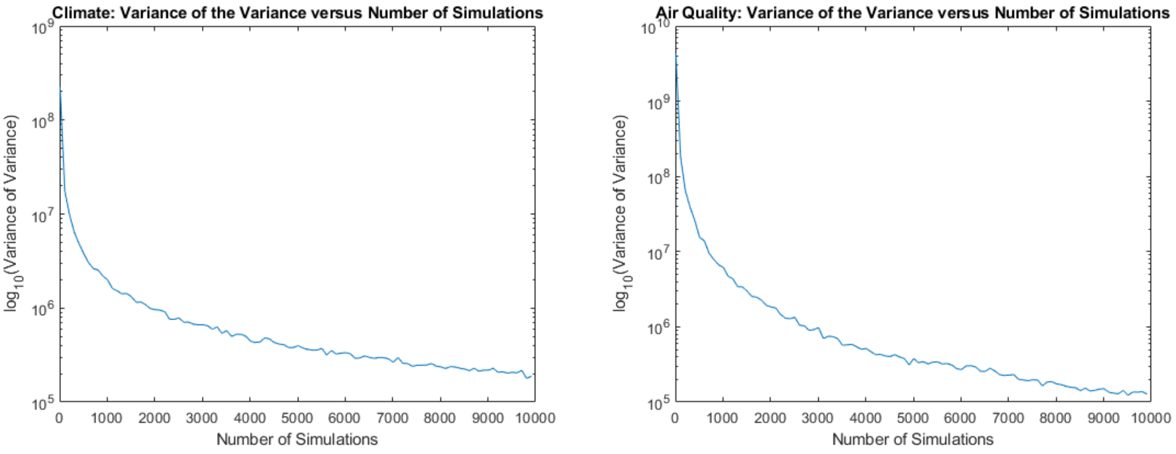

(a)

(b)

Figure 49: Variance of variance of (a) climate and (b) air quality model outputs

E.8. Sensitivity to Uncertain Variables

Methods

Mathematically, the total effect index can be written as

$$\mathrm{S_{T_i}} = 1 - \frac{\mathrm{V[E(Y|E_{\sim i})]}}{\mathrm{V(Y)}} \qquad \text{Eq 41}$$

Total effect indices are estimated using Saltelli's method (Saltelli et al., 2008). Derivation steps are outlined below following the description in Saltelli (2008).

We define two matrices, A and B, which each includes a set of input variables suitable for one Monte Carlo simulation. This leads to two (N, k) matrices of random numbers, where N is the number of members included in the Monte Carlo simulation, and k represents the number of uncertain variables considered. Furthermore, we define the matrix C_i, which is the matrix B, with one column (i.e., values for the uncertain input variable *i*) replaced with the values from matrix A for the same uncertain input variable *i*.

Then we use our climate or air quality Monte Carlo simulation code to compute the output for *f*(A), *f*(B) and *f*(C_i), where *f* indicates the climate or air quality damage quantification for the given inputs. This leads to the set of column vectors

$$\begin{aligned} y_{\mathrm{A}} &= f(\mathrm{A}) \\ y_{\mathrm{B}} &= f(\mathrm{B}) \\ y_{\mathrm{C_i}} &= f(\mathrm{C}_i) \end{aligned} \qquad \text{Eq 42}$$

These column vectors are used then used to derive the $\mathrm{S_{T_i}}$, for input variable *i*, using the formula

$$\mathrm{S_{T_i}} = 1 - \frac{y_B^T \cdot y_{C_i} - f_0^2}{y_A^T \cdot y_A - f_0^2} \qquad \text{Eq 43}$$

Where T indicates the transpose, and f_0 represents the output mean

$$f_0 = \frac{1}{N} \sum_{j=1}^{N} y_{\mathrm{A}} \qquad \text{Eq 44}$$

Using this method, the $\mathrm{S_{T_i}}$s are only approximate, because these values are based on Monte Carlo simulation. To ensure adequate convergence, we use a sobol' set with N=100,000 to draw the initial (N, 2k) matrix for the climate results, and for air quality we use 1,000,000 members to derive this sensitivity study.

Results

Table 30 and Table 31 present the total effect indices for air quality and climate, respectively. We find that the largest contributors to output uncertainty in the overall sensitivity of climate impact per unit of fuel burn are (i) climate sensitivity and (ii) the climate damage function, with total effect indices of 0.66 and 0.43, respectively. The indices of all other uncertain variables are below 0.04.

For air quality, we find the uncertainty in the VSL_{1990} to be the largest contributor to the overall uncertainty, with a total-effect index of 0.83. Income elasticity has a total-effect index of 0.13, while the concentration response function has indices of less than 0.06 or less.

When calculated analytically these indices sum to one for a purely additive model but can exceed one if interaction effects exist. For the climate model, the sum over all the total-effect indices is

1.16, while for air quality the sum is 1.15. This indicates significant effect interaction for both models.

Table 30: Estimates of the total order sensitivity indices computed using Saltelli's method for air quality impact per unit of fuel burn

Variable	**Total Effect Index (STi)**
VSL Elasticity	0.12
$PM_{2.5}$ CRF	0.07
O_3 CRF	0.05
VSL 1990	0.77
GEOS-Chem Uncertainty – $PM_{2.5}$	0.13
GEOS-Chem Uncertainty – O_3	0.02
Total	1.15

Table 31: Estimates of the total order sensitivity indices computed using Saltelli's method for climate impact per unit of fuel burn

Variable	**Total Effect Index (S_{Ti})**
CO_2 RF model	0.00
NO_x Model	0.00
RF Contrails	0.04
RF Sulfates	0.00
RF BC	0.00
RF H_2O	0.00
RF Nitrate	0.00
$RF_{Doubling\ CO2}$	0.00
Heat Capacity of Ocean Mixed-layer	0.00
Climate Sensitivity	0.66
Temp model Diffusion Coef	0.00
Temp model Advection Coef	0.01
Heat Capacity of Deep Ocean	0.00
Ocean Turbulent Mixing Depth	0.01
DICE Damage Function	0.43
Total	1.16

Appendix F Additional marginal climate and air quality cost metrics results

Since Chapter 4 predates the rest of the work of this thesis, its results are derived using APMT-IC before additional updates were made to the code to capture recent research results. These updates are described in Section 5.3.2. In short, they include:

(1) Updates to the contrail-cirrus radiative forcing and subsequent expected atmospheric temperature response to this forcing to explicitly separate the estimation of RF and effective RF (ERF, the change in energy forcing after certain short-term climate feedbacks have occurred), in line with recent literature investigating RF & ERF differences for contrails (Bickel et al., 2020a; Bock and Burkhardt, 2016; Burkhardt and Kärcher, 2011; Chen and Gettelman, 2013; Lee et al., 2020; Ponater et al., 2006; Rap et al., 2010; Schumann et al., 2015);

(2) Updates to the NO_x-related methane forcing. Following the method Lee et al. (2020) we increase the forcing of NO_x related methane forcing by 14%. This accounts for additional short-wave RF previously not accounted for in the methane radiative transfer function calculations (Etminan et al., 2016);

(3) Updates to the cost of global warming. In Chapter 4, APMT-IC used the damage function from the Dynamic Integrated Climate-Economy (DICE) model (Nordhaus, 2017), which is consistent with the social cost of carbon as proposed by the US Interagency Working Group on Social Cost of Carbon (US Government, 2016). This damage function was based on a meta-analysis of 17 studies quantifying market and non-market damages (Nordhaus, 2017). Recent

> reports indicate that traditional integrated assessment models, including DICE, lag recent research on climate damages (Greenstone, 2016; US Government, 2021). After work from Chapter 4 had been published, the damage function in APMT-IC was updated to the damage function from Howard and Sterner (2017). This damage function is based on a meta-analysis of a larger number of damage estimates from literature and explicitly treats dependencies between different underlying studies to avoid overrepresentation of results from specific studies. This change leads to social cost of carbon of 246 USD_{2020}/tonne CO_2 (90% confidence interval 61.4 to 624) for RCP2.6 and SSP2 background scenarios and a 2% discount rate. For a 3% discount rate, RCP4.5 and SSP1 the social cost of carbon in 2020 is 158 USD_{2020}/tonne CO_2 (90% confidence interval 46.4 to 352) in 2020 USD.

For comprehensiveness, and consistency between the different chapters of this thesis, we additionally present a second set of results for Chapter 4 here.

Table 32: Cost metrics for full flight emissions using updated APMT-IC

		Climate					Air Quality	
		2% Disc. Rate	2.5% Disc. Rate	3% Disc. Rate	5% Disc. Rate	7% Disc. Rate	3% Disc. Rate Country Specific VSL	3% Disc. Rate Global Average VSL
CO2	[$/tonne CO2]	270 (76, 600)	180 (52, 400)	130 (38, 290)	52 (16, 120)	28 (8.9, 62)	N/A	N/A
NOx: CH4	[$/tonne NOx as NO2]	-8900 (-21000, -2400)	-7700 (-18000, -2100)	-6800 (-16000, -1900)	-4600 (-10000, -1400)	-3400 (-7400, -1000)	N/A	N/A
NOx: O3 Short	[$/tonne NOx as NO2]	8800 (2100, 22000)	7900 (2000, 20000)	7300 (1900, 18000)	6000 (1600, 14000)	5200 (1500, 12000)	N/A	N/A
NOx: O3 Long	[$/tonne NOx as NO2]	-2500 (-6300, -610)	-2200 (-5400, -540)	-1900 (-4700, -490)	-1300 (-3100, -340)	-960 (-2200, -260)	N/A	N/A
NOx: Nitrate Aerosols	[$/tonne NOx as NO2]	-2600 (-6500, -590)	-2300 (-5800, -550)	-2100 (-5300, -520)	-1700 (-4200, -460)	-1500 (-3600, -420)	N/A	N/A
NOx: Total	[$/tonne NOx as NO2]	-5200 (-12000, -1400)	-4200 (-10000, -1200)	-3500 (-8400, -940)	-1600 (-4300, -270)	-580 (-2400, 490)	23000 (3600, 73000)	22000 (3500, 72000)
Contrail-Cirrus	[$/tonne Fuel Burn]	200 (42, 530)	180 (39, 470)	170 (37, 430)	140 (32, 340)	120 (29, 290)	N/A	N/A
Contrail-Cirrus	[$/Flight km]	0.97 (0.2, 2.6)	0.87 (0.19, 2.3)	0.81 (0.18, 2.1)	0.66 (0.15, 1.7)	0.58 (0.14, 1.4)	N/A	N/A
Fuel Sulfur	[$/tonne S]	-64000 (-160000, -15000)	-58000 (-140000, -14000)	-53000 (-130000, -13000)	-44000 (-100000, -12000)	-38000 (-88000, -11000)	30000 (4700, 100000)	31000 (4800, 110000)
BC	[$/tonne BC]	170000 (44000, 430000)	160000 (41000, 380000)	140000 (39000, 350000)	120000 (34000, 270000)	100000 (31000, 230000)	14000 (1800, 45000)	12000 (1600, 41000)
H2O	[$/tonne H2O]	9.2 (2.4, 23)	8.3 (2.2, 20)	7.7 (2.1, 18)	6.3 (1.8, 14)	5.5 (1.6, 12)	N/A	N/A
NMVOC	[$/tonne HC]	N/A	N/A	N/A	N/A	N/A	7700 (1100, 22000)	5200 (840, 17000)
CO	[$/tonne CO]	N/A	N/A	N/A	N/A	N/A	290 (44, 870)	230 (36, 780)
OC	[$/tonne OC]	N/A	N/A	N/A	N/A	N/A	11000 (1500, 37000)	9800 (1400, 34000)
Total	[$/tonne Fuel Burn]	950 (260, 2200)	660 (190, 1500)	510 (140, 1200)	260 (73, 610)	190 (53, 430)	360 (57, 1200)	350 (55, 1100)

Table 33: Cost metrics for cruise emissions using updated APMT-IC

		Climate					Air Quality	
		2% Disc. Rate	2.5% Disc. Rate	3% Disc. Rate	5% Disc. Rate	7% Disc. Rate	3% Disc. Rate Country Specific VSL	3% Disc. Rate Global Average VSL
CO_2	[\$/tonne CO_2]	270 (76, 600)	180 (52, 400)	130 (38, 290)	52 (16, 120)	28 (8.9, 62)	N/A	N/A
NO_x: CH_4	[\$/tonne NO_x as NO_2]	-9800 (-23000, -2700)	-8400 (-20000, -2400)	-7500 (-17000, -2100)	-5000 (-11000, -1500)	-3700 (-8100, -1100)	N/A	N/A
NO_x: O_3 Short	[\$/tonne NO_x as NO_2]	9700 (2400, 25000)	8700 (2200, 22000)	8000 (2100, 20000)	6600 (1800, 15000)	5800 (1700, 13000)	N/A	N/A
NO_x: O_3 Long	[\$/tonne NO_x as NO_2]	-2800 (-6900, -670)	-2400 (-5900, -600)	-2100 (-5200, -540)	-1400 (-3400, -380)	-1000 (-2400, -290)	N/A	N/A
NO_x: Nitrate Aerosols	[\$/tonne NO_x as NO_2]	-2700 (-6800, -610)	-2400 (-6000, -570)	-2200 (-5500, -540)	-1800 (-4400, -470)	-1600 (-3700, -430)	N/A	N/A
NO_x: Total	[\$/tonne NO_x as NO_2]	-5500 (-13000, -1500)	-4500 (-11000, -1200)	-3700 (-8900, -1000)	-1700 (-4500, -260)	-550 (-2500, 630)	21000 (3300, 70000)	21000 (3400, 70000)
Contrail-Cirrus	[\$/tonne Fuel Burn]	230 (48, 600)	200 (44, 530)	190 (42, 480)	150 (36, 390)	130 (33, 330)	N/A	N/A
Fuel Sulfur	[\$/tonne S]	-72000 (-180000, -17000)	-64000 (-160000, -16000)	-59000 (-150000, -15000)	-49000 (-110000, -13000)	-43000 (-98000, -12000)	30000 (4700, 100000)	32000 (4900, 110000)
BC	[\$/tonne BC]	190000 (49000, 480000)	170000 (45000, 430000)	160000 (43000, 390000)	130000 (37000, 310000)	120000 (34000, 260000)	7000 (980, 25000)	7200 (1000, 25000)
H_2O	[\$/tonne H_2O]	10 (2.7, 26)	9.4 (2.5, 23)	8.7 (2.3, 21)	7.1 (2.1, 16)	6.2 (1.9, 14)	0 (0, 0)	0 (0, 0)
NMVOC	[\$/tonne HC]	N/A	N/A	N/A	N/A	N/A	2300 (370, 7400)	2100 (340, 7100)
CO	[\$/tonne CO]	N/A	N/A	N/A	N/A	N/A	200 (31, 640)	180 (28, 610)
OC	[\$/tonne OC]	N/A	N/A	N/A	N/A	N/A	7000 (980, 25000)	7200 (1000, 25000)
Total	[\$/tonne Fuel Burn]	970 (270, 2200)	680 (190, 1600)	520 (150, 1200)	280 (77, 640)	200 (56, 470)	340 (53, 1100)	340 (54, 1100)

Table 34: Cost metrics for LTO emissions using updated APMT-IC

		Climate					Air Quality	
		2% Disc. Rate	2.5% Disc. Rate	3% Disc. Rate	5% Disc. Rate	7% Disc. Rate	3% Disc. Rate Country Specific VSL	3% Disc. Rate Global Average VSL
CO_2	[\$/tonne CO_2]	270 (77, 610)	180 (52, 410)	130 (38, 290)	52 (16, 120)	28 (9.1, 63)	N/A	N/A
NO_x: CH_4	[\$/tonne NO_x as NO_2]	-1800 (-4400, -510)	-1600 (-3800, -450)	-1400 (-3300, -410)	-940 (-2100, -290)	-690 (-1500, -210)	N/A	N/A
NO_x: O_3 Short	[\$/tonne NO_x as NO_2]	1200 (310, 2900)	1000 (290, 2600)	970 (270, 2300)	800 (240, 1800)	700 (220, 1600)	N/A	N/A
NO_x: O_3 Long	[\$/tonne NO_x as NO_2]	-540 (-1300, -150)	-470 (-1100, -130)	-410 (-970, -120)	-280 (-630, -84)	-200 (-450, -63)	N/A	N/A
NO_x: Nitrate Aerosols	[\$/tonne NO_x as NO_2]	-1300 (-3600, -250)	-1200 (-3200, -230)	-1100 (-2900, -220)	-910 (-2300, -190)	-790 (-2000, -180)	N/A	N/A
NO_x: Total	[\$/tonne NO_x as NO_2]	-2600 (-6300, -650)	-2200 (-5400, -570)	-2000 (-4700, -510)	-1300 (-3200, -350)	-980 (-2300, -250)	37000 (5300, 110000)	26000 (4100, 89000)
Contrail-Cirrus	[\$/tonne Fuel Burn]	0 (0, 0)	0 (0, 0)	0 (0, 0)	0 (0, 0)	0 (0, 0)	N/A	N/A
Fuel Sulfur	[\$/tonne S]	-9500 (-24000, -2300)	-8600 (-21000, -2100)	-7900 (-19000, -2000)	-6500 (-15000, -1800)	-5700 (-13000, -1600)	32000 (4400, 99000)	24000 (3500, 85000)
BC	[\$/tonne BC]	66000 (12000, 180000)	60000 (11000, 160000)	55000 (11000, 140000)	45000 (9300, 110000)	39000 (8400, 98000)	66000 (8800, 200000)	45000 (6500, 160000)
H_2O	[\$/tonne H_2O]	N/A	N/A	N/A	N/A	N/A	0 (0, 0)	0 (0, 0)
NMVOC	[\$/tonne HC]	N/A	N/A	N/A	N/A	N/A	19000 (2800, 53000)	12000 (1900, 39000)
CO	[\$/tonne CO]	N/A	N/A	N/A	N/A	N/A	520 (77, 1500)	360 (56, 1200)
OC	[\$/tonne OC]	N/A	N/A	N/A	N/A	N/A	110000 (14000, 310000)	66000 (9400, 230000)
Total	[\$/tonne Fuel Burn]	810 (230, 1800)	530 (160, 1200)	380 (110, 870)	140 (44, 330)	76 (24, 170)	590 (86, 1700)	430 (66, 1400)

Table 35: CAQSC cost of fuel burn in different flight phases (USD/Tonne Fuel Burn in 2015) (3% discount rate) using updated APMT-IC

	Landing and Take-off			Cruise			Full Flight		
	Climate	Air Quality	Total	Climate	Air Quality	Total	Climate	Air Quality	Total
CO_2	410 (120, 930)	N/A	410 (120, 930)	410 (120, 910)	N/A	410 (120, 910)	410 (120, 910)	N/A	410 (120, 910)
NO_x	-30 (-72, -7.7)	560 (81, 1600)	530 (50, 1600)	-56 (-130, -15)	320 (50, 1000)	260 (-11, 990)	-53 (-130, -14)	340 (53, 1100)	290 (-3.7, 1000)
Contrail-Cirrus*	0 (0, 0)	0 (0, 0)	0 (0, 0)	190 (42, 480)	N/A	190 (42, 480)	170 (37, 430)	N/A	170 (37, 430)
Fuel Sulfur	-4.8 (-12, -1.2)	19 (2.6, 59)	15 (-3.2, 55)	-36 (-88, -8.9)	18 (2.8, 63)	-18 (-70, 37)	-32 (-79, -8.1)	18 (2.8, 62)	-14 (-62, 39)
BC	2.7 (0.53, 7.1)	3.2 (0.43, 9.6)	5.9 (1.8, 14)	5.6 (1.5, 14)	0.25 (0.034, 0.87)	5.9 (1.8, 14)	5.2 (1.4, 13)	0.5 (0.066, 1.6)	5.7 (1.8, 13)
H_2O	0 (0, 0)	0 (0, 0)	0 (0, 0)	11 (2.9, 26)	N/A	11 (2.9, 26)	9.4 (2.5, 23)	N/A	9.4 (2.5, 23)
NMVOC	N/A	11 (1.7, 31)	11 (1.7, 31)	N/A	0.27 (0.043, 0.86)	0.27 (0.043, 0.86)	N/A	1.2 (0.17, 3.4)	1.2 (0.17, 3.4)
CO	N/A	4.3 (0.63, 12)	4.3 (0.63, 12)	N/A	0.39 (0.06, 1.2)	0.39 (0.06, 1.2)	N/A	0.72 (0.11, 2.2)	0.72 (0.11, 2.2)
OC	N/A	0.77 (0.1, 2.2)	0.77 (0.1, 2.2)	N/A	0.11 (0.015, 0.37)	0.11 (0.015, 0.37)	N/A	0.16 (0.022, 0.53)	0.16 (0.022, 0.53)
Total Cost	380 (110, 870)	590 (86, 1700)	980 (340, 2200)	520 (150, 1200)	340 (53, 1100)	860 (330, 1900)	510 (140, 1200)	360 (57, 1200)	870 (330, 1900)

Table 36: CAQSC cost of full flight fuel burn (USD/Tonne Fuel Burn in 2015) for 2% and 7% discount rates using updated APMT-IC

	2% Discount Rate			7% Discount Rate		
	Climate	Air Quality	Total	Climate	Air Quality	Total
CO_2	840 (240, 1900)	N/A	840 (240, 1900)	90 (28, 200)	N/A	90 (28, 200)
NO_x	-77 (-180, -21)	350 (55, 1100)	270 (-31, 1100)	-8.7 (-35, 7.4)	310 (48, 980)	300 (39, 970)
Contrail-Cirrus*	200 (42, 530)	N/A	200 (42, 530)	120 (29, 290)	N/A	120 (29, 290)
Fuel Sulfur	-39 (-98, -9.2)	19 (2.9, 64)	-20 (-79, 38)	-23 (-53, -6.4)	16 (2.5, 56)	-6.6 (-39, 38)
BC	6.3 (1.6, 16)	0.51 (0.069, 1.7)	6.8 (2.1, 16)	3.7 (1.1, 8.4)	0.45 (0.06, 1.5)	4.2 (1.5, 9)
H_2O	11 (2.9, 28)	N/A	11 (2.9, 28)	6.8 (2, 15)	N/A	6.8 (2, 15)
NMVOC	N/A	1.2 (0.18, 3.5)	1.2 (0.18, 3.5)	N/A	1.1 (0.16, 3.1)	1.1 (0.16, 3.1)
CO	N/A	0.74 (0.11, 2.2)	0.74 (0.11, 2.2)	N/A	0.65 (0.099, 1.9)	0.65 (0.099, 1.9)
OC	N/A	0.17 (0.022, 0.55)	0.17 (0.022, 0.55)	N/A	0.15 (0.02, 0.48)	0.15 (0.02, 0.48)
Total Cost	950 (260, 2200)	370 (58, 1200)	1300 (510, 2800)	190 (53, 430)	320 (51, 1000)	510 (180, 1300)

Table 37: CAQSC cost of full flight fuel burn apportioned to the different flight phases (USD/Tonne Fuel Burn in 2015) (3% discount rate) using updated APMT-IC

	Landing and Take-off			Cruise			Full Flight		
	Climate	Air Quality	Total	Climate	Air Quality	Total	Climate	Air Quality	Total
CO_2	34 (10, 78)	0 (0, 0)	34 (10, 78)	370 (110, 840)	0 (0, 0)	370 (110, 840)	410 (120, 910)	0 (0, 0)	410 (120, 910)
NO_x	-2.5 (-6.1, -0.66)	47 (6.8, 140)	45 (4.2, 130)	-51 (-120, -14)	290 (46, 960)	240 (-10, 910)	-53 (-130, -14)	340 (53, 1100)	290 (-3.7, 1000)
Contrail-Cirrus*	0 (0, 0)	0 (0, 0)	0 (0, 0)	170 (38, 440)	0 (0, 0)	170 (38, 440)	170 (37, 430)	0 (0, 0)	170 (37, 430)
Fuel Sulfur	-0.4 (-0.98, -0.1)	1.6 (0.22, 5)	1.2 (-0.27, 4.6)	-33 (-80, -8.2)	17 (2.6, 57)	-16 (-64, 34)	-32 (-79, -8.1)	18 (2.8, 62)	-14 (-62, 39)
BC	0.23 (0.045, 0.6)	0.27 (0.037, 0.81)	0.5 (0.16, 1.2)	5.2 (1.4, 12)	0.23 (0.031, 0.8)	5.4 (1.6, 13)	5.2 (1.4, 13)	0.5 (0.066, 1.6)	5.7 (1.8, 13)
H_2O	0 (0, 0)	0 (0, 0)	0 (0, 0)	9.8 (2.6, 23)	0 (0, 0)	9.8 (2.6, 23)	9.4 (2.5, 23)	0 (0, 0)	9.4 (2.5, 23)
NMVOC	0 (0, 0)	0.96 (0.14, 2.6)	0.96 (0.14, 2.6)	0 (0, 0)	0.25 (0.039, 0.79)	0.25 (0.039, 0.79)	0 (0, 0)	1.2 (0.17, 3.4)	1.2 (0.17, 3.4)
CO	0 (0, 0)	0.36 (0.053, 1)	0.36 (0.053, 1)	0 (0, 0)	0.36 (0.055, 1.1)	0.36 (0.055, 1.1)	0 (0, 0)	0.72 (0.11, 2.2)	0.72 (0.11, 2.2)
OC	0 (0, 0)	0.065 (0.0086, 0.19)	0.065 (0.0086, 0.19)	0 (0, 0)	0.097 (0.013, 0.34)	0.097 (0.013, 0.34)	0 (0, 0)	0.16 (0.022, 0.53)	0.16 (0.022, 0.53)
Total Cost	32 (9.5, 73)	50 (7.3, 140)	83 (29, 180)	480 (130, 1100)	310 (48, 1000)	790 (310, 1700)	510 (140, 1200)	360 (57, 1200)	870 (330, 1900)

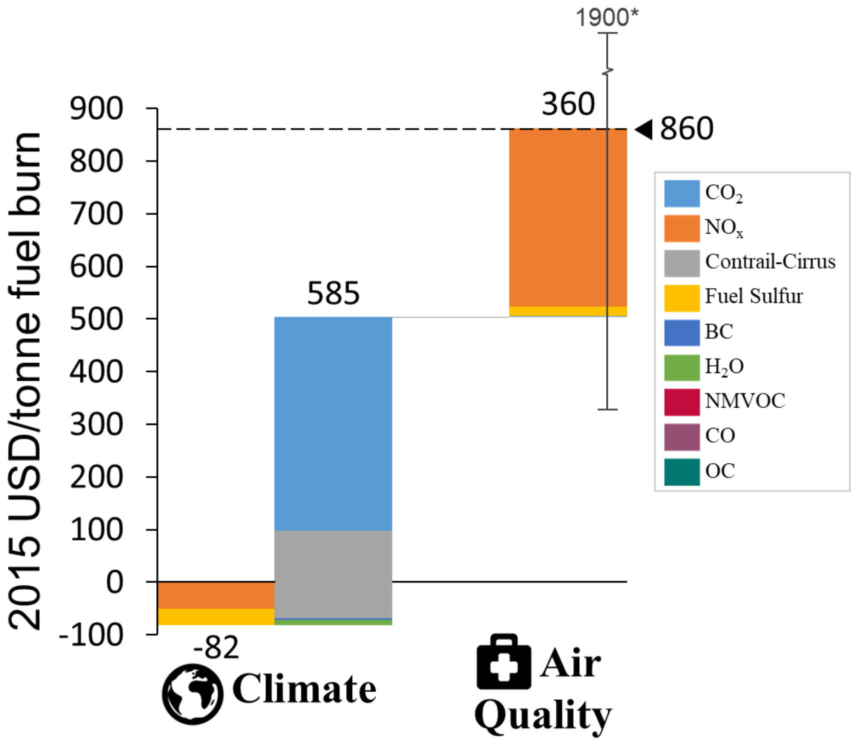

Figure 50: Climate and air quality costs per unit fuel burn for 3% discount rate derived using updated APMT-IC

Appendix G Pathway to zero: Contrail avoidance trade-off literature discussion

Reaching net zero climate impacts from aviation will require avoiding contrail formation. One strategy of contrail avoidance relies on aircraft to avoid flying through regions with sufficiently cold and moist ambient conditions, so that the exhaust plume does not become super saturated with respect to ice while cooling (Schumann et al. 2011, Kärcher 2018). These regions have been found to cover large continuous horizontal distances (up to 400 km), but usually only small altitude bands, typically not exceeding 610 m (2000 ft) (Mannstein et al. 2005, Spichtinger et al. 2003). Resultingly, contrail formation can be avoided through small scale adjustments in cruise altitude (Schumann et al. 2011, Sridhar et al. 2011, Avila et al. 2019). These minor diversions lead to a small fuel burn penalty (typically less than 5% of fleetwide fuel consumption) assuming a counterfactual case where aircraft are flying fuel-optimally. In addition, only 2% of flights have been found to be responsible for 80% of contrail forcing in some regions; in turn, less than 2% of flights would have to be diverted to avoid 80% of contrail warming impacts (Teoh et al. 2020a).

For our quantitative assessment, we consider the results of five studies, which cover different geographic regions.

Two studies of contrail avoidance relate to transatlantic flights (Yin et al, 2018; Noppel et al, 2006). Yin et al. (2018) focus on real time contrail avoidance for 103 transatlantic flights during a full year, while optimizing for the transatlantic winds. They find a 90% contrail length reduction to be obtainable through an increase in fuel consumption of 2.5% in autumn and 4% in winter. The variation by season results from differences in wind patterns and changes in troposphere-stratosphere exchange between the different seasons. Noppel et al. (2006) analyze contrail avoidance for transatlantic flights from London to New York. Using annually averaged meteorology, they find that 40% of contrail length can be avoided for less than a 0.5% fuel burn penalty. As more contrail length is avoided, the fuel burn penalty increases, e.g., reducing contrail length by 60% leads to a fuel burn penalty of approximately 2%. For both studies, annually averaged fuel burn penalties associated with different levels of contrail avoidance are plotted in *Figure 39*.

Two additional studies for contrail avoidance over the continental US are included (Sridhar et al, 2011 and Sridhar et al, 2012). Both studies analyze flights between 12 city pairs and assume wind-optimal routings for observed flight conditions on three days. Contrail avoidance through both altitude and lateral adjustments is modeled. The results indicate that contrail formation time could be reduced by 60% for less than a 2% fuel burn penalty and 100% avoidance for less than 6% fuel burn penalty on the days analyzed. Results are presented for each of the three days, for various levels of contrail avoidance. The averaged results over the three-day study period are included in *Figure 39*.

One final study, Kilma (2005), examined contrail avoidance for flights in one week of November 2001 over the continental US and the North Atlantic. The study finds that contrail formation could be reduced by 83.6% for a 3.5% fuel burn penalty over the continental US. Over the North Atlantic, contrail formation is found to be reduced by 56.5% through contrail avoidance strategies resulting in a fuel burn penalty of 2.8%. This data has also been included in *Figure 39*.

Other contrail avoidance studies were not included in our analysis, because they either don't capture the maximum obtainable benefit of tailored adjustments (Fichter et al. 2005, Williams et al. 2002) or do not calculate fuel burn penalties relative to fuel- or cost-optimal flight routings, which may lead to an underreporting of fuel burn penalties.

The trade-off relationship presented in *Figure 39* captures contrail length avoided rather than contrail radiative impacts. This likely introduces a bias in the results where the meta-analysis predicts larger additional fuel requirements to avoid a given percentage of contrail length than would be necessary to avoid a similar percentage of contrail forcing. Targeting contrail radiative forcing could lead to net contrail cooling, since aircraft could avoid warming contrails, while still forming cooling contrails (Teoh et al., 2020). In contrast, fuel burn penalties might be underestimated due to the use of Base of Aircraft Data 3 (BADA3) data used to approximate aircraft performance (Eurocontrol 2018). BADA3 was developed as a tool for aircraft traffic controllers to rapidly calculate fuel requirements in case of rerouting a flight. However, it was not intended to capture the impact of small-scale cruise altitude adjustments and is known for decreased accuracy at suboptimal flight conditions (Klima 2005, Teoh et al. 2020a). Kilma (2005) found that BADA underestimates the change in specific fuel consumption for adjustments in cruise altitudes by comparing the BADA engine data of three aircraft to the aircraft operating manual engine data and the high-fidelity engine model GasTurb. Assuming this extends to the rest of the fleet, the fuel burn penalty would be underestimated by these studies. Except for Noppel and Singh (2006) all studies included in the meta-analysis used BADA data.

Several other strategies for reducing contrail impacts are also discussed in the literature. These include rescheduling of flights to only occur during daylight hours (Stuber et al. 2006). This has been shown to have an insignificant benefit due to the large variability in contrail lifetimes, and long lifetime (>8 hours) of the contrails responsible for the largest impact (Newinger and

Burkhardt 2012). Reducing aircraft soot particle emissions by 80-90% might also reduce contrail radiative impacts by 8%-50% (Teoh et al. 2020a, Burkhardt et al. 2018). This could be achieved by using either low soot combustor technology or by removing naphthalene from aircraft fuel. Finally, aircraft formation flying has the potential to decrease aviation climate impacts by 22-24%, while reducing fuel consumption by 5–6% (Marks et al. 2021). However, formation flight would additionally strain current air traffic control, and require changes to current aircraft minimum separation distances (5nm horizontal separation) by requiring that aircraft flying within 30 wingspans of one another at the same flight level.

Appendix H Pathway to zero: Derived global warming potentials (GWP)

Global Warming Potential (GWP) provides a comparison measure of a non-CO_2 climate forcing precursor emission to an equivalent CO_2 emissions quantity. This CO_2 equivalency metric is defined as the integrated RF to a specified time horizon following an emissions pulse of one kg of a precursor emission, normalized to the integrated RF following a one kg emissions pulse of CO_2, where the RF of CO_2 is integrated over the same time horizon as the non-CO_2 forcer.

We derive GWP values for each of the precursor emissions and climate impact pathways considered in this chapter. Using the reduced order climate model described above, we derive GWP values for each of the climate forcers by simulating the radiative forcing following an emissions pulse in 2020 (Table 38).

Since a precursor emission is not easily defined for contrails, we normalize the contrail radiative forcing to flight distance, consistent with previous studies (Lund et al. 2017, Fuglestvedt et al. 2010, Grobler et al. 2019, Lee et al. 2020). Contrail RF per flight distance is determined by using the flight distance and fuel burn from AEDT as reported in Brasseur et al. (2016), which corresponds to 188.1 Tg fuel for a collective 3.87×10^{10} km, resulting in a factor of 4.86 kg/km. Finally, the GWP for contrails is reported in Table 38 is for Jet-A fuel. To capture the contrail impacts of the alternative fuels, we apply an adjustment for each alternative energy carrier as presented in Table 8, as well as adjusting effective distance flown to account for contrail avoidance.

These GWP values are used to derive CO_2-equivalent (CO_2eq) emissions for emission pathways reported in Chapter 5. These CO_2eq emissions are derived by multiplying these GWP values by emissions from each pathway.

Table 38: Global Warming Potential (GWP) used in Chapter 5, for GWP time horizons covering 20 to 500 years. Contrails are normalized to 1km of flight length. The NO_x impacts are normalized to emission of 1kg NOx as NO_2 and the sulfur impact is normalized to quantity of fuel sulfur (S). Uncertainty results are presented in the brackets covering the 95-percentile range. These GWPs are derived using an APMT-IC derived AGWP for CO_2 as tabulated in the last row of the table. These AGWP potential values are for a RCP2.4 scenario.

	20 Years	**50 Years**	**100 Years**	**500 Years**
Fuel sulfur	-2,100 (-3,200 to -1,300)	-1,000 (-1,600 to -610)	-580 (-910 to -340)	-160 (-270 to -85)
NO_x	-20 (-100 to 48)	-31 (-70 to 0.089)	-18 (-42 to -1.1)	-4.9 (-12 to -0.29)
H_2O	0.30 (0.22 to 0.39)	0.15 (0.10 to 0.19)	0.083 (0.058 to 0.12)	0.022 (0.014 to 0.035)
nvPM	5,600 (4,100 to 7,500)	2,700 (1,900 to 3,800)	1,600 (1,100 to 2,200)	420 (260 to 670)
Contrails	32 (14 to 54)	15 (6.5 to 26)	8.8 (3.7 to 15)	2.3 (0.94 to 4.4)
CH_4	99 (74 to 130)	60 (42 to 83)	36 (24 to 51)	11 (6.9 to 16)
N_2O	320 (260 to 390)	340 (270 to 430)	320 (240 to 430)	150 (98 to 230)
CO_2 AGWP *[10^{-14} $W m^{-2} yr kg^{-1}$]*	*2.4* *(2.0 to 2.8)*	*5.0* *(4.0 to 6.1)*	*8.7* *(6.6 to 11)*	*33* *(21 to 46)*

For some factors, no information is available regarding their impacts. First, a few uncertain climate feedback mechanisms are not captured here. These include cloud-aerosol interactions (Lee et al. 2020, Lund et al. 2017), climate-carbon feedback for non-CO_2 forcers (Gasser et al. 2017), the currently poorly understood impact of fuel sulfur on contrail formation (Kärcher 2018), and the impact of soot on arctic ice darkening (Fuglestvedt et al. 2010). Furthermore, we assume changes in contrail impacts from the use of alternative energy carriers is not affected by contrail avoidance.

Additionally, we do not account for the impact of methane or hydrogen leakage at altitude. Although this leakage is expected to be two orders of magnitude lower than leakage at ground level, little is yet known about the chemical and climate effects of high-altitude leakage (EPA 2009).

Finally, changes in region of emissions, in flight altitude, and time of day of flights, are expected to change the resulting climate impacts. As a result, the RF scaling approach followed here only remains valid if spatial and temporal flight patterns remain similar to today's flight patterns.

Appendix I Pathway to zero: Climate costs derived using APMT-IC

Using the climate model APMT-IC, as described in the methods section, climate costs for CO_2 and contrails are derived and tabulated in Table 9. Cost values are presented for discount rates of 1.5%, 2%, and 3%. For comparison between the direct in-flight CO_2 emissions impact and the contrail impact from Jet-A, the table also presents costs normalized by a metric tonne of Jet-A fuel burn. For the low discount rate, the impact of contrails per unit fuel burn is between 22% to 37% of the direct in-flight CO_2 impact. This ratio changes with the discount rate. For a discount rate of 3%, contrails account for 58% to 87% the costs of direct in-flight CO_2 emissions per unit fuel burn. Table 10 presents the costs per metric tonne of CO_2, CH_4, and N_2O, derived using the radiative transfer functions of Etminan et al. (2016). Finally, Table 11 to Table 14 present non-CO_2 costs per fuel energy for each of the fuel carriers by a unit fuel energy.

Table 9: Climate damages (in 2020 USD) for CO_2 and contrails from Jet-A fuel.

	Emissions in 2020			Emissions in 2035			Emissions in 2050		
	1.5 % Discount Rate	**2.0 % Discount Rate**	**3.0 % Discount Rate**	**1.5 % Discount Rate**	**2.0 % Discount Rate**	**3.0 % Discount Rate**	**1.5 % Discount Rate**	**2.0 % Discount Rate**	**3.0 % Discount Rate**
CO_2 [USD/tonne CO_2]	413 (96.8, 1090)	246 (61.4, 624)	121 (32.8, 292)	497 (116, 1310)	309 (76.8, 786)	163 (43.6, 395)	586 (135, 1550)	377 (92.2, 965)	207 (54.3, 507)
Contrail [USD/km]	1.40 (0.290, 3.76)	1.24 (0.268, 3.22)	1.07 (0.244, 2.72)	2.34 (0.501, 6.15)	2.13 (0.475, 5.50)	1.91 (0.440, 4.82)	3.30 (0.704, 8.73)	3.06 (0.674, 7.94)	2.78 (0.633, 7.06)
CO_2 [USD/tonne fuel]	1300 (306, 3440)	777 (194, 1970)	383 (104, 924)	1570 (367, 4150)	978 (243, 2480)	514 (138, 1250)	1850 (427, 4910)	1190 (291, 3050)	654 (172, 1600)
Contrail [USD/tonne fuel]	288 (59.7, 775)	254 (55.2, 664)	221 (50.3, 561)	481 (103, 1270)	439 (97.8, 1130)	394 (90.6, 992)	680 (145, 1800)	630 (139, 1640)	572 (130, 1450)

Uncertainty results represent the 5th to 95th percentile range for this table and other cost values in the tables below.

Table 10: Climate damages (in 2020 USD) for life cycle emissions of CH_4, CO_2, and N_2O

	Emissions in 2020			Emissions in 2035			Emissions in 2050		
	1.5 % Discount Rate	**2.0 % Discount Rate**	**3.0 % Discount Rate**	**1.5 % Discount Rate**	**2.0 % Discount Rate**	**3.0 % Discount Rate**	**1.5 % Discount Rate**	**2.0 % Discount Rate**	**3.0 % Discount Rate**
[USD/tonne CH_4]	7,380 (1,850, 18,400)	6,090 (1,570, 14,700)	4,670 (1,250, 10,900)	11,200 (2,830, 27,800)	9,530 (2,460, 23,000)	7,550 (2,040, 17,700)	15,500 (3,860, 38,800)	13,400 (3,420, 32,700)	10,800 (2,860, 25,700)
[USD/tonne CO_2]	414 (96.6, 1090)	247 (61.3, 627)	122 (32.6, 294)	498 (116, 1320)	311 (76.4, 789)	164 (43.3, 398)	587 (135, 1560)	378 (91.6, 968)	208 (54.1, 512)
[USD/tonne N_2O]	96,700 (23,900, 248,000)	64,700 (16,800, 161,000)	35,500 (9,860, 85,500)	121,000 (29,600, 311,000)	83,300 (21,400, 209,000)	48,100 (13,100, 117,000)	146,000 (35,300, 379,000)	103,000 (26,100, 262,000)	61,500 (16,400, 151,000)

Table 11: Climate damages (in 2020 USD) damages for emissions from Jet-A combustion

	Emissions in 2020			**Emissions in 2035**			**Emissions in 2050**		
	1.5 % Discount Rate	**2.0 % Discount Rate**	**3.0 % Discount Rate**	**1.5 % Discount Rate**	**2.0 % Discount Rate**	**3.0 % Discount Rate**	**1.5 % Discount Rate**	**2.0 % Discount Rate**	**3.0 % Discount Rate**
Contrail [USD/km]	1.40 (0.290, 3.76)	1.24 (0.268, 3.22)	1.07 (0.244, 2.72)	2.34 (0.501, 6.15)	2.13 (0.475, 5.50)	1.91 (0.440, 4.82)	3.30 (0.704, 8.73)	3.06 (0.674, 7.94)	2.78 (0.633, 7.06)
Contrail [USD/GJ fuel energy]	6.67 (1.38, 17.9)	5.89 (1.28, 15.4)	5.12 (1.16, 13.0)	11.1 (2.39, 29.3)	10.2 (2.26, 26.2)	9.12 (2.10, 23.0)	15.7 (3.36, 41.6)	14.6 (3.21, 37.9)	13.2 (3.02, 33.6)
Total non-CO_2 [USD/GJ fuel energy]	4.14 (0.337, 12.4)	3.80 (0.389, 11.1)	3.61 (0.500, 9.99)	7.77 (1.01, 22.0)	7.38 (1.09, 20.4)	7.12 (1.25, 18.9)	11.5 (1.67, 32.1)	11.1 (1.79, 30.2)	10.7 (1.97, 28.4)
Total non-CO_2 (excl. contrails) [USD/GJ fuel energy]	-2.53 (-6.39, -0.616)	-2.09 (-5.20, -0.511)	-1.51 (-3.73, -0.351)	-3.37 (-8.82, -0.726)	-2.79 (-7.21, -0.579)	-2.00 (-5.31, -0.327)	-4.24 (-11.4, -0.817)	-3.52 (-9.55, -0.620)	-2.51 (-7.04, -0.256)

Table 12: Climate damages (in 2020 USD) damages for emissions from drop-in alternative fuels combustion

	Emissions in 2020			**Emissions in 2035**			**Emissions in 2050**		
	1.5 % Discount Rate	**2.0 % Discount Rate**	**3.0 % Discount Rate**	**1.5 % Discount Rate**	**2.0 % Discount Rate**	**3.0 % Discount Rate**	**1.5 % Discount Rate**	**2.0 % Discount Rate**	**3.0 % Discount Rate**
Contrail [USD/km]	0.908 (0.154, 2.52)	0.801 (0.143, 2.19)	0.697 (0.129, 1.85)	1.52 (0.266, 4.15)	1.38 (0.252, 3.73)	1.24 (0.234, 3.27)	2.14 (0.377, 5.87)	1.98 (0.358, 5.34)	1.80 (0.335, 4.78)
Contrail [USD/GJ fuel energy]	4.33 (0.737, 12.0)	3.82 (0.680, 10.4)	3.32 (0.617, 8.83)	7.23 (1.27, 19.8)	6.60 (1.20, 17.8)	5.92 (1.12, 15.6)	10.2 (1.80, 28.0)	9.46 (1.71, 25.5)	8.59 (1.60, 22.8)
Total non-CO_2 [USD/GJ fuel energy]	2.98 (0.0644, 9.58)	2.78 (0.145, 8.60)	2.72 (0.299, 7.86)	5.84 (0.588, 17.3)	5.61 (0.696, 16.1)	5.54 (0.859, 15.1)	8.76 (1.08, 25.3)	8.53 (1.21, 24.0)	8.44 (1.43, 22.8)
Total non-CO_2 (excl. contrails) [USD/GJ fuel energy]	-1.35 (-3.54, -0.286)	-1.04 (-2.76, -0.190)	-0.598 (-1.81, 0.0197)	-1.39 (-4.30, -0.0164)	-0.982 (-3.38, 0.219)	-0.380 (-2.23, 0.810)	-1.45 (-5.25, 0.411)	-0.929 (-4.10, 0.837)	-0.155 (-2.70, 1.78)

Table 13: Climate damages (in 2020 USD) damages for emissions from LNG combustion

	Emissions in 2020			**Emissions in 2035**			**Emissions in 2050**		
	1.5 % Discount Rate	**2.0 % Discount Rate**	**3.0 % Discount Rate**	**1.5 % Discount Rate**	**2.0 % Discount Rate**	**3.0 % Discount Rate**	**1.5 % Discount Rate**	**2.0 % Discount Rate**	**3.0 % Discount Rate**
Contrail [USD/km]	1.40 (0.242, 3.84)	1.23 (0.224, 3.33)	1.07 (0.204, 2.83)	2.33 (0.419, 6.32)	2.13 (0.394, 5.68)	1.91 (0.368, 4.98)	3.29 (0.590, 8.94)	3.05 (0.560, 8.17)	2.77 (0.526, 7.27)
Contrail [USD/GJ fuel energy]	6.66 (1.15, 18.3)	5.88 (1.07, 15.9)	5.11 (0.971, 13.5)	11.1 (2.00, 30.1)	10.1 (1.88, 27.1)	9.10 (1.75, 23.8)	15.7 (2.82, 42.6)	14.6 (2.67, 39.0)	13.2 (2.51, 34.7)
Total non-CO_2 [USD/GJ fuel energy]	5.48 (0.644, 16.1)	4.98 (0.665, 14.3)	4.64 (0.744, 12.7)	10.0 (1.53, 28.0)	9.42 (1.56, 25.7)	8.95 (1.66, 23.7)	14.7 (2.36, 40.5)	14.0 (2.41, 37.9)	13.4 (2.56, 35.2)
Total non-CO_2 (excl. contrails) [USD/GJ fuel energy]	-1.18 (-3.16, -0.221)	-0.893 (-2.46, -0.120)	-0.470 (-1.59, 0.126)	-1.11 (-3.77, 0.183)	-0.728 (-2.92, 0.478)	-0.153 (-1.87, 1.15)	-1.05 (-4.50, 0.809)	-0.565 (-3.52, 1.32)	0.175 (-2.17, 2.32)

Table 14: Climate damages (in 2020 USD) damages for emissions from LH2 combustion

	Emissions in 2020			**Emissions in 2035**			**Emissions in 2050**		
	1.5 % Discount Rate	**2.0 % Discount Rate**	**3.0 % Discount Rate**	**1.5 % Discount Rate**	**2.0 % Discount Rate**	**3.0 % Discount Rate**	**1.5 % Discount Rate**	**2.0 % Discount Rate**	**3.0 % Discount Rate**
Contrail [USD/km]	1.19 (0.180, 3.38)	1.05 (0.167, 2.92)	0.911 (0.152, 2.47)	1.98 (0.313, 5.54)	1.81 (0.296, 4.95)	1.62 (0.275, 4.37)	2.80 (0.441, 7.82)	2.59 (0.421, 7.13)	2.36 (0.393, 6.39)
Contrail [USD/GJ fuel energy]	5.66 (0.860, 16.1)	5.00 (0.798, 13.9)	4.34 (0.727, 11.8)	9.45 (1.49, 26.4)	8.62 (1.41, 23.6)	7.74 (1.31, 20.9)	13.4 (2.10, 37.3)	12.4 (2.01, 34.0)	11.2 (1.88, 30.5)
Total non-CO_2 [USD/GJ fuel energy]	4.84 (0.432, 14.7)	4.42 (0.494, 13.0)	4.15 (0.590, 11.6)	8.93 (1.20, 25.7)	8.44 (1.26, 23.6)	8.07 (1.38, 21.7)	13.1 (1.93, 37.0)	12.6 (1.99, 34.8)	12.1 (2.15, 32.4)
Total non-CO_2 (excl. contrails) [USD/GJ fuel energy]	-0.822 (-2.43, -0.0368)	-0.577 (-1.87, 0.0990)	-0.195 (-1.15, 0.478)	-0.514 (-2.73, 0.885)	-0.182 (-2.05, 1.24)	0.337 (-1.15, 1.95)	-0.210 (-3.11, 2.05)	0.217 (-2.27, 2.59)	0.886 (-1.22, 3.57)

Appendix J Aircraft-Engine matchings based on NASA-Boeing Studies

Table 39: Year 1980 aircraft-engine matchings based on NASA-Boeing studies (Baughcum et al., 1996b, 1996a; Sutkus et al., 2001). *In this thesis, these matchings are applied for the years 1980 and 1985.*

OAG Aircraft Code	BADA aircraft	Engine	Combustor Option	Fraction
747	B741	JT9D-7A	-	1
72S	B722	JT8D-15	Reduced-emissions	1
D10	DC10	CF6-6D	-	1
727	B721	JT8D-7-series	Reduced-emissions	1
L10	L101	RB211-22B	Package-1	1
707	B703	JT3D-3B	-	1
D9S	DC93	JT8D-7-series	Reduced-emissions	1
737	B732	JT8D-7-series	Reduced-emissions	1
AB3	A30B	CF6-50C1 --C2	-	1
73S	B732	JT8D-7-series	Reduced-emissions	1
DC9	DC91	JT8D-7-series	Reduced-emissions	1
74L	B74S	JT8D-7-series	Reduced-emissions	1

Table 40: Year 1990 aircraft-engine matchings based on NASA-Boeing studies (Baughcum et al., 1996b, 1996a; Sutkus et al., 2001). *In this thesis, these matchings are applied for the years 1990 and 1995.*

OAG Aircraft Code	BADA aircraft	Engine	Combustor Option	Fraction
747	B741	JT9D-7A	-	0.398405
747	B742	CF6-50E2	-	0.136785
747	B742	JT9D-7A	-	0.085230
747	B742	JT9D-7Q	-	0.128825
747	B744	RB211-524G	-	0.100703
747	B744	PW4056	-	0.094168
747	B744	CF6-80C2B1F	-	0.055885

OAG Aircraft Code	BADA aircraft	Engine	Combustor Option	Fraction
72S	B722	JT8D-15	Reduced-emissions	0.776666
72S	B722	JT8D-9-series	Reduced-emissions	0.223334
M80	MD82	JT8D-217-series	-	0.795750
M80	MD88	JT8D-219	-	0.204250
767	B762	CF6-80A	-	0.798933
767	B762	JT9D-7R4D --7R4D1	-	0.201067
AB3	A30B	CF6-50C2R	-	0.538882
AB3	A30B	CF6-50C1 --C2	-	0.461118
733	B733	CFM56-3-B1	-	1.000000
73S	B732	JT8D-15	Reduced-emissions	0.409668
73S	B732	JT8D-9-series	Reduced-emissions	0.250019
73S	B732	JT8D-7-series	Reduced-emissions	0.198060
73S	B732	JT8D-15A	-	0.142252
L10	L101	RB211-22B	Package-1	0.666868
L10	L101	RB211-524B-series	Phase-2	0.333132
D9S	DC93	JT8D-7-series	Reduced-emissions	0.681046
D9S	DC93	JT8D-9-series	Reduced-emissions	0.318954
757	B752	PW2037	-	0.646925
757	B752	PW2040	-	0.234909
757	B752	RB211-535E4	-	0.118166
737	B732	JT8D-15	Reduced-emissions	1.000000
310	A310	CF6-80A3	-	0.678273
310	A310	JT9D-7R4E --7R4E1	-	0.321727
744	B744	RB211-524G	-	0.401597
744	B744	PW4056	-	0.375536
744	B744	CF6-80C2B1F	-	0.222867

Table 41: Year 2000 aircraft-engine matchings based on NASA-Boeing studies (Baughcum et al., 1996b, 1996a; Sutkus et al., 2001). *In this thesis, these matchings are applied for the years 2000 to 2019.*

OAG Aircraft Code	BADA aircraft	Engine	Combustor Option	Fraction
744	B744	CF6-80C2B1F	-	0.378594
744	B744	PW4056	-	0.291975
744	B744	RB211-524G	-	0.212398
744	B744	CF6-80C2B1F	-	0.117033
747	B742	JT9D-7Q	-	0.508852
747	B743	RB211-524D4	Phase-2	0.140283
747	B742	CF6-50E2	-	0.243699
747	B743	JT9D-7R4G2	-	0.107165
757	B752	PW2037	-	0.510511
757	B752	RB211-535E4	-	0.246246
757	B752	RB211-535E4B	-	0.243243
M80	MD82	JT8D-217-series	-	0.500314
M80	MD83	JT8D-219	-	0.285861
M80	MD88	JT8D-219	-	0.213824
763	B763	PW4056	-	0.573711
763	B763	CF6-80C2B4	-	0.264636
763	B763	CF6-80C2B4F	-	0.161653
733	B733	CFM56-3-B1	-	1.000000
320	A320	CFM56-5-A1	-	0.603158
320	A320	V2527-A5	-	0.198934
320	A320	V2500-A1	-	0.197908
777	B772	PW4084	-	0.343403
777	B772	GE90-90B	DAC-II	0.288704
777	B772	Trent-877	-	0.217931
777	B772	GE90-85B	DAC-II	0.149962
767	B763	PW4056	-	0.513376
767	B763	CF6-80C2B4	-	0.236805
767	B763	CF6-80C2B4F	-	0.144652
767	B762	JT9D-7R4D --7R4D1	-	0.105166
737	B734	CFM56-3-B1	-	0.360966

OAG Aircraft Code	BADA aircraft	Engine	Combustor Option	Fraction
737	B732	JT8D-9-series	Smoke-fix	0.278552
737	B735	CFM56-3-B1	-	0.208308
737	B732	JT8D-15	Smoke-fix	0.152174
D10	DC10	CF6-50C	-	0.520339
D10	DC10	JT9D-20	-	0.328568
D10	DC10	CF6-6K	-	0.151093
M11	MD11	CF6-80C2D1F	1862M39	0.521941
M11	MD11	PW4460	Reduced-smoke	0.279917
M11	MD11	PW4x62	Reduced-smoke	0.198142
72S	B722	JT8D-15	Reduced-emissions	0.646351
72S	B722	JT8D-9-series	Reduced-emissions	0.232536
72S	B722	JT8D-17	Smoke-fix	0.121113
343	A343	CFM56-5C4	-	0.652288
343	A343	CFM56-5C2	-	0.347712
734	B734	CFM56-3-B1	-	1.000000
310	A310	CF6-80C2A2	-	0.646147
310	A310	CF6-80C2A8	-	0.226306
310	A310	CF6-80A3	-	0.127547
340	A343	CFM56-5C4	-	0.652288
340	A343	CFM56-5C2	-	0.347712
738	B738	CFM56-7B26	-	1.000000
73S	B732	JT8D-9-series	Reduced-emissions	0.465516
73S	B732	JT8D-15	Reduced-emissions	0.253761
73S	B732	JT8D-15A	-	0.159548
73S	B732	JT8D-17	Smoke-fix	0.121175
330	A333	PW4168	Floatwall	0.391271
330	A333	CF6-80E1A2	-	0.321593
330	A333	Trent-768	-	0.287136
735	B735	CFM56-3C-1	-	1.000000
319	A319	V2522-A5	-	0.419986
319	A319	CFM56-5A5	-	0.392978

OAG Aircraft Code	BADA aircraft	Engine	Combustor Option	Fraction
319	A319	CFM56-5B6/P	-	0.187036
D9S	DC93	JT8D-7-series	Smoke-fix	0.382470
D9S	DC93	JT8D-9-series	Reduced-emissions	0.452038
D9S	DC93	JT8D-17	Smoke-fix	0.165492
73G	B737	CFM56-7B26	-	0.506083
73G	B737	CFM56-7B20	-	0.493917

Appendix K Aircraft-Engine matchings based on Quadros et al. (2022)

Table 42: Aircraft-engine matchings based on Quadros et al. (2022)

OAG Aircraft Code	BADA aircraft	Engine	Combustor Option	Fraction
310	A310	CF6-80C2A2	1862M39	0.90
310	A310	PW4156	Reduced-smoke	0.10
312	A310	CF6-80C2A2	1862M39	0.90
312	A310	PW4156	Reduced-smoke	0.10
313	A310	CF6-80C2A2	1862M39	0.90
313	A310	PW4156	Reduced-smoke	0.10
318	A318	CFM56-5B8/3	Tech-Insertion	0.58
318	A318	PW6122A	Talon-II	0.42
319	A319	CFM56-5B5/3	Tech-Insertion	0.58
319	A319	V2524-A5-SelectOne™-Upgrade-Package	Floatwall	0.42
320	A320	CFM56-5B4/3	Tech-Insertion	0.58
320	A320	V2527-A5-SelectOne™-Upgrade-Package	Floatwall	0.42
321	A321	CFM56-5B3/3	Tech-Insertion	0.58
321	A321	V2533-A5-SelectOne™-Upgrade-Package	Floatwall	0.42
330	A332	Trent-772	Phase5	0.68
330	A332	CF6-80E1A4	Low-emissions	0.17
330	A332	PW4168A-1D	Talon-IIB	0.15
332	A332	Trent-772	Phase5	0.68
332	A332	CF6-80E1A4	Low-emissions	0.17
332	A332	PW4168A-1D	Talon-IIB	0.15
333	A333	Trent-772	Phase5	0.58
333	A333	CF6-80E1A4	Low-emissions	0.28
333	A333	PW4168A	Talon-II	0.14
380	A388	GP7270	-	0.52

OAG Aircraft Code	BADA aircraft	Engine	Combustor Option	Fraction
380	A388	Trent-972E-84	Phase5-Tiled	0.48
388	A388	GP7270	-	0.52
388	A388	Trent-972E-84	Phase5-Tiled	0.48
744	B744	CF6-80C2B1F	-	0.48
744	B744	RB211-524H-T	-	0.34
744	B744	PW4062	Phase-III	0.18
747	B744	CF6-80C2B1F	-	0.48
747	B744	RB211-524H-T	-	0.34
747	B744	PW4062	Phase-III	0.18
752	B752	RB211-535E4B	Phase5	0.58
752	B752	PW2037	-	0.42
753	B753	RB211-535E4B	Phase5	0.71
753	B753	PW2040	-	0.29
757	B752	RB211-535E4B	Phase5	0.58
757	B752	PW2037	-	0.42
762	B762	CF6-80A2	-	0.50
762	B762	PW4060	Phase-III	0.50
763	B763	CF6-80C2B7F	1862M39	0.72
763	B763	PW4060	Reduced-smoke	0.25
763	B763	RB211-524H-T	-	0.03
767	B763	CF6-80C2B7F	1862M39	0.72
767	B763	PW4060	Reduced-smoke	0.25
767	B763	RB211-524H-T	-	0.03
772	B772	Trent-895	-	0.36
772	B772	GE90-90B	DAC-II	0.33
772	B772	PW4090	Floatwall	0.31
773	B773	Trent-892	-	0.70
773	B773	PW4098	-	0.30
777	B773	Trent-892	-	0.70
777	B773	PW4098	-	0.30
781	B78X	GEnx-1B76A/P2	TAPS	0.69
781	B78X	Trent-1000-K3	Phase5-Tiled	0.31

OAG Aircraft Code	BADA aircraft	Engine	Combustor Option	Fraction
787	B788	GEnx-1B70/75/P2	TAPS	0.65
787	B788	Trent-1000-H3	Phase5-Tiled	0.35
788	B788	GEnx-1B70/75/P2	TAPS	0.65
788	B788	Trent-1000-H3	Phase5-Tiled	0.35
789	B789	GEnx-1B74/75/P2	TAPS	0.63
789	B789	Trent-1000-K3	Phase5-Tiled	0.37
31B	A319	CFM56-5B5/3	Tech-Insertion	0.58
31B	A319	V2524-A5-SelectOne™-Upgrade-Package	Floatwall	0.42
31F	A310	CF6-80C2A2	1862M39	0.90
31F	A310	PW4156	Reduced-smoke	0.10
31X	A310	CF6-80C2A2	1862M39	0.90
31X	A310	PW4156	Reduced-smoke	0.10
31Y	A310	CF6-80C2A2	1862M39	0.90
31Y	A310	PW4156	Reduced-smoke	0.10
32A	A320	CFM56-5B4/3	Tech-Insertion	0.58
32A	A320	V2527-A5-SelectOne™-Upgrade-Package	Floatwall	0.42
32B	A321	CFM56-5B3/3	Tech-Insertion	0.58
32B	A321	V2533-A5-SelectOne™-Upgrade-Package	Floatwall	0.42
32N	A20N	LEAP-1A26/26E1	TAPS-II	0.53
32N	A20N	PW1127G-JM TALON-X	-Block-D	0.47
32Q	A21N	LEAP-1A35A/33/33B2/32/30	TAPS-II	0.53
32Q	A21N	PW1133G-JM TALON-X	-Block-D	0.47
32S	A320	CFM56-5B4/3	Tech-Insertion	0.58
32S	A320	V2527-A5-SelectOne™-Upgrade-Package	Floatwall	0.42
33F	A332	Trent-772	Phase5	0.68
33F	A332	CF6-80E1A4	Low-emissions	0.17
33F	A332	PW4168A-1D	Talon-IIB	0.15
33X	A332	Trent-772	Phase5	0.68
33X	A332	CF6-80E1A4	Low-emissions	0.17

OAG Aircraft Code	BADA aircraft	Engine	Combustor Option	Fraction
33X	A332	PW4168A-1D	Talon-IIB	0.15
38F	A388	GP7270	-	0.52
38F	A388	Trent-972E-84	Phase5-Tiled	0.48
74E	B744	CF6-80C2B1F	-	0.48
74E	B744	RB211-524H-T	-	0.34
74E	B744	PW4062	Phase-III	0.18
74F	B744	CF6-80C2B1F	-	0.48
74F	B744	RB211-524H-T	-	0.34
74F	B744	PW4062	Phase-III	0.18
74J	B744	CF6-80C2B1F	-	0.48
74J	B744	RB211-524H-T	-	0.34
74J	B744	PW4062	Phase-III	0.18
74M	B744	CF6-80C2B1F	-	0.48
74M	B744	RB211-524H-T	-	0.34
74M	B744	PW4062	Phase-III	0.18
74Y	B744	CF6-80C2B1F	-	0.48
74Y	B744	RB211-524H-T	-	0.34
74Y	B744	PW4062	Phase-III	0.18
75F	B752	RB211-535E4B	Phase5	0.58
75F	B752	PW2037	-	0.42
75M	B752	RB211-535E4B	Phase5	0.58
75M	B752	PW2037	-	0.42
75T	B753	RB211-535E4B	Phase5	0.71
75T	B753	PW2040	-	0.29
75V	B752	RB211-535E4B	Phase5	0.58
75V	B752	PW2037	-	0.42
75W	B752	RB211-535E4B	Phase5	0.58
75W	B752	PW2037	-	0.42
76F	B763	CF6-80C2B7F	1862M39	0.72
76F	B763	PW4060	Reduced-smoke	0.25
76F	B763	RB211-524H-T	-	0.03
76V	B763	CF6-80C2B7F	1862M39	0.72

OAG Aircraft Code	BADA aircraft	Engine	Combustor Option	Fraction
76V	B763	PW4060	Reduced-smoke	0.25
76V	B763	RB211-524H-T	-	0.03
76W	B763	CF6-80C2B7F	1862M39	0.72
76W	B763	PW4060	Reduced-smoke	0.25
76W	B763	RB211-524H-T	-	0.03
76X	B762	CF6-80A2	-	0.50
76X	B762	PW4060	Phase-III	0.50
76Y	B763	CF6-80C2B7F	1862M39	0.72
76Y	B763	PW4060	Reduced-smoke	0.25
76Y	B763	RB211-524H-T	-	0.03
A380	A388	GP7270	-	0.52
A380	A388	Trent-972E-84	Phase5-Tiled	0.48
AB6	A306	CF6-80C2A5F	1862M39	0.56
AB6	A306	PW4158	Reduced-smoke	0.44
ABY	A306	CF6-80C2A5F	1862M39	0.56
ABY	A306	PW4158	Reduced-smoke	0.44
D10	DC10	CF6-50C2	Low-emissions-fuel-nozzle	0.91
D10	DC10	JT9D-59A	-	0.09
D11	DC10	CF6-50C2	Low-emissions-fuel-nozzle	0.91
D11	DC10	JT9D-59A	-	0.09
D1C	DC10	CF6-50C2	Low-emissions-fuel-nozzle	0.91
D1C	DC10	JT9D-59A	-	0.09
D1F	DC10	CF6-50C2	Low-emissions-fuel-nozzle	0.91
D1F	DC10	JT9D-59A	-	0.09
D1M	DC10	CF6-50C2	Low-emissions-fuel-nozzle	0.91
D1M	DC10	JT9D-59A	-	0.09
D1X	DC10	CF6-50C2	Low-emissions-fuel-nozzle	0.91
D1X	DC10	JT9D-59A	-	0.09
D1Y	DC10	CF6-50C2	Low-emissions-fuel-nozzle	0.91
D1Y	DC10	JT9D-59A	-	0.09
M11	MD11	CF6-80C2D1F	1862M39	0.59
M11	MD11	PW4460	Reduced-smoke	0.41

OAG Aircraft Code	BADA aircraft	Engine	Combustor Option	Fraction
M1F	MD11	CF6-80C2D1F	1862M39	0.59
M1F	MD11	PW4460	Reduced-smoke	0.41
M1M	MD11	CF6-80C2D1F	1862M39	0.59
M1M	MD11	PW4460	Reduced-smoke	0.41

References

Agarwal, A., 2021. Quantifying and reducing the uncertainties in global contrail radiative forcing (PhD Thesis). Massachusetts Institute of Technology, Cambridge.

Agarwal, A., Meijer, V.R., Eastham, S.D., Speth, R.L., Barrett, S.R.H., 2022. Reanalysis-driven simulations may overestimate persistent contrail formation by 100%–250%. Environmental Research Letters 17, 014045. https://doi.org/10.1088/1748-9326/ac38d9

Agarwal, A., Speth, R.L., Fritz, T.M., Jacob, S.D., Rindlisbacher, T., Iovinelli, R., Owen, B., Miake-Lye, R.C., Sabnis, J.S., Barrett, S.R.H., 2019. SCOPE11 Method for Estimating Aircraft Black Carbon Mass and Particle Number Emissions. Environ Sci Technol 53, 1364–1373. https://doi.org/10.1021/acs.est.8b04060

Ahrens, D., Méry, Y., Guénard, A., Miake-Lye, R.C., 2022. A New Approach to Estimate Particulate Matter Emissions From Ground Certification Data: The nvPM Mission Emissions Estimation Methodology (MEEM). Volume 3A: Combustion, Fuels, and Emissions. https://doi.org/10.1115/GT2022-81277

Air Transport Action Group, 2021. Waypoint 2050. Second edition: September 2021.

Airlines For America, 2022a. World Airlines Traffic and Capacity [WWW Document]. URL https://www.airlines.org/dataset/world-airlines-traffic-and-capacity/ (accessed 10.11.23).

Airlines For America, 2022b. U.S. Airline Traffic and Capacity [WWW Document]. URL https://www.airlines.org/dataset/annual-results-u-s-airlines-2/ (accessed 10.11.23).

Åkerman, J., Kamb, A., Larsson, J., Nässén, J., 2021. Low-carbon scenarios for long-distance travel 2060. Transp Res D Transp Environ 99, 103010. https://doi.org/10.1016/J.TRD.2021.103010

Arunachalam, S., Wang, B., Davis, N., Baek, B.H., Levy, J.I., 2011. Effect of chemistry-transport model scale and resolution on population exposure to $PM_{2.5}$ from aircraft emissions during landing and takeoff. Atmos Environ 45, 3294–3300. https://doi.org/10.1016/J.ATMOSENV.2011.03.029

Ashok, A., Dedoussi, I.C., Yim, S.H.L., Balakrishnan, H., Barrett, S.R.H., 2014. Quantifying the air quality-CO_2 tradeoff potential for airports. Atmos Environ 99, 546–555. https://doi.org/10.1016/J.ATMOSENV.2014.10.024

ATA and Ellondee, 2018. Understanding the potential and costs for reducing UK aviation emissions, Report to the Committee on Climate Change and the Department for Transport.

ATAG, 2018. Aviation benefits beyond borders.

Avila, D., Sherry, L., Thompson, T., 2019. Reducing global warming by airline contrail avoidance: A case study of annual benefits for the contiguous United States. Transp Res Interdiscip Perspect 2, 100033. https://doi.org/10.1016/j.trip.2019.100033

Bann, S.J., Malina, R., Staples, M.D., Suresh, P., Pearlson, M., Tyner, W.E., Hileman, J.I., Barrett, S., 2017. The costs of production of alternative jet fuel: A harmonized stochastic assessment. Bioresour Technol 227, 179–187. https://doi.org/10.1016/J.BIORTECH.2016.12.032

Ban-Weiss, G.A., Cao, L., Bala, G., Caldeira, K., 2012. Dependence of climate forcing and response on the altitude of black carbon aerosols. Clim Dyn 38, 897–911. https://doi.org/10.1007/s00382-011-1052-y

Barrett, S.R.H., Britter, R.E., Waitz, I.A., 2010a. Global Mortality Attributable to Aircraft Cruise Emissions. Environ Sci Technol 44, 7736–7742. https://doi.org/10.1021/es101325r

Barrett, S.R.H., Prather, M., Penner, J., Selkirk, H., Balasubramanian, S.N., Dopelheuer, A., Fleming, G., Gupta, M., Halthore, R., Hileman, J., Jacobson, M., Kuhn, S., Lukachko, S., Miake-Lye, R., Petzold, A., Roof, C., Schaefer, M., Schumann, U., Waitz, I., Wayson, R., 2010b. Guidance on the use of AEDT gridded aircraft emissions in atmospheric models Guidance on the use of AEDT Gridded Aircraft Emissions in Atmospheric Models Federal Aviation Administration Washington, DC Guidance for Using AEDT Gridded Emissions Data.

Barrett, S.R.H., Speth, R.L., Eastham, S.D., Dedoussi, I.C., Ashok, A., Malina, R., Keith, D.W., 2015. Impact of the Volkswagen emissions control defeat device on US public health. Environmental Research Letters 10, 114005. https://doi.org/10.1088/1748-9326/10/11/114005

Barrett, S.R.H., Yim, S.H.L., Gilmore, C.K., Murray, L.T., Kuhn, S.R., Tai, A.P.K., Yantosca, R.M., Byun, D.W., Ngan, F., Li, X., Levy, J.I., Ashok, A., Koo, J., Wong, H.M., Dessens, O., Balasubramanian, S.N., Fleming, G.G., Pearlson, M.N., Wollersheim, C., Malina, R., Arunachalam, S., Binkowski, F.S., Leibensperger, E.M., Jacob, D.J., Hileman, J.I., Waitz, I.A., 2012. Public Health, Climate, and Economic Impacts of Desulfurizing Jet Fuel. Environ Sci Technol 46, 4275–4282. https://doi.org/10.1021/es203325a

Baughcum, S.L., Henderson, S.C., Tritz, T.G., 1996a. Scheduled Civil Aircraft Emission Inventories for 1976 and 1984: Database Development and Analysis.

Baughcum, S.L., Tritz, T.G., Henderson, S.C., Pickett, D.C., 1996b. Scheduled Civil Aircraft Emission Inventories for 1992: Database Development and Analysis.

Berk, M.M., Bollen, J.C., Eerens, H.C., Manders, A.J.G., Van Vuuren, D.P., Bollen, J.C., 2006. Sustainable energy: trade-offs and synergies between energy security, competitiveness, and environment. Bilthoven.

Berntsen, T.K., Fuglestvedt, J.S., 2008. Global temperature responses to current emissions from the transport sectors. Proc Natl Acad Sci U S A 105, 19154–19159. https://doi.org/10.1073/pnas.0804844105

Berntsen, T.K., Tanaka, K., Fuglestvedt, J.S., 2010. Does black carbon abatement hamper CO 2 abatement? Clim Change 103, 627–633. https://doi.org/10.1007/s10584-010-9941-3

Beyersdorf, A.J., Timko, M.T., Ziemba, L.D., Bulzan, D., Corporan, E., Herndon, S.C., Howard, R., Miake-Lye, R., Thornhill, K.L., Winstead, E., Wey, C., Yu, Z., Anderson, B.E., 2014. Reductions in aircraft particulate emissions due to the use of Fischer-Tropsch fuels. Atmos Chem Phys 14, 11–23. https://doi.org/10.5194/acp-14-11-2014

Bickel, M., Ponater, M., Bock, L., Burkhardt, U., Reineke, S., 2020a. Estimating the effective radiative forcing of contrail cirrus. J Clim 33, 1991–2005. https://doi.org/10.1175/JCLI-D-19-0467.1

Bickel, M., Ponater, M., Bock, L., Burkhardt, U., Reineke, S., 2020b. Estimating the effective radiative forcing of contrail cirrus. J Clim 33, 1991–2005. https://doi.org/10.1175/JCLI-D-19-0467.1

Bishop, S., 2022. pytz: World timezone definitions, modern and historical.

Bock, L., 2014. Modellierung von Kondensstreifenzirren: Mikrophysikalische und optische Eigenschaften. Ludwig-Maximilians-Universität, München.

Bock, L., Burkhardt, U., 2019. Contrail cirrus radiative forcing for future air traffic. Atmos Chem Phys 19, 8163–8174. https://doi.org/10.5194/acp-19-8163-2019

Bock, L., Burkhardt, U., 2016. Reassessing properties and radiative forcing of contrail cirrus using a climate model. J Geophys Res 121, 9717–9736. https://doi.org/10.1002/2016JD025112

Brasseur, G.P., Gupta, M., Anderson, B.E., Balasubramanian, S.N., Barrett, S.R.H., Duda, D., Fleming, G., Forster, P.M., Fuglestvedt, J.S., Gettelman, A., Halthore, R.N., Jacob, S.D., Jacobson, M.Z., Khodayari, A., Liou, K.-N.N., Lund, M.T., Miake-Lye, R.C., Minnis, P., Olsen, S., Penner, J.E., Prinn, R., Schumann, U., Selkirk, H.B., Sokolov, A., Unger, N., Wolfe, P., Wong, H.-W.W., Wuebbles, D.W., Yi, B., Yang, P., Zhou, C., 2016. Impact of aviation on climate: FAA's Aviation Climate Change Research Initiative (ACCRI) phase II. Bull Am Meteorol Soc 97, 561–583. https://doi.org/10.1175/BAMS-D-13-00089.1

Brewer, G., 1991. Hydrogen Aircraft Technology. CRC Press.

Brunelle-Yeung, E., Masek, T., Rojo, J.J., Levy, J.I., Arunachalam, S., Miller, S.M., Barrett, S.R.H., Kuhn, S.R., Waitz, I.A., 2014. Assessing the impact of aviation environmental policies on public health. Transp Policy (Oxf) 34, 21–28. https://doi.org/10.1016/J.TRANPOL.2014.02.015

Burkhardt, U., Bock, L., Bier, A., 2018. Mitigating the contrail cirrus climate impact by reducing aircraft soot number emissions. NPJ Clim Atmos Sci 1, 37. https://doi.org/10.1038/s41612-018-0046-4

Burkhardt, U., Kärcher, B., 2011. Global radiative forcing from contrail cirrus. Nat Clim Chang 1, 54–58. https://doi.org/10.1038/nclimate1068

CAAFI, n.d. CAAFI - Fuel Qualification [WWW Document]. URL https://www.caafi.org/focus_areas/fuel_qualification.html (accessed 5.13.21).

Caiazzo, F., Agarwal, A., Speth, R.L., Barrett, S.R.H., 2017. Impact of biofuels on contrail warming. Environmental Research Letters 12, 114013. https://doi.org/10.1088/1748-9326/aa893b

Cameron, M.A., Jacobson, M.Z., Barrett, S.R.H., Bian, H., Chen, C.C., Eastham, S.D., Gettelman, A., Khodayari, A., Liang, Q., Selkirk, H.B., Unger, N., Wuebbles, D.J., Yue, X., 2017. An intercomparative study of the effects of aircraft emissions on surface air quality. Journal of Geophysical Research: Atmospheres 122, 8325–8344. https://doi.org/10.1002/2016JD025594

Cames, M., Harthan, R.O., Füssler, J., Lazarus, M., Lee, C.M., Erickson, P., Spalding-Fecher, R., 2016. How additional is the Clean Development Mechanism? Berlin.

Chen, C.-C., Gettelman, A., 2016. Simulated 2050 aviation radiative forcing from contrails and aerosols 16, 7317–7333. https://doi.org/10.5194/acp-16-7317-2016

Chen, C.C., Gettelman, A., 2013. Simulated radiative forcing from contrails and contrail cirrus. Atmos Chem Phys 13, 12525–12536. https://doi.org/10.5194/acp-13-12525-2013

Clean Sky, 2020. Hydrogen-powered aviation: preparing for take-off.

Cooper, J., Dubey, L., Bakkaloglu, S., Hawkes, A., 2022. Hydrogen emissions from the hydrogen value chain-emissions profile and impact to global warming. Science of The Total Environment 830, 154624. https://doi.org/10.1016/J.SCITOTENV.2022.154624

Crippa, M., Janssens-Maenhout, G., Dentener, F., Guizzardi, D., Sindelarova, K., Muntean, M., Van Dingenen, R., Granier, C., 2016. Forty years of improvements in European air quality: regional policy-industry interactions with global impacts. Atmos. Chem. Phys 16, 3825–3841. https://doi.org/10.5194/acp-16-3825-2016

Cumpsty, N., Heyes, A., 2015. Jet Propulsion. A simple guide to the aerodynamics and thermodynamic design and performance of jet engines, Third edition. ed. Cambridge University press.

Davis, S.M., Hegglin, M.I., Fujiwara, M., Dragani, R., Harada, Y., Kobayashi, C., Long, C., Manney, G.L., Nash, E.R., Potter, G.L., Tegtmeier, S., Wang, T., Wargan, K., Wright, J.S., 2017. Assessment of upper tropospheric and stratospheric water vapor and ozone in reanalyses as part of S-RIP. Atmos Chem Phys 17, 12743–12778. https://doi.org/10.5194/acp-17-12743-2017

de Jong, S., Staples, M., Grobler, C., Daioglou, V., Malina, R., Barrett, S., Hoefnagels, R., Faaij, A., Junginger, M.,

2018. Using dynamic relative climate impact curves to quantify the climate impact of bioenergy production systems over time. GCB Bioenergy 11, 427–443. https://doi.org/10.1111/gcbb.12573

Dedoussi, I.C., Allroggen, F., Flanagan, R., Hansen, T., Taylor, B., Barrett, S.R.H.H., Boyce, J.K., 2019. The Co-Pollutant Cost of Carbon: An Analysis of the U.S. Electric Power Generation Sector. Under consideration for publication with ERL. https://doi.org/10.1088/1748-9326/ab34e3

Dedoussi, I.C., Barrett, S.R.H., 2014. Air pollution and early deaths in the United States. Part II: Attribution of PM2.5 exposure to emissions species, time, location and sector. Atmos Environ 99, 610–617. https://doi.org/10.1016/j.atmosenv.2014.10.033

Dellink, R., Chateau, J., Lanzi, E., Magné, B., 2017. Long-term economic growth projections in the Shared Socioeconomic Pathways. Global Environmental Change 42, 200–214. https://doi.org/10.1016/J.GLOENVCHA.2015.06.004

DfT, 2017. UK Aviation Forecasts 2017.

Dorbian, C.S., Wolfe, P.J., Waitz, I.A., 2011. Estimating the climate and air quality benefits of aviation fuel and emissions reductions. Atmos Environ 45, 2750–2759. https://doi.org/10.1016/j.atmosenv.2011.02.025

Dray, L., Doyme, K., 2019. Carbon leakage in aviation policy. Climate Policy 19, 1284–1296. https://doi.org/10.1080/14693062.2019.1668745/SUPPL_FILE/TCPO_A_1668745_SM8274.DOCX

Dray, L., Schäfer, A.W., 2021. Initial Long-Term Scenarios for COVID-19's Impact on Aviation and Implications for Climate Policy: https://doi.org/10.1177/03611981211045067 036119812110450. https://doi.org/10.1177/03611981211045067

Dray, L., Schäfer, A.W., Grobler, C., Falter, C., Allroggen, F., Stettler, M.E.J., Barrett, S.R.H., 2022. Cost and emissions pathways towards net-zero climate impacts in aviation. Nature Climate Change 2022 12:10 12, 956–962. https://doi.org/10.1038/s41558-022-01485-4

Dray, L.M., Krammer, P., Doyme, K., Wang, B., Al Zayat, K., O'Sullivan, A., Schäfer, A.W., 2019. AIM2015: Validation and initial results from an open-source aviation systems model. Transp Policy (Oxf) 79, 93–102. https://doi.org/10.1016/J.TRANPOL.2019.04.013

Dray, L.M., Schäfer, A.W., Al Zayat, K., 2018. The Global Potential for CO2 Emissions Reduction from Jet Engine Passenger Aircraft. Transportation Research Record: Journal of the Transportation Research Board 2672, 40–51. https://doi.org/10.1177/0361198118787361

Driscoll, C.T., Buonocore, J.J., Levy, J.I., Lambert, K.F., Burtraw, D., Reid, S.B., Fakhraei, H., Schwartz, J., 2015. US power plant carbon standards and clean air and health co-benefits. Nat Clim Chang 5, 535–540. https://doi.org/10.1038/nclimate2598

Eastham, S.D., Barrett, S.R.H., 2016. Aviation-attributable ozone as a driver for changes in mortality related to air quality and skin cancer. Atmos Environ 144, 17–23. https://doi.org/10.1016/J.ATMOSENV.2016.08.040

Edwards, T., Moses, C., Dryer, F., 2010. Evaluation of combustion performance of alternative aviation fuels, in: 46th AIAA/ASME/SAE/ASEE Joint Propulsion Conference and Exhibit. https://doi.org/10.2514/6.2010-7155

Elmourad, J.A., 2023. Evaluating Fuel-Climate Tradeoffs in Contrail Avoidance.

EPA, U., 2009. Stationary Gas Turbines, in: AP-42, Fifth Edition Compilation of Air Pollutant Emissions Factors, Volume 1: Stationary Point and Area Sources.

Etminan, M., Myhre, G., Highwood, E.J., Shine, K.P., 2016. Radiative forcing of carbon dioxide, methane, and nitrous oxide: A significant revision of the methane radiative forcing. Geophys Res Lett 43, 614–623. https://doi.org/10.1002/2016GL071930

Eurocontrol, 2022. User Manual Base of Aircraft Data (BADA) Revision 3.16.

Eurocontrol, 2003. AERO2K Filght Movement Inventory Project Report.

Fenech, S., Doherty, R.M., Heaviside, C., Vardoulakis, S., Macintyre, H.L., O&apos;Connor, F.M., O'connor, F.M., O&apos;Connor, F.M., 2018. The influence of model spatial resolution on simulated ozone and fine particulate matter for Europe: implications for health impact assessments. Atmos Chem Phys 18, 5765–5784. https://doi.org/10.5194/acp-18-5765-2018

Fichter, C., Marquart, S., Sausen, R., Lee, D.S., 2005. The impact of cruise altitude on contrails and related radiative forcing. Meteorologische Zeitschrift 14, 563–572. https://doi.org/10.1127/0941-2948/2005/0048

Flato, G., Marotzke, J., Abiodun, B., Braconnot, P., Chou, S.C., Collins, W., Cox, P., Driouech, F., Emori, S., Eyring, V., Forest, C., Gleckler, P., Guilyardi, E., Jakob, C., Kattsov, V., Reason, C., Rummukainen, M., 2013. Evaluation of Climate Models, in: Stocker, T.F., Qin, D., Plattner, G.-K., Tignor, M., Allen, S.K., Boschung, J., Nauels, A., Xia, Y., Bex, V., Midgley, P.M. (Eds.), Climate Change 2013: The Physical Science Basis. Contribution of Working Group I to the Fifth Assessment Report of the Intergovernmental Panel on Climate Change. Cambridge University Press, Cambridge, United Kingdom and New York, NY, USA, pp. 741–866. https://doi.org/10.1017/CBO9781107415324.020

Freeman, S., Lee, D.S., Lim, L.L., Skowron, A., De Leon, R.R., 2018. Trading off Aircraft Fuel Burn and NOx Emissions for Optimal Climate Policy. Environ. Sci. Technol 52, 11. https://doi.org/10.1021/acs.est.7b05719

Fritz, T.M., Eastham, S.D., Speth, R.L., Barrett, S.R.H., 2020. The role of plume-scale processes in long-term impacts of aircraft emissions. Atmos Chem Phys 20, 5697–5727. https://doi.org/10.5194/ACP-20-5697-2020

Frömming, C., Ponater, M., Dahlmann, K., Grewe, V., Lee, D.S., Sausen, R., 2012. Aviation-induced radiative forcing and surface temperature change in dependency of the emission altitude. Journal of Geophysical Research: Atmospheres 117, n/a-n/a. https://doi.org/10.1029/2012JD018204

Fuglestvedt, J., Rogelj, J., Millar, R.J., Allen, M., Boucher, O., Cain, M., Forster, P.M., Kriegler, E., Shindell, D., 2018. Implications of possible interpretations of greenhouse gas balance in the Paris Agreement. Philosophical Transactions of the Royal Society A: Mathematical, Physical and Engineering Sciences 376. https://doi.org/10.1098/RSTA.2016.0445

Fuglestvedt, J.S., Shine, K.P., Berntsen, T., Cook, J., Lee, D.S., Stenke, A., Skeie, R.B., Velders, G.J.M., Waitz, I.A., 2010. Transport impacts on atmosphere and climate: Metrics. Atmos Environ 44, 4648–4677. https://doi.org/10.1016/j.atmosenv.2009.04.044

Gasser, T., Peters, G.P., Fuglestvedt, J.S., Collins, W.J., Shindell, D.T., Ciais, P., 2017. Accounting for the climate-carbon feedback in emission metrics. Earth Syst. Dynam 8, 235–253. https://doi.org/10.5194/esd-8-235-2017

GBD 2016 Risk Factors Collaborators, 2017. Global, regional, and national comparative risk assessment of 84 behavioural, environmental and occupational, and metabolic risks or clusters of risks, 1990–2016: a systematic analysis for the Global Burden of Disease Study 2016. The Lancet 390, 1345–1422. https://doi.org/10.1016/S0140-6736(17)32366-8

GEA, 2012. Global Energy Assessment – Toward a Sustainable Future. Cambridge University Press, Cambridge, UK and New York, NY, USA and and the International Institute for Applied Systems Analysis, Laxenburg, Austria.

Gierens, K., Braun-Unkhoff, M., Le Clercq, P., Plohr, M., Schlager, H., Wolters, F., 2016. Condensation trails from biofuels/kerosene blends scoping study.

Gierens, K., Lim, L., Eleftheratos, K., 2008. A Review of Various Strategies for Contrail Avoidance, The Open Atmospheric Science Journal.

Gierens, K., Matthes, S., Rohs, S., 2020. How Well Can Persistent Contrails Be Predicted? Aerospace 7, 169. https://doi.org/10.3390/aerospace7120169

Gierens, K., Vázquez-Navarro, M., 2018. Statistical analysis of contrail lifetimes from a satellite perspective. Meteorologische Zeitschrift 27, 183–193. https://doi.org/10.1127/METZ/2018/0888

Gilmore, C.K., Barrett, S.R.H., Koo, J., Wang, Q., 2013. Temporal and spatial variability in the aviation NOx-related O3 impact. Environmental Research Letters 8. https://doi.org/10.1088/1748-9326/8/3/034027

Girod, B., van Vuuren, D.P., Deetman, S., 2012. Global travel within the 2°C climate target. Energy Policy 45, 152–166. https://doi.org/10.1016/j.enpol.2012.02.008

Gnadt, A.R., Speth, R.L., Sabnis, J.S., Barrett, S.R.H., 2019. Technical and environmental assessment of all-electric 180-passenger commercial aircraft. Progress in Aerospace Sciences 105, 1–30. https://doi.org/10.1016/J.PAEROSCI.2018.11.002

Gössling, S., Humpe, A., Fichert, F., Creutzig, F., 2021. COVID-19 and pathways to low-carbon air transport until 2050. Environmental Research Letters 16, 034063. https://doi.org/10.1088/1748-9326/ABE90B

Gottlieb, D., Orszag, S.A., 1977. Numerical Analysis of Spectral Methods. Society for Industrial and Applied Mathematics. https://doi.org/10.1137/1.9781611970425

Greenstone, M., 2016. A New Path Forward for an Empirical Social Cost of Carbon.

Grewe, V., Bock, L., Burkhardt, U., Dahlmann, K., Gierens, K., Hüttenhofer, L., Unterstrasser, S., Rao, A.G., Bhat, A., Yin, F., Reichel, T.G., Paschereit, O., Levy, Y., 2017a. Assessing the climate impact of the AHEAD multi-fuel blended wing body. Meteorologische Zeitschrift 26, 711–725. https://doi.org/10.1127/metz/2016/0758

Grewe, V., Bock, L., Burkhardt, U., Dahlmann, K., Gierens, K., Hüttenhofer, L., Unterstrasser, S., Rao, A.G., Bhat, A., Yin, F., Reichel, T.G., Paschereit, O., Levy, Y., 2017b. Assessing the climate impact of the AHEAD multi-fuel blended wing body. Meteorologische Zeitschrift 26, 711–725. https://doi.org/10.1127/metz/2016/0758

Grewe, V., Gangoli Rao, A., Grönstedt, T., Xisto, C., Linke, F., Melkert, J., Middel, J., Ohlenforst, B., Blakey, S., Christie, S., Matthes, S., Dahlmann, K., 2021. Evaluating the climate impact of aviation emission scenarios towards the Paris agreement including COVID-19 effects. Nature Communications 2021 12:1 12, 1–10. https://doi.org/10.1038/s41467-021-24091-y

Grobler, C., Wolfe, P.J., Dasadhikari, K., Dedoussi, I.C., Allroggen, F., Speth, R.L., Eastham, S.D., Agarwal, A., Staples, M.D., Sabnis, J., Barrett, S.R.H., 2019. Marginal climate and air quality costs of aviation emissions. Environmental Research Letters 14, 114031. https://doi.org/10.1088/1748-9326/ab4942

Hänsel, M.C., Drupp, M.A., Johansson, D.J.A., Nesje, F., Azar, C., Freeman, M.C., Groom, B., Sterner, T., 2020. Climate economics support for the UN climate targets. Nat Clim Chang 10, 781–789. https://doi.org/10.1038/s41558-020-0833-x

Hansen, J., Sato, M., Ruedy, R., Nazarenko, L., Lacis, A., Schmidt, G.A., Russell, G., Aleinov, I., Bauer, M., Bauer, S., Bell, N., Cairns, B., Canuto, V., Chandler, M., Cheng, Y., Genio, A. Del, Faluvegi, G., Fleming, E., Friend, A., Hall, T., Jackman, C., Kelley, M., Kiang, N., Koch, D., Lean, J., Lerner, J., Lo, K., Menon, S., Miller, R., Minnis, P., Novakov, T., Oinas, V., Perlwitz, Ja., Perlwitz, Ju., Rind, D., Romanou, A., Shindell, D., Stone, P., Sun, S., Tausnev, N., Thresher, D., Wielicki, B., Wong, T., Yao, M., Zhang, S., 2005. Efficacy of climate forcings. J Geophys Res 110, D18104. https://doi.org/10.1029/2005JD005776

Hassan, M., Pfaender, H., Mavris, D., 2018. Probabilistic assessment of aviation CO2 emission targets. Transp Res D Transp Environ 63, 362–376. https://doi.org/10.1016/J.TRD.2018.06.006

Heald, C.L., Collett, J.L., Lee, T., Benedict, K.B., Schwandner, F.M., Li, Y., Clarisse, L., Hurtmans, D.R., Van Damme, M., Clerbaux, C., Coheur, P.-F., Philip, S., Martin, R. V, Pye, H.O.T., 2012. Atmospheric ammonia and particulate inorganic nitrogen over the United States. Atmos. Chem. Phys 12, 10295–10312. https://doi.org/10.5194/acp-12-10295-2012

Henze, D.K., Hakami, A., Seinfeld, J.H., 2007. Development of the adjoint of GEOS-Chem. Atmos Chem Phys 7, 2413–2433. https://doi.org/10.5194/acp-7-2413-2007

Hepperle, M., 2012. Electric flight – potential and limitations, in: Energy Efficient Technologies and Concepts of Operation.

Hersbach, H., Bell, B., Berrisford, P., Hirahara, S., Horányi, A., Muñoz-Sabater, J., Nicolas, J., Peubey, C., Radu, R., Schepers, D., Simmons, A., Soci, C., Abdalla, S., Abellan, X., Balsamo, G., Bechtold, P., Biavati, G., Bidlot, J., Bonavita, M., De Chiara, G., Dahlgren, P., Dee, D., Diamantakis, M., Dragani, R., Flemming, J., Forbes, R., Fuentes, M., Geer, A., Haimberger, L., Healy, S., Hogan, R.J., Hólm, E., Janisková, M., Keeley, S., Laloyaux, P., Lopez, P., Lupu, C., Radnoti, G., de Rosnay, P., Rozum, I., Vamborg, F., Villaume, S., Thépaut, J., 2020. The ERA5 global reanalysis. Quarterly Journal of the Royal Meteorological Society 146, 1999–2049. https://doi.org/10.1002/qj.3803

Hileman, J., Katz, J.B., Mantilla, J.G., Fleming, G., 2008. Payload Fuel Energy Efficiency as a Metric for Aviation Environmental Performance. International Congress of Aeronautical Sciences.

Hileman, J.I., Stratton, R.W., Donohoo, P.E., 2010. Energy Content and Alternative Jet Fuel Viability. https://doi.org/10.2514/1.46232

Hoek, G., Krishnan, R.M., Beelen, R., Peters, A., Ostro, B., Brunekreef, B., Kaufman, J.D., 2013. Long-term air pollution exposure and cardio- respiratory mortality: a review. Environmental Health 12, 43. https://doi.org/10.1186/1476-069X-12-43

Holmes, C.D., Tang, Q.Q., Prather, M.J., 2011. Uncertainties in climate assessment for the case of aviation NO. Proceedings of the National Academy of Sciences 108, 10997–11002. https://doi.org/10.1073/pnas.1101458108

Hoor, P., Borken-Kleefeld, J., Caro, D., Dessens, O., Endresen, O., Gauss, M., Grewe, V., Hauglustaine, D., Isaksen, I.S.A.A., Jöckel, P., Lelieveld, J., Myhre, G., Meijer, E., Olivie, D., Prather, M., Schnadt Poberaj, C., Shine, K.P., Staehelin, J., Tang, Q., van Aardenne, J., van Velthoven, P., Sausen, R., 2009. The impact of traffic emissions on atmospheric ozone and OH: Results from QUANTIFY. Atmos Chem Phys 9, 3113–3136. https://doi.org/10.5194/acp-9-3113-2009

Howard, P.H., Sterner, T., 2017. Few and Not So Far Between: A Meta-analysis of Climate Damage Estimates. Environ Resour Econ (Dordr) 68, 197–225. https://doi.org/10.1007/s10640-017-0166-z

IATA, 2021. COVID-19: Airline industry financial outlook update.

ICAO, 2022. ICAO Aircraft Engine Emissions Databank.

ICAO, 2021. Effects of Novel Coronavirus on Civil Aviation: Economic Impact Analysis.

ICAO, 2020. Presentation of 2019 Air Transport Statistical Results.

ICAO, 2019. Aviation benefits report.

ICAO, 2018. Annex 16: Environmental Protection, Volume IV - Carbon Offsetting and Reduction Scheme for International Aviation (CORSIA).

ICAO, 2017. Annex 16: Environmental Protection, Volume III - CO_2 Certification Requirement.

ICAO, 2016a. Environmental Report.

ICAO, 2016b. ICAO Long-Term Traffic Forecasts Passenger and Cargo.

ICAO, 2008. Environmental Protection: Annex 16 to the Convention of International Civil Aviation. Volume 2.

ICAO, 2007. ICAO Environmental Report.

ICF Consulting, 2020. Assessment of ICAO's Global Market-Based Measure (CORSIA) pursuant to Article 28b and for studying cost pass-through pursuant to Article 3d of the EU ETS Directive.

IEA, 2021. Net Zero by 2050. Paris.

IEA, 2020a. Energy Technology Perspectives.

IEA, 2020b. Outlook for biogas and biomethane: Prospects for Organic Growth, in: World Energy Outlook Special Report. IEA/OECD, Paris.

IEA, 2019. The Future of Hydrogen. Paris.

IMF, 2021. World Economic Outlook: April 2021.

IRENA, 2021. World Energy Transitions Outlook: 1.5°C Pathway. International Renewable Energy Agency. Abu Dhabi.

Ivanovich, C.C., Ocko, I.I., Piris-Cabezas, P., Petsonk, A., 2019. Climate benefits of proposed carbon dioxide mitigation strategies for international shipping and aviation. Atmos Chem Phys 19, 14949–14965. https://doi.org/10.5194/ACP-19-14949-2019

Jerrett, M., Burnett, R.T., Pope, C.A., Ito, K., Thurston, G., Krewski, D., Shi, Y., Calle, E., Thun, M., 2009. Long-Term Ozone Exposure and Mortality. New England Journal of Medicine 360, 1085–1095. https://doi.org/10.1056/NEJMoa0803894

Jiang, J.H., Su, H., Zhai, C., Wu, L., Minschwaner, K., Molod, A.M., Tompkins, A.M., 2015. An assessment of upper troposphere and lower stratosphere water vapor in MERRA, MERRA2, and ECMWF reanalyses using Aura MLS observations. Journal of Geophysical Research: Atmospheres 120. https://doi.org/10.1002/2015JD023752

Johansson, T.B., Patwardhan, A., Nakicenovic, N., Gomez-Echeverri, L., 2012. Global Energy Assessment - Toward a Sustainable Future. Cambridge University Press, Cambridge, UK and New York, NY, USA and and the International Institute for Applied Systems Analysis, Laxenburg, Austria.

Joos, F., Roth, R., Fuglestvedt, J.S., Peters, G.P., Enting, I.G., Von Bloh, W., Brovkin, V., Burke, E.J., Eby, M., Edwards, N.R., Friedrich, T., Frölicher, T.L., Halloran, P.R., Holden, P.B., Jones, C., Kleinen, T., Mackenzie, F.T., Matsumoto, K., Meinshausen, M., Plattner, G.K., Reisinger, A., Segschneider, J., Shaffer, G., Steinacher, M., Strassmann, K., Tanaka, K., Timmermann, A., Weaver, A.J., 2013. Carbon dioxide and climate impulse response functions for the computation of greenhouse gas metrics: A multi-model analysis. Atmos Chem Phys 13, 2793–2825. https://doi.org/10.5194/acp-13-2793-2013

Kar, R., Bonnefoy, P.A., Hansman, R.J., Sgouridis, S., 2009. Dynamics of Implementation of Mitigating Measures to Reduce Commercial Aviation's Environmental Impacts, in: 9th AIAA Aviation Technology, Integration, and Operations Conference (ATIO). Hilton Head, South Carolina. https://doi.org/10.2514/6.2009-6935

Kärcher, B., 2018. Formation and radiative forcing of contrail cirrus. Nat Commun 9, 1824. https://doi.org/10.1038/s41467-018-04068-0

Kärcher, B., 1998. Physicochemistry of aircraft-generated liquid aerosols, soot, and ice particles 1. Model description. Journal of Geophysical Research Atmospheres 103, 17111–17128. https://doi.org/10.1029/98JD01044

Kärcher, B., 1995. A trajectory box model for aircraft exhaust plumes. Journal of Geophysical Research: Atmospheres 100, 18835–18844. https://doi.org/10.1029/95JD01638

Kärcher, B., Yu, F., 2009. Role of aircraft soot emissions in contrail formation. Geophys Res Lett 36. https://doi.org/10.1029/2008GL036649

Klima, K., 2005. Assessment of a Global Contrail Modeling Method and Operational Strategies for Contrail Mitigation. Massachusetts Institute of Technology.

Klöwer, M., Allen, M., Lee, D., Proud, S., Gallagher, L., Skowron, A., 2021. Quantifying aviation's contribution to global warming. https://doi.org/10.1002/ESSOAR.10507359.1

Köhler, M.O., Rädel, G., Dessens, O., Shine, K.P., Rogers, H.L., Wild, O., Pyle, J.A., 2008. Impact of perturbations to nitrogen oxide emissions from global aviation. Journal of Geophysical Research Atmospheres 113, 1–15. https://doi.org/10.1029/2007JD009140

Koo, J., Wang, Q., Henze, D.K., Waitz, I.A., Barrett, S.R.H., 2013. Spatial sensitivities of human health risk to intercontinental and high-altitude pollution. Atmos Environ 71, 140–147. https://doi.org/10.1016/J.ATMOSENV.2013.01.025

Kundu, K.P., Penkot, P.J., Yang, S.L., 1998. Simplified Jet-A/Air Combustion Mechanisms for Calculation of NOx Emissions. https://doi.org/10.2514/6.1998-3986

Lee, C.J., Martin, R. V., Henze, D.K., Brauer, M., Cohen, A., Donkelaar, A. van, 2015. Response of Global Particulate-Matter-Related Mortality to Changes in Local Precursor Emissions. Environ Sci Technol 49, 4335–4344. https://doi.org/10.1021/acs.est.5b00873

Lee, D.S., Fahey, D.W., Forster, P.M., Newton, P.J., Wit, R.C.N., Lim, L.L., Owen, B., Sausen, R., 2009. Aviation and global climate change in the 21st century. Atmos Environ 43, 3520–3537. https://doi.org/10.1016/j.atmosenv.2009.04.024

Lee, D.S., Pitari, G., Grewe, V., Gierens, K., Penner, J.E., Petzold, A., Prather, M.J., Schumann, U., Bais, A., Berntsen, T., Iachetti, D., Lim, L.L., Sausen, R., 2010. Transport impacts on atmosphere and climate: Aviation. Atmos Environ 44, 4678–4734. https://doi.org/10.1016/j.atmosenv.2009.06.005

Lee, D.S.S., Fahey, D.W.W., Skowron, A., Allen, M.R.R., Burkhardt, U., Chen, Q., Doherty, S.J.J., Freeman, S., Forster, P.M.M., Fuglestvedt, J., Gettelman, A., De León, R.R., Lim, L.L.L., Lund, M.T.T., Millar, R.J.J., Owen, B., Penner, J.E.E., Pitari, G., Prather, M.J.J., Sausen, R., Wilcox, L.J., León, R.R. De, Lim, L.L.L., Lund, M.T.T., Millar, R.J.J., Owen, B., Penner, J.E.E., Pitari, G., Prather, M.J.J., Sausen, R., 2020. The contribution of global aviation to anthropogenic climate forcing for 2000 to 2018. Atmos Environ 117834. https://doi.org/10.1016/j.atmosenv.2020.117834

Lee, J.J. 1974-, 2005. Modeling aviation's global emissions, uncertainty analysis, and applications to policy.

Lefebvre, A., 1983. Gas Turbine Combustion. Taylor & Francis.

Leipold, A., Aptsiauri Richard-Gregor, Berghof, R., Claßen Katrin, Dzikus, N., Flüthmann, N., Grewe, V., Göhlich, L., Grimme, W., Günther, Y., Jaksche, R., Jung, M., Knabe, F., Kutne, P., Le Clercq, P., Pabst, H., Poggel, S., Staggat, M., Wicke, K., Wolters, F., Zanger, J., Zill, T., 2021. DEPA 2050 Development Pathways for Aviation up to 2050 - Final Report .

Levy, J.I., Diez, D., Dou, Y., Barr, C.D., Dominici, F., 2012a. A Meta-Analysis and Multisite Time-Series Analysis of the Differential Toxicity of Major Fine Particulate Matter Constituents. Am J Epidemiol 175, 1091–1099. https://doi.org/10.1093/aje/kwr457

Levy, J.I., Woody, M., Baek, B.H., Shankar, U., Arunachalam, S., 2012b. Current and Future Particulate-Matter-Related Mortality Risks in the United States from Aviation Emissions During Landing and Takeoff. Risk Analysis 32, 237–249. https://doi.org/10.1111/j.1539-6924.2011.01660.x

Li, Y., Henze, D.K., Jack, D., Kinney, P.L., 2016. The influence of air quality model resolution on health impact assessment for fine particulate matter and its components. Air Qual Atmos Health 9, 51–68. https://doi.org/10.1007/s11869-015-0321-z

Lieuwen, T.C., Yang, V., 2013. Gas Turbine Emissions. Cambridge University Press, Cambridge.

Lund, M.T., Aamaas, B., Berntsen, T.K., Bock, L., Burkhardt, U., Fuglestvedt, J.S., Shine, K.P., 2017a. Emission metrics for quantifying regional climate impacts of aviation. Earth System Dynamics 8, 547–563. https://doi.org/10.5194/esd-8-547-2017

Lund, M.T., Berntsen, T.K., Samset, B.H., 2017b. Sensitivity of black carbon concentrations and climate impact to aging and scavenging in OsloCTM2-M7. Atmos. Chem. Phys 17, 6003–6022. https://doi.org/10.5194/acp-17-6003-2017

Mahashabde, A., Wolfe, P., Ashok, A., Dorbian, C.S., He, Q., Fan, A., Lukachko, S., Mozdzanowska, A., Wollersheim, C., Barrett, S.R.H., Locke, M., Waitz, I.A., 2011. Assessing the environmental impacts of aircraft noise and emissions. Progress in Aerospace Sciences 47, 15–52. https://doi.org/10.1016/j.paerosci.2010.04.003

Mannstein, H., Spichtinger, P., Gierens, K., 2005. A note on how to avoid contrail cirrus. Transp Res D Transp Environ 10, 421–426. https://doi.org/10.1016/j.trd.2005.04.012

Marais, K.B., Lukachko, S.P., Jun, M., Mahashabde, A., Waitz, I.A., 2008. Assessing the impact of aviation on climate. Meteorologische Zeitschrift 17, 157–172. https://doi.org/10.1127/0941-2948/2008/0274

Marais, K.B., Reynolds, T.G., Uday, P., Muller, D., Lovegren, J., Dumont, J.-M., Hansman, R.J., 2013. Evaluation of potential near-term operational changes to mitigate environmental impacts of aviation. Proc Inst Mech Eng G J Aerosp Eng 227, 1277–1299. https://doi.org/10.1177/0954410012454095

Marquart, S., Ponater, M., Ström, L., Gierens, K., 2005. An upgraded estimate of the radiative forcing of cryoplane contrails. Meteorologische Zeitschrift 14, 573–582.

Marquart, S., Sausen, R., Ponater, M., Grewe, V., 2001. Estimate of the climate impact of cryoplanes. Aerosp Sci Technol 5, 73–84. https://doi.org/10.1016/S1270-9638(00)01084-1

Masiol, M., Harrison, R.M., 2014. Aircraft engine exhaust emissions and other airport-related contributions to ambient air pollution: A review. Atmos Environ 95, 409–455.

Meijer, V., 2023. Thesis proposal: Observation-driven mitigation of the climate impact of aircraft contrails.

Meinshausen, M., Raper, S.C.B., Wigley, T.M.L., 2011a. Emulating coupled atmosphere-ocean and carbon cycle models with a simpler model, MAGICC6 - Part 1: Model description and calibration. Atmos Chem Phys 11, 1417–1456. https://doi.org/10.5194/acp-11-1417-2011

Meinshausen, M., Smith, S.J., Calvin, K., Daniel, J.S., Kainuma, M.L.T., Lamarque, J.-F., Matsumoto, K., Montzka, S.A., Raper, S.C.B., Riahi, K., Thomson, A., Velders, G.J.M., van Vuuren, D.P.P., 2011b. The RCP greenhouse gas concentrations and their extensions from 1765 to 2300. Clim Change 109, 213–241. https://doi.org/10.1007/s10584-011-0156-z

Miller, C.J., Prashanth, P., Allroggen, F., Grobler, C., Sabnis, J.S., Speth, R.L., H Barrett, S.R., 2022. An environmental cost basis for regulating aviation NOx emissions. Environ Res Commun 4, 055002. https://doi.org/10.1088/2515-7620/AC6938

Mlawer, E.J., Taubman, S.J., Brown, P.D., Iacono, M.J., Clough, S.A., 1997. Radiative transfer for inhomogeneous atmospheres: RRTM, a validated correlated-k model for the longwave. Journal of Geophysical Research: Atmospheres 102, 16663–16682. https://doi.org/10.1029/97JD00237

Moore, R.H., Thornhill, K.L., Weinzierl, B., Sauer, D., D'Ascoli, E., Kim, J., Lichtenstern, M., Scheibe, M., Beaton, B., Beyersdorf, A.J., Barrick, J., Bulzan, D., Corr, C.A., Crosbie, E., Jurkat, T., Martin, R., Riddick, D., Shook, M., Slover, G., Voigt, C., White, R., Winstead, E., Yasky, R., Ziemba, L.D., Brown, A., Schlager, H., Anderson, B.E., 2017. Biofuel blending reduces particle emissions from aircraft engines at cruise conditions. Nature 543, 411–415. https://doi.org/10.1038/nature21420

Moss, R.H., Edmonds, J.A., Hibbard, K.A., Manning, M.R., Rose, S.K., van Vuuren, D.P., Carter, T.R., Emori, S., Kainuma, M., Kram, T., Meehl, G.A., Mitchell, J.F.B., Nakicenovic, N., Riahi, K., Smith, S.J., Stouffer, R.J., Thomson, A.M., Weyant, J.P., Wilbanks, T.J., 2010. The next generation of scenarios for climate change research and assessment. Nature 463, 747–756. https://doi.org/10.1038/nature08823

Murray, Lee T Jacob, Daniel J Logan, Jennifer A Hudman, Rynda C Koshak, William J, Murray, L T, Jacob, D J, Logan, J A, Hudman, R C, Koshak, W J, 2012. Optimized regional and interannual variability of lightning in a global chemical transport model constrained by LIS/OTD satellite data. J. Geophys. Res 117, 20307. https://doi.org/10.1029/2012JD017934

Myhre, G., Highwood, E.J., Shine, K.P., Stordal, F., 1998. New estimates of radiative forcing due to wel mixed greenhouse gases. Geophys Res Lett 25, 2715–2718.

Myhre, G., Shindell, D., Bréon, F., Collins, W., Fuglestvedt, J., Huang, J., Koch, D., Lamarque, J., Lee, D., Mendoza, B., Nakajima, T., Robock, A., Stephens, G., Takemura, T., Zhang, H., et al., 2013. Anthropogenic and Natural Radiative Forcing. In: Climate Change 2013: The Physical Science Basis. Contribution of Working Group I, in: Stocker, T.F., Qin, D., Plattner, G.-K., Tignor, M., Allen, S.K., Boschung, J., Nauels, A., Xia, Y., Bex, V., Midgley, P.M. (Eds.), Climate Change 2013: The Physical Science Basis. Contribution of Working Group I to the Fifth Assessment Report of the Intergovernmental Panel on Climate Change. Cambridge University Press, Cambridge, United Kingdom and New York, NY, USA.

Noppel, F., Singh, R., 2007. Overview on Contrail and Cirrus Cloud Avoidance Technology. https://doi.org/10.2514/1.28655

Noppel, F., Singh, R., Taylor, M., 2006. Contrail and cirrus cloud avoidance, in: Noppel, F., Singh, R., Taylor, M. (Eds.), 25th International Congress of the Aeronautical Sciences .

Nordhaus, W.D., 2017. Revisiting the social cost of carbon. Proceedings of the National Academy of Sciences 114, 1518–1523. https://doi.org/10.1073/pnas.1609244114

Oak Ridge National Laboratory, 2015. LandScan Global Population Distribution Data.

Ocko, I.B., Hamburg, S.P., 2022. Climate consequences of hydrogen leakage.

Olsen, S.C., Wuebbles, D.J., Owen, B., 2013. Comparison of global 3-D aviation emissions datasets. Atmos. Chem. Phys. 13, 429–441. https://doi.org/10.5194/acp-13-429-2013

OMB, 2003. Circular A-4.

O'Neill, B.C., Kriegler, E., Riahi, K., Ebi, K.L., Hallegatte, S., Carter, T.R., Mathur, R., van Vuuren, D.P., 2014. A new scenario framework for climate change research: The concept of shared socioeconomic pathways. Clim Change 122, 387–400. https://doi.org/10.1007/S10584-013-0905-2/TABLES/2

Paoli, R., Shariff, K., 2016. Contrail Modeling and Simulation. Annu Rev Fluid Mech 48, 393–427. https://doi.org/10.1146/annurev-fluid-010814-013619

Peck, J., Oluwole, O.O., Wong, H.-W., Miake-Lye, R.C., 2013. An algorithm to estimate aircraft cruise black carbon emissions for use in developing a cruise emissions inventory. J Air Waste Manage Assoc 63, 367–375. https://doi.org/10.1080/10962247.2012.751467

Penner, J.E., Lister, D.H., Griggs, D.J., Dokken, D.J., McFarland, M., 1999. Aviation and the global atmosphere. – A special report of IPCC working groups I and III. Cambridge University Press, Cambridge, UK and New York, NY, USA.

Pindyck, R.S., 2019. The social cost of carbon revisited. J Environ Econ Manage 94, 140–160. https://doi.org/10.1016/J.JEEM.2019.02.003

Ponater, M., Bickel, M., Bock, L., Burkhardt, U., 2021. Towards determining the contrail cirrus efficacy. Aerospace 8, 1–10. https://doi.org/10.3390/aerospace8020042

Ponater, M., Pechtl, S., Sausen, R., Schumann, U., Hüttig, G., 2006. Potential of the cryoplane technology to reduce aircraft climate impact: A state-of-the-art assessment. Atmos Environ 40, 6928–6944. https://doi.org/10.1016/j.atmosenv.2006.06.036

Prashanth, P., Eastham, S.D., Speth, R.L., Barrett, S.R.H., 2022. Aerosol formation pathways from aviation emissions. Environ Res Commun 4, 021002. https://doi.org/10.1088/2515-7620/ac5229

Quadros, F.D.A., Snellen, M., Dedoussi, I.C., 2020. Regional sensitivities of air quality and human health impacts to aviation emissions. Environmental Research Letters 15, 105013. https://doi.org/10.1088/1748-9326/ABB2C5

Quadros, F.D.A., Snellen, M., Sun, J., Dedoussi, I.C., 2022. Global Civil Aviation Emissions Estimates for 2017–2020 Using ADS-B Data. https://doi.org/10.2514/1.C036763 1–11. https://doi.org/10.2514/1.C036763

Rädel, G., Shine, K.P., 2010. Validating ECMWF forecasts for the occurrence of ice supersaturation using visual observations of persistent contrails and radiosonde measurements over England. Quarterly Journal of the Royal Meteorological Society 136, 1723–1732. https://doi.org/10.1002/qj.670

Rap, A., Forster, P.M., Haywood, J.M., Jones, A., Boucher, O., 2010. Estimating the climate impact of linear contrails using the UK Met Office climate model. Geophys Res Lett 37, 20703. https://doi.org/10.1029/2010GL045161

Reutter, P., Neis, P., Rohs, S., Sauvage, B., 2020. Ice supersaturated regions: properties and validation of ERA-Interim reanalysis with IAGOS in situ water vapour measurements. Atmos Chem Phys 20, 787–804. https://doi.org/10.5194/acp-20-787-2020

Reynolds, T.G., 2008. Analysis of Lateral Flight Inefficiency in Global Air Traffic Management, in: The 26th Congress of International Council of the Aeronautical Sciences (ICAS). Anchorage. https://doi.org/10.2514/6.2008-8865

Ricke, K., Drouet, L., Caldeira, K., Tavoni, M., 2018. Country-level social cost of carbon. Nat Clim Chang 8, 895–900. https://doi.org/10.1038/s41558-018-0282-y

Robinson, L.A., Hammitt, J.K., 2015. The effect of income on the value of mortality and morbidity risk reductions.

Roe, G.H., Baker, M.B., 2007. Why is climate sensitivity so unpredictable? Science 318, 629–32. https://doi.org/10.1126/science.1144735

Saltelli, A., Ratto, M., Andres, T., Campolongo, F., Cariboni, J., Gatelli, D., Saisana, M., Tarantola, S., 2008. Global Sensitivity Analysis. The Primer, Global Sensitivity Analysis. The Primer. https://doi.org/10.1002/9780470725184

Sanz-Morère, I., Eastham, S.D., Speth, R.L., Barrett, S.R.H., 2020. Reducing Uncertainty in Contrail Radiative Forcing Resulting from Uncertainty in Ice Crystal Properties. Environ Sci Technol Lett 7, 371–375. https://doi.org/10.1021/acs.estlett.0c00150

Sausen, R., Isaksen, I., Grewe, V., Hauglustaine, D., Lee, D.S., Myhre, G., Köhler, M.O., Pitari, G., Schumann, U., Stordal, F., Zerefos, C., 2005. Aviation radiative forcing in 2000: An update on IPCC (1999). Meteorologische Zeitschrift 14, 555–561. https://doi.org/10.1127/0941-2948/2005/0049

Sausen, R., Schumann, U., 2000. Estimates of the Climate Response to Aircraft CO2 and NOx Emissions Scenarios. Clim Change 44, 27–58. https://doi.org/10.1023/A:1005579306109

Schäfer, A.W., Barrett, S.R.H., Doyme, K., Dray, L.M., Gnadt, A.R., Self, R., O'Sullivan, A., Synodinos, A.P., Torija, A.J., 2018. Technological, economic and environmental prospects of all-electric aircraft. Nature Energy 2018 4:2 4, 160–166. https://doi.org/10.1038/s41560-018-0294-x

Schäfer, A.W., Evans, A.D., Reynolds, T.G., Dray, L., 2015. Costs of mitigating CO2 emissions from passenger aircraft. Nature Climate Change 2015 6:4 6, 412–417. https://doi.org/10.1038/nclimate2865

Schumann, U., 1996. On conditions for contrail formation from aircraft exhausts. Meteorologische Zeitschrift 5, 4–23. https://doi.org/10.1127/metz/5/1996/4

Schumann, U., Graf, K., 2013. Aviation-induced cirrus and radiation changes at diurnal timescales. Journal of Geophysical Research: Atmospheres 118, 2404–2421. https://doi.org/10.1002/jgrd.50184

Schumann, U., Graf, K., Mannstein, H., 2011. Potential to reduce the climate impact of aviation by flight level changes. https://doi.org/10.2514/6.2011-3376

Schumann, U., Penner, J.E., Chen, Y., Zhou, C., Graf, K., 2015. Dehydration effects from contrails in a coupled contrail-climate model. Atmos Chem Phys 15, 11179–11199. https://doi.org/10.5194/acp-15-11179-2015

Schumann, U., Poll, I., Teoh, R., Koelle, R., Spinielli, E., Molloy, J., Koudis, G.S., Baumann, R., Bugliaro, L., Stettler, M., Voigt, C., 2021. Air traffic and contrail changes over Europe during COVID-19: a model study. Atmos Chem Phys 21, 7429–7450. https://doi.org/10.5194/acp-21-7429-2021

Seber, G., Malina, R., Pearlson, M.N., Olcay, H., Hileman, J.I., Barrett, S.R.H., 2014. Environmental and economic assessment of producing hydroprocessed jet and diesel fuel from waste oils and tallow. Biomass Bioenergy 67, 108–118. https://doi.org/10.1016/J.BIOMBIOE.2014.04.024

Seinfeld, J.H., Pandis, S.N., 2016. Atmospheric chemistry and physics : from air pollution to climate change, Third Edit. ed. Wiley.

Sharmina, M., Edelenbosch, O.Y., Wilson, C., Freeman, R., Gernaat, D.E.H.J., Gilbert, P., Larkin, A., Littleton, E.W., Traut, M., van Vuuren, D.P., Vaughan, N.E., Wood, F.R., Le Quéré, C., 2021. Decarbonising the critical sectors of aviation, shipping, road freight and industry to limit warming to 1.5–2°C. Climate Policy 21, 455–474. https://doi.org/10.1080/14693062.2020.1831430/SUPPL_FILE/TCPO_A_1831430_SM2186.DOCX

Shell, 2021. Decarbonizing Aviation: Cleared for Take-off.

Shindell, D.T., Lee, Y., Faluvegi, G., 2016. Climate and health impacts of US emissions reductions consistent with 2 °C. Nat Clim Chang 6, 503–507. https://doi.org/10.1038/nclimate2935

Simone, N.W., Stettler, M.E.J., Barrett, S.R.H., 2013. Rapid estimation of global civil aviation emissions with uncertainty quantification. Transp Res D Transp Environ 25, 33–41. https://doi.org/10.1016/J.TRD.2013.07.001

Skowron, A., Lee, D.S., De León, R.R., 2015. Variation of radiative forcings and global warming potentials from regional aviation NOx emissions. Atmos Environ. https://doi.org/10.1016/j.atmosenv.2014.12.043

Solomon, S., Daniel, J.S., Sanford, T.J., Murphy, D.M., Plattner, G.-K., Knutti, R., Friedlingstein, P., 2010. Persistence of climate changes due to a range of greenhouse gases. Proceedings of the National Academy of Sciences 107, 18354–18359. https://doi.org/10.1073/pnas.1006282107

Søvde, O.A., Matthes, S., Skowron, A., Iachetti, D., Lim, L., Owen, B., Hodnebrog, O., Di Genova, G., Pitari, G., Lee, D.S., Myhre, G., Isaksen, I.S.A., 2014. Aircraft emission mitigation by changing route altitude: A multi-model estimate of aircraft NOx emission impact on O3 photochemistry. Atmos Environ 95, 468–479. https://doi.org/10.1016/j.atmosenv.2014.06.049

Speth, R.L., Rojo, C., Malina, R., Barrett, S.R.H., 2015. Black carbon emissions reductions from combustion of alternative jet fuels. Atmos Environ 105, 37–42. https://doi.org/10.1016/j.atmosenv.2015.01.040

Spichtinger, P., Gierens, K., Leiterer, U., Dier, H., 2003. Ice supersaturation in the tropopause region over Lindenberg, Germany. Meteorologische Zeitschrift 12, 143–156. https://doi.org/10.1127/0941-2948/2003/0012-0143

Sridhar, B., Ng, H.K., Chen, N., 2012. Uncertainty quantification in the development of aviation operations to reduce aviation emissions and contrails, in: 28th International Congress of the Aeronautical Sciences.

Sridhar, B., Ng, H.K., Chen, N.Y., 2011. Aircraft trajectory optimization and contrails avoidance in the presence of winds, in: Journal of Guidance, Control, and Dynamics. American Institute of Aeronautics and Astronautics Inc., pp. 1577–1583. https://doi.org/10.2514/1.53378

Staples, M.D., Malina, R., Olcay, H., Pearlson, M.N., Hileman, J.I., Boies, A., Barrett, S.R.H., 2014. Lifecycle greenhouse gas footprint and minimum selling price of renewable diesel and jet fuel from fermentation and advanced fermentation production technologies. Energy Environ Sci 7, 1545–1554. https://doi.org/10.1039/C3EE43655A

Staples, M.D., Malina, R., Suresh, P., Hileman, J.I., Barrett, S.R.H., 2018. Aviation CO2 emissions reductions from the use of alternative jet fuels. Energy Policy 114, 342–354. https://doi.org/10.1016/J.ENPOL.2017.12.007

Stettler, M.E.J., Boies, A.M., Petzold, A., Barrett, S.R.H., 2013. Global civil aviation black carbon emissions. Environ Sci Technol 47, 10397–10404. https://doi.org/10.1021/es401356v

Stettler, M.E.J., Eastham, S., Barrett, S.R.H., 2011. Air quality and public health impacts of UK airports. Part I: Emissions. Atmos Environ 45, 5415–5424. https://doi.org/10.1016/J.ATMOSENV.2011.07.012

Stevenson, D.S., Doherty, R.M., Sanderson, M.G., Collins, W.J., Johnson, C.E., Derwent, R.G., 2004. Radiative forcing from aircraft NOx emissions: Mechanisms and seasonal dependence. J Geophys Res 109, D17307. https://doi.org/10.1029/2004JD004759

Stratton, R.W., Wong, H.M., Hileman, J.I., 2010. Life cycle greenhouse gas emissions from alternative jet fuel, PARTNER Project 28 report, Version 1.2, MIT. Cambridge.

Ström, L., Gierens, K., 2002. First simulations of cryoplane contrails. Journal of Geophysical Research Atmospheres 107, AAC 2-1-AAC 2-13. https://doi.org/10.1029/2001JD000838

Stuber, N., Forster, P., Rädel, G., Shine, K., 2006. The importance of the diurnal and annual cycle of air traffic for contrail radiative forcing. Nature 441, 864–867. https://doi.org/10.1038/nature04877

Suresh, P., 2016. Environmental and economic assessment of transportation fuels from municipal solid waste. Massachusetts Institute of Technology.

Sutkus, D.J., Baughcum, S.L., DeBois, D.P., 2001. Scheduled Civil Aircraft Emission Inventories for 1999: Database Development and Analysis.

Teoh, R., Engberg, Z., Shapiro, M., Dray, L., Stettler, M.E.J., 2023. A high-resolution Global Aviation emissions Inventory based on ADS-B (GAIA) for 2019-2021. https://doi.org/10.5194/egusphere-2023-724

Teoh, R., Schumann, U., Gryspeerdt, E., Shapiro, M., Molloy, J., Koudis, G., Voigt, C., Stettler, M.E.J., 2022. Aviation contrail climate effects in the North Atlantic from 2016 to 2021. Atmos Chem Phys 22, 10919–10935. https://doi.org/10.5194/acp-22-10919-2022

Teoh, R., Schumann, U., Majumdar, A., Stettler, M.E.J., 2020. Mitigating the Climate Forcing of Aircraft Contrails by Small-Scale Diversions and Technology Adoption. Environ Sci Technol 54, acs.est.9b05608. https://doi.org/10.1021/acs.est.9b05608

Terrenoire, E., Hauglustaine, D.A., Gasser, T., Penanhoat, O., 2019. The contribution of carbon dioxide emissions from the aviation sector to future climate change. https://doi.org/10.1088/1748-9326/ab3086

Thompson, T.M., Saari, R.K., Selin, N.E., 2014. Atmospheric Chemistry and Physics Air quality resolution for health impact assessment: influence of regional characteristics. Atmos. Chem. Phys 14, 969–978. https://doi.org/10.5194/acp-14-969-2014

Timko, M.T., Yu, Z., Onasch, T.B., Wong, H.W., Miake-Lye, R.C., Beyersdorf, A.J., Anderson, B.E., Thornhill, K.L., Winstead, E.L., Corporan, E., Dewitt, M.J., Klingshirn, C.D., Wey, C., Tacina, K., Liscinsky, D.S., Howard, R., Bhargava, A., 2010. Particulate emissions of gas turbine engine combustion of a fischer-tropsch synthetic fuel. Energy and Fuels 24, 5883–5896. https://doi.org/10.1021/ef100727t

Tollefsen, P., Rypdal, K., Torvanger, A., Rive, N., 2009. Air pollution policies in Europe: efficiency gains from integrating climate effects with damage costs to health and crops. Environ Sci Policy 12, 870–881. https://doi.org/10.1016/J.ENVSCI.2009.08.006

Tompkins, A.M., Gierens, K., Rädel, G., 2007. Ice supersaturation in the ECMWF integrated forecast system. Quarterly Journal of the Royal Meteorological Society 133, 53–63. https://doi.org/10.1002/qj.14

Turner, M.C., Jerrett, M., Pope, C.A., Krewski, D., Gapstur, S.M., Diver, W.R., Beckerman, B.S., Marshall, J.D., Su, J., Crouse, D.L., Burnett, R.T., 2016. Long-Term Ozone Exposure and Mortality in a Large Prospective Study. Am J Respir Crit Care Med 193, 1134–1142. https://doi.org/10.1164/rccm.201508-1633OC

Turner, M.D., Henze, D.K., Capps, S.L., Hakami, A., Zhao, S., Resler, J., Carmichael, G.R., Stanier, C.O., Baek, J., Sandu, A., Russell, A.G., Nenes, A., Pinder, R.W., Napelenok, S.L., Bash, J.O., Percell, P.B., Chai, T., 2015. Premature deaths attributed to source-specific BC emissions in six urban US regions. Environmental Research Letters 10, 114014. https://doi.org/10.1088/1748-9326/10/11/114014

Unal, A., Hu, Y., Chang, M.E., Talat Odman, M., Russell, A.G., 2005. Airport related emissions and impacts on air quality: Application to the Atlanta International Airport. Atmos Environ 39, 5787–5798. https://doi.org/10.1016/J.ATMOSENV.2005.05.051

UNFCCC, 2017. What is the Paris Agreement [WWW Document]. URL https://unfccc.int/process-and-meetings/the-paris-agreement/what-is-the-paris-agreement (accessed 12.18.19).

United Nations, 2023. For a livable climate: Net-zero commitments must be backed by credible action [WWW Document]. URL https://www.un.org/en/climatechange/net-zero-coalition (accessed 11.6.23).

US EPA, 2016. Recommended Income Elasticity and Income Growth Estimates: Technical Memorandum.

US EPA, 2015. 2011 National Emissions Inventory, version 2 Technical Support Document. North Carolina.

US EPA, 2014. Guidelines for Preparing Economic Analysis (2010, revised 2014).

US EPA, 2004. Advisory Council on Clean Air Compliance Analysis Response to Agency Request on Cessation Lag. Washington D.C.

US Government, 2021. Technical Support Document: Social Cost of Carbon, Methane, and Nitrous Oxide: Interim Estimates under Executive Order 13990.

US Government, 2016. Technical Support Document: - Technical Update of the Social Cost of Carbon for Regulatory Impact Analysis.

US Government, 2015. Aviation greenhouse gas emissions reduction plan.

van der Sman, E., Peerlings, B., Kos, J., Lieshout, R., Boonekamp, T., 2021. Destination 2050-A route to net zero European aviation.

van Vuuren, D.P., Edmonds, J., Kainuma, M., Riahi, K., Thomson, A., Hibbard, K., Hurtt, G.C., Kram, T., Krey, V., Lamarque, J.-F., Masui, T., Meinshausen, M., Nakicenovic, N., Smith, S.J., Rose, S.K., 2011. The representative concentration pathways: an overview. Clim Change 109, 5–31. https://doi.org/10.1007/s10584-011-0148-z

Voigt, C., Kleine, J., Sauer, D., Moore, R.H., Bräuer, T., Le Clercq, P., Kaufmann, S., Scheibe, M., Jurkat-Witschas, T., Aigner, M., Bauder, U., Boose, Y., Borrmann, S., Crosbie, E., Diskin, G.S., DiGangi, J., Hahn, V., Heckl, C., Huber, F., Nowak, J.B., Rapp, M., Rauch, B., Robinson, C., Schripp, T., Shook, M., Winstead, E., Ziemba, L., Schlager, H., Anderson, B.E., 2021. Cleaner burning aviation fuels can reduce contrail cloudiness. Commun Earth Environ 2, 114. https://doi.org/10.1038/s43247-021-00174-y

Walker, J.M., Philip, S., Martin, R. V, Seinfeld, J.H., 2012. Simulation of nitrate, sulfate, and ammonium aerosols over the United States. Atmos. Chem. Phys 12, 11213–11227. https://doi.org/10.5194/acp-12-11213-2012

WEF, 2020. Clean Skies for Tomorrow: Sustainable Aviation Fuel as a Pathway to Net-Zero Aviation.

WHO, 2018. Global Health Estimates 2016: Disease burden by Cause, Age, Sex, by Country and by Region, 2000-2016. Geneva.

Wild, O., Prather, M.J., Akimoto, H., 2001. Indirect long-term global radiative cooling from NOx emissions. Geophys Res Lett 28, 1719–1722. https://doi.org/10.1029/2000GL012573

Wilkerson, J.T., Jacobson, M.Z., Malwitz, A., Balasubramanian, S.N., Wayson, R., Fleming, G., Naiman, A.D., Lele, S.K., 2010. Analysis of emission data from global commercial aviation: 2004 and 2006. Atmos Chem Phys 10, 6391–6408. https://doi.org/10.5194/acp-10-6391-2010

Withers, M.R., Malina, R., Gilmore, C.K., Gibbs, J.M., Trigg, C., Wolfe, P.J., Trivedi, P., Barrett, S.R.H., 2014. Economic and environmental assessment of liquefied natural gas as a supplemental aircraft fuel. Progress in Aerospace Sciences. https://doi.org/10.1016/j.paerosci.2013.12.002

Wolfe, P.J., 2015. Chapter 3: Modeling aviation's impact on the environment, in: Aviation Environmental Policy and Issues of Timescale. Massachusetts Institute of Technology.

Wolfe, P.J., 2012. Aviation environmental policy effects on national- and regional- scale air quality , noise , and climate impacts. Massachusetts Institute of Technology.

World Bank Group, 2018. State and Trends of Carbon Pricing 2018. Washington DC. https://doi.org/10.1596/978-1-4648-1292-7

Wuebbles, D., Forster, P., Rogers, H., Herman, R., Wuebbles, D., Forster, P., Rogers, H., Herman, R., 2010. Issues and Uncertainties Affecting Metrics For Aviation Impacts on Climate. Bull Am Meteorol Soc 91, 491–496. https://doi.org/10.1175/2009BAMS2840.1

Yim, S.H.L., Lee, G.L., Lee, I.H., Allroggen, F., Ashok, A., Caiazzo, F., Eastham, S.D., Malina, R., Barrett, S.R.H., 2015. Global, regional and local health impacts of civil aviation emissions. Environmental Research Letters 10, 034001. https://doi.org/10.1088/1748-9326/10/3/034001

Yim, S.H.L., Stettler, M.E.J., Barrett, S.R.H., 2013. Air quality and public health impacts of UK airports. Part II: Impacts and policy assessment. Atmos Environ 67, 184–192. https://doi.org/10.1016/J.ATMOSENV.2012.10.017

Yin, F., Grewe, V., Frömming, C., Yamashita, H., 2018. Impact on flight trajectory characteristics when avoiding the formation of persistent contrails for transatlantic flights. Transp Res D Transp Environ 65, 466–484. https://doi.org/10.1016/j.trd.2018.09.017